

Power Oscillation Damping in Hybrid Power Plants

Stability Analysis and Experimental Validation

Kaare L. Lund and Simon M. Élev

Electrical Power System and High Voltage Engineering, EPSH4-1035, 2025-05

Master's Thesis, 4th Semester





AALBORG UNIVERSITY

STUDENT REPORT

AAU Energy
Aalborg University
9220 Aalborg Øst
Pontoppidanstræde 111
<http://www.energy.aau.dk/>

Title:

Power Oscillation Damping in Hybrid Power Plants

Theme:

Master's Thesis

Project Period:

Spring Semester 2025

Project Group:

EPSH4-1035

Participant(s):

Kaare Lybech Lund
Simon Madsen Élev

Supervisor(s):

Yajuan Guan

Page Numbers: 136**Date of Completion:**

May 28, 2025

Abstract:

As power systems transition away from synchronous generators to inverter-based resources, concerns about stability and insufficient system damping continue to grow. This thesis investigates the implementation of *power oscillation damping* (POD) in hybrid power plants composed of wind turbines, photovoltaic panels, and battery energy storage systems. Two control approaches, POD-P and POD-Q, based on active and reactive power deviations respectively, were designed using lead-lag compensators. A state-space modelling framework was developed to analyse system stability and guide the tuning of these controllers. The models were validated through time-domain simulations and experimental tests using a dSPACE hardware-in-the-loop setup. While both POD-P and POD-Q reduced oscillation amplitudes under specific conditions, the results highlighted the limitations of using static compensators in dynamic grid environments. POD-P, in particular, was sensitive to signal disturbances, requiring the addition of a low-pass filter to be practically viable. The findings indicate that while passive POD strategies can offer some improvement, more adaptive control approaches may be necessary to meet evolving grid stability requirements.

Summary

The global transition from synchronous generators to inverter-based renewable energy sources has introduced new challenges to power system stability. *Hybrid power plants* (HPPs) combining wind turbines, photovoltaic panels, and battery energy storage systems have become more common. However, these systems rely on grid-following inverters that lack the inherent inertia and damping provided by synchronous machines, prompting updates in modern grid codes to include *power oscillation damping* (POD) requirements for large-scale plants.

This thesis explores POD control in HPPs with a focus on two types of controllers: POD-P (based on active power deviation) and POD-Q (based on reactive power deviation). In collaboration with Eurowind Energy, the feasibility, effectiveness, and practical limitations of these strategies were assessed. The controllers were implemented using passive lead-lag compensators and integrated into a grid-following inverter structure. Initial evaluation was performed through time-domain simulations in MATLAB/Simulink, and a comprehensive small-signal state-space model was developed for both single- and multi-inverter systems. This allowed eigenvalue analysis and participation factor studies to determine the impact of the POD schemes on system stability and identify which states most influenced oscillatory behavior.

Experimental validation was carried out using a dSPACE control-in-the-loop setup. The tests confirmed that both POD-P and POD-Q effectively reduced oscillation amplitudes in the 0.2–1.25 Hz range, though their performance varied. In particular, the POD-P controller struggled with noise in power measurements, which limited the observable oscillation-to-noise ratio; this was mitigated by introducing a second-order low-pass filter to improve signal quality. In contrast, POD-Q, based on voltage magnitude deviation, was less affected by noise.

Despite their basic effectiveness, the passive compensators pose a key limitation because they are tuned for a specific frequency range and degrade at higher oscillations—especially for POD-P—making them unsuitable for the dynamic environments of real-world grids, where grid impedance and oscillation modes can shift over time. Furthermore, practical implementation challenges such as communication delays, sensor noise, and control loop limitations underscore the gap between theoretical models and performance in the field.

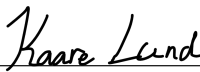
In conclusion, while the implemented POD-P and POD-Q controllers reduced power oscillations under controlled conditions, their limited adaptability restricts their usefulness in variable grid environments. These findings point to the need for more flexible or adaptive control strategies in future work. Nonetheless, this thesis provides a solid foundation for evaluating POD in hybrid power plants and offers practical insights into the modelling and implementation process.


Preface

This fourth-semester master's thesis was done as a project collaboration with Eurowind Energy. The project was done by group EPSH4-1035 and was supervised by Yajuan Guan. This project focuses on the implementation of power oscillation damping control in hybrid power plants. We would like to sincerely thank our supervisor for their valuable feedback, guidance and support throughout the project. The group would furthermore like to thank Eurowind Energy for making the project possible.

The following software and hardware have been used during the writing of this report:

- Overleaf for text processing
- MathWorks MATLAB/Simulink for modeling, simulation and experimental implementation
- dSPACE for hardware-in-the-loop testing
- ControlDesk for real-time interaction with the experimental setup
- Inkscape for figure composing


Kaare Lybech Lund


Simon Madsen Élev

Abbreviations

Abbreviation	Meaning
BESS	Battery Energy Storage System
CSI	Current-Source Inverter
DC	Direct current
DER	Distributed Energy Resource
DSO	Distribution System Operator
EMS	Energy Management System
FRT	Fault Ride Through
HPPC	Hybrid Power Plant Controller
HPP	Hybrid Power Plant
IBR	Inverter-Based Resource
LC	Inductor-Capacitor
LCL	Inductor-Capacitor-Inductor
LPF	Low-Pass Filter
MIMO	Multiple-Input Multiple-Output
MPPT	Maximum Power Point Tracking
PCC	Point of Common Coupling
PI	Proportional-Integral
PLL	Phase-Locked Loop
POD	Power Oscillation Damping
POD-P	Power Oscillation Damping – Active Power
POD-Q	Power Oscillation Damping – Reactive Power
POC	Point of Connection
PPC	Power Plant Controller
PSS	Power System Stabiliser
PV	Photovoltaic
RES	Renewable Energy Sources
RfG	Requirements for Generators
SISO	Single-Input Single-Output
SSM	State-Space Model
SRF-PLL	Synchronous Reference Frame Phase-Locked Loop
TSO	Transmission System Operator
VSI	Voltage-Source Inverter

Nomenclature

Units of measurement		
Symbol	Explanation	Unit
A	State-space matrix A	[–]
A_{POD}	POD state matrix	[–]
B	State-space matrix B	[–]
$B_{INV+POD}$	Input matrix of inverter+POD model	[–]
B_{POD}	POD input matrix	[–]
C	State-space matrix C	[–]
C_1	Capacitance 1 in cable PI section	[F]
C_2	Capacitance 2 in cable PI section	[F]
C_f	Filter capacitance	[F]
$C_{CL}(s)$	Closed-loop transfer function	[–]
$C_{LL}(s)$	Lead-lag compensator transfer function	[–]
$C_{POD}(s)$	POD compensator transfer function	[–]
C_{POD}	POD output matrix	[–]
C_{INV}	Inverter output matrix	[–]
D	State-space matrix D	[–]
f	Frequency	[Hz]
$H_{LPF}(s)$	Low-pass filter transfer function	[–]
$H_{VQ}(s)$	Transfer from voltage to reactive power	[–]
$H_{wo}(s)$	Washout filter transfer function	[–]
k	POD gain factor	[–]
k_{POD}	POD gain	[–]
$k_{POD-P,init}$	Initial gain for POD-P	[–]
k_{POD-Q}	Gain for POD-Q	[–]
L_c	Output impedance inductance	[H]
L_f	Filter inductance	[H]
λ	Regularization factor	[–]
P	Active power	[W]
Q	Reactive power	[VAr]
R_c	Output impedance resistance	[Ω]
R_f	Filter resistance	[Ω]
T_s	Sampling time	[s]
T_{1-4}	Lead/lag time constants	[s]
T_{LP}	Time constant of LPF	[s]
T_W	Time constant of washout filter	[s]
$u(t)$	State-space input vector	[–]
v_{cd}, v_{cq}	Capacitor voltage dq-components	[V]
v_o	Output voltage	[V]
$x(t)$	State-space state vector	[–]

Units of measurement (cont'd)		
Symbol	Explanation	Unit
$y(t)$	State-space output vector	[–]
$\dot{x}(t)$	Time derivative of state vector	[–]
ΔP	Active power deviation	[W]
ΔQ	Reactive power deviation	[VAr]
$\Delta d'$	Washout filter intermediate state	[–]
$\Delta h'$	Intermediate state for lag element	[–]
$\Delta i_{o,dq}$	Output current deviation (dq-frame)	[A]
$\Delta i_{t,dq}$	Filter inductor current deviation	[A]
$\Delta \gamma_{dq}$	Integrator state (current controller)	[–]
$\Delta \omega$	Frequency deviation	[rad/s]
$\Delta \phi_{dq}$	Integrator state (power controller)	[–]
$\Delta \rho$	PLL integrator state	[rad]
$\Delta \theta$	PLL angle deviation	[rad]
$\Delta v_{t,dq}^*$	Modulation voltage reference	[V]
$\Delta v_{b,dq}$	Bus voltage deviation (dq-frame)	[V]
$\Delta v_{del,dq}$	Delayed modulation signal	[V]
$\Delta v_{o,dq}$	Output voltage deviation (dq-frame)	[V]
Δw	Intermediate filter state	[–]
$\Delta z'$	Intermediate state for lead-lag filter	[–]
ω	Angular frequency	[rad/s]
ω_n	Nominal angular frequency	[rad/s]
$\theta_{CL}(\omega)$	Phase shift of closed-loop power controller	[rad]
$\theta_{ll,PODQ}(\omega)$	Total POD-Q compensator phase shift	[rad]
$\theta_{ll,PODP}(\omega)$	Total POD-P compensator phase shift	[rad]
$\theta_{lpf}(\omega)$	LPF phase shift	[rad]
θ_{target}	Desired phase shift at ω	[rad]
$\theta_{VQ}(\omega)$	Phase shift between voltage and Q	[rad]
$\theta_{wo}(\omega)$	Washout filter phase shift	[rad]

List of Tables

2.1	Definition of oscillation modes from different articles and books.	6
3.1	System parameter values.	16
3.2	POD-P parameters used for simulation results	27
3.3	POD-Q parameters used for simulation results	28
4.1	Overview of single-inverter state-space model inputs (u) and explicit outputs ($\Delta y_k \neq \Delta x_k$).	41
4.2	Overview of state-space model errors compared to simulation with bold font highlighting the larger deviations.	54
4.3	Summary of values used for convergence plots, where $L_{g,s}$ is the starting inductance and $L_{g,u}$ is the value at which the system is unstable.	59
4.4	Comparison of eigenvalues for with and without POD-P control.	69
4.5	Comparison of eigenvalues for with and without POD-Q control.	72
5.1	Data for experimental setup.	76
5.2	POD parameters used for experimental results	82
5.3	Amplitude reduction at various oscillation frequencies for POD-P.	84
5.4	Amplitude reduction at various oscillation frequencies for POD-Q.	85

List of Figures

1.1	Hybrid power plant concept illustration.	1
2.1	Hybrid power plant configurations: a) common DC bus, b) WT AC connection and BESS + PV DC bus, c) common AC bus.	2
2.2	Hybrid power plant control architecture.	3
2.3	Simple grid-connected inverter with control diagram.	5
2.4	Illustration of generating unit with governor-, AVR- and PSS control.	7
2.5	Block diagram of a standard power system stabiliser.	8
2.6	Bode plot of washout filter.	8
2.7	Bode plot of phase compensation.	9
2.8	Bode plot of washout filter, phase compensation and gain.	10
2.9	Example of POD-P and POD-Q control fed into the error signal.	10
2.10	POD-P and POD-Q control structure. Adapted from [2].	11
3.1	Inverter system.	15
3.2	Inverter with LC-filter and KVL loop.	16
3.3	Block diagram of current control loop.	17
3.4	Compensated inner current loop bode plots.	18
3.5	Power control block diagram.	19
3.6	Block diagram representation of the d- and q component equations with cross-decoupling and feed-forward compensation (red).	20
3.7	Block diagram representation of the KVL and KCL dq0 equations.	21
3.8	Block diagram reduction: current control loop plant transfer function.	21
3.9	Block diagram reduction: power control loop transfer function.	21
3.10	Comparison of simple and detailed power plant transfer function.	22
3.11	Compensated outer power loop bode plots.	23
3.12	Block diagram of the SRF-PLL	24
3.13	POD control schemes.	24
3.14	Simulation results for POD-P	28
3.15	Simulation results for POD-Q.	29
4.1	Basic representation of a state-space model.	30
4.2	Overview of the single-inverter state-space model.	33
4.3	Control diagram of the power controller with highlighted state variables and outputs.	34
4.4	Control diagram of the current control loop with state variables and outputs highlighted.	36
4.5	Control diagram of the PLL with the state variables and output highlighted.	39
4.6	Illustration of PLL dq frame rotation.	40
4.7	Overview of multi-inverter system configuration.	43

4.8	Block diagrams of POD control scheme with the top showing the standard form and the bottom showing the extended version with intermediate states.	47
4.9	POD control in the power controllers.	49
4.10	Comparison of non-integrator state variables to simulation results	52
4.11	Bar chart of absolute errors and percentage errors for an active power step up.	53
4.12	Bode plot comparison of closed-loop transfer functions.	54
4.13	Eigenvalue plot at $P = 300$ W for L_g varying from $= 0.11$ H to 0.15 H, becoming unstable at 0.1405 H as the real part crosses zero.	56
4.14	Eigenvalue plot at $P = 600$ W for L_g varying from $= 0.055$ H to 0.07 H, becoming unstable at 0.06546 H as the real part crosses zero.	56
4.15	Eigenvalue plot at $P = 900$ W for L_g varying from $= 0.035$ H to 0.05 H, becoming unstable at 0.04883 H as the real part crosses zero.	57
4.16	Heat map of participation factors of each state variable for each eigenvector with the inverter operating at an active power of 900 W.	57
4.17	Diagram of instability trend with a varying L_g and active power.	58
4.18	Convergence of instability against starting inductance for active power of 900 W.	59
4.19	Varying the coupling inductance until the system is unstable.	61
4.20	Zoom-in of voltages and current when instability occurs.	61
4.21	Active- and reactive power, voltage and current comparison during active power steps for the multi inverter models.	62
4.22	Active- and reactive power zoom-in comparison during active power steps for the multi-inverter models.	63
4.23	Voltage zoom-in comparison during active power steps for the multi-inverter models.	64
4.24	Current zoom-in comparison during active power steps for the multi-inverter models.	64
4.25	Zoom-in of bus voltage and grid current during active power steps.	65
4.26	Bar chart of absolute errors and percentage errors for inverter 1 for the active power step up of inverter 1.	65
4.27	Comparison of multi-inverter eigenvalues with those of the single inverter.	66
4.28	Eigenvalue plot at $P = 900$ W (300 W for each inverter) for L_g varying from $= 0.035$ H to 0.06 H, becoming unstable at 0.05545 H as the real part crosses zero.	67
4.29	State-space simulation with and without POD-P.	68
4.30	Eigenvalues of single-inverter A -matrix with and without POD-P control.	68
4.31	Participation factors of the matrices with and without POD-P control.	69
4.32	Eigenvalue parameter sweep of POD-P gain, where $k = -0.0001 \dots -0.03$	70
4.33	State-space simulation with and without POD-Q.	71
4.34	Eigenvalues of single-inverter A -matrix with and without POD-Q control.	71
4.35	Participation factors of the matrices with and without POD-Q control.	72
4.36	Eigenvalue parameter sweep of POD-Q gain, where $k = -0.0001 \dots -0.03$	73
5.1	Front of lab setup.	74
5.2	Back of lab setup.	74
5.3	Illustration of the configuration of the inverters in the experimental setup.	75

5.4	Block diagram of Phase Synchronization	76
5.5	Block diagram of voltage magnitude synchronisation.	77
5.6	Comparison of experimental results to SSM for a 300W active power step up.	77
5.7	Experimental results during a 300W active power step up.	78
5.8	Multi inverter active power steps.	79
5.9	Output current of each inverter for each active power step.	80
5.10	Power measurement response to a force frequency oscillation	81
5.11	Active Power oscillation damping at different frequencies	83
5.12	FFT analysis of measured active power before and after POD-P.	84
5.13	Reactive Power oscillation damping at different frequencies.	85
5.14	FFT analysis of the measured reactive power before and after activation of POD-Q.	86
B.4.1	Comparison of non-integrator state variables to simulation results	XII
B.4.2	Comparison of non-integrator state variables to simulation results	XIII
B.4.3	Comparison of non-integrator state variables to simulation results	XIV
B.4.4	Bar chart of absolute errors and percentage errors for an active power step down.	XV
B.4.5	Bar chart of absolute errors and percentage errors for an reactive power step up.	XV
B.4.6	Bar chart of absolute errors and percentage errors for an reactive power step down.	XV
B.4.7	Comparison of results for two different solver settings (solid: state-space model; dashed: simulation).	XVI
B.4.8	Bar chart of absolute errors and percentage errors for inverter 1 for an active power step down.	XVII
B.4.9	Bar chart of absolute errors and percentage errors for inverter 2 for an active power step up.	XVIII
B.4.10	Bar chart of absolute errors and percentage errors for inverter 2 for an active power step down.	XVIII
B.4.11	Bar chart of absolute errors and percentage errors for inverter 3 for an active power step up.	XVIII
B.4.12	Bar chart of absolute errors and percentage errors for inverter 3 for an active power step down.	XIX
B.4.13	Heat map of participation factor of each state variable belonging to each eigenvector at 600 W.	XIX
B.4.14	Heat map of participation factor of each state variable belonging to each eigenvector at 300 W.	XX
B.4.15	Convergence of instability against starting inductance for active power of 600 W.	XX
B.4.16	Convergence of instability against starting inductance for active power of 300 W.	XX
C.1.1	Comparison of experimental results to SSM for a 300W active power step down.	XXI
C.1.2	Comparison of experimental results to SSM for a 300VAr reactive power step up.	XXI
C.1.3	Comparison of experimental results to SSM for a 300VAr reactive power step down.	XXII
C.1.4	Experimental results during a 300W active power step down.	XXII
C.1.5	Experimental results during a 300VAr reactive power step up.	XXII

C.1.6	Experimental results during a 300VAr reactive power step down.	XXIII
C.2.1	Multi inverter reactive power steps.	XXIII
C.2.2	Capacitor voltage of each inverter for each active power step.	XXIV
C.2.3	Output current of each inverter for each reactive power step.	XXIV
C.2.4	Capacitor voltage of each inverter for each active power step.	XXV

Contents

1	Introduction	1
2	State of the Art	2
2.1	Hybrid Power Plants	2
2.1.1	Configuration of Hybrid Power Plants	2
2.1.2	Control Architecture	3
2.1.3	Converter System Control	4
2.2	Power Oscillations	6
2.2.1	Power System Stabiliser	7
2.2.2	Power Oscillation Damping Control	10
2.3	Power Oscillation Damping in Grid Codes	12
2.4	Specifying the Project Scope	13
2.4.1	Project Outline	14
3	Modelling and Control Design	15
3.1	System	15
3.2	Control Design	16
3.2.1	Current Control	16
3.2.2	Power Controll	18
3.2.3	Grid Synchronisation	23
3.3	POD Control Design	24
3.3.1	Delay and Gain	24
3.3.2	Delay Compensation	26
3.3.3	Simulation of POD Control	27
3.4	Summary	29
4	Stability Analysis	30
4.1	State-Space Modelling	30
4.1.1	State-Space Representation	30
4.1.2	Small-Signal Linearisation	31
4.1.3	Eigenvalue Stability Analysis	32
4.2	State-Space Model of a Single Inverter	32
4.2.1	Power Controller	34
4.2.2	Current Controller	36
4.2.3	Delay	37
4.2.4	LCL Filter	38
4.2.5	PLL	39
4.2.6	Combined Single-Inverter Model	41
4.3	State-Space Model of Multiple Inverters	42
4.3.1	Grid Model	43
4.3.2	Bus Voltage and Current Relation	44

4.3.3	Single-Inverter Modification	44
4.3.4	PLL Modification	45
4.3.5	Combined Multi-Inverter State-Space Model	46
4.4	State-Space Model of the POD Control	47
4.4.1	POD State-Space Model	47
4.4.2	Combined POD and Inverter State-Space Model	49
4.5	Comparison of Simulation and State-Space Results	51
4.5.1	Comparison of Single-Inverter Dynamics	51
4.5.2	Comparison of Single-Inverter Closed-Loop Transfer Functions	54
4.5.3	Comparison of Single-Inverter Stability	55
4.5.4	Comparison of Multi-Inverter Dynamics	62
4.5.5	Comparison of Multi-Inverter Eigenvalues	66
4.6	POD Control Stability Analysis	67
4.6.1	POD-P Stability Analysis	67
4.6.2	POD-Q Stability Analysis	71
4.7	Summary	73
5	Experimental Validation	74
5.1	Experimental Setup	74
5.2	Initial Grid Synchronisation	76
5.3	Single Inverter	77
5.4	Multi Inverter	78
5.5	POD Control	81
5.5.1	Implementation	81
5.5.2	POD-P Results	82
5.5.3	POD-Q Results	84
5.6	Summary	87
6	Discussion	89
7	Conclusion	92
8	Future Work	93
	Bibliography	95
A	Modelling	I
A.1	Control	I
A.1.1	Current Control	I
A.1.2	SRF-PLL Transfer Function Derivation	II
B	Stability	III
B.1	Single Inverter State-Space Model	III
B.1.1	Power Controller	III
B.1.2	Current Controller	IV
B.1.3	Delay	V

B.1.4	LCL Filter	V
B.1.5	PLL	VI
B.1.6	Single Inverter	VII
B.2	Multi Inverter State-Space Model	IX
B.2.1	Modified Single Inverter	IX
B.3	POD State-Space Model	X
B.4	Comparison of SSM to Simulation	XII
B.4.1	Single Inverter Comparison	XII
B.4.2	Multi Inverter Comparison	XVII
B.4.3	Stability Analysis Comparison	XIX
C	Experimental Validation	XXI
C.1	Single Inverter	XXI
C.2	Multi Inverter	XXIII

1 Introduction

The penetration of *renewable energy sources* (RES) in the grid is increasing. Many concerns are being raised regarding power system stability in the near future. The addition of *hybrid power plants* (HPPs), most commonly consisting of *wind turbines* (WTs), *photovoltaic* (PV) panels, and a *battery energy storage system* (BESS), but may also incorporate other technologies (generators, PtX, biogas, etc.), can offer reliable and stable electricity supply. By employing multiple technologies, such as PV, WTs and BESS, the inherent intermittency of RES can be mitigated, resulting in a more stable electricity supply [1].

However, since the characteristics of *inverter-based resources* (IBRs) are different from traditional synchronous generators, grid codes have been updated to take this into account and will continue to be updated in the future [2]. Synchronous generators have inherent properties that add inertia and damping to the system [3]. When replaced by IBRs, these important properties will be lacking in the power system and control algorithms and grid codes need to be updated to ensure stable and reliable operation of the grid.

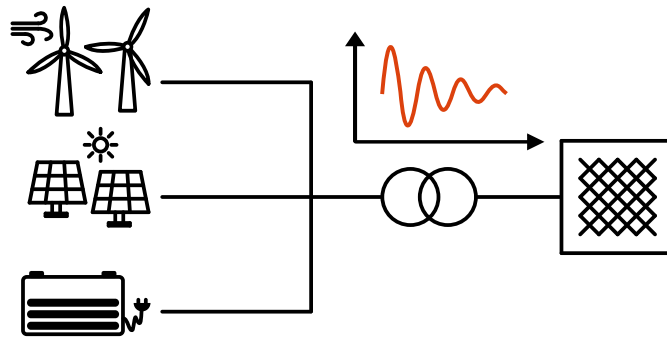


Figure 1.1 Hybrid power plant concept illustration.

The inherent damping of synchronous generators helps mitigate power oscillations in the grid. However, the parallel operation of multiple synchronous generators and interconnected power systems has historically contributed to the occurrence of power oscillations. Therefore, various methodologies were developed and used to mitigate these oscillations. One of these were the *power system stabiliser* (PSS) added to the control scheme of synchronous generators [4] [5].

As synchronous generators are replaced by IBRs, the system loses both the inherent damping and inertia provided by synchronous machines, as well as the damping capability of the PSS. This leads to the future, or for some current, issue of adding *power oscillation damping* (POD) control to IBRs and renewable power plants [6]. Several countries have already added some kind of POD requirement to their grid codes [2] [5].

This project is written in collaboration with Eurowind Energy. They are interested in the investigation into POD control, as it is a possibility that there will also be added POD requirements to the Danish grid codes in the future. Additionally, they have power plants in many parts of the world and will be dealing with issues related to POD at some point.

2 State of the Art

This chapter will present the relevant state of the art for the project. First, hybrid power plants will be described and explained, including the configuration, control architecture and converter control. Secondly, the definition of power oscillations will be presented, followed by an explanation of PSS and POD. Then, grid codes relevant for POD from several countries will be presented. Finally, the scope of the project and the project goals will be defined.

2.1 Hybrid Power Plants

A hybrid power plant is a collection of *distributed energy resources* (DERs) that are all behind the same POC and under control of the same high-level controller. The collection of different DERs helps ensure stability of power supply and allows for increased profits if combined with BESS. Therefore, HPPs are both interesting concepts for the grid operators (TSO and DSO) and power plant owner/operator. The DERs can be many different technologies, but WTs, PV panels and BESS are the most common [1].

2.1.1 Configuration of Hybrid Power Plants

The DERs inside the HPP can be connected in many ways and the conversions can happen at various places. Generally, there are three ways of configuring the HPP. These are, as seen in Figure 2.1: common DC bus with separate connections, DC bus for PV + BESS with WTs connected separately, and common AC bus with separate connections.

Configuration a offers a solution where WTs, PV panels, and BESS are connected separately to a common DC bus. This arrangement enables a simplified grid connection, requiring only a single DC-AC conversion stage to the POC. If the DERs are physically close to one another, this configuration can also reduce cabling and wiring costs. However, the limited availability of mature DC protection equipment and turn-key DC solutions currently makes this configuration less practical [1].

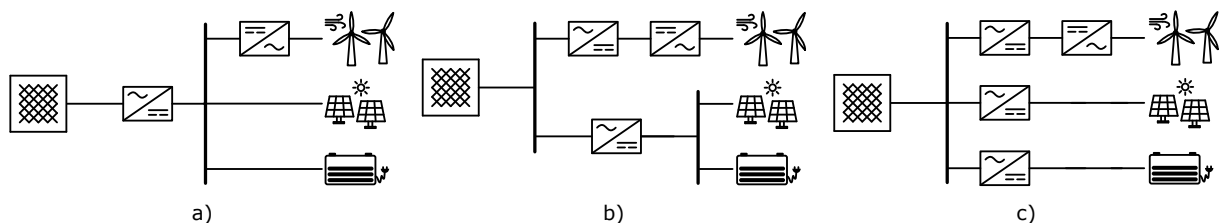


Figure 2.1 Hybrid power plant configurations: a) common DC bus, b) WT AC connection and BESS + PV DC bus, c) common AC bus.

Configuration b consists of PV panels and BESS connected to a common DC bus, while WTs are connected to the AC bus at the POC. This configuration enables close coordination between the PV panels and the BESS, particularly for efficient charging and discharging. Compared to configuration a, this DC architecture is more readily available and practical. It is especially

advantageous if a significant portion of the energy stored in the BESS is expected to originate from the PV panels [1]. However, if the BESS capacity is significantly larger than the PV panel capacity, or if the wind turbines are widely distributed, this configuration becomes less favourable.

Configuration c is a solution where the DERs are connected separately to the AC bus at the POC. This configuration is market-ready, with many turn-key solutions available. It is particularly suitable if the energy stored in the BESS is expected to originate in comparable proportions from WTs, PV panels, and the grid. Additionally, this arrangement offers greater modularity and scalability than the other configurations [1].

2.1.2 Control Architecture

The control architecture of a HPP is often done in a hierarchical way. The highest level controller gives setpoints and commands to the lower level controllers. Depending on the size and configuration of the HPP there can be multiple layers of control. For this explanation, configuration c is taken as example and can be seen in Figure 2.2.

The highest level control is the decisions made by the traders or the *energy management system* (EMS). A reference for active power will be given by the traders or EMS depending on an analysis and prediction of weather, BESS *state of charge* (SOC), demand and electricity prices. Additionally, information regarding the active power dispatch can be given by the EMS and trader. This determines the distribution of active power amongst the DERs and whether the BESS should charge or discharge. Furthermore, the TSO, or in some case DSO, can give references and change operational mode to ensure grid stability. According to the Danish grid codes [7], the power plant should be able to operate in three different Q modes: voltage control, reactive power control and power factor control.

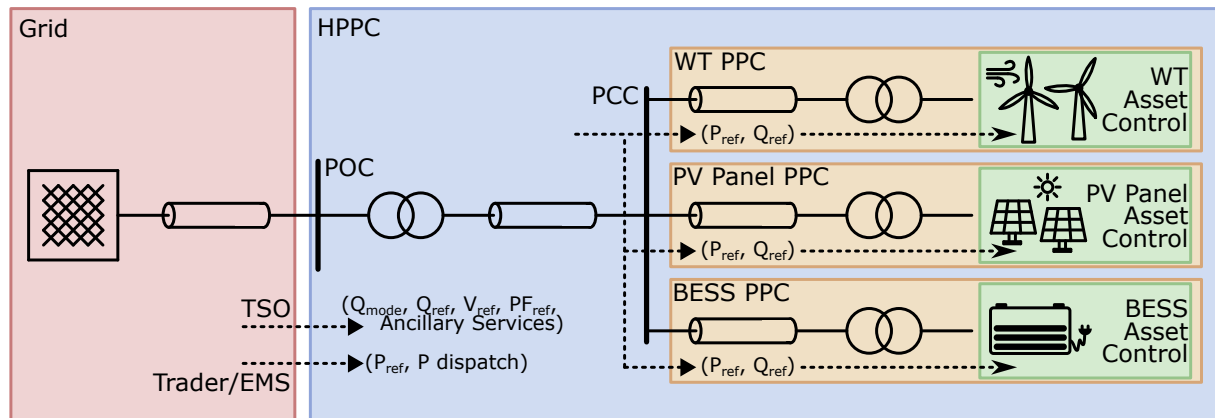


Figure 2.2 Hybrid power plant control architecture.

An order to do voltage control can be given to the power plant controller and the power plant has to utilise its reactive power capability to follow a voltage reference based on droop control. Similarly, an order to operate in reactive power control mode can be given. Here the power plant receives a reactive power reference and must follow it. Normally, the park will be operating in reactive power control mode with a reactive power reference of zero. Additionally, an order to operate with a specific power factor can be given. In this case, the power plant will adjust its

reactive power based on the current active power and the power factor reference. Additionally, commands and references related to ancillary services can also be given by the relevant operator [1] [7].

It is the *hybrid power plant controller* (HPPC) that ensures the active- and reactive power is distributed amongst the DERs to ensure the references given by the trader, EMS, TSO or DSO are met at the POC [1]. Thus, the HPPC does active- and reactive power control loops to ensure accurate reference tracking at the POC. Additionally, the HPPC will distribute the active- and reactive power setpoints amongst the DERs based on available power, trader or EMS commands, and/or a standard distribution.

The references from the HPPC are sent to the *power plant controllers* (PPCs) of the DERs (yellow in Figure 2.2). The PPCs are responsible for meeting the references given by the HPPC at their connection/radial to the *point of common coupling* (PCC). The PPCs will distribute references amongst the assets within its control based on communications of power availability from the assets [1].

The asset level control is the lowest level of control. For WTs, the asset level control is the WT control itself, i.e. AC-DC, DC-AC and pitch angle control. For PV panels and BESS it is the first power electronic system that they meet, i.e. a string of PV panels or batteries connected to a single inverter system. The asset level control determines the voltage and current output of the inverter or rectifier and is also responsible for functions such as *fault ride through* (FRT), *maximum power point tracking* (MPPT), safety functions and SOC [1].

2.1.3 Converter System Control

A converter system for WTs, PV panels, BESS, and other IBRs is categorised as either a *current-source inverter* (CSI) or a *voltage-source inverter* (VSI). A CSI typically features a proportionally large series inductor at the DC connection, stabilizing the DC input current. In contrast, a VSI incorporates a proportionally large shunt capacitor at the DC connection, maintaining a stable DC voltage. The presence of the inductor or capacitor determines whether the converter primarily regulates current (in the case of a CSI) or voltage (in the case of a VSI), hence the respective names. A VSI is more commonly used due to its effective power control and transient response, which is why the following control description will be based on a VSI [6]. A control scheme for a grid-connected VSI can be seen in Figure 2.3.

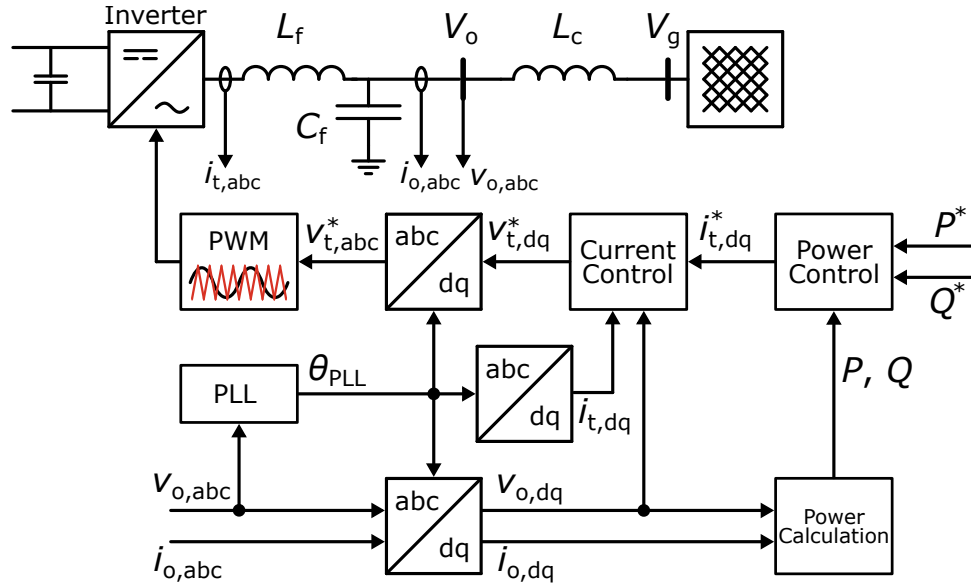


Figure 2.3 Simple grid-connected inverter with control diagram.

The inverter can be connected with an L , LC , or LCL filter [6]. The VSI in Figure 2.3 is connected with an LC filter, though it could be argued that the coupling inductance, L_c , is making it an LCL filter. The coupling inductance can represent the second L in the LCL filter, line inductance and/or grid inductance. What is relevant is that only the capacitor voltage is measured, and not the voltage after the coupling inductance. The terminal current, i_t , and output current, i_o , are measured as well. In practical use it might be necessary to measure the terminal voltage as well for protection and other control options [8].

In the control block diagram in Figure 2.3, dq0 reference frame is utilised. This allows decoupling of the active- and reactive components, i.e. d- and q components. The active- and reactive power reference, P^* and Q^* , are fed to the power control block. Its output is a current reference in the dq0 reference frame, $i_{t,dq}^*$. This is then fed to the current controller, which generates a voltage reference in the dq0 reference frame for the inverter terminals, $v_{t,dq}^*$. This is then transformed to the abc-phases, $v_{t,abc}^*$, which forms the basis for the *pulse-width modulation* (PWM). In other words, the current controller adjusts the terminal voltage until the desired terminal current is reached and the power controller adjusts the terminal current until the desired power output is reached. The dq to abc and abc to dq transformations utilise the phase angle determined by the *phase-locked loop* (PLL) [8].

2.2 Power Oscillations

Power system oscillations are electromechanical oscillations. They were first discovered when multiple synchronous generators were put in parallel. Many methods have been used to mitigate these oscillations, such as *flexible AC transmission system* (FACTS) devices, capacitors and control methods. One of the control methods is implementing a PSS in the synchronous generators. These can be tuned to target a specific frequency range and dampen their oscillation. However, even though solutions exist, power oscillations have led to adverse effects on power system components, voltage instability and blackouts. Power system oscillations are generalised in categories based on the areas and/or components of the power system that they affect. These are [9]:

- Intra-plant mode oscillations
- Local plant mode oscillations
- Inter-area mode oscillations
- Torsional mode oscillations
- Control mode oscillations

Intra-plant mode oscillations refers to machines inside the same power plant oscillating against each other. These oscillations are often localised within or near to the plant. **Local plant mode oscillations** are when a small group of machines are oscillating against the larger grid. **Inter-area mode oscillations** are when a large area is oscillating against another large area. Thus, the oscillation is observable across many measurement points. **Torsional mode oscillations** refer to the mechanical oscillation of rotating masses in the power system, such as turbine shaft and rotor. **Control mode oscillations** refer to oscillations caused by power system controllers, which may result from improper tuning or sensitivity to changing grid conditions. For instance, these oscillations could stem from a poorly tuned PLL or improper PLL operation under weak grid conditions. Generally, intra-plant mode oscillations have a higher frequency than local plant mode oscillations, and local plant mode oscillations have a higher frequency than inter-area mode oscillations [9]. Torsional mode oscillations have the highest frequency of them all and control mode oscillations can be within the range of intra-plant-, local plant- and inter-area mode oscillations. A table showing the frequency ranges stated by different articles and books can be seen in Table 2.1.

Table 2.1 Definition of oscillation modes from different articles and books.

Intra-plant	Local plant	Inter-area	Torsional	Control	Reference
-	0.7 - 2.0 Hz	0.1 - 0.7 Hz	-	-	[6]
2.0 - 3.0 Hz	1.0 - 2.0 Hz	< 1.0 Hz	10 - 46 Hz	-	[9]
-	0.7 - 2.0 Hz	0.1 - 0.7 Hz	-	-	[10]
-	0.7 - 2.0 Hz	0.1 - 0.7 Hz	> 2 Hz*	> 2 Hz	[11]
2.0 - 3.0 Hz	0.8 - 1.6 Hz	0.2 - 0.7 Hz	-	1.5 - 2.5 Hz*	[12]
1.5 - 3.0 Hz	0.8 - 1.8 Hz	0.2 - 0.5 Hz	-	-	[13]

*Similar definition of oscillation mode

As can be seen, there are some disagreements about the frequency ranges of oscillation modes, though they are generally similar with some exceptions. The publication year varies a lot and no

tendency can be seen related to this. However, several articles indicate that an increased share of IBRs increase the oscillation frequency due to lack of energy stored in the rotating masses [6].

However, the frequency range for which POD is required will be specified by the relevant *transmission system operator* (TSO) or *distribution system operator* (DSO) in grid codes or similar regulatory frameworks. It should be noted, however, that existing grid codes already impose limits on power oscillations caused by power plants themselves [14]. As a result, intra-plant oscillations must be addressed in accordance with those requirements and are not considered part of POD services provided to the grid. Relevant parts of grid codes from various countries will be further explored in Section 2.3.

2.2.1 Power System Stabiliser

To understand PSS, the conventional control scheme of a synchronous generator has to be explained. The control scheme includes governor control, *automatic voltage regulator* (AVR) and PSS control [3] [9]. An illustration of a synchronous generator control scheme can be seen in Figure 2.4.

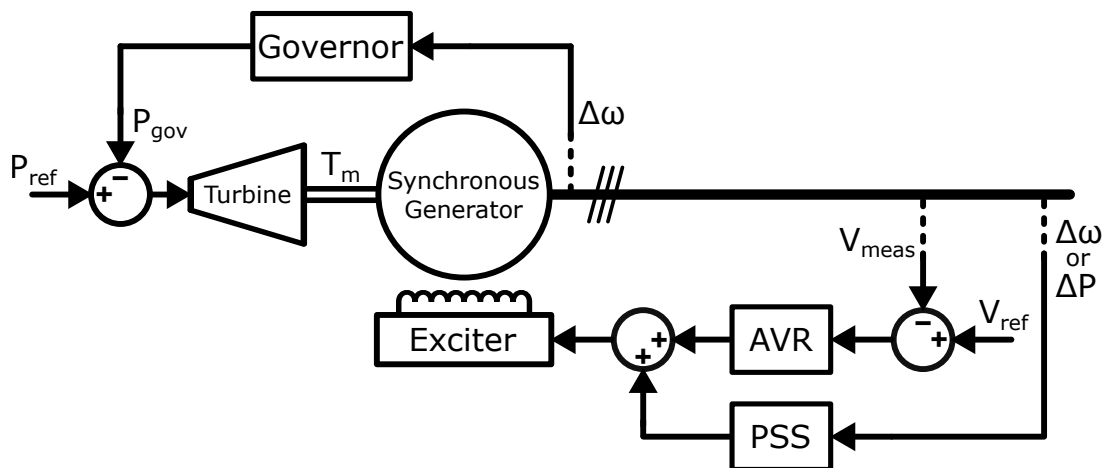


Figure 2.4 Illustration of generating unit with governor-, AVR- and PSS control.

Governor control is used to maintain a stable frequency and speed by adjusting the power input to the turbine (e.g., fuel input, flow, etc.). This ensures the generator's mechanical speed stays constant despite fluctuations in load. The AVR maintains a desired terminal voltage by regulating the excitation current supplied to the rotor windings. By adjusting the excitation current, the AVR changes the strength of the magnetic field in the rotor. A stronger magnetic field results in a higher induced voltage in the stator windings, thus increasing the terminal voltage [3]. One of the reasons for power oscillations in the grid was the fast-acting high gain of the AVR, implemented to deal with transient stability issues related to system voltage. The oscillation issues was especially pronounced during high active power output and weak grid conditions [9].

The PSS is a control algorithm that takes an oscillation or variation as input and then counteracts the oscillation in order to actively add damping to the system. Traditionally, PSS was used to add damping to synchronous generator rotor oscillations. The PSS would take the speed deviation,

$\Delta\omega$, as input, often measured at the generator shaft [3]. However, as more accurate and reliable equipment for measuring have been developed, the active power oscillation or electrical frequency have also been used. Additionally, *wide-area measurement system* (WAMS) have been employed to monitor the oscillations in the grid at various point to more accurately dampen oscillations and detect oscillation modes [6]. PSS have mostly been used to dampen active power oscillations, which is why the shaft speed, i.e. frequency, has been used as measurement.

Unlike governor control and AVR, PSS is designed to act only on a specific frequency range. Most commonly, PSS consists of a gain, a washout filter and phase compensation [3]. The block diagram of a standard PSS can be seen in Figure 2.5.

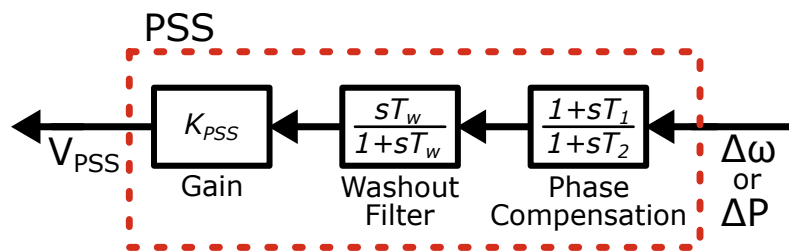


Figure 2.5 Block diagram of a standard power system stabiliser.

The **washout filter** or high-pass filter is tuned so that frequencies below the relevant frequency range are attenuated. This ensures that steady, low-frequency changes in the system are ignored. While the value of T_w is not critical for system stability, it does involve a trade-off. If the breakpoint is set too close to the relevant frequency range, it may cause some attenuation and phase shift in parts of the desired signal. Conversely, if the breakpoint is set too far from the relevant frequency range, unwanted signals may remain, potentially causing the PSS to act when it is not desired [3] [9]. Using $T_w = 1.4$ s from Example 12.4 in [3], the bode plot can be drawn, as seen in Figure 2.6. Noticeably, frequencies above 0.2 Hz are not significantly attenuated, though there are some significant phase shifts on the relevant frequencies.

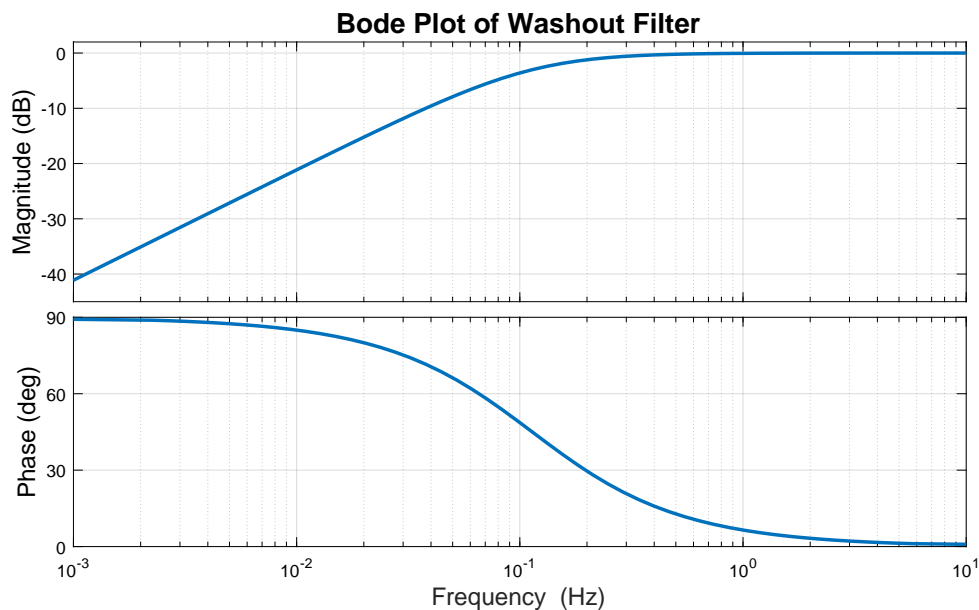


Figure 2.6 Bode plot of washout filter.

The **phase compensation** or lead-lag block ensures the proper phase shift of signals within the relevant frequency range, thereby contributing to positive damping of oscillations. In synchronous generators, the excitation system typically exhibits a phase lag relative to the turbine's torque. To address this, a phase-lead compensator is often used, where $T_1 > T_2$. Depending on the required phase shift, multiple phase compensation blocks may be implemented, and in some cases, a combination of phase-lead and phase-lag compensation (phase-lead-lag) is employed. However, due to the nature of phase compensation blocks, some signal attenuation may occur [3] [10]. Using $T_1 = 0.154\text{s}$ and $T_2 = 0.033\text{s}$ from Example 12.4 in [3], a bode plot may be drawn, as seen in Figure 2.7. Noticeably, there is significant phase shift for frequencies 0.5 to 10 Hz and an increasing attenuation over this interval.

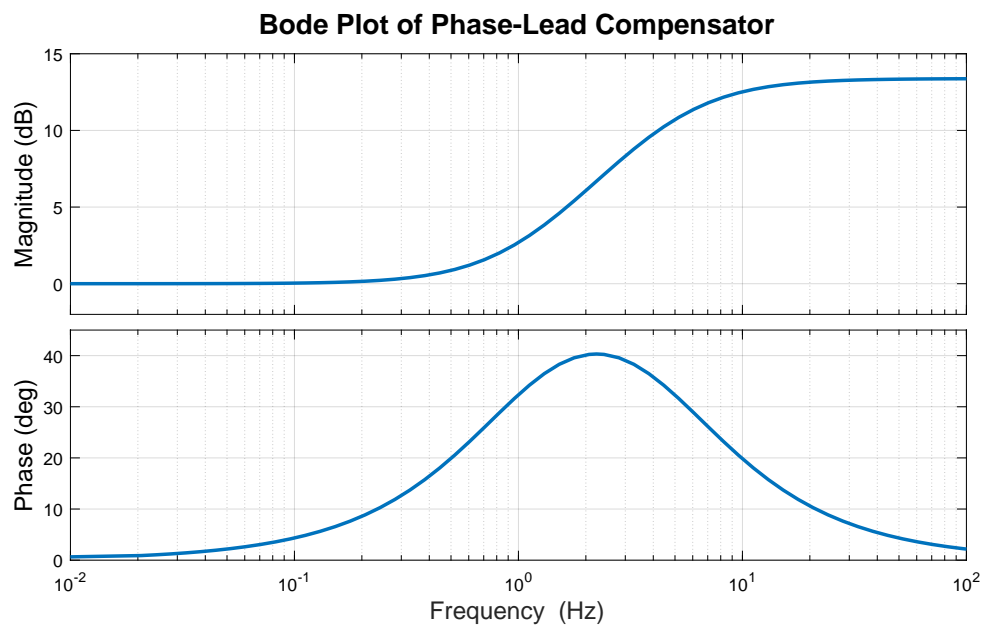


Figure 2.7 Bode plot of phase compensation.

The **gain** should be tuned last in the process. If the entire system, including the PSS, is taken into account, a root locus can be performed. This allows visualisation of the impact of changing the gain and helps make an informed decision based on both stability and damping requirements. Ideally, the highest possible damping should be selected without compromising the overall system stability [3] [9]. Using a gain of 9.5 from Example 12.4 in [3], a bode plot may be drawn of the entire PSS, as seen in Figure 2.8. It can be seen that from around 0.15 to 2 Hz there is a relatively flat gain and phase compensation, which is desired. However, the phase does have some curvature to it, which explains why a lead-lag compensator has been used as well [3] [9].

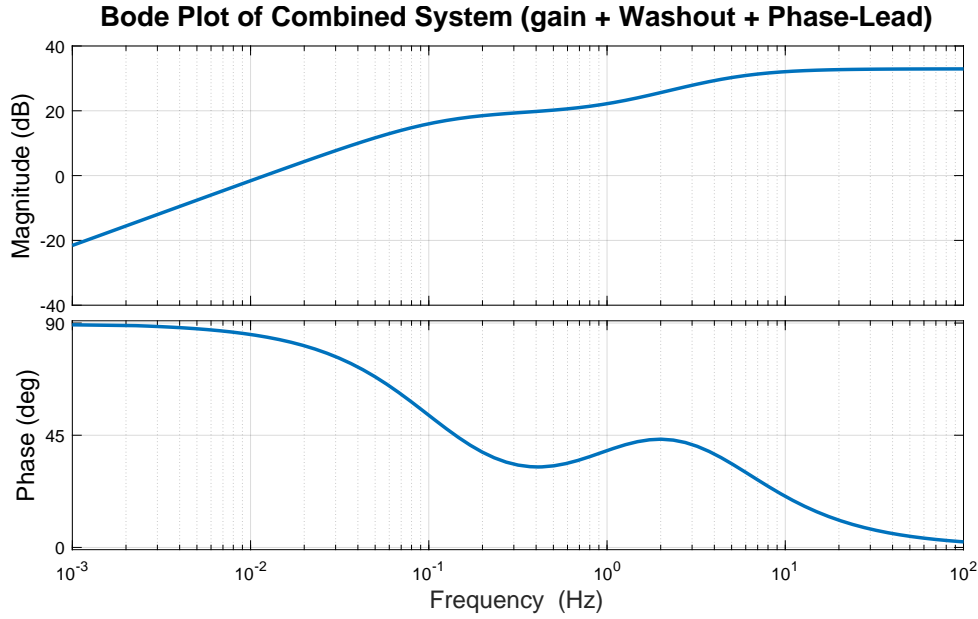


Figure 2.8 Bode plot of washout filter, phase compensation and gain.

2.2.2 Power Oscillation Damping Control

POD control is based on the synchronous generator PSS. It resembles the nature of adding an oscillation to counteract the oscillation happening. However, POD control is implemented for non-synchronous generating units like WTs, PV panels, BESS and FACTS devices [6]. The POD control will be added to the relevant part of inverter or power plant control algorithm. POD control can be divided into *active POD* (POD-P) and *reactive POD* (POD-Q), based on the characteristics of IBRs [2]. Other ways of doing POD control can be to add the damping signal to the i_d or i_q errors and add the damping signals to the magnitude and phase of the polar $u_{dq,ref}$ signal [6]. These differ from PSS, where active power oscillations are damped through the excitation system, thus affecting both active- and reactive power. POD control for WTs also depend on what type of WT is referred to. When doing POD control, active- and reactive power is split into dq-components, which allows separate control for each of them. Furthermore, the POD control does not have to be based on lead-lag phase compensation, as for PSS. Additionally, the damping can be done with many different control techniques [6].

In Figure 2.9 a control structure can be seen with POD-P and POD-Q fed into the error signal. As input to the POD-P, the speed- or frequency deviation can be used. Alternatively, the active power deviation can be used, as it gives a more direct view of the active power oscillation [6]. Similarly to PSS, WAMS can also be used.

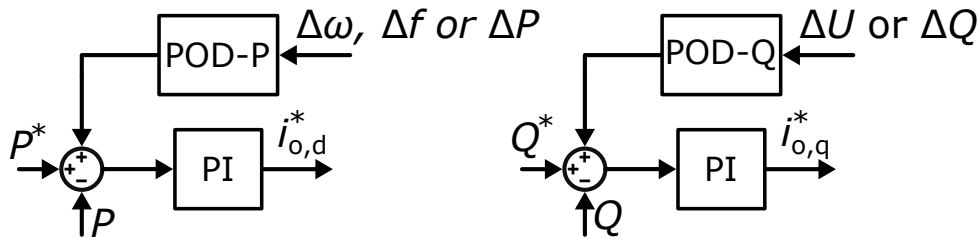


Figure 2.9 Example of POD-P and POD-Q control fed into the error signal.

The input to the POD-Q can be either the voltage- or reactive power deviation. Again, using

the reactive power gives a better indication of the reactive power oscillation.

The control structure of POD-P and POD-Q is similar to that of PSS, as can be seen in Figure 2.10. However, there are some distinct differences. The control structure for POD-P and POD-Q are similar to each other but the parameters may vary. As can be seen, the first block (from the left) is a limiter block, used to limit the output of the POD control. This is used to avoid generating excessive oscillating signals on the power plants side. It can also be combined with active power availability, PQ capabilities or other limiters. The purpose of the gain is the same as for PSS [2].

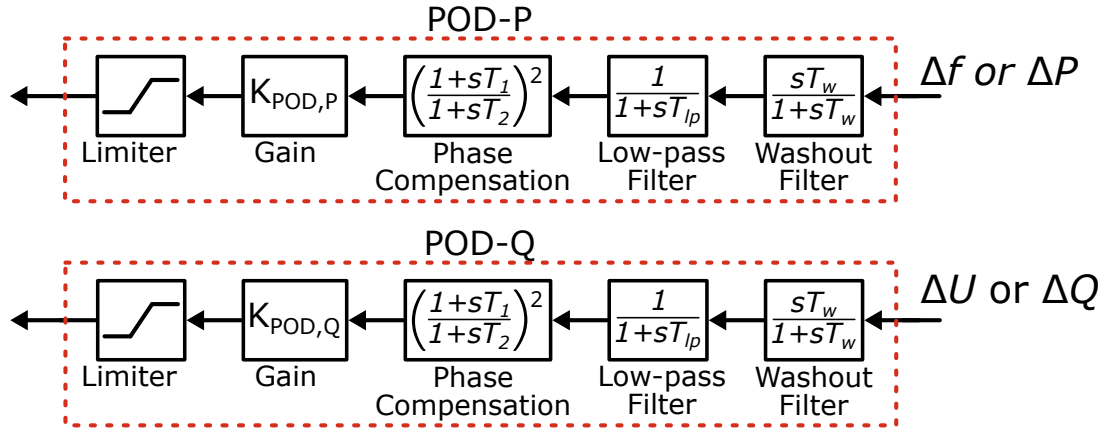


Figure 2.10 POD-P and POD-Q control structure. Adapted from [2].

The phase compensation block is squared to achieve a large enough phase compensation. Unlike PSS, where the phase compensation must account for the exciter lagging behind the mechanical torque, the POD phase compensation block must create a total phase shift of -180° for POD-P and -90° for POD-Q, including delays and other system dynamics [2]. The washout filter and the low-pass filter are together a band-pass filter that targets a specific frequency range. They should be tuned to the desired frequency range of power oscillations to be damped [2]. Compared to PSS, the washout filter serves the same purpose and a low-pass filter can also be implemented in PSS.

2.3 Power Oscillation Damping in Grid Codes

Power oscillation damping is not widely represented in existing grid codes. They are, however, becoming more common as the electrical power systems move away from synchronous generators. In the RfG, published back in 2016, POD is not mentioned, but states that facilities of Type C and Type D shall have adequate damping of oscillations [14]. However, in the draft document known as RfG 2.0, POD requirements are introduced [15]. The document only includes *The European Union Agency for the Cooperation of Energy Regulators'* (ACER's) recommendation for amendments to the current RfG. It states that power park modules of the type C and D shall be able to dampen out power oscillations in the range 0.1 Hz to 1.0 Hz. Some countries have already introduced or is currently introducing POD in the grid codes. These include but are not limited to; Denmark, Sweden, Spain and Finland.

The Danish grid codes state that for type C or D facilities, active power oscillations generated within 0.1 Hz and 50.0 Hz may not exceed the least restrictive of $\pm 0.5\%$ of delivered active power and $\pm 0.25\%$ nominal active power. If exceeded, it shall be restored to acceptable levels within 180 seconds [7]. These requirements are not currently in effect, but have been sent to the Danish Utility Regulator for approval.

The Swedish grid codes differentiate between active- and reactive power oscillation damping, denoted as POD-P and POD-Q respectively. For POD-P, the function should be implemented as a feedback loop to the active power regulation with the local frequency as input to the POD-P. For POD-Q, the function should be implemented as a feedback loop to the reactive power regulation with the positive sequence voltage as input to the POD-Q. For both types of POD the frequency range of interest are 0.25 Hz to 1.0 Hz and the TSO has a right to determine if the functions should be used [16].

The Finnish grid codes state that Type D facilities must have the capability to use POD or similar to dampen oscillations. The frequency of interest is not specified by the POD requirement, but it does state later, under PSS, that the frequency of interest when it comes to inter-area oscillations in the Nordic synchronous area is between 0.2 Hz and 1 Hz. Furthermore it states that the most prevalent oscillation mode is approximately 0.3 Hz [17].

Similar proposal for regulation and operation of POD controllers have been put forward by Red Eléctrica in Spain. Here, the frequency range of interest is 0.2 to 2.5 Hz and should be implemented for Type C and Type D. Red Eléctrica also distinguishes between POD-P and POD-Q [18].

Based on the classification in [18], POD controllers are expected to be effective primarily in the frequency range between 0.1 Hz and 0.3 Hz, corresponding to the critical inter-area modes in the Continental European system. Between 0.3 Hz and 1.5 Hz, they may still provide some improvement, though the impact is likely limited. Above 1.5 Hz, no performance enhancement is expected, but the controllers should avoid negatively affecting other system modes.

2.4 Specifying the Project Scope

As the penetration of IBRs increase and synchronous generators are decommissioned, the inertia and damping of the power grid decreases. Additionally, the control algorithm PSS, which is implemented for synchronous generators, is no longer applicable as these are being replaced by IBRs. This is leading to growing concerns over power system damping, as power oscillations will be more likely to occur. Therefore, grid codes in Europe, along with the new RfG 2.0, are being updated to include requirements for power oscillation damping capabilities of larger power plants [7] [15] [18]. Because of this, Eurowind Energy has found it of interest for this project group to investigate the possible implementation of POD control and its impact on the stability of the park. This is the basis for the project theme and an investigation into the implementation of POD control and its impact will be done based on several project goals.

The goal of this project will be to:

- **Design and Development**
 - Model a single-inverter power plant
 - Model a three-inverter power plant representing a hybrid power plant consisting of WTs, PV panels, and a BESS
 - Design current and power control loops for grid-following inverters
 - Develop POD-P and POD-Q control schemes
- **Stability Assessment**
 - Develop state-space models of the single-inverter and three-inverter power plants, including POD-P and POD-Q
 - Validate the state-space models against time-domain simulations in MATLAB Simulink
 - Evaluate the small-signal stability of the single- and three-inverter power plants
 - Assess the impact of POD-P and POD-Q on system stability
- **Experimental Validation**
 - Implement the developed control schemes on a hardware setup comprising of dSPACE and four inverters with LCL filters
 - Experimentally validate the inverter control design
 - Experimentally validate the functionality of the developed POD-P and POD-Q control schemes

Success for this project will be determined by the following criteria:

- The inverter control design operates stably and as intended in both simulation and experimental setups
- The POD-P and POD-Q controllers provide measurable damping of power oscillations in both simulated and experimental tests
- The state-space models accurately reflect the dynamic behaviour observed in time-domain simulations
- The experimental setup using dSPACE and multiple inverters successfully reproduces key control functions and validates system behaviour under test conditions

2.4.1 Project Outline

From this point on, the report is structured as follows. **Chapter 3** presents the single- and three-inverter systems under study and describes the design of the current and power control loops. The developed POD-P and POD-Q control schemes are introduced, and their performance is demonstrated through time-domain simulations.

Chapter 4 provides the theoretical background for small-signal state-space modelling and formulates the models for both the single- and three-inverter power plants, including the POD control schemes. The dynamic response of the state-space models is validated against MATLAB/Simulink time-domain simulations. Furthermore, the small-signal stability of the models is assessed, and the impact of incorporating POD-P and POD-Q on system stability is evaluated.

Chapter 5 presents the experimental setup and describes the methodology used for validation. The current and power control loops are experimentally validated for both the single- and three-inverter configurations. Additionally, the functionality of the developed POD-P and POD-Q control schemes is tested and verified.

Chapter 6 discusses the results obtained in the preceding chapters, highlighting key insights, limitations, and sources of error. **Chapter 7** summarises the main findings of the work, and **Chapter 8** outlines suggestions for future work and potential improvements.

3 Modelling and Control Design

This chapter presents the single- and three-inverter power plant systems to be modelled, along with the relevant system parameters and input data. The design and implementation of the grid-following current and power control loops are described in detail. Furthermore, the development of the POD-P and POD-Q control schemes is presented. Time-domain simulation results are included to demonstrate the performance of the POD control designs.

3.1 System

The system to be modelled is based on the experimental setup described in Chapter 5. The system consists of three identical inverters with identical LCL filters. In the experimental setup, only the terminal current, i_t , output current, i_o , capacitor voltage, v_o , and the grid current, i_g , are measured. Therefore, this chapter and the control design will also be limited to these measurements. The system can be seen in Figure 3.1.

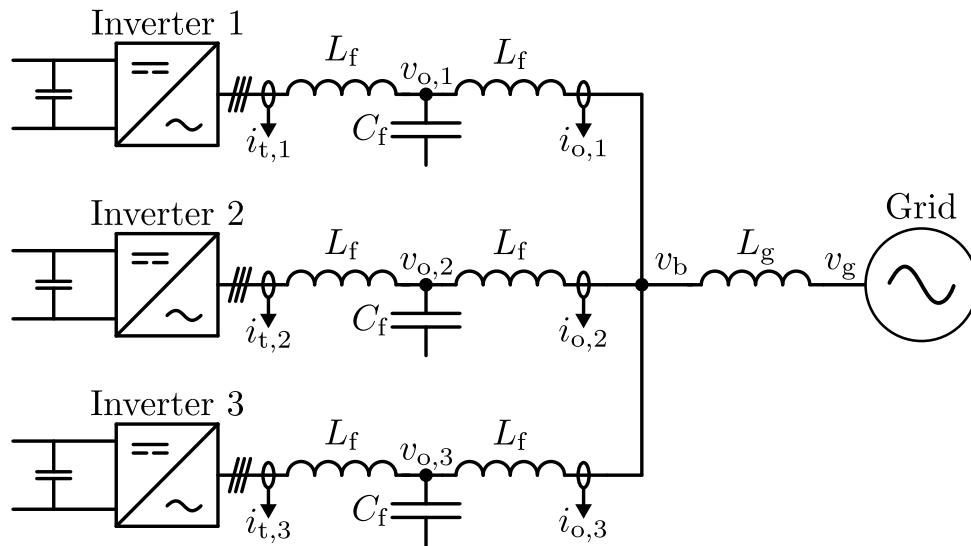


Figure 3.1 Inverter system.

The parameter values are also based on the experimental setup. An overview of the parameter values used for the control design and transfer function derivation can be seen in Table 3.1.

Table 3.1 System parameter values.

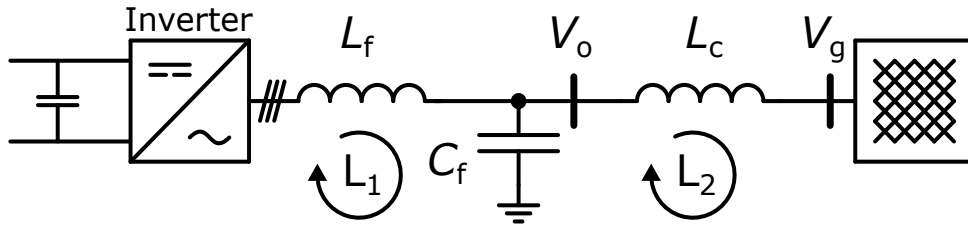
Parameter	Value
$V_{\text{nom,peak}}$	120 V
f	50 Hz
f_{sw}	10 kHz
T_s	0.0001 s
S_{nom}	900 VA
L_f	1.8 mH
R_f	0.02 Ω
C_f	3 μF
L_g	0.17 mH
R_g	0.001 Ω

3.2 Control Design

This section presents the modelling of the system and related transfer functions. Furthermore, the current and power control loops will be tuned based on the derived transfer functions. Additionally, the grid synchronisation will also be explained.

3.2.1 Current Control

The primary function of the current control loop in a grid-connected VSI is to regulate the dq-axis current components independently and generate appropriate modulation signals for PWM. Assuming the inductances include a resistive component, the single-line equivalent circuit can be represented as shown in Figure 3.2. Since the control objective is to control the terminal currents, the current control loop is designed based on the first KVL loop, which governs the terminal inductor current dynamics.

**Figure 3.2** Inverter with LC-filter and KVL loop.

By applying KVL from the terminal voltage, v_t , to the capacitor voltage, v_o , the following KVL equation can be written.

$$\begin{bmatrix} v_{t,a} \\ v_{t,b} \\ v_{t,c} \end{bmatrix} = R_f \begin{bmatrix} i_{t,a} \\ i_{t,b} \\ i_{t,c} \end{bmatrix} + L_f \frac{d}{dt} \begin{bmatrix} i_{t,a} \\ i_{t,b} \\ i_{t,c} \end{bmatrix} + \begin{bmatrix} v_{o,a} \\ v_{o,b} \\ v_{o,c} \end{bmatrix} \quad (3.1)$$

Transforming Equation (3.1) to dq0 reference frame, applying the Laplace transform and isolating for the terminal current that is not related to the cross coupling, the following equation is obtained.

$$\begin{bmatrix} i_{t,d} \\ i_{t,q} \\ i_{t,0} \end{bmatrix} = \frac{1}{sL_f + R_f} \left(\begin{bmatrix} v_{t,d} \\ v_{t,q} \\ v_{t,0} \end{bmatrix} - \begin{bmatrix} v_{o,d} \\ v_{o,q} \\ v_{o,0} \end{bmatrix} + \begin{bmatrix} 0 & \omega L_f & 0 \\ -\omega L_f & 0 & 0 \\ 0 & 0 & 0 \end{bmatrix} \begin{bmatrix} i_{t,d} \\ i_{t,q} \\ i_{t,0} \end{bmatrix} \right) \quad (3.2)$$

As can be seen, the terminal current depends on the terminal voltage, capacitor voltage, and a cross-coupling term introduced by the dq transformation of the inductor derivative term. To simplify the system dynamics, the capacitor voltage is treated as a disturbance and compensated through feed-forward compensation, while the cross-coupling terms are decoupled, also using feed-forward compensation. In other words, the $v_{o,dq0}$ is added to the $v_{t,dq0}$ and the ωL_f -matrix and $i_{t,dq0}$ term are subtracted from the $v_{t,dq0}$ term. Consequently, the resulting equation shows the input-output relations of the terminal voltage to the terminal current. In a block diagram, the current control loop will appear as seen in Figure 3.3.

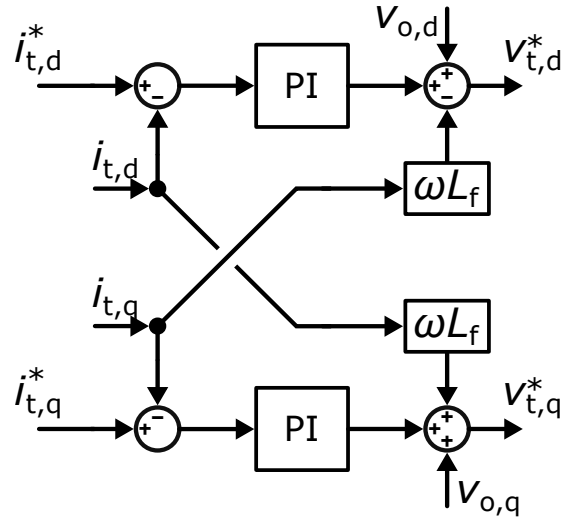


Figure 3.3 Block diagram of current control loop.

It can be deduced from Equation (3.2), that the plant transfer function of the current control loop is the remaining inductance and resistance term, i.e. the input-output relation, as seen in Equation (3.3).

$$G_{i,\text{plant}}(s) = \frac{i_{t,dq}(s)}{v_{t,dq}^*(s)} = \frac{1}{sL_f + R_f} \quad (3.3)$$

The full derivation of the KVL loop, transformation to dq0 reference frame and isolation of the terminal current can be found in Appendix A.1.1.

Furthermore, since the current controller generates the modulating signals, the delay associated with the PWM is often applied as well. Due to sampling, it takes one sampling period to measure the voltage and a half sampling period to generate the PWM signal [19].

$$G_d(s) = e^{-1.5T_s s} \approx \frac{1}{1 + 1.5T_s s} \quad (3.4)$$

The delay can be approximated by a first-order Taylor series, which gives the first-order transfer function, as seen in Equation (3.4). From this, a new plant transfer function can be derived, as seen in Equation (3.5).

$$G_{i,\text{plant}} = \frac{i_{t,dq}(s)}{v_{t,dq}^*(s)} = G_d(s) \cdot \frac{1}{sL_f + R_f} \quad (3.5)$$

A PWM gain can also be included in the plant transfer function if relevant.

Tuning

When selecting values for the current PI controller, the closed-loop stability in the frequency domain is of importance. To assess this, the *gain margin* (GM) and *phase margin* (PM) of the open-loop transfer function are evaluated for the specific design. Although there are no formal standards for GM and PM in current controllers for grid-connected inverters, many papers try to achieve $GM \gtrapprox 6\text{ dB}$ and a PM between 35° and 60° [20]. With these criteria, a high bandwidth and quick current control can be achieved. However, having a phase margin lower than 60° can give issues with overshoot, depending on the proportional gain and the bandwidth of the system. Additionally, these control parameters are to be implemented for experimental validation, which consequently includes noisy signals, parameter uncertainties, parasitics and non-linearities. Therefore, the stability margins will be designed to be more robust than is perhaps necessary, i.e. $GM > 20\text{ dB}$ and $PM > 60^\circ$. Additionally, the design will aim for 0% overshoot, which inherently limits the achievable system bandwidth.

Using the values presented in Section 3.1, the PI controller was designed based on the current controller plant transfer function, Equation (3.3). The PI controller gains are $k_{p,c} = 3.3$ and $k_{i,c} = 37.851$. The resulting open-loop and closed-loop bode plots can be seen in Figure 3.4.

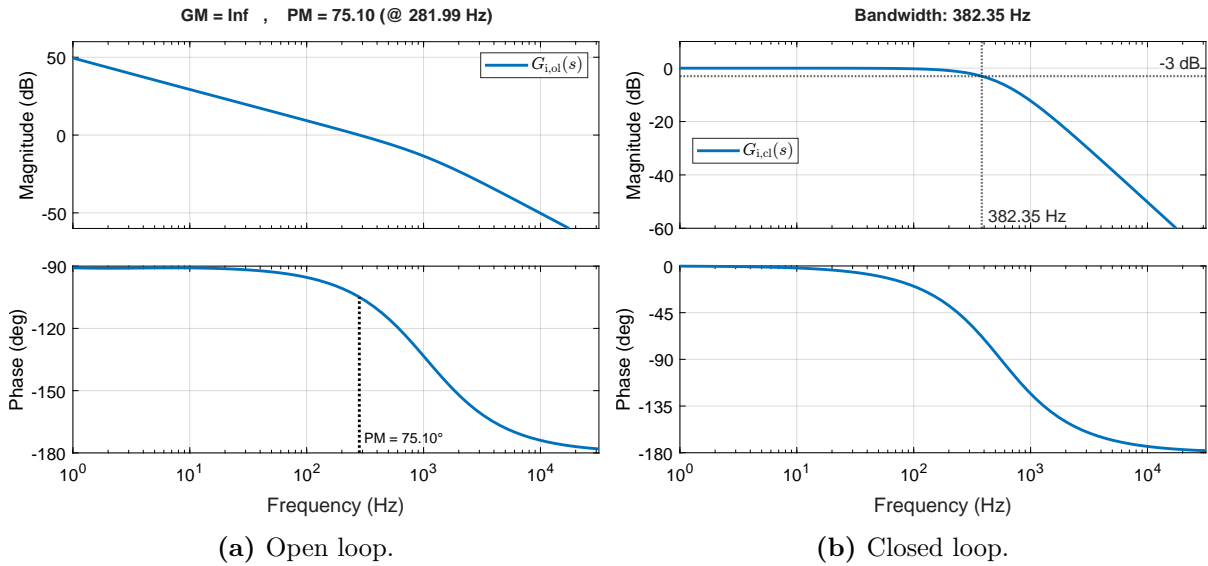


Figure 3.4 Compensated inner current loop bode plots.

In Figure 3.4a, the bode plot shows smooth attenuation with no resonance and the phase transitions smoothly from -90° to -180° . A GM of ∞ and a PM of 75.1° are achieved, meeting the design requirements. In Figure 3.4b, a bandwidth of 382.35 Hz or 2402 rad/s is achieved, which could be considerably faster if slight overshoot is allowed. However, the bandwidth is still fast and the design is thus deemed adequate.

3.2.2 Power Control

The purpose of the power controller for a grid-following inverter is to regulate active current and reactive current in order to track the desired active- and reactive power reference. Though, for practical implementation, many functions should be included to comply with grid codes. The power control used for this project is based on the dq0 reference frame instantaneous power

theory calculation, as seen in Equation (3.6) [21].

$$P = \frac{3}{2}(v_d i_d + v_q i_q + v_0 i_0) \quad Q = \frac{3}{2}(v_q i_d - v_d i_q) \quad (3.6)$$

If assuming that there is no 0-component and that the PLL has fully aligned the phase with v_d , then the equations simplify to Equation (3.7), since $v_q, v_0, i_0 = 0$.

$$P = \frac{3}{2}v_d i_d \quad Q = -\frac{3}{2}v_d i_q \quad (3.7)$$

Since the current controller decouples the d- and q-components and the PLL aligns the phase with v_d , the active- and reactive power can be determined from the d- and q-component, respectively. In this case, a PI controller is used to regulate the active- and reactive power error, as seen in Figure 3.5.

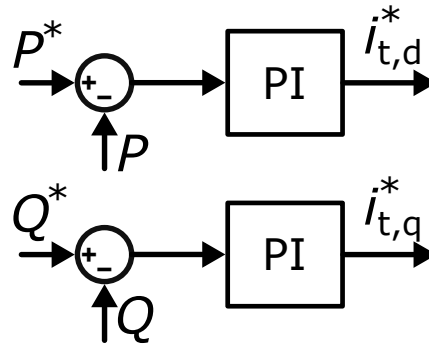


Figure 3.5 Power control block diagram.

Notice, that the references here are for $i_{t,dq}$. This is because the terminal current reference is what is passed to the current controller. Since there is a shunt capacitor in the filter, some current will take this path. This relationship can be written as seen in Equation (3.8) by doing KCL on the capacitor node.

$$i_t(t) = i_o(t) + i_{cap}(t) \quad (3.8)$$

As can be seen, there is a difference between the current going to the grid and the current coming out of the inverter. For a 50 Hz signal, the current entering the shunt capacitor will be relatively small for a smaller capacitance, though will of course still introduce an error. The steady-state error will be compensated for by the integral part of the PI controller.

Since the power is usually measured with a low-pass filter, and the control loop has a relatively slow bandwidth, the plant transfer function of the outer power loop is commonly represented by the power calculation and the low-pass filter [21], as seen in Equation (3.9).

$$G_{p,plant}(s) = \frac{P(s)}{i_{o,d}^*(s)} = \frac{3}{2}V_d \frac{\omega_{LPF}}{s + \omega_{LPF}} \quad G_{q,plant}(s) = \frac{Q(s)}{i_{o,q}^*(s)} = -\frac{3}{2}V_d \frac{\omega_{LPF}}{s + \omega_{LPF}} \quad (3.9)$$

There is no delay implemented here, as delay was already considered in the current controller.

However, these plant transfer functions are simplified and do not include any filter capacitance, line- and grid impedance dynamics [8]. Also, they do not represent the different currents used for current control and power control, i.e. i_t and i_o .

To include these dynamics of the system, additional circuit analysis have to be done, defined by the second KVL loop and capacitor node in Figure 3.2. If using Equation (3.8), and doing a similar transformation to the dq0 reference frame, an equation for the KCL relation at the capacitor node can be found.

$$\begin{bmatrix} v_{o,d} \\ v_{o,q} \\ v_{o,0} \end{bmatrix} = \frac{1}{sC_f} \left(\begin{bmatrix} i_{t,d} \\ i_{t,q} \\ i_{t,0} \end{bmatrix} - \begin{bmatrix} i_{o,d} \\ i_{o,q} \\ i_{o,0} \end{bmatrix} + \begin{bmatrix} 0 & \omega C_f & 0 \\ -\omega C_f & 0 & 0 \\ 0 & 0 & 0 \end{bmatrix} \begin{bmatrix} v_{o,d} \\ v_{o,q} \\ v_{o,0} \end{bmatrix} \right) \quad (3.10)$$

As can be seen in Equation (3.10), there is cross coupling due to the dq0 transformation and the capacitor derivative term. Since there is no voltage control loop for grid-following inverters, no decoupling of these terms will happen.

Similarly, to include the grid- and line impedance effects, a KVL loop can be done from the capacitor voltage to the Thévenin grid voltage, as can be seen in Equation (3.11), where it has also been transformed to the dq0 reference frame.

$$\begin{bmatrix} i_{o,d} \\ i_{o,q} \\ i_{o,0} \end{bmatrix} = \frac{1}{sL_c + R_c} \left(\begin{bmatrix} v_{o,d} \\ v_{o,q} \\ v_{o,0} \end{bmatrix} - \begin{bmatrix} v_{g,d} \\ v_{g,q} \\ v_{g,0} \end{bmatrix} + \begin{bmatrix} 0 & \omega L_f & 0 \\ -\omega L_f & 0 & 0 \\ 0 & 0 & 0 \end{bmatrix} \begin{bmatrix} i_{o,d} \\ i_{o,q} \\ i_{o,0} \end{bmatrix} \right) \quad (3.11)$$

Notice again, that there is a cross-coupling term due to the dq0 transformation and the inductor. Similarly, these terms can not be decoupled.

Combining Equations (3.2), (3.8), (3.9) and (3.11), a block diagram representation can be made, as seen in Figure 3.6. The upper part shows the d-component, or the parts related to active power. The bottom part shows the q-component, or the parts related to reactive power. The cross-coupling terms can be seen in the middle.

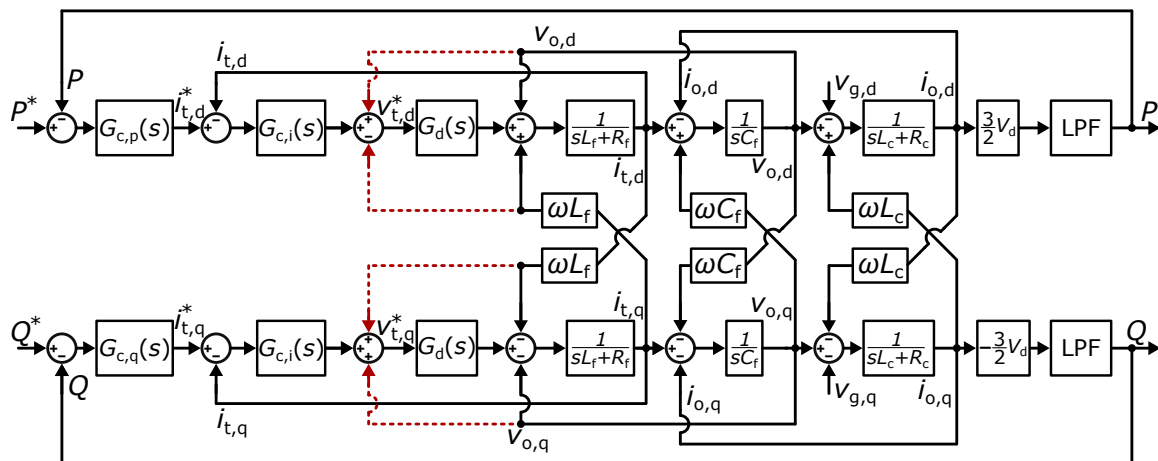


Figure 3.6 Block diagram representation of the d- and q component equations with cross-decoupling and feed-forward compensation (red).

As was explained previously, cross-decoupling of the inverter dq currents and feed-forward compensation of the capacitor voltage is utilised in the current control. These parts are marked by dashed red lines. Notice, that the cross-decoupling and feed-forward compensation are added before the delay, and therefore do not exactly cancel out. This will result in some of the dynamics from these terms being present, though at a reduced level.

By assuming that the cross-decoupling and feed-forward compensation is exact, and that the rest of the cross-coupling terms are negligible, a simplified block diagram representation can be written, as seen in Figure 3.7.

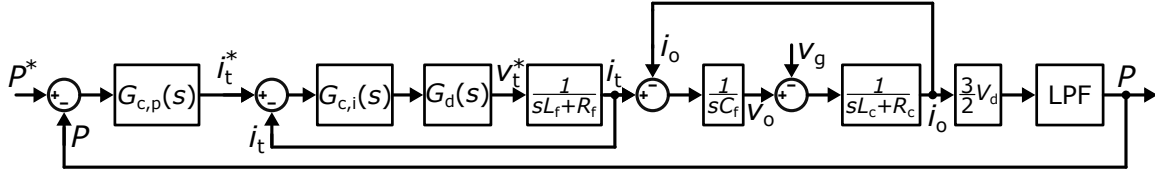


Figure 3.7 Block diagram representation of the KVL and KCL dq0 equations.

Additionally, the current and voltage d- or q-components are not differentiated, as there is no interaction between the two given the assumptions made. However, only in the current control have the cross-coupling terms been decoupled. Therefore, an error in dynamics is expected due to not having decoupled the capacitor- and coupling inductor cross-coupling terms, which is not possible to do without adding more control layers.

Notice, that the power calculation term can still be found at the end of the block diagram to convert the grid current to power. Thus, the block diagram includes the simple plant transfer function, as was presented in Equation (3.9), but also includes the dynamics of adjusting i_t^* to achieving a certain i_o based on the power calculation.

To reduce the block diagram, the take-off points of several of the variables are moved. Then, loops can be closed and the diagram reduced. Notice, that there is a subtraction of the Thévenin equivalent grid voltage. This value is not measurable and will be set equal to zero, $v_g = 0$, as any dynamics associated with this are unknown. From this, the take-off point from i_g can be moved, as can be seen in Figure 3.8.

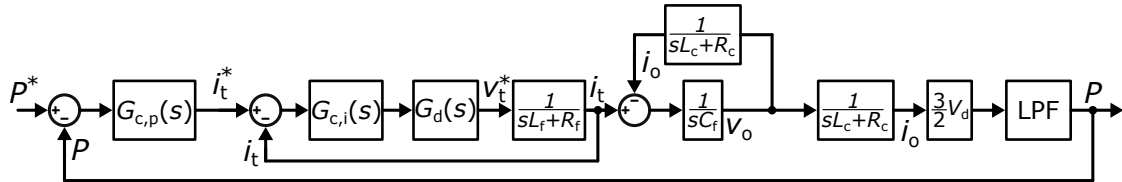


Figure 3.8 Block diagram reduction: current control loop plant transfer function.

The current control loop plant is the same as presented during the explanation of the current controller. Thus, the current control loop can be closed, which simply reduces to unity gain, assuming the closed-loop current control is much faster than the power loop.

The next step is to close the loop containing the coupling impedance and filter capacitor, which reduces to Figure 3.9.

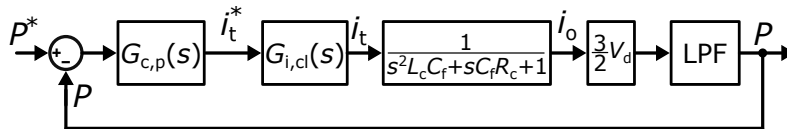


Figure 3.9 Block diagram reduction: power control loop transfer function.

From this, a plant transfer function for the active power outer loop can be found, as seen in

Equation (3.12).

$$G_{p,\text{plant}}(s) = \frac{P(s)}{i_{t,d}^*(s)} = \frac{3}{2} V_d \frac{\omega_{\text{LPF}}}{\omega_{\text{LPF}} + s} \frac{1}{s^2 L_c C_f + s C_f R_c + 1} \quad (3.12)$$

$$G_{q,\text{plant}}(s) = \frac{Q(s)}{i_{t,q}^*(s)} = -\frac{3}{2} V_d \frac{\omega_{\text{LPF}}}{\omega_{\text{LPF}} + s} \frac{1}{s^2 L_c C_f + s C_f R_c + 1} \quad (3.13)$$

The plant transfer function includes the remaining dynamics of the filter capacitance and coupling impedance, including the resonance and damping effects. The open-loop plant transfer function is a Type 0 system, which will result in a non-zero steady-state error given a step input. Therefore, the outer active power controller should have an integrator to eliminate steady-state error, such as a PI controller.

Tuning

Similar to the tuning of the current controller, the design requirements for the power controller will be a $GM > 20$ dB and a $PM > 60^\circ$. Especially for the power controller, avoiding overshoot is important since the accurate reference tracking is of concern. Also, considering that there will be three inverters in parallel. A design requirement for the power controller is that the bandwidth is at least 10 times less than that of the current controller [8]. This allows the closed current loop to be taken as unity gain, and ensures that current regulation has minimum effect on the active- and reactive power. As presented throughout this section, both a simple and a more accurate transfer function for the power plant have been derived. Based on the values presented in Section 3.1, a comparison of their bode plot can be made, as seen in Figure 3.10.

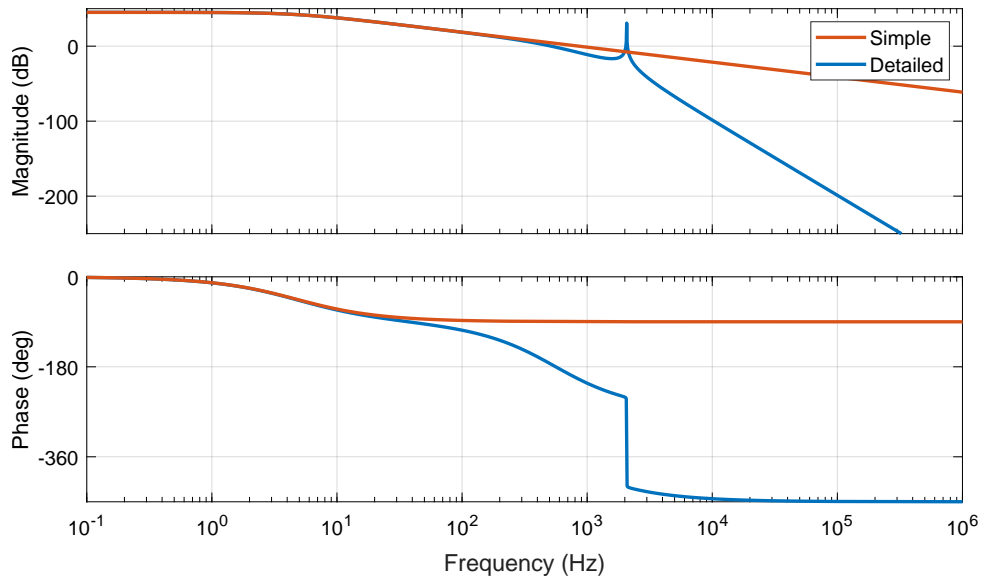


Figure 3.10 Comparison of simple and detailed power plant transfer function.

The simple plant transfer function is simply a LPF with a gain. Noticeably, the detailed plant transfer function shows a resonance peak caused by the filter capacitance and the coupling inductance. It also shows greater attenuation and phase shift at higher frequencies. Using the simple plant transfer function can lead to undesirable closed-loop system response, which is why the detailed plant transfer function will be used.

After tuning the PI controller to meet the design requirements with $k_{p,p} = 0.0029$ and $k_{i,p} = 0.1071$, the open-loop and closed-loop bode plots can be made, as seen in Figure 3.11.

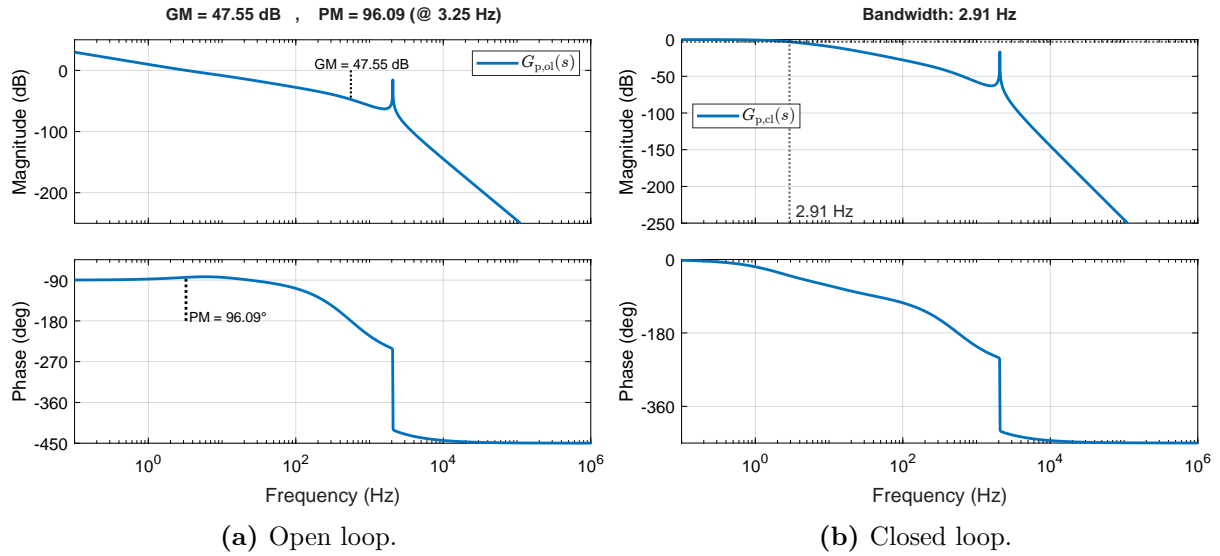


Figure 3.11 Compensated outer power loop bode plots.

The open-loop bode plot in Figure 3.11a shows a $GM = 47.55$ dB and $PM = 96.09^\circ$. These are both well above the design requirements. The closed-loop bode plot in Figure 3.11b shows a bandwidth of 2.91 Hz, which is considerably slower than the current controller.

It was attempted to tune the PI controller so that the system response was faster. However, the resonance peak and associated phase shift, along with the requirements, limited the achievable system bandwidth. The open-loop resonance peaks with -10 dB at 2070 Hz (resonance frequency of C_f and L_f). At this point the phase has already crossed -180° . Thus, if the gain is increased, such that the resonance peak crosses 0 dB, the dynamics at that frequency will stop being attenuated and will make the system oscillate at the resonance frequency with a magnitude increasing with gain. However, that is not the major limiting factor to system bandwidth. If the open-loop phase is compared with that of the simple plant, it can be seen that the detailed plant's phase decreases much faster and actually crosses -180° relatively early. This will result in lower PM at higher gains and will limit the gain to a certain range. To clarify, the resonance peak is not the cause of instability, as the first 0 dB crossing already leads to a critically low phase margin at higher gains. Due to these reasons, the power controller was tuned slower than desired. However, it is still adequately fast with a settling time of 226 ms.

3.2.3 Grid Synchronisation

All three inverters will be operating in grid-following mode and it is therefore necessary to make sure that the phase of each inverter are aligned with the grid. A typical approach used for synchronisation during operation is a *synchronous reference frame phase-locked loop* (SRF-PLL). The objective of the SRF-PLL is to obtain the phase angle of the grid voltage or POC voltage, which is then used when generating the modulation signal for the inverters.

The SRF-PLL estimates the phase angle of the three-phase input by using the park

transformation to convert the input to the dq0 reference frame. Then, the angle θ is changed with a PI controller until the quadrature component becomes zero. Which means that the phase angle used for the transformation is in line with the phase angle of the input [22]. The block diagram of the used SRF-PLL can be seen in Figure 3.12.

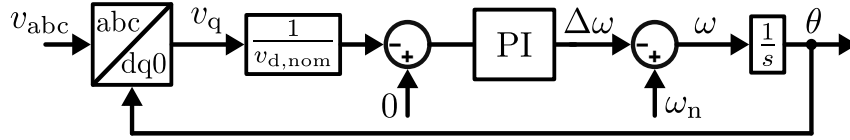


Figure 3.12 Block diagram of the SRF-PLL

The closed-loop of the SRF-PLL can be described as second order filter [22]. The transfer function for the phase angle estimation is given by Equation (3.14).

$$H(s) = \frac{K_{p,pll}s + K_{i,pll}}{s^2 + K_{p,pll}s + K_{i,pll}} \quad (3.14)$$

The closed-loop dynamics are controlled by the characteristic equation, i.e. the denominator of the transfer function.

$$\text{Characteristic equation: } s^2 + K_{p,pll}s + K_{i,pll} = 0$$

$$\text{Comparing with standard form: } s^2 + 2\zeta\omega_n s + \omega_n^2 = 0$$

By comparing the characteristic equation to the standard form, equations for $K_{p,pll}$ and $K_{i,pll}$ can be found.

$$K_{p,pll} = 2\zeta\omega_n K_{i,pll} = \omega_n^2$$

Utilising a damping factor ζ of 0.707 and aiming for a bandwidth of 30 Hz, $K_{p,pll}$ and $K_{i,pll}$ are found to be 266.57 and 35530.57 respectively. Derivation of the SRF-PLL transfer function can be found in Appendix A.1.2.

3.3 POD Control Design

This section presents the POD-P and POD-Q control design. In Section 2.2, the POD control function for inverters was introduced. As was mentioned, it seeks to emulate the PSS of synchronous generators in order to dampen any oscillations in the power grid. A generic form of a POD-P and POD-Q was introduced in Section 2.2 and these will serve as basis for the POD functions implemented in this project. The POD control schemes can be seen in Figure 3.13.

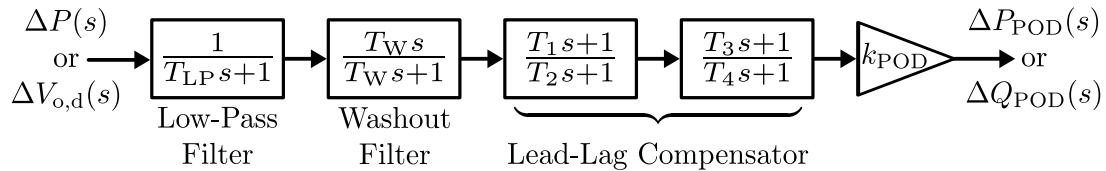


Figure 3.13 POD control schemes.

3.3.1 Delay and Gain

For the POD to be effectively used to damp power oscillations, a few additional delays of the system has to be considered in order for the output signal of the POD to align correctly. Firstly,

the PODs are set to control the reference power of the inverter, but the input is not necessarily the measured power. The input must therefore first be related to the output signal. Secondly, since the POD output is fed into the reference for the power controller it is necessary to take into account the frequency response of the power control loop.

These delays, along with the phase shifts introduced by the LPF and washout filter in the POD, need to be compensated by another filter. A lead-lag compensator or two series lead-lag compensators are usually used to obtain the desired phase shift [6]. The advantage of using the series compensator is that it can achieve greater phase compensation.

The transfer function of the POD $C_{pod}(s)$ is described by Equation 3.15.

$$C_{pod}(s) = H_{LPF}(s)H_{wo}(s)C_{LL}(s)k_{POD} \quad (3.15)$$

Where $H_{LPF}(s)$ is the transfer function of the low-pass filter, $H_{wo}(s)$ is the washout or high-pass filter, $C_{LL}(s)$ is the lead-lag compensator and k_{POD} is a gain.

If the frequency is used as the input to the POD-P then the lead-lag compensator needs to not only compensate for the phase shift of the two filters but also the phase angle between the power and frequency. The phase angle between the active power and the frequency needs to be incorporated in order to ensure correct phase alignment of the delivered active power. Phase angle difference is dependent on the system impedance and the control method in power control loop. The frequency's impact on the measured power can be modelled as disturbance on the power controller's feedback signal as the frequency is induced on the grid side and are propagated through the system thus affecting the power measurement. If instead the active power measurement is used as the input for the POD-P then the phase angle between the power and frequency is not needed for the tuning of the lead-lag controllers.

Furthermore, the delay from the closed-loop control of the power controller also needs to be taken into account. Thus, the total phase delay that the lead-lag compensators need to take into account is given by Equation 3.16. Each delay are dependent of the oscillation frequency, ω .

$$\theta_{ll,podp}(\omega) = -1 \cdot (\theta_{lpf}(\omega) + \theta_{wo}(\omega) + \theta_{CL}(\omega)) \quad (3.16)$$

Where θ_{lpf} and θ_{wo} are the phase shifts from the low-pass filter and washout filter, respectively. θ_{CL} is phase shift from the power controller. If the input of for POD-P differs from the signal it is regulating, ie. if the frequency is used, an additional term is needed.

The tuning of the POD-P gain was done iteratively until a satisfactory damping of the power oscillation was achieved. An initial value for k_{POD-P} was calculated based on the magnitude change through the POD-P, as seen in Equation 3.17

$$k_{POD-P,init} = \frac{1}{|H_{LPF}(s)H_{wo}(s)C_{LL}(s)C_{CL}(s)|} \quad (3.17)$$

Where $C_{CL}(s)$ is the the inverters' power control closed-loop. The $k_{POD-P,init}$ was used as a starting point for the tuning and was then slowly increased until satisfactory damping was achieved.

The tuning of POD-Q is similar to POD-P, with the only difference being that instead of frequency or active power as input, it takes either voltage magnitude or reactive power. If the voltage is used then a term for the phase difference between the voltage oscillation and reactive power needs to be included. Otherwise if the reactive power is used as input this term is omitted. The total phase shift for lead-lag compensators is then described by Equation 3.18

$$\theta_{ll,podq}(\omega) = -1 \cdot (\theta_{VQ}(\omega) + \theta_{lpf}(\omega) + \theta_{wo}(\omega) + \theta_{CL}(\omega)) \quad (3.18)$$

Where θ_{VdQ} is the angle difference between the voltage and the reactive power. The voltage used is voltage magnitude and not the sinusoidal signal.

In contrast to POD-P, the gain of POD-Q was not found iteratively. Instead the gain k_{POD-Q} is found by Equation 3.19

$$k_{POD-Q} = \frac{|H_{VQ}(s)|}{|H_{LPF}(s)H_{wo}(s)C_{LL}(s)C_{CL}(s)|} \quad (3.19)$$

Where H_{VQ} is the transfer function describing the relation between the voltage and reactive power and C_{CL} is the inverters' closed power control loop.

3.3.2 Delay Compensation

The analytical approach introduced in the previous section yield the phase compensation needed from the lead-lag compensators at a given frequency. These can then be used to find the optimal time-constant for the compensators either to a given frequency or a whole frequency range. However, while it possible to design a two series lead-lag controller to give the correct phase a shift at a single frequency during it over a range may not be possible, depending on the needed phase shift. The approach introduced in this section therefore tries to minimise the error between the target phase response and lead-lag phase response in order to get as close to optimal alignment over the whole frequency range.

Section 2.2 specified the expected frequency of oscillations in a power grid to be within 0.1-3 Hz. This is supported by the Spanish TSO Red Eléctrica, which defines the frequencies of the oscillation to be between 0.1 Hz and 2.5 Hz as described in Section 2.3. Further adding that the POD is not be expected to deliver the same damping for the whole frequency range. Instead, they state that POD should be more effective at lower frequencies, while not contributing to additional oscillations for higher frequencies.

Utilising Equations 3.16 and 3.18 along with the frequency range 0.1-2.5Hz, it now possible to find the expected phase angle shift for the different frequencies. This is then used in a single-objective constrained optimisation function in order to find the lead-lag time constants that best fit the needed response.

The cost function is given by Equation 3.20.

$$\begin{aligned} \text{cost} = & \|\arctan(\omega\tau_{lead1}) - \arctan(\omega\tau_{lag1}) + \arctan(\omega\tau_{lead2}) - \arctan(\omega\tau_{lag2}) - \theta_{target}\|_2 \\ & + \lambda(|\tau_{lead1} - \tau_{lead2}| + |\tau_{lag1} - \tau_{lag2}|) \end{aligned} \quad (3.20)$$

Where ω is the frequency in rad/s, τ are the time constants of the lead-lag compensators, θ_{target} is phase angle target for the given frequency and λ is the regularisation factor to penalize differences between the two compensators.

The cost function consists of two objectives: the primary aims to match the phase response of the lead-lag compensators to the provided θ_{target} , while the secondary objective introduces a regularisation factor λ to encourage the use of similar time constants in both compensators by penalizing their differences.

Both ω and θ_{target} are $1 \times n$ vectors, which means the primary objective also yields a $1 \times n$ vector representing phase errors at each frequency point. The Euclidean norm is applied to this vector to produce a single scalar cost, where larger errors contribute more to the total. By weighting large errors more strongly, the optimization is biased toward reducing significant mismatches in phase response, ensuring better overall alignment with the target.

3.3.3 Simulation of POD Control

This section contains the simulation results for power oscillation damping. The system contains two inverters one as a grid-following inverter and the second as a stand in for the grid. The second inverter sets the voltage with dual-loop control, which the first inverter synchronises to using a PLL.

This section is split into two parts. One for active power oscillations, where a forced oscillation on the grid side frequency is introduced, which is visible in the measured active power of the inverter and a second part for the reactive power oscillation damping, where the grid side voltage magnitude is varied.

The POD-P is set up as described in Section 3.3.1, where the input to the POD-P is the measured active power. It contains a low-pass filter, a washout filter, two lead-lag compensators and a gain. The values for each component can be seen in Table 3.2.

Table 3.2 POD-P parameters used for simulation results

Parameter	Value
Time constant LPF	0.1
Time constant wo	5
Time constant lead 1	8.6684
Time constant lag 1	0.084359
Time constant lead 2	8.6684
Time constant lag 2	0.084359
Gain	-0.01000477

The parameter of the filters are based on [18] and compensators time constants are found according to the method described in Section 3.3.1.

The forced frequency oscillation for this simulation is at 2 Hz with a magnitude of 0.4 Hz. The

impact of adding POD-P for damping of active power oscillations can be seen in Figure 3.14. The POD-P is activated after 5 seconds and the oscillation magnitude is then reduced from 0.46 W down to 0.014 W. This illustrates how the POD can be used to dampen power oscillations. The oscillation are not completely removed and the POD-P effectiveness is dependent on the frequency, thus at different oscillation frequencies, the result will change.

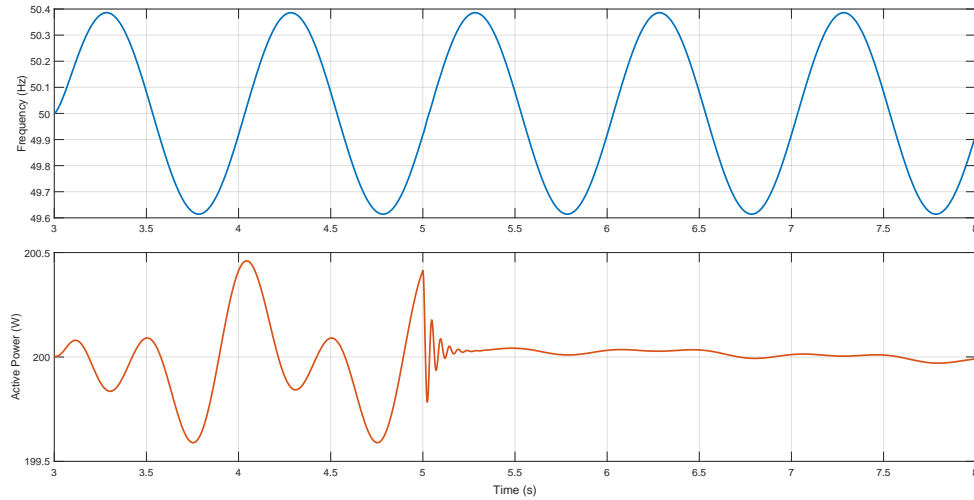


Figure 3.14 Simulation results for POD-P

From Figure 3.14, it can be observed that the power measurements prior to the activation of POD-P exhibit oscillatory behavior. Although the input disturbance introduced at the grid side is a single-frequency oscillation, the resulting power signal on the plant side displays two distinct frequency components. This is due to the non-linear effects of power measurements.

The POD-Q uses similar filter as POD-P but has different values for the lead-lag compensators and a different gain. These parameter values are found according to the method introduced in Section 3.3.1. The parameters of the POD-Q filters and compensators can be seen in Table 3.3

Table 3.3 POD-Q parameters used for simulation results

Parameter	Value
Time constant LPF	0.1
Time constant wo	5
Time constant lead 1	1.1322
Time constant lag 2	0.036697
Time constant lead 1	1.1322
Time constant lag 2	0.036697
Gain	-0.0105396

The oscillation in reactive power is generated by varying the grid side voltage magnitude. A 2 Hz sinusoidal signal with a magnitude of 12 V is added to the v_d component of Inverter 2's voltage reference. This results in an observable reactive power oscillation seen at the POC, as can be seen in Figure 3.15.

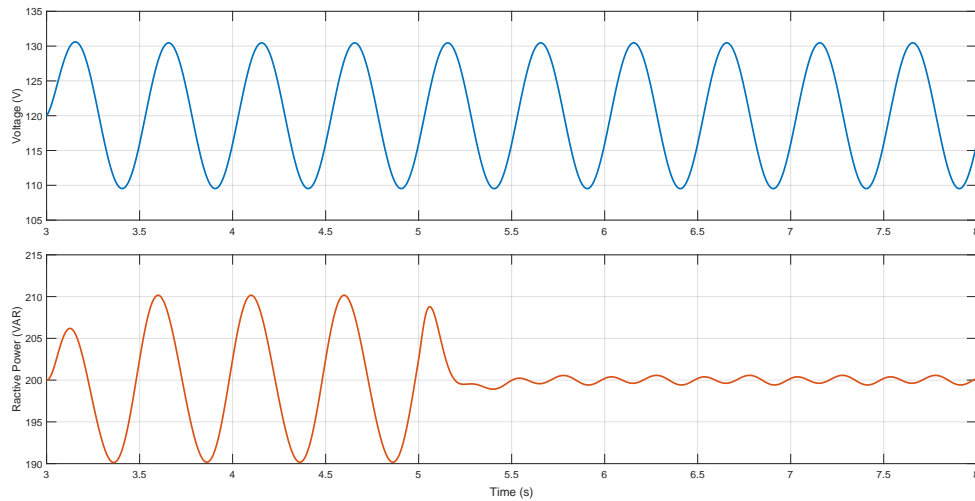


Figure 3.15 Simulation results for POD-Q.

The POD-Q takes the oscillation in voltage magnitude of its own capacitor voltage as the input. The POD-Q is activated after 5 seconds and the oscillation magnitude is then reduced from 10.1 VAR down to 0.388 VAR.

3.4 Summary

This chapter presented the modelling of the three-inverter system along with the design and tuning of the current, power, and POD controllers. The inverters were configured for grid-following operation, with a SRF-PLL used for phase estimation. The current controller was implemented in the dq-frame and designed using decoupling and PI regulation, while the outer power controller regulates active and reactive power references. Power oscillation damping was added through POD-P and POD-Q controllers, implemented as lead-lag compensators acting on power and voltage deviation signals. The chapter also covered how these controllers were tuned based on system characteristics and desired damping performance.

4 Stability Analysis

This chapter will present the stability analysis of the inverter system. First, the theory behind the techniques used to evaluate the inverter system stability will be explained. Secondly, the state-space model of the single- and three-inverter system will be derived. Then, the POD control scheme will be added to the single-inverter state-space model. Finally, a comparison will be made to the simulation results, as well as an evaluation of the inverter system small-signal stability with and without POD control.

4.1 State-Space Modelling

This sections presents the theory and principle of small-signal linearisation and state-space modelling. Ultimately, these techniques will be combined and used to derive a small-signal state-space model of the paralleled inverters.

4.1.1 State-Space Representation

In control theory, the *state-space representation* is a mathematical representation of a control system. It uses the differential terms to distinguish between different states in the system, e.g. \dot{x} and x . The system can be a *single-input single-output* (SISO) system or a *multiple-input multiple-output* (MIMO) system. There are also sub-variants such as systems with single inputs but multiple outputs and vice versa. Nonetheless, the *state-space representation* (SSR) can generally be written in the form seen in Figure 4.1 or Equation (4.1) [23].

$$\begin{aligned}\dot{x}(t) &= A(t)x(t) + B(t)u(t) \\ y(t) &= C(t)x(t) + D(t)x(t)\end{aligned}\tag{4.1}$$

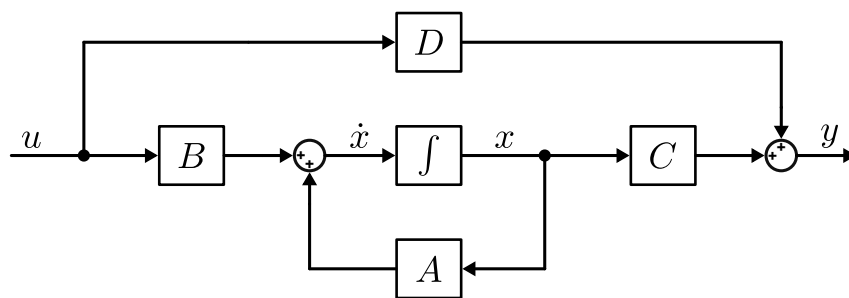


Figure 4.1 Basic representation of a state-space model.

In Figure 4.1 and Equation (4.1), \dot{x} are the derivative terms of x , y is the output of the system and u is the input to the system. These are vectors for most cases. Furthermore, A , B , C and D are matrices involving the system. A is the state or system matrix, describing the feedback relation between x and \dot{x} , i.e. how the current x is relating to its derivative. B is the input matrix, defining how the input affects the derivative term. C is the output matrix, defining how the states affect the output. Finally, D is the feed-forward matrix, defining how the input directly affects the output. The specific dimensions of each vector and matrix are as follows:

- $x(\cdot), n \times 1$
- $\dot{x}(\cdot), n \times 1$
- $y(\cdot), q \times 1$
- $u(\cdot), p \times 1$
- $A(\cdot), n \times n$
- $B(\cdot), n \times p$
- $C(\cdot), q \times n$
- $D(\cdot), q \times p$

Notice, that the matrices in Equation (4.1) are time dependant, which makes the the state-space model time variant [23]. For this project, the state-space models will be time invariant, i.e. the matrices are not time dependant. These are also called *linear time-invariant* (LTI) systems and can be written as seen in Equation (4.2) [23].

$$\begin{aligned}\dot{x}(t) &= Ax(t) + Bu(t) \\ y(t) &= Cx(t) + Dx(t)\end{aligned}\tag{4.2}$$

Depending on the state-space model, there can be no direct feed-forward of the input signals. If that is so, D is a zero matrix of the same dimension. Additionally, the output matrix C can simply be chosen as the identity matrix, in which case the outputs are just the state variables, i.e. $y(t) = x(t)$.

4.1.2 Small-Signal Linearisation

Small-signal linearisation is based on the Taylor series expansion of a non-linear function around an equilibrium point. By retaining only the first-order term, the linear effect of small deviations, referred to as perturbations, can be captured. The *higher-order terms* (H.O.T.) are omitted to preserve linearity, as shown in Equation (4.3) [3].

$$f(x) \approx f(X) + \left. \frac{df}{dx} \right|_{x=X} \Delta x + \cancel{\frac{1}{2} \left. \frac{d^2 f}{dx^2} \right|_{x=X} \Delta x^2} + \text{H.O.T.}\tag{4.3}$$

In a non-linear state-space system defined by $\dot{x} = f(x, u)$ and $y = g(x, u)$, the same linearisation principle can be applied to both the state and input variables using partial derivatives, as shown in Equation (4.4) [3].

$$\dot{x} \approx f(X, U) + \left. \frac{\partial f}{\partial x} \right|_{(X, U)} \Delta x + \left. \frac{\partial f}{\partial u} \right|_{(X, U)} \Delta u\tag{4.4}$$

Because the point (X, U) is an equilibrium, it satisfies $\dot{X} = f(X, U) = 0$. As a result, the linearised system can be expressed in terms of perturbations only, as shown in Equation (4.5) [3].

$$\dot{\Delta x} \approx \left. \frac{\partial f}{\partial x} \right|_{(X, U)} \Delta x + \left. \frac{\partial f}{\partial u} \right|_{(X, U)} \Delta u = A \Delta x + B \Delta u\tag{4.5}$$

Logically, this is done for each $\Delta \dot{x}_i$ -equation and includes the partial derivative of each variable Δx_i and u_j in every equation. The output equation is linearised similarly, as seen in Equation (4.6) [3].

$$\Delta y \approx \left. \frac{\partial g}{\partial x} \right|_{(X, U)} \Delta x + \left. \frac{\partial g}{\partial u} \right|_{(X, U)} \Delta u = C \Delta x + D \Delta u\tag{4.6}$$

Thus the A , B , C and D -matrices are formed based on the Jacobian of the set of equations, with partial derivatives taken with respect to x and u [3]. In practice, each variable of interest is often expressed as the sum of its equilibrium value and a perturbation, as shown in Equation (4.7).

$$x = X + \Delta x, \quad u = U + \Delta u, \quad y = Y + \Delta y\tag{4.7}$$

This simplification is valid because the state-space model consists of first-order differential equations, and all non-linear terms involving products of perturbations, such as $\Delta x_i \Delta x_j$, are neglected in the linear approximation.

4.1.3 Eigenvalue Stability Analysis

To determine system small-signal stability, eigenvalue analysis can often be done. For a state matrix A , the corresponding eigenvalues λ_1, λ_2 to λ_n , for a $n \times n$ state matrix, determine the damping and oscillation of system modes of the linearised system. The real part of the eigenvalue refers to the damping of the mode, where a negative real value indicates positive damping, and a positive real value indicates negative damping and system instability. The imaginary part of the eigenvalue describes the oscillation of the mode. The relationship between the real and imaginary part, and the damping and natural frequency can be described as seen in Equation (4.8) [1].

$$\begin{cases} \lambda_i = \sigma_i \pm j\omega_i \\ f_i = \frac{\omega_i}{2\pi} \\ \zeta_i = \frac{-\sigma_i}{\sqrt{\sigma_i^2 + \omega_i^2}} \end{cases} \quad (4.8)$$

Although eigenvalues indicate system stability, they do not identify which state variables contribute to a given mode's stability or instability. To relate stability to the state variables, the participation factor is often calculated.

$$P_{[n \times n]} = \begin{bmatrix} p_{1,[n \times 1]} & p_{2,[n \times 1]} & \dots & p_{n,[n \times 1]} \end{bmatrix} \quad (4.9)$$

Each participation factor is calculated by the right, $V_{k,i}$, and left, $W_{i,k}$, eigenvector [1]. The calculation of each column of participation factors in Equation (4.9) can be calculated, as seen in Equation (4.10).

$$p_i = \begin{bmatrix} p_{1,i} \\ p_{2,i} \\ \vdots \\ p_{n,i} \end{bmatrix} = \begin{bmatrix} V_{1,i}W_{i,1} \\ V_{2,i}W_{i,2} \\ \vdots \\ V_{n,i}W_{i,n} \end{bmatrix} \quad (4.10)$$

This allows the determination of which state variables are participating in the stability, or instability, of each mode.

4.2 State-Space Model of a Single Inverter

When modelling a single inverter using the small-signal state-space approach, the resulting equations often become too complex to represent within a single state-space model. Therefore, the model is divided into several smaller state-space representations, each corresponding to a subsystem [24] [25]. For this part, the inverter is split into the:

1. Power Controller
2. Current Controller
3. Delay
4. LCL Filter

5. PLL
6. Grid* (Taken as input)

These are chosen based on input-output relations and logical differences. A representation of the different state-space models and their connections can be seen in Figure 4.2.

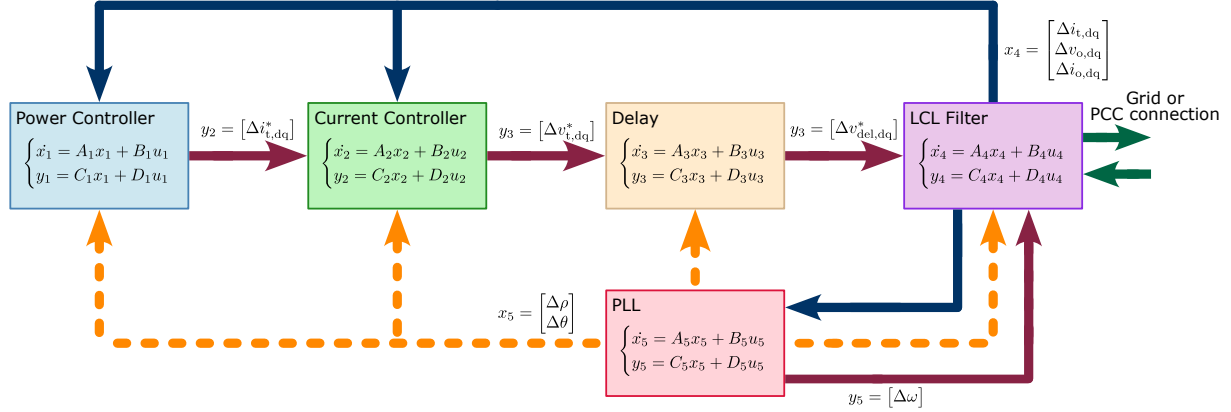


Figure 4.2 Overview of the single-inverter state-space model. Dark blue: state feedback; dark red solid: explicit outputs; orange dashed: dq-frame rotation.

Each state-space model connects to some of the other state-space models, identical to the relations described in Chapter 3. However, the way they connect are different. Some of the state-space models have explicit outputs, meaning that the output is not just the state variables, i.e. $y_k \neq x_k$, but that it is a specific algebraic equation. In Figure 4.2, these are marked by dark red arrows. The outputs where $y_k = x_k$ are marked with dark blue arrows and are state feedbacks. The grid or PCC connection is marked with green, but is not directly covered by the single-inverter state-space model.

The PLL has a significant impact on the abc-to-dq transformations and the inverse. To include the effect of the transformation, equations are inserted for each of the transformed state variables. In other words, the frame rotation, which is not an output to any state-space model, is inserted in the state-space models and is dependant on the state feedback of the PLL. This makes this relation a special case, since it represents both an input and a state feedback.

It should be noted that the frame rotation is applied to the LCL filter, meaning that the voltages and currents associated with the filter are expressed in the dq-frame aligned with the PLL. This differs from the approach commonly found in the literature, such as in [25] and [26], where the frame rotation is applied within the power controller, current controller, and PLL, and the terminal voltage reference is typically transformed back to the original dq-frame. Such a procedure deviates from the physical system, where both the LCL filter dynamics and the voltage reference inherently operate in the PLL-aligned frame. In contrast, the state-space model developed in this project avoids this discrepancy by keeping the voltage reference and filter representation consistently within the same dq-frame. This also allows for more accurate comparison with simulation results. The impact on eigenvalue-based stability analysis between these two methods are unknown.

The derivation of the small-signal linearised equations and state-space representation of each

state-space model will be explained in the next sections, though most of the derivation will take place in the appendix. The control structure and values used will be identical to that of Chapter 3. The state-space modelling approach will be based on [24], [25], [26] and the principles of small-signal state-space modelling, explained in Sections 4.1.1 and 4.1.2.

4.2.1 Power Controller

The power controller consists of two parts, the power calculation used for the feedback signal and the PI controller used to generate the current reference based on an error between the reference signal and the measured power. The control scheme can be seen in Figure 4.3, which includes the state variables and outputs.

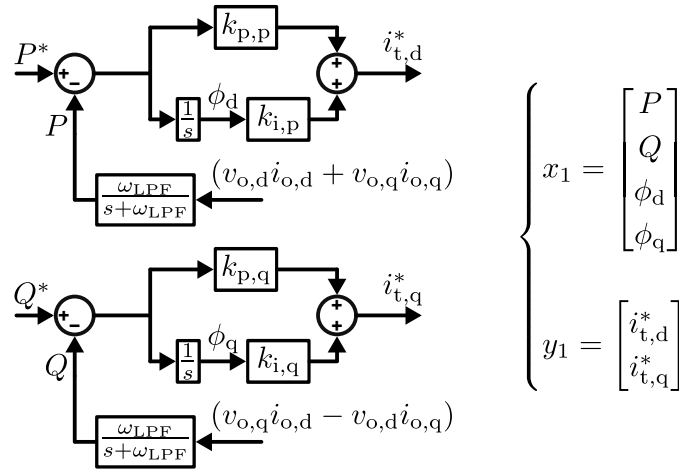


Figure 4.3 Control diagram of the power controller with highlighted state variables and outputs.

The power calculations and control equations can be seen in Equation (4.11).

$$\left\{ \begin{array}{l} \textbf{Power Calculations:} \\ P = \frac{\omega_{LPF}}{\omega_{LPF} + s} \frac{3}{2} (v_{o,d}i_{o,d} + v_{o,q}i_{o,q}) \\ Q = \frac{\omega_{LPF}}{\omega_{LPF} + s} \frac{3}{2} (v_{o,q}i_{o,d} - v_{o,d}i_{o,q}) \\ \textbf{Control Equations:} \\ \phi_d = \int (P^* - P) dt \Rightarrow \frac{d\phi_d}{dt} = P^* - P \\ \phi_q = \int (Q^* - Q) dt \Rightarrow \frac{d\phi_q}{dt} = Q^* - Q \\ i_{o,d}^* = k_{p,p} (P^* - P) + k_{i,p} \phi_d \\ i_{o,q}^* = k_{p,q} (Q^* - Q) + k_{i,q} \phi_q \end{array} \right. \quad (4.11)$$

As can be seen, intermediate equations are created for the integral action of the PI controller, i.e. ϕ_d and ϕ_q are the integral term of the error signals. By moving around and doing small-signal linearisation, the state equations and algebraic equations can be reached in Equation (4.12).

$$\begin{cases}
\textbf{State Equations:} \\
\begin{aligned}
\dot{\Delta P} &= -\omega_{\text{LPF}} \Delta P + \omega_{\text{LPF}} \frac{3}{2} (V_{o,d} \Delta i_{o,d} + I_{o,d} \Delta v_{o,d} + V_{o,q} \Delta i_{o,q} + I_{o,q} \Delta v_{o,q}) \\
\dot{\Delta Q} &= -\omega_{\text{LPF}} \Delta Q + \omega_{\text{LPF}} \frac{3}{2} (V_{o,q} \Delta i_{o,d} + I_{o,d} \Delta v_{o,q} - V_{o,d} \Delta i_{o,q} - I_{o,q} \Delta v_{o,d}) \\
\dot{\Delta \phi_d} &= \Delta P^* - \Delta P \\
\dot{\Delta \phi_q} &= \Delta Q^* - \Delta Q
\end{aligned} \\
\textbf{Algebraic Equations:} \\
\begin{aligned}
\Delta i_{o,d}^* &= k_{p,p} (\Delta P^* - \Delta P) + k_{i,p} \Delta \phi_d \\
\Delta i_{o,q}^* &= k_{p,q} (\Delta Q^* - \Delta Q) + k_{i,q} \Delta \phi_q
\end{aligned}
\end{cases} \quad (4.12)$$

As can be seen, the s in the LPF and the integral action of the PI controller creates 4 state equations and 2 algebraic equations. The full derivation of this can be found in Section B.1.1. In a state-space representation, the 4 state equations form the $\dot{\Delta x}_1$ and the algebraic equations form the Δy_1 . The $\dot{\Delta x}_1$ can be seen in Equation (4.13).

$$\dot{\Delta x}_1 = \begin{bmatrix} \dot{\Delta P} \\ \dot{\Delta Q} \\ \dot{\Delta \phi_d} \\ \dot{\Delta \phi_q} \end{bmatrix} = A_P \begin{bmatrix} \Delta P \\ \Delta Q \\ \Delta \phi_d \\ \Delta \phi_q \end{bmatrix} + B_{P1} \begin{bmatrix} \Delta i_{t,dq} \\ \Delta v_{o,dq} \\ \Delta i_{o,dq} \end{bmatrix} + B_{P2} \begin{bmatrix} \Delta P^* \\ \Delta Q^* \end{bmatrix} \quad (4.13)$$

Where the system A-matrix can be written as seen in Equation (4.14) and the two system input matrices can be written, as seen in Equation (4.15).

$$A_P = \begin{bmatrix} -\omega_{\text{LPF}} & 0 & 0 & 0 \\ 0 & -\omega_{\text{LPF}} & 0 & 0 \\ -1 & 0 & 0 & 0 \\ 0 & -1 & 0 & 0 \end{bmatrix} \quad (4.14)$$

$$B_{P1} = \begin{bmatrix} 0 & 0 & \frac{3}{2}\omega_{\text{LPF}}I_{o,d} & \frac{3}{2}\omega_{\text{LPF}}I_{o,q} & \frac{3}{2}\omega_{\text{LPF}}V_{o,d} & \frac{3}{2}\omega_{\text{LPF}}V_{o,q} \\ 0 & 0 & -\frac{3}{2}\omega_{\text{LPF}}I_{o,q} & \frac{3}{2}\omega_{\text{LPF}}I_{o,d} & \frac{3}{2}\omega_{\text{LPF}}V_{o,q} & -\frac{3}{2}\omega_{\text{LPF}}V_{o,d} \\ 0 & 0 & 0 & 0 & 0 & 0 \\ 0 & 0 & 0 & 0 & 0 & 0 \end{bmatrix} \quad B_{P2} = \begin{bmatrix} 0 & 0 \\ 0 & 0 \\ 1 & 0 \\ 0 & 1 \end{bmatrix} \quad (4.15)$$

Notice, that the input matrix has been split into two matrices. The first matrix, B_{P1} , relates to the state variables of the LCL Filter and the second matrix, B_{P2} , relates to the reference signals given. The logic of this will become clear when the state-space models are finally combined. The system output can be written, as seen in Equation (4.16).

$$\Delta y_1 = \begin{bmatrix} \Delta i_{o,d}^* \\ \Delta i_{o,q}^* \end{bmatrix} = C_P \begin{bmatrix} \Delta P \\ \Delta Q \\ \Delta \phi_d \\ \Delta \phi_q \end{bmatrix} + D_P \begin{bmatrix} \Delta P^* \\ \Delta Q^* \end{bmatrix} \quad (4.16)$$

Where the system output matrix and feed-forward matrix can be written, as seen in Equation (4.17).

$$C_P = \begin{bmatrix} -k_{p,p} & 0 & k_{i,p} & 0 \\ 0 & -k_{p,q} & 0 & k_{i,q} \end{bmatrix} \quad D_P = \begin{bmatrix} k_{p,p} & 0 \\ 0 & k_{p,q} \end{bmatrix} \quad (4.17)$$

4.2.2 Current Controller

The state-space model of the current control loop only consists of the control equations. However, the integral action of the PI controller creates the need to add intermediate equations. A control diagram of the current control loop can be seen in Figure 4.4, where the state variables and outputs are highlighted.

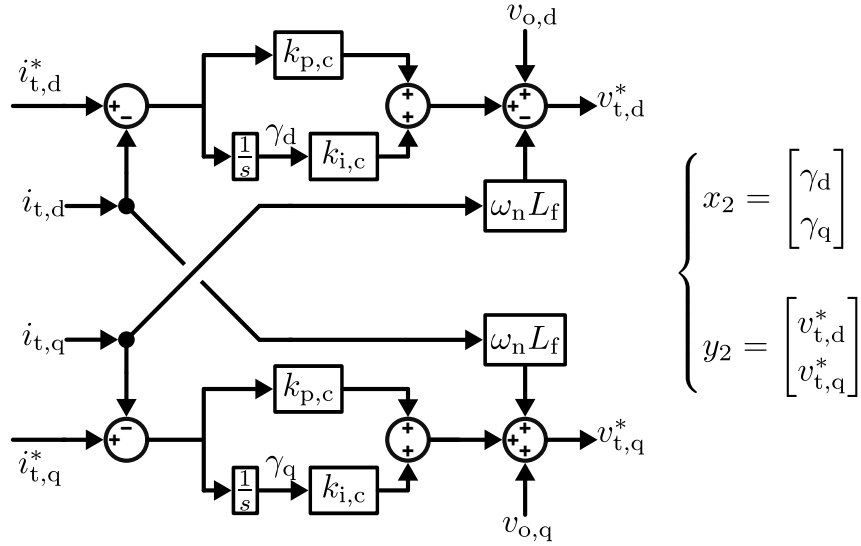


Figure 4.4 Control diagram of the current control loop with state variables and outputs highlighted.

The control equations can be seen in Equation (4.18).

$$\left\{ \begin{array}{l} \textbf{Control Equations:} \\ \gamma_d = \int (i_{t,d}^* - i_{t,d}) dt \Rightarrow \frac{d\gamma_d}{dt} = i_{t,d}^* - i_{t,d} \\ \gamma_q = \int (i_{t,q}^* - i_{t,q}) dt \Rightarrow \frac{d\gamma_q}{dt} = i_{t,q}^* - i_{t,q} \\ v_{t,d}^* = -\omega_n L_f i_{t,q} + v_{o,d} + k_{p,c} (i_{t,d}^* - i_{t,d}) + k_{i,c} \gamma_d \\ v_{t,q}^* = \omega_n L_f i_{t,d} + v_{o,q} + k_{p,c} (i_{t,q}^* - i_{t,q}) + k_{i,c} \gamma_q \end{array} \right. \quad (4.18)$$

By doing small-signal linearisation, 2 state equations from the integral part and 2 algebraic equations can be created, as seen in Equation (4.19).

$$\left\{ \begin{array}{l} \textbf{State Equations:} \\ \frac{d\Delta\gamma_d}{dt} = \Delta i_{t,d}^* - \Delta i_{t,d} \\ \frac{d\Delta\gamma_q}{dt} = \Delta i_{t,q}^* - \Delta i_{t,q} \\ \textbf{Algebraic Equations:} \\ \Delta v_{t,d}^* = -\omega_n L_f \Delta i_{t,q} + \Delta v_{o,d} + k_{p,c} (\Delta i_{t,d}^* - \Delta i_{t,d}) + k_{i,c} \Delta\gamma_d \\ \Delta v_{t,q}^* = \omega_n L_f \Delta i_{t,d} + \Delta v_{o,q} + k_{p,c} (\Delta i_{t,q}^* - \Delta i_{t,q}) + k_{i,c} \Delta\gamma_q \end{array} \right. \quad (4.19)$$

The full derivation of the state equations and algebraic equations can be found in Section B.1.2. The 2 state equations form the $\Delta \dot{x}_2$ and the two algebraic equations form the Δy_2 . The $\Delta \dot{x}_2$ can be seen in Equation (4.20).

$$\Delta \dot{x}_2 = \left[\Delta \dot{\gamma}_{dq} \right] = A_C \left[\Delta \gamma_{dq} \right] + B_{C1} \left[\Delta i_{t,dq}^* \right] + B_{C2} \begin{bmatrix} \Delta i_{t,dq} \\ \Delta v_{o,dq} \\ \Delta i_{o,dq} \end{bmatrix} \quad (4.20)$$

Where the system A -matrix and input B -matrices can be seen in Equation (4.21).

$$A_C = \begin{bmatrix} 0 & 0 \\ 0 & 0 \end{bmatrix} \quad B_{C1} = \begin{bmatrix} 1 & 0 \\ 0 & 1 \end{bmatrix} \quad B_{C2} = \begin{bmatrix} -1 & 0 & 0 & 0 & 0 & 0 \\ 0 & -1 & 0 & 0 & 0 & 0 \end{bmatrix} \quad (4.21)$$

Notice once more, that the input matrix is split into two matrices. Similarly as for the power controller, the first matrix is related to the current references and the second matrix is related to the LCL filter state variables. The output can be seen in Equation (4.22).

$$\Delta y_2 = \begin{bmatrix} \Delta v_{t,dq}^* \end{bmatrix} = C_C \begin{bmatrix} \Delta \gamma_{dq} \end{bmatrix} + D_{C1} \begin{bmatrix} \Delta i_{t,dq}^* \end{bmatrix} + D_{C2} \begin{bmatrix} \Delta i_{t,dq} \\ \Delta v_{o,dq} \\ \Delta i_{o,dq} \end{bmatrix} \quad (4.22)$$

Where the output matrix and feed-forward matrix can be seen in Equation (4.23).

$$C_C = \begin{bmatrix} k_{i,c} & 0 \\ 0 & k_{i,c} \end{bmatrix} \quad D_{C1} = \begin{bmatrix} k_{p,c} & 0 \\ 0 & k_{p,c} \end{bmatrix} \quad D_{C2} = \begin{bmatrix} -k_{p,c} & -\omega_n L_f & 1 & 0 & 0 & 0 \\ \omega_n L_f & -k_{p,c} & 0 & 1 & 0 & 0 \end{bmatrix} \quad (4.23)$$

4.2.3 Delay

For the controller tuning, the delay was implemented as a transfer function approximation. Similar can be done for a state-space representation. The equations for the delayed modulation signals can be seen in Equation (4.24).

$$\begin{cases} \text{Delay Equations:} \\ v_{del,d} = -\frac{1}{1.5T_s} v_{del,d} + \frac{1}{1.5T_s} v_{t,d}^* \\ v_{del,q} = -\frac{1}{1.5T_s} v_{del,q} + \frac{1}{1.5T_s} v_{t,q}^* \end{cases} \quad (4.24)$$

The s in the delay approximation creates state variables. The equations can be small-signal linearised, which leads to the equations in Equation (4.25).

$$\begin{cases} \text{State Equations:} \\ \Delta \dot{v}_{del,d} = -\frac{1}{1.5T_s} \Delta v_{del,d} + \frac{1}{1.5T_s} \Delta v_{t,d}^* \\ \Delta \dot{v}_{del,q} = -\frac{1}{1.5T_s} \Delta v_{del,q} + \frac{1}{1.5T_s} \Delta v_{t,q}^* \end{cases} \quad (4.25)$$

The state equations can be written in state-space representation, as seen in Equation (4.26).

$$\Delta \dot{x}_3 = \begin{bmatrix} \Delta \dot{v}_{del,d} \\ \Delta \dot{v}_{del,q} \end{bmatrix} = A_{del} \begin{bmatrix} \Delta v_{del,d} \\ \Delta v_{del,q} \end{bmatrix} + B_{del} \begin{bmatrix} \Delta v_{t,d}^* \\ \Delta v_{t,q}^* \end{bmatrix} \quad (4.26)$$

Where the system A -matrix and input matrix can be seen in Equation (4.27).

$$A_{del} = \begin{bmatrix} -\frac{1}{1.5T_s} & 0 \\ 0 & -\frac{1}{1.5T_s} \end{bmatrix} \quad B_{del} = \begin{bmatrix} \frac{1}{1.5T_s} & 0 \\ 0 & \frac{1}{1.5T_s} \end{bmatrix} \quad (4.27)$$

Note that, in this state-space model, there is no explicit output. In other words, C -matrix is an identity matrix of the same size as the A -matrix and the D -matrix is a zero matrix.

4.2.4 LCL Filter

The equations for the LCL filter can be defined as was done in Chapter 3 for the transfer function derivation. This leads to 6 equations in the dq domain, as seen in Equation (4.28).

$$\left\{ \begin{array}{l} \textbf{KVL \& KCL Equations:} \\ \frac{di_{t,d}}{dt} = \frac{-R_f}{L_f} i_{t,d} + \omega i_{t,q} + \frac{1}{L_f} v_{del,d}^* - \frac{1}{L_f} v_{o,d} \\ \frac{di_{t,q}}{dt} = \frac{-R_f}{L_f} i_{t,q} - \omega i_{t,d} + \frac{1}{L_f} v_{del,q}^* - \frac{1}{L_f} v_{o,q} \\ \frac{dv_{o,d}}{dt} = \omega v_{o,q} + \frac{1}{C_f} i_{t,d} - \frac{1}{C_f} i_{o,d} \\ \frac{dv_{o,q}}{dt} = -\omega v_{o,d} + \frac{1}{C_f} i_{t,q} - \frac{1}{C_f} i_{o,q} \\ \frac{di_{o,d}}{dt} = \frac{-R_c}{L_c} i_{o,d} + \omega i_{o,q} + \frac{1}{L_c} v_{o,d} - \frac{1}{L_c} v_{b,d} \\ \frac{di_{o,q}}{dt} = \frac{-R_c}{L_c} i_{o,q} - \omega i_{o,d} + \frac{1}{L_c} v_{o,q} - \frac{1}{L_c} v_{b,q} \end{array} \right. \quad (4.28)$$

The ω is determined by the PLL in order to align the dq0 reference frame. Therefore, any mismatch between the actual frequency and the PLL frequency will have an effect on the dynamics. When small-signal linearising, the multiplication between ω and the voltages and currents will introduce non-linear second order terms, i.e. $\Delta\omega \cdot (\Delta i_{t,dq} + \Delta v_{o,dq} + \Delta i_{o,dq})$. These are ignored since they are non-linear and typically small. However, for linear simulation with large step changes, the assumption that the values are typically small is untrue. Therefore, an increased mismatch in dynamics is expected when doing large changes in the system. The small-signal linearised equations can be seen in Equation (4.29).

$$\left\{ \begin{array}{l} \textbf{State Equations:} \\ \frac{d\Delta i_{t,d}}{dt} = \frac{-R_f}{L_f} \Delta i_{t,d} + \omega_n \Delta i_{t,q} + \Delta\omega I_{t,q} + \frac{1}{L_f} \Delta v_{del,d}^* - \frac{1}{L_f} \Delta v_{o,d} \\ \frac{d\Delta i_{t,q}}{dt} = \frac{-R_f}{L_f} \Delta i_{t,q} - \omega_n \Delta i_{t,d} - \Delta\omega I_{t,d} + \frac{1}{L_f} \Delta v_{del,q}^* - \frac{1}{L_f} \Delta v_{o,q} \\ \frac{d\Delta v_{o,d}}{dt} = \omega_n \Delta v_{o,q} + \Delta\omega V_{o,q} + \frac{1}{C_f} \Delta i_{t,d} - \frac{1}{C_f} \Delta i_{o,d} \\ \frac{d\Delta v_{o,q}}{dt} = -\omega_n \Delta v_{o,d} - \Delta\omega V_{o,d} + \frac{1}{C_f} \Delta i_{t,q} - \frac{1}{C_f} \Delta i_{o,q} \\ \frac{d\Delta i_{o,d}}{dt} = \frac{-R_c}{L_c} \Delta i_{o,d} + \omega_n \Delta i_{o,q} + \Delta\omega I_{o,q} + \frac{1}{L_c} \Delta v_{o,d} - \frac{1}{L_c} \Delta v_{b,d} \\ \frac{d\Delta i_{o,q}}{dt} = \frac{-R_c}{L_c} \Delta i_{o,q} - \omega_n \Delta i_{o,d} - \Delta\omega I_{o,d} + \frac{1}{L_c} \Delta v_{o,q} - \frac{1}{L_c} \Delta v_{b,q} \end{array} \right. \quad (4.29)$$

The full derivation of the small-signal linearised equations can be found in Section B.1.4. There are 6 state equations that form the Δx_4 , as seen in Equation (4.30).

$$\dot{\Delta x}_4 = A_{LCL} \begin{bmatrix} \Delta i_{t,dq} \\ \Delta v_{o,dq} \\ \Delta i_{o,dq} \end{bmatrix} + B_{LCL1} [\Delta v_{del,dq}^*] + B_{LCL2} [\Delta v_{b,dq}] + B_{LCL3} [\Delta\omega] \quad (4.30)$$

Where the system A -matrix can be seen in Equation (4.31).

$$A_{LCL} = \begin{bmatrix} -\frac{R_f}{L_f} & \omega_n & -\frac{1}{L_f} & 0 & 0 & 0 \\ -\omega_n & -\frac{R_f}{L_f} & 0 & -\frac{1}{L_f} & 0 & 0 \\ \frac{1}{C_f} & 0 & 0 & \omega_n & -\frac{1}{C_f} & 0 \\ 0 & \frac{1}{C_f} & -\omega_n & 0 & 0 & -\frac{1}{C_f} \\ 0 & 0 & \frac{1}{L_c} & 0 & -\frac{R_c}{L_c} & \omega_n \\ 0 & 0 & 0 & \frac{1}{L_c} & -\omega_n & -\frac{R_c}{L_c} \end{bmatrix} \quad (4.31)$$

And the input matrices can be defined as seen in Equation (4.32).

$$B_{LCL1} = \begin{bmatrix} \frac{1}{L_f} & 0 \\ 0 & \frac{1}{L_f} \\ 0 & 0 \\ 0 & 0 \\ 0 & 0 \\ 0 & 0 \end{bmatrix} \quad B_{LCL2} = \begin{bmatrix} 0 & 0 \\ 0 & 0 \\ 0 & 0 \\ 0 & 0 \\ -\frac{1}{L_c} & 0 \\ 0 & -\frac{1}{L_c} \end{bmatrix} \quad B_{LCL3} = \begin{bmatrix} I_{t,q} \\ -I_{t,d} \\ V_{o,q} \\ -V_{o,d} \\ I_{o,q} \\ -I_{o,d} \end{bmatrix} \quad (4.32)$$

Notice, that the system B -matrix is split into three B -matrices. The first is related to the voltage driven by the inverter and the second is related to the voltage of the connecting bus or PCC. The third matrix carries the operating points or equilibrium points. These alter the dq components based on the $\Delta\omega$ from the PLL. The purpose of splitting the matrix will become evident later.

4.2.5 PLL

The PLL is identical to what was presented in Chapter 3. In the dq frame, the PLL can be illustrated as shown in Figure 4.5, where the state variables and output have been highlighted.

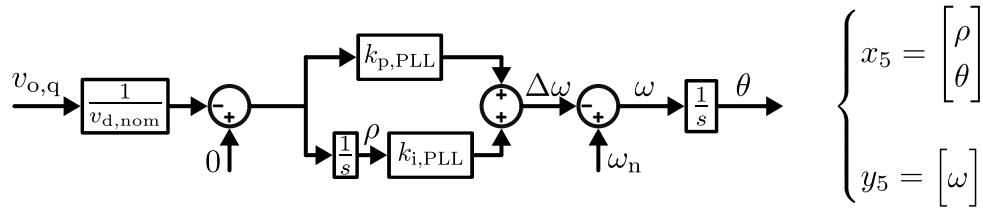


Figure 4.5 Control diagram of the PLL with the state variables and output highlighted.

Note that, the $k_{p,PLL}$ and $k_{i,PLL}$ can just be scaled with $1/v_{d,nom}$ for simplicity. The control equation can be written, as seen in Equation (4.33).

$$\left\{ \begin{array}{l} \textbf{Control Equations:} \\ \rho = \int (0 - v_{o,q}) dt \Rightarrow \frac{d\rho}{dt} = -v_{o,q} \\ \omega = \dot{\theta} = k_{p,PLL}(0 - v_{o,q}) + k_{i,PLL}\rho + \omega_n \end{array} \right. \quad (4.33)$$

The intermediate variable, ρ , is created to account for the integral action of the PI controller. The PLL control equations can be small-signal linearised, as seen in Equation (4.34).

$$\left\{ \begin{array}{l} \textbf{State Equations:} \\ \Delta\dot{\rho} = 0 - \Delta v_{o,q} \\ \Delta\dot{\theta} = k_{p,PLL}(0 - \Delta v_{o,q}) + k_{i,PLL}\Delta\rho \\ \textbf{Algebraic Equations:} \\ \Delta\omega = -k_{p,PLL}\Delta v_{o,q} + k_{i,PLL}\Delta\rho \end{array} \right. \quad (4.34)$$

The output required from the PLL state-space model is the angular frequency, due to the dependency on it in the LCL filter. The full derivation of the small-signal linearised equations can be found in Section B.1.5. Writing the equations in a state-space representation, the $\Delta\dot{x}_5$

in Equation (4.35) can be reached.

$$\Delta \dot{x}_5 = \begin{bmatrix} \dot{\Delta \rho} \\ \dot{\Delta \theta} \end{bmatrix} = A_{\text{PLL}} \begin{bmatrix} \Delta \rho \\ \Delta \theta \end{bmatrix} + B_{\text{PLL}} \begin{bmatrix} \Delta i_{t,dq} \\ \Delta v_{o,dq} \\ \Delta i_{o,dq} \end{bmatrix} \quad (4.35)$$

Where the A -matrix and B -matrix can be seen in Equation (4.36).

$$A_{\text{PLL}} = \begin{bmatrix} 0 & 0 \\ k_{i,\text{PLL}} & 0 \end{bmatrix} \quad B_{\text{PLL}} = \begin{bmatrix} 0 & 0 & 0 & -1 & 0 & 0 \\ 0 & 0 & 0 & -k_{p,\text{PLL}} & 0 & 0 \end{bmatrix} \quad (4.36)$$

The output can be explained from the algebraic equations and can be seen in Equation (4.37).

$$\Delta y_5 = \begin{bmatrix} \Delta \omega \end{bmatrix} = C_{\text{PLL}} \begin{bmatrix} \Delta \rho \\ \Delta \theta \end{bmatrix} + D_{\text{PLL}} \begin{bmatrix} \Delta i_{t,dq} \\ \Delta v_{o,dq} \\ \Delta i_{o,dq} \end{bmatrix} \quad (4.37)$$

Where the C -matrix and D -matrix can be seen in Equation (4.38).

$$C_{\text{PLL}} = \begin{bmatrix} k_{i,\text{PLL}} & 0 \end{bmatrix} \quad D_{\text{PLL}} = \begin{bmatrix} 0 & 0 & 0 & -k_{p,\text{PLL}} & 0 & 0 \end{bmatrix} \quad (4.38)$$

However, if the PLL is only implemented like this, only the stability of the PLL it self is taken into account. Additionally, $\Delta \theta$ is never used in the PLL state-space model, nor in any of the other state-space models. In the PLL block diagram from Chapter 3, the PLL used its calculated θ to adjust all the abc-to-dq0 transformations. Thus, the PLL does influence it self, like a feedback loop, but this is not present in anything presented yet. Consequently, if a disturbance happens to the state-space system, no realignment of the dq0 frame would happen [25] [26]. An illustration of a dq frame misalignment can be seen in Figure 4.6.

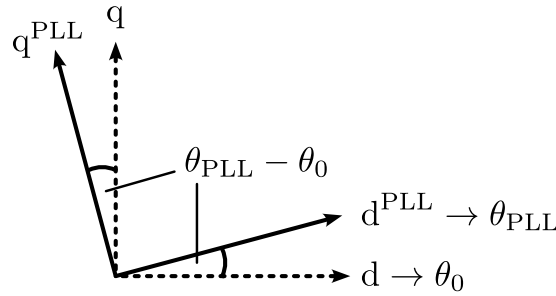


Figure 4.6 Illustration of PLL dq frame rotation.

The figure shows a mismatch between some initial or actual dq frame, described by θ_0 , and the PLL calculated dq frame, described by θ_{PLL} . To account for this dynamic behaviour, a rotation has to be applied to the dq0 voltages and currents. Thus, for the state variables of the LCL filter, the transformation can be seen as in Equation (4.39).

$$\begin{bmatrix} \Delta i_{t,d}^{\text{PLL}} \\ \Delta i_{t,q}^{\text{PLL}} \\ \Delta v_{o,d}^{\text{PLL}} \\ \Delta v_{o,q}^{\text{PLL}} \\ \Delta i_{o,d}^{\text{PLL}} \\ \Delta i_{o,q}^{\text{PLL}} \end{bmatrix} = \begin{bmatrix} \Delta i_{t,d}^0 \\ \Delta i_{t,q}^0 \\ \Delta v_{o,d}^0 \\ \Delta v_{o,q}^0 \\ \Delta i_{o,d}^0 \\ \Delta i_{o,q}^0 \end{bmatrix} + \begin{bmatrix} 0 & I_{t,q}^0 \\ 0 & -I_{t,d}^0 \\ 0 & V_{o,q}^0 \\ 0 & -V_{o,d}^0 \\ 0 & I_{o,q}^0 \\ 0 & -I_{o,d}^0 \end{bmatrix} \begin{bmatrix} \Delta \rho \\ \Delta \theta \end{bmatrix} = \begin{bmatrix} \Delta i_{t,dq}^0 \\ \Delta v_{o,dq}^0 \\ \Delta i_{o,dq}^0 \end{bmatrix} + B_E \begin{bmatrix} \Delta \rho \\ \Delta \theta \end{bmatrix} \quad (4.39)$$

In other words, the $\begin{bmatrix} \Delta i_{t,dq} & \Delta v_{o,dq} & \Delta i_{o,dq} \end{bmatrix}^T$ in all the other state-space models should be replaced with Equation (4.39). This ensures that the dq frame used for control accurately reflects the dynamics of the PLL. The full derivation and small-signal linearisation can be found in Section B.1.5.

4.2.6 Combined Single-Inverter Model

To combine the state-space models into one single state-space model, representing an inverter with filter, the explicit outputs of the state-space models have to be inserted into the belonging inputs of the $\Delta \dot{x}_k$ state-space models. Afterwards, the combined state-space model can be represented as seen in Equation (4.40).

$$\Delta \dot{x}_{INV} = A_{INV} [\Delta x_{INV}] + B_{INV} [\Delta v_{b,dq}] + B_{CTRL} [\Delta PQ^*] \quad (4.40)$$

As can be seen, the state variables are Δx_{INV} and the inputs are the connecting bus voltage, $[\Delta v_{b,dq}]$, and the active- and reactive power references, ΔP^* and ΔQ^* . In Equation (4.40), the combined state variables are as seen in Equation (4.41).

$$\Delta x_{INV} = \begin{bmatrix} \Delta P & \Delta Q & \Delta \phi_{dq} & \Delta \gamma_{dq} & \Delta v_{del,dq}^* & \Delta i_{t,dq} & \Delta v_{o,dq} & \Delta i_{o,dq} & \Delta \rho & \Delta \theta \end{bmatrix}^T \quad (4.41)$$

Thus, there are a total of 16 state variables, 5 of them coming from the integral action of PI controllers and 11 of them being the powers, voltages, currents and angle of the system.

An overview can be seen in Table 4.1 for the state-space models and the relevant inputs and outputs. Only explicit outputs can be found in the table, since they are the outputs that have to be inserted into the $\Delta \dot{x}_k$ -equation of other state-space models. If the output is just the state variables, then these will be assigned by the placement in the combined A -matrix.

Table 4.1 Overview of single-inverter state-space model inputs (u) and explicit outputs ($\Delta y_k \neq \Delta x_k$).

SSM	Input	Output
$\Delta \dot{x}_1$ Power Controller	$\begin{bmatrix} \Delta i_{t,dq} & \Delta v_{o,dq} & \Delta i_{o,dq} \end{bmatrix}^T$ and $\begin{bmatrix} \Delta P^* \\ \Delta Q^* \end{bmatrix}$	$[\Delta i_{t,dq}^*]$
$\Delta \dot{x}_2$ Current Controller	$\begin{bmatrix} \Delta i_{t,dq} & \Delta v_{o,dq} & \Delta i_{o,dq} \end{bmatrix}^T$ and $[\Delta i_{t,dq}^*]$	$[\Delta v_{t,dq}^*]$
$\Delta \dot{x}_3$ Delay	$[\Delta v_{t,dq}^*]$	$[-]$
$\Delta \dot{x}_4$ LCL Filter	$[\Delta v_{del,dq}^*]$, $[\Delta v_{b,dq}]$, $[\Delta \omega]$ and $\begin{bmatrix} \Delta \rho \\ \Delta \theta \end{bmatrix}$	$[-]$
$\Delta \dot{x}_5$ PLL	$\begin{bmatrix} \Delta i_{t,dq} & \Delta v_{o,dq} & \Delta i_{o,dq} \end{bmatrix}^T$	$[\Delta \omega]$

Similarly to the control structure presented in Chapter 3, the output of the power controller, $\Delta y_1 = [\Delta i_{t,dq}^*]$, will be input into the state-space model of the current controller. Then, the new output of the current controller, $\Delta y_2 = [\Delta v_{t,dq}^*]$, will be inserted into the state-space model of the delay. Finally, the dq frame rotation will be inserted into the other state-space models and the output of the state-space model of the PLL, $\Delta y_5 = [\Delta \omega]$, will be inserted into the state-space model of the LCL filter.

Now, all the $\Delta \dot{x}_k$ can be combined into a large state-space model, as seen in Equation (4.42) [24]. The full process of inserting inputs and combining the state-space models can be found in Section B.1.6.

$$\Delta \dot{x}_{\text{INV}} = \begin{bmatrix} \Delta x_1 \\ \Delta x_2 \\ \Delta x_3 \\ \Delta x_4 \\ \Delta x_5 \end{bmatrix} = A_{\text{INV}} [\Delta x_{\text{INV}}] + B_{\text{INV}} [\Delta v_{\text{b,dq}}] + B_{\text{CTRL}} \begin{bmatrix} \Delta P^* \\ \Delta Q^* \end{bmatrix} \quad (4.42)$$

The A -matrix is 16-by-16 and can be seen in Equation (4.43), reduced to a 5-by-5 matrix.

$$A_{\text{INV}} = \begin{bmatrix} \overbrace{A_P}^{\Delta x_1} & \overbrace{0_{[4 \times 2]}}^{\Delta x_2} & \overbrace{0_{[4 \times 2]}}^{\Delta x_3} & \overbrace{B_{P1}}^{\Delta x_4} & \overbrace{B_{P1} B_E}^{\Delta x_5} \\ B_{C1} C_P & 0_{[2 \times 2]} & 0_{[2 \times 2]} & B_{C2} & B_{C2} B_E \\ B_{\text{del}} D_{C1} C_P & B_{\text{del}} C_C & A_{\text{del}} & B_{\text{del}} D_{C2} & B_{\text{del}} D_{C2} B_E \\ 0_{[6 \times 4]} & 0_{[6 \times 2]} & B_{\text{LCL1}} & A_{\text{LCL}} + B_{\text{LCL3}} D_{\text{PLL}} & A_{\text{LCL}} B_E + B_{\text{LCL3}} C_{\text{PLL}} \\ 0_{[2 \times 4]} & 0_{[2 \times 2]} & 0_{[2 \times 2]} & B_{\text{PLL}} & A_{\text{PLL}} \end{bmatrix} \quad (4.43)$$

The B -matrices can be seen in Equation (4.44), where the first B -matrix relates to the connecting bus or PCC voltage, and the second B -matrix relates to the active- and reactive power reference signals given.

$$B_{\text{INV}} = \begin{bmatrix} 0_{[4 \times 2]} \\ 0_{[2 \times 2]} \\ 0_{[2 \times 2]} \\ B_{\text{LCL2}} \\ 0_{[2 \times 2]} \end{bmatrix} \quad B_{\text{CTRL}} = \begin{bmatrix} B_{P2} \\ B_{C1} D_P \\ B_{\text{del}} D_{C1} D_P \\ 0_{[6 \times 2]} \\ 0_{[2 \times 2]} \end{bmatrix} \quad (4.44)$$

The single-inverter state-space model is now complete. There are no explicit output of the state-space model, and the output can be chosen using the C -matrix. The D -matrix is a zero matrix. For linear simulation of the single inverter system, the bus voltage can be set to a constant value, like the grid voltage or similar. The active- and reactive power reference can then be changed to emulate a step response or similar. Alternatively, the bus voltage input can be used to combine several inverters in various types of connection.

4.3 State-Space Model of Multiple Inverters

For the multi-inverter small-signal state-space model, the inverters have to be combined depending on their connection configuration and control logic. For this system, the 3 inverter models are in parallel and connected to a grid, as seen in Figure 4.7. The bus voltage, $\Delta v_{\text{b,dq}}$, will be used to make the connection. However, the bus voltage does not have its own differential equation, meaning that it can not be a state variable. Therefore, a special method has to be implemented for it to act as a floating bus. The grid current is the sum of the inverter currents, but also passes through the grid inductance and resistance, making it a separate differential equation. Therefore, the current relationship and the grid impedance have to be modelled for the multi-inverter model to be made. Additionally, the single-inverter model has to be modified, as the inverters will share the same single PLL.

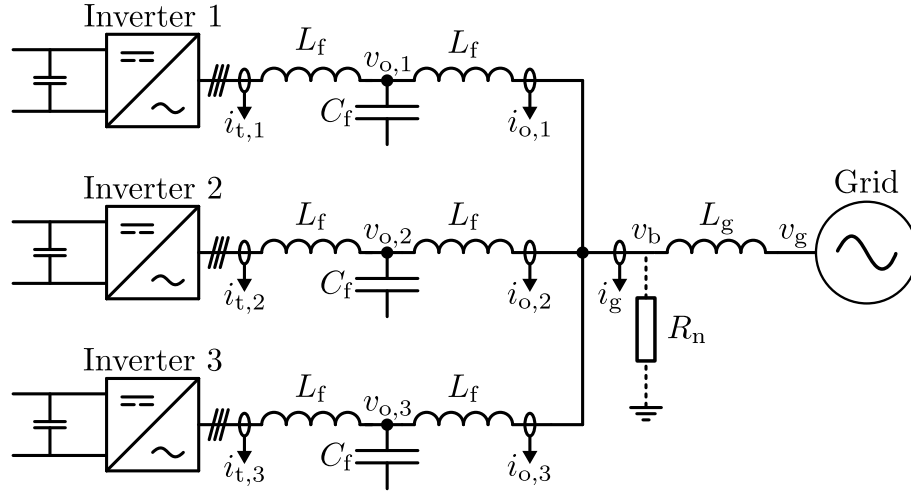


Figure 4.7 Overview of multi-inverter system configuration.

4.3.1 Grid Model

The grid, in this case, is modelled as an inductive line with resistance, where on one end is a fixed voltage, v_g , and on the other is the bus voltage, v_b . This can be seen in Figure 4.7. The grid equations for this line, are similar to the KVL equations presented for the LCL filter in Section 4.28 and can be seen in Equation (4.45).

$$\left\{ \begin{array}{l} \text{KVL Equations:} \\ \frac{di_{g,d}}{dt} = \frac{-R_g}{L_g} i_{g,d} + \omega i_{g,q} + \frac{1}{L_g} v_{b,d} - \frac{1}{L_g} v_{g,d} \\ \frac{di_{g,q}}{dt} = \frac{-R_g}{L_g} i_{g,q} - \omega i_{g,d} + \frac{1}{L_g} v_{b,q} - \frac{1}{L_g} v_{g,q} \end{array} \right. \quad (4.45)$$

Similar to the LCL filter, the grid equations have cross-coupling terms and can be small-signal linearised as seen in Equation (4.46).

$$\left\{ \begin{array}{l} \text{State Equations:} \\ \frac{d\Delta i_{g,d}}{dt} = \frac{-R_g}{L_g} \Delta i_{g,d} + \omega_n \Delta i_{g,q} + \Delta \omega I_{g,q} + \frac{1}{L_g} \Delta v_{b,d} - \frac{1}{L_g} \Delta v_{g,d} \\ \frac{d\Delta i_{g,q}}{dt} = \frac{-R_g}{L_g} \Delta i_{g,q} - \omega_n \Delta i_{g,d} - \Delta \omega I_{g,d} + \frac{1}{L_g} \Delta v_{b,q} - \frac{1}{L_g} \Delta v_{g,q} \end{array} \right. \quad (4.46)$$

The equations in Equation (4.46) shows both a fixed cross-coupling term depending on the dq currents, but also a changing cross-coupling term depending on the change in angular frequency. The equations can be combined into a state-space model, as seen in Equation (4.47).

$$\Delta \dot{x}_{\text{grid}} = \begin{bmatrix} \Delta i_{g,d} \\ \Delta i_{g,q} \end{bmatrix} = A_G \begin{bmatrix} \Delta i_{g,d} \\ \Delta i_{g,q} \end{bmatrix} + B_{G1} \begin{bmatrix} \Delta v_{b,d} \\ \Delta v_{b,q} \end{bmatrix} + B_{G2} \begin{bmatrix} \Delta v_{g,d} \\ \Delta v_{g,q} \end{bmatrix} + B_{EQ} [\Delta \omega] \quad (4.47)$$

The system A -matrix and the B -matrices of the grid model can be seen in Equation (4.48). Note that, the sign of B_{G1} and B_{G2} swap depending on the sign definition of the bus voltage equation.

$$A_G = \begin{bmatrix} -\frac{R_g}{L_g} & \omega_n \\ -\omega_n & -\frac{R_g}{L_g} \end{bmatrix} \quad B_{G1} = \begin{bmatrix} \frac{1}{L_g} & 0 \\ 0 & \frac{1}{L_g} \end{bmatrix} \quad B_{G2} = \begin{bmatrix} -\frac{1}{L_g} & 0 \\ 0 & -\frac{1}{L_g} \end{bmatrix} \quad B_{EQ} = \begin{bmatrix} I_{g,q} \\ -I_{g,d} \end{bmatrix} \quad (4.48)$$

This is the state-space model of the grid, where $\Delta v_{g,dq}$ represents the Thévenin equivalent grid voltage magnitude.

4.3.2 Bus Voltage and Current Relation

So far, no model has yet been made for the bus voltage, $\Delta v_{b,dq}$, and the current relation, $i_{g,dq} = i_{o,dq,1} + i_{o,dq,2} + i_{o,dq,3}$, has not been included. To include this, a virtual shunt resistor to ground is implemented at the bus [24], as was seen in Figure 4.7. The equations can be seen in Equation (4.49).

$$\left\{ \begin{array}{l} \textbf{Equation:} \\ v_{b,d} = r_N(-i_{g,d} + i_{o,d,1} + i_{o,d,2} + i_{o,d,3}) \\ v_{b,q} = r_N(-i_{g,q} + i_{o,q,1} + i_{o,q,2} + i_{o,q,3}) \\ \textbf{Small-signal Equation:} \\ \Delta v_{b,d} = r_N(-\Delta i_{g,d} + \Delta i_{o,d,1} + \Delta i_{o,d,2} + \Delta i_{o,d,3}) \\ \Delta v_{b,q} = r_N(-\Delta i_{g,q} + \Delta i_{o,q,1} + \Delta i_{o,q,2} + \Delta i_{o,q,3}) \end{array} \right. \quad (4.49)$$

The sign of the equation is chosen to properly reflect the voltage change happening in the system, and is tied to some of the signs in the grid model. Now, the equation can be combined to an algebraic equation in state-space representation, as seen in Equation (4.50).

$$\Delta y_{bus} = \begin{bmatrix} \Delta v_{b,d} \\ \Delta v_{b,q} \end{bmatrix} = H \begin{bmatrix} \Delta i_{g,d} \\ \Delta i_{g,q} \end{bmatrix} + M \begin{bmatrix} \Delta i_{o,d,1} \\ \Delta i_{o,q,1} \end{bmatrix} + M \begin{bmatrix} \Delta i_{o,d,2} \\ \Delta i_{o,q,2} \end{bmatrix} + M \begin{bmatrix} \Delta i_{o,d,3} \\ \Delta i_{o,q,3} \end{bmatrix} \quad (4.50)$$

Where the matrices are as seen in Equation (4.51).

$$H = \begin{bmatrix} -r_N & 0 \\ 0 & -r_N \end{bmatrix} \quad M = \begin{bmatrix} r_N & 0 \\ 0 & r_N \end{bmatrix} \quad (4.51)$$

The equation not only defines the bus voltage, but also governs the current relation between the inverters. The virtual resistor will be chosen as a large value to not affect the dynamics of the system, e.g. 1000Ω as was done in [24], resulting in $i_{g,dq} \approx i_{o,dq,1} + i_{o,dq,2} + i_{o,dq,3}$ or $i_{g,dq} = i_{o,dq,1} + i_{o,dq,2} + i_{o,dq,3} + \varepsilon$, where ε is an error associated with the virtual resistor. Consequently, some discrepancy between the state-space model and the simulation is expected, though should be within reasonable bounds, depending on the chosen value of resistance. For this model, the resistance has been chosen as $1 \text{ M}\Omega$, as it was found to yield good results.

4.3.3 Single-Inverter Modification

The single-inverter model should be modified by removing the PLL from the A -matrix and making it purely an input to the rest of the single-inverter model. Additionally, small changes have to be made to the PLL state-space model, since the bus voltage will now be used as input.

The modified single-inverter state-space model can be seen in Equation (4.52). Notice, that the frame correction term, $B_{\text{CORR}i}$, and cross-coupling term, B_{Xi} , have been moved outside of the original A -matrix and will need the PLL output $[\Delta\omega]$ to be input. Additionally, the rows associated with the PLL have been removed entirely, as they will be implemented in a separate

PLL model.

$$\Delta \dot{x}_{\text{INV}i} = A_{\text{INV}i} \begin{bmatrix} \Delta x_1 \\ \Delta x_2 \\ \Delta x_3 \\ \Delta x_4 \end{bmatrix} + B_{\text{CORR}i} [\Delta x_{\text{PLL}}] + B_{\text{Xi}} [\Delta \omega] + B_{\text{INV}i} [\Delta v_{\text{b,dq}}] + B_{\text{CTRL}} [\Delta \text{PQ}^*] \quad (4.52)$$

The modified A -matrix can be seen in Equation (4.53).

$$A_{\text{INV}i} = \begin{bmatrix} \overbrace{A_P}^{\Delta x_1} & \overbrace{0_{[4 \times 2]}}^{\Delta x_2} & \overbrace{0_{[4 \times 2]}}^{\Delta x_3} & \overbrace{B_{P1}}^{\Delta x_4} \\ B_{C1}C_P & 0_{[2 \times 2]} & 0_{[2 \times 2]} & B_{C2} \\ B_{\text{del}}D_{C1}C_P & B_{\text{del}}C_C & A_{\text{del}} & B_{\text{del}}D_{C2} \\ 0_{[6 \times 4]} & 0_{[6 \times 2]} & B_{\text{LCL}1} & A_{\text{LCL}} \end{bmatrix} \quad (4.53)$$

And the modified B -matrices can be seen in Equation (4.54).

$$B_{\text{CORR}i} = \begin{bmatrix} B_{P1}B_E \\ B_{C2}B_E \\ B_{\text{del}}D_{C2}B_E \\ A_{\text{LCL}}B_E \end{bmatrix} \quad B_{\text{Xi}} = \begin{bmatrix} 0_{[4 \times 1]} \\ 0_{[2 \times 1]} \\ 0_{[2 \times 1]} \\ B_{\text{LCL}3} \end{bmatrix} \quad B_{\text{INV}i} = \begin{bmatrix} 0_{[4 \times 2]} \\ 0_{[2 \times 2]} \\ 0_{[2 \times 2]} \\ B_{\text{LCL}2} \end{bmatrix} \quad B_{\text{CTRL}i} = \begin{bmatrix} B_{P2} \\ B_{C1}D_P \\ B_{\text{del}}D_{C1}D_P \\ 0_{[6 \times 2]} \end{bmatrix} \quad (4.54)$$

The inverter state-space model has now been modified, so that the output of the external PLL state-space model can be inserted into the single-inverter model. Note that, the i in the matrices indicate the inverter number and will become important when combining multiple inverters later.

4.3.4 PLL Modification

The PLL has to be modified, so that it uses the bus voltage, $\Delta v_{\text{b,dq}}$, as the synchronising voltage. As the bus voltage is not a state variable, this unfortunately involves defining it based on several inputs from the other models and, consequently, results in a lot of variables being inserted where the bus voltage appears. The resulting state-space model can be seen in Equation (4.55).

$$\Delta \dot{x}_{\text{PLL}} = \begin{bmatrix} \Delta \rho \\ \Delta \theta \end{bmatrix} = A_{\text{PLL}} \begin{bmatrix} \Delta \rho \\ \Delta \theta \end{bmatrix} + B_{\text{PLL}} \begin{bmatrix} \Delta v_{\text{b,d}} \\ \Delta v_{\text{b,q}} \end{bmatrix} \quad (4.55)$$

Where the A - and B -matrices are seen in Equation (4.56).

$$A_{\text{PLL}} = \begin{bmatrix} 0 & 0 \\ k_{\text{i,PLL}} & 0 \end{bmatrix} \quad B_{\text{PLL}} = \begin{bmatrix} 0 & -1 \\ 0 & -k_{\text{p,PLL}} \end{bmatrix} \quad (4.56)$$

Similarly, the output can be modified.

$$\Delta y_{\text{PLL}} = [\Delta \omega] = C_{\text{PLL}} \begin{bmatrix} \Delta \rho \\ \Delta \theta \end{bmatrix} + D_{\text{PLL}} \begin{bmatrix} \Delta v_{\text{b,d}} \\ \Delta v_{\text{b,q}} \end{bmatrix} \quad (4.57)$$

Where the C - and D -matrices are seen in Equation (4.58).

$$C_{\text{PLL}} = \begin{bmatrix} k_{\text{i,PLL}} & 0 \end{bmatrix} \quad D_{\text{PLL}} = \begin{bmatrix} 0 & -k_{\text{p,PLL}} \end{bmatrix} \quad (4.58)$$

Now, the bus voltage in Equation (4.50) can be inserted into the PLL model with C -matrices to select the currents from the inverter models, as seen in Equation (4.59)

$$\begin{aligned} \Delta \dot{x}_{\text{PLL}} = & A_{\text{PLL}} \begin{bmatrix} \Delta \rho \\ \Delta \theta \end{bmatrix} + B_{\text{PLL}} H \begin{bmatrix} \Delta i_{g,d} \\ \Delta i_{g,q} \end{bmatrix} + B_{\text{PLL}} M C_{\text{INV1}} \begin{bmatrix} \Delta x_{\text{INV1}} \end{bmatrix} \\ & + B_{\text{PLL}} M C_{\text{INV2}} \begin{bmatrix} \Delta x_{\text{INV2}} \end{bmatrix} + B_{\text{PLL}} M C_{\text{INV3}} \begin{bmatrix} \Delta x_{\text{INV3}} \end{bmatrix} \end{aligned} \quad (4.59)$$

Where $C_{\text{INV}i}$ can be seen in Equation (4.60), i.e. it simply selects the correct state variables of the inverter model.

$$C_{\text{INV}i} = \begin{bmatrix} 0_{[1 \times 12]} & 1 & 0 \\ 0_{[1 \times 12]} & 0 & 1 \end{bmatrix} \quad (4.60)$$

The bus voltage can also be inserted into the PLL output, as seen in Equation (4.61).

$$\begin{aligned} \Delta y_{\text{PLL}} = & C_{\text{PLL}} \begin{bmatrix} \Delta \rho \\ \Delta \theta \end{bmatrix} + D_{\text{PLL}} H \begin{bmatrix} \Delta i_{g,d} \\ \Delta i_{g,q} \end{bmatrix} + D_{\text{PLL}} M C_{\text{INV1}} \begin{bmatrix} \Delta x_{\text{INV1}} \end{bmatrix} \\ & + D_{\text{PLL}} M C_{\text{INV2}} \begin{bmatrix} \Delta x_{\text{INV2}} \end{bmatrix} + D_{\text{PLL}} M C_{\text{INV3}} \begin{bmatrix} \Delta x_{\text{INV3}} \end{bmatrix} \end{aligned} \quad (4.61)$$

Now, the PLL output and the bus voltage equation can be inserted into the modified single-inverter model and the grid model. This is covered in Section B.2.1 and the final equations where the PLL output and bus voltage has been inserted are Equations (B.55) and (B.57).

4.3.5 Combined Multi-Inverter State-Space Model

Combining the single-inverter state-space model in Equation (B.55) with the grid model in Equation (B.57) and the PLL model in Equation (4.59), a multi inverter state-space model representing a power plant can be made, as seen in Equation (4.62).

$$\Delta \dot{x}_{\text{PP}} = \begin{bmatrix} \Delta x_{\text{INV1}} \\ \Delta x_{\text{INV2}} \\ \Delta x_{\text{INV3}} \\ \Delta x_{\text{PLL}} \\ \Delta x_{\text{grid}} \end{bmatrix} = A_{\text{PP}} \begin{bmatrix} \Delta x_{\text{INV1}} \\ \Delta x_{\text{INV2}} \\ \Delta x_{\text{INV3}} \\ \Delta x_{\text{PLL}} \\ \Delta x_{\text{grid}} \end{bmatrix} + B_{\text{GRID}} \begin{bmatrix} \Delta v_{g,d} \\ \Delta v_{g,q} \end{bmatrix} + B_{\text{REF1}} \begin{bmatrix} \Delta P_1^* \\ \Delta Q_1^* \end{bmatrix} + B_{\text{REF2}} \begin{bmatrix} \Delta P_2^* \\ \Delta Q_2^* \end{bmatrix} + B_{\text{REF3}} \begin{bmatrix} \Delta P_3^* \\ \Delta Q_3^* \end{bmatrix} \quad (4.62)$$

The A -matrix is 46-by-46, made up of 14 state variables from each inverter, 2 state variables from the PLL and 2 state variables from the grid model. The A -matrix can be seen in Equation (4.63), reduced to a 5-by-5 matrix.

$$A_{\text{PP}} = \begin{bmatrix} A_{\text{INV1}} + B_{\text{S1}} M C_{\text{INV1}} & B_{\text{S1}} M C_{\text{INV2}} & B_{\text{S1}} M C_{\text{INV3}} & B_{\text{CORR1}} + B_{\text{X1}} C_{\text{PLL}} + B_{\text{INV1}} B_{\text{VB}} & B_{\text{S1}} H \\ B_{\text{S2}} M C_{\text{INV1}} & A_{\text{INV2}} + B_{\text{S2}} M C_{\text{INV2}} & B_{\text{S2}} M C_{\text{INV3}} & B_{\text{CORR2}} + B_{\text{X2}} C_{\text{PLL}} + B_{\text{INV2}} B_{\text{VB}} & B_{\text{S2}} H \\ B_{\text{S3}} M C_{\text{INV1}} & B_{\text{S3}} M C_{\text{INV2}} & A_{\text{INV3}} + B_{\text{S3}} M C_{\text{INV3}} & B_{\text{CORR3}} + B_{\text{X3}} C_{\text{PLL}} + B_{\text{INV3}} B_{\text{VB}} & B_{\text{S3}} H \\ B_{\text{PLL}} M C_{\text{INV1}} & B_{\text{PLL}} M C_{\text{INV2}} & B_{\text{PLL}} M C_{\text{INV3}} & A_{\text{PLL}} & B_{\text{PLL}} H \\ B_{\text{J}} M C_{\text{INV1}} & B_{\text{J}} M C_{\text{INV2}} & B_{\text{J}} M C_{\text{INV3}} & A_{\text{G}} B_{\text{EG}} + B_{\text{G1}} B_{\text{VB}} + B_{\text{EQ}} C_{\text{PLL}} & A_{\text{G}} + B_{\text{J}} H \end{bmatrix} \quad (4.63)$$

To reduce the size of the matrix, repetitive terms have been shortened to what is seen in Equation (4.64), where i represents the inverter number, i.e. the row in the state matrix.

$$B_{\text{Si}} = B_{\text{Xi}} D_{\text{PLL}} + B_{\text{INV}i} \quad B_{\text{J}} = B_{\text{G1}} + B_{\text{EQ}} D_{\text{PLL}} \quad (4.64)$$

Additionally, frame rotation has been applied to the grid current and bus voltage, which can be seen by the matrices in Equation (4.65).

$$B_{VB} = \begin{bmatrix} 0 & V_{b,q} \\ 0 & -V_{b,d} \end{bmatrix} \quad B_{EG} = \begin{bmatrix} 0 & I_{g,q} \\ 0 & -I_{g,d} \end{bmatrix} \quad (4.65)$$

Note that, a C -matrix has been implemented to select the correct output of the single inverter models, i.e. the output currents. The B -matrices can be seen in Equation (4.66), where the first relates to the grid voltage and the rest relates to the control reference of the i^{th} inverter.

$$B_{\text{GRID}} = \begin{bmatrix} 0_{[14 \times 2]} \\ 0_{[14 \times 2]} \\ 0_{[14 \times 2]} \\ 0_{[2 \times 2]} \\ B_{G2} \end{bmatrix} \quad B_{\text{REF1}} = \begin{bmatrix} B_{\text{CTRL1}} \\ 0_{[14 \times 2]} \\ 0_{[14 \times 2]} \\ 0_{[2 \times 2]} \\ 0_{[2 \times 2]} \end{bmatrix} \quad B_{\text{REF2}} = \begin{bmatrix} 0_{[14 \times 2]} \\ B_{\text{CTRL2}} \\ 0_{[14 \times 2]} \\ 0_{[2 \times 2]} \\ 0_{[2 \times 2]} \end{bmatrix} \quad B_{\text{REF3}} = \begin{bmatrix} 0_{[14 \times 2]} \\ 0_{[14 \times 2]} \\ B_{\text{CTRL3}} \\ 0_{[2 \times 2]} \\ 0_{[2 \times 2]} \end{bmatrix} \quad (4.66)$$

4.4 State-Space Model of the POD Control

This section will formulate the single-inverter state-space model with POD included. First the POD stat-space model will be made. Then, the POD state-space model will be inserted into the single-inverter state-space model.

4.4.1 POD State-Space Model

The POD control scheme involves many filters, as described in Section 2.2. These are a low-pass filter, a washout filter and two lead-lag filters, as seen in the top of Figure 4.8. The implementation of the low-pass filter in a state-space model was covered in Section 4.2.6 when deriving the state-space model for the power controller. However, when the filter includes an s in the numerator, the derivation of a state-space model becomes more complex. To simplify the derivation, an intermediate state is introduced, denoted by X' . This can be seen in the bottom of Figure 4.8.

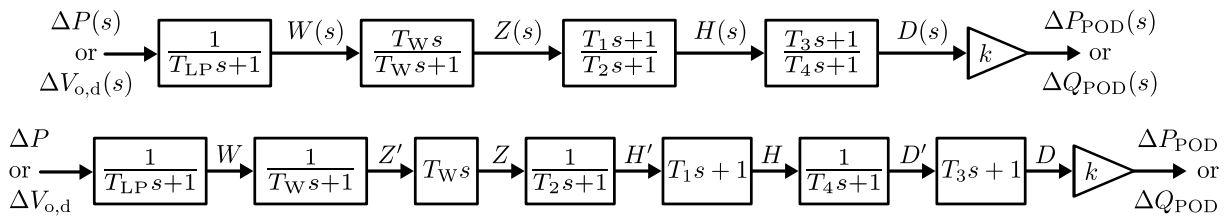


Figure 4.8 Block diagrams of POD control scheme with the top showing the standard form and the bottom showing the extended version with intermediate states.

Starting from the left, the state-space model can be derived for the low-pass filter. The transfer function can be written on the form as seen in the following equation, assuming ΔP as the input.

$$\frac{W(s)}{\Delta P(s)} = \frac{1}{T_{LP}} \Rightarrow W(s)(T_{LP}s + 1) = \Delta P(s) \quad (4.67)$$

By doing small-signal linearisation and isolating for the derivative term, the transfer function can be written in a state-space representation as follows.

$$\Delta \dot{w} T_{LP} + \Delta w = \Delta P \Rightarrow \Delta \dot{w} = -\frac{1}{T_{LP}} \Delta w + \frac{1}{T_{LP}} \Delta P \quad (4.68)$$

Combining the state equation, Equation (B.60), and the output equation, Equation (B.62), the full state-space model of the washout filter can be seen in Equation (4.69).

$$\begin{cases} \Delta \dot{z}' = -\frac{1}{T_W} \Delta z' + \frac{1}{T_W} \Delta w \\ \Delta z = -\Delta z' + \Delta w \end{cases} \quad (4.69)$$

By combining the state equation, Equation (B.65), and the output equation, Equation (B.67), the state-space model for the lead-lag filter can be made, as seen in Equation (4.70).

$$\begin{cases} \Delta \dot{h}' = -\frac{1}{T_2} \Delta h' + \frac{1}{T_2} \Delta z \\ \Delta h = \left(1 - \frac{T_1}{T_2}\right) \Delta h' + \frac{T_1}{T_2} \Delta z \end{cases} \quad (4.70)$$

Similar can be done for the second lead-lag filter, which results in the state-space model seen in Equation (4.71).

$$\begin{cases} \Delta \dot{d}' = -\frac{1}{T_4} \Delta d' + \frac{1}{T_4} \Delta h \\ \Delta d = \left(1 - \frac{T_3}{T_4}\right) \Delta d' + \frac{T_3}{T_4} \Delta h \end{cases} \quad (4.71)$$

The full derivation of the filter state-space models can be found in Section B.3. Some of the state equations and outputs are dependant on the outputs of the other state-space models. Therefore, the output equations should be inserted into the other equations. The derivation of this can be found in Section B.3, and the result of this can be summarised in Equation (4.72).

$$\begin{cases} \textbf{State Equations:} \\ \Delta \dot{w} = -\frac{1}{T_{LP}} \Delta w + \frac{1}{T_{LP}} \Delta P \\ \Delta \dot{z}' = \frac{1}{T_W} \Delta w - \frac{1}{T_W} \Delta z' \\ \Delta \dot{h}' = \frac{1}{T_2} \Delta w - \frac{1}{T_2} \Delta z' - \frac{1}{T_2} \Delta h' \\ \Delta \dot{d}' = \frac{T_1}{T_2 T_4} \Delta w - \frac{T_1}{T_2 T_4} \Delta z' + \left(\frac{1}{T_4} - \frac{T_1}{T_2 T_4}\right) \Delta h' - \frac{1}{T_4} \Delta d' \\ \textbf{Algebraic Equations :} \\ \Delta d = \frac{T_1 T_3}{T_2 T_4} \Delta w - \frac{T_1 T_3}{T_2 T_4} \Delta z' + \left(\frac{T_3}{T_4} - \frac{T_1 T_3}{T_2 T_4}\right) \Delta h' + \left(1 - \frac{T_3}{T_4}\right) \Delta d' \end{cases} \quad (4.72)$$

The state-space models can be combined into a combined state-space model of the POD control scheme, as seen in Equation (4.73).

$$\Delta \dot{x}_{POD} = \begin{bmatrix} \Delta \dot{w} \\ \Delta \dot{z}' \\ \Delta \dot{h}' \\ \Delta \dot{d}' \end{bmatrix} = A_{POD} \begin{bmatrix} \Delta w \\ \Delta z' \\ \Delta h' \\ \Delta d' \end{bmatrix} + B_{POD} [\Delta P] \quad (4.73)$$

Where the A - and B -matrix can be seen in Equation (4.74).

$$A_{POD} = \begin{bmatrix} -\frac{1}{T_{LP}} & 0 & 0 & 0 \\ \frac{1}{T_W} & -\frac{1}{T_W} & 0 & 0 \\ \frac{1}{T_2} & -\frac{1}{T_2} & -\frac{1}{T_2} & 0 \\ \frac{T_1}{T_4 T_2} & -\frac{T_1}{T_4 T_2} & \frac{1}{T_4} - \frac{T_1}{T_4 T_2} & -\frac{1}{T_4} \end{bmatrix} \quad B_{POD} = \begin{bmatrix} \frac{1}{T_{LP}} \\ 0 \\ 0 \\ 0 \end{bmatrix} \quad (4.74)$$

As seen in Figure 4.8, the output d is multiplied with a gain, which defines the output equation of the combined POD state-space model, as seen in Equation (4.75).

$$\Delta y_{\text{POD}} = k\Delta d' = C_{\text{POD-P/Q}} \begin{bmatrix} \Delta w \\ \Delta z' \\ \Delta h' \\ \Delta d' \end{bmatrix} = \begin{bmatrix} k \frac{T_1 T_3}{T_2 T_4} & -k \frac{T_1 T_3}{T_2 T_4} & k \left(\frac{T_3}{T_4} - \frac{T_1 T_3}{T_2 T_4} \right) & k \left(1 - \frac{T_3}{T_4} \right) \end{bmatrix} \begin{bmatrix} \Delta w \\ \Delta z' \\ \Delta h' \\ \Delta d' \end{bmatrix} \quad (4.75)$$

4.4.2 Combined POD and Inverter State-Space Model

The POD state-space model can be added to the single-inverter state-space model by inserting the POD output into the active- and/or reactive power reference of the single-inverter model. For the sake of simplicity, only one POD, i.e. POD-P or POD-Q, will be implemented at a time. The combined model will be made by substituting the active- and reactive power reference with Equation (4.76).

$$\begin{bmatrix} \Delta P^* \\ \Delta Q^* \end{bmatrix} \mapsto \begin{bmatrix} \Delta P^* \\ \Delta Q^* \end{bmatrix} + \begin{bmatrix} \Delta P_{\text{POD}}^* \\ \Delta Q_{\text{POD}}^* \end{bmatrix} \quad (4.76)$$

This can be done because of the way the POD control is implemented, as seen in Figure 4.9.

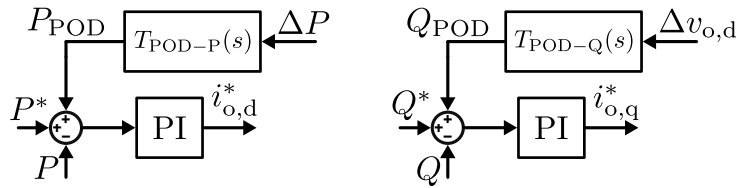


Figure 4.9 POD control in the power controllers.

The combined state-space model of the inverter and POD control can be seen in Equation (4.77).

$$\dot{\Delta x}_{\text{INV+POD}} = A_{\text{INV+POD}} \begin{bmatrix} \Delta x_{\text{INV}} \\ \Delta x_{\text{POD}} \end{bmatrix} + B_{\text{INV+POD}} \begin{bmatrix} \Delta v_{b,d} \\ \Delta v_{b,q} \end{bmatrix} + B_{\text{CTRL+POD}} \begin{bmatrix} \Delta P^* \\ \Delta Q^* \end{bmatrix} \quad (4.77)$$

In the combined state-space model, the A -matrix and B -matrices can be seen in Equation (4.78)

$$A_{\text{INV+POD}} = \begin{bmatrix} A_{\text{INV}} & B_{\text{CTRL}} C_{\text{POD}} \\ B_{\text{POD}} C_{\text{INV}} & A_{\text{POD}} \end{bmatrix} \quad B_{\text{INV+POD}} = \begin{bmatrix} B_{\text{INV}} \\ 0_{[4 \times 2]} \end{bmatrix} \quad B_{\text{CTRL+POD}} = \begin{bmatrix} B_{\text{CTRL}} \\ 0_{[4 \times 2]} \end{bmatrix} \quad (4.78)$$

Where C_{INV} can be chosen as either $C_{\text{INV},P}$ or $C_{\text{INV},Q}$, as seen in Equation (4.79).

$$\Delta P = C_{\text{INV},P} \begin{bmatrix} \Delta x_1 \\ \Delta x_2 \\ \Delta x_3 \\ \Delta x_4 \\ \Delta x_5 \end{bmatrix} \quad \Delta v_{o,d} = C_{\text{INV},Q} \begin{bmatrix} \Delta x_1 \\ \Delta x_2 \\ \Delta x_3 \\ \Delta x_4 \\ \Delta x_5 \end{bmatrix} \quad (4.79)$$

Where the C -matrices are as seen in Equation (4.80).

$$C_{\text{INV},P} = \begin{bmatrix} 1 & 0 & 0 & \cdots & 0 \end{bmatrix} \quad C_{\text{INV},Q} = \begin{bmatrix} 0_{[1 \times 9]} & 0 & 1 & 0 & 0_{[1 \times 4]} \end{bmatrix} \quad (4.80)$$

The C -matrix used for adjusting the active- or reactive power reference can be chosen as seen in Equation (4.81), depending on what POD control is desired.

$$C_{\text{POD}} = \begin{bmatrix} C_{\text{POD-P}} \\ 0_{[1 \times 4]} \end{bmatrix} \quad \text{or} \quad \begin{bmatrix} 0_{[1 \times 4]} \\ C_{\text{POD-Q}} \end{bmatrix} \quad \text{or} \quad \begin{bmatrix} C_{\text{POD-P}} \\ C_{\text{POD-Q}} \end{bmatrix} \quad (4.81)$$

In case of implementation in the multi-inverter state-space model, the implementation depends on how the POD is desired to be performed. The POD could be implemented in the BESS control scheme or in the central controller, which could involve various ways of distributing the POD regulation setpoint. However, this will not be explored further.

4.5 Comparison of Simulation and State-Space Results

This section will compare the state-space simulation results to time-domain simulations performed in MATLAB Simulink. First, the single-inverter dynamics will be compared, followed by the stability prediction of increasing the grid inductance. Then, the multi-inverter dynamics will be compared to the time-domain simulation. Afterward, a comparison between single-inverter stability and multi-inverter stability will be made. Finally, the small-signal stability impact of implementing POD will be evaluated.

4.5.1 Comparison of Single-Inverter Dynamics

Initially, a comparison can be made of the single-inverter state-space model without POD control to a simulation. This is done to validate the accuracy of the state-space model. A simulation is made where the active- and reactive power is stepped as follows:

$$\begin{cases} t = 1.0 \text{ s}, & P = 0 \text{ W} \rightarrow 300 \text{ W} \\ t = 2.0 \text{ s}, & P = 300 \text{ W} \rightarrow 0 \text{ W} \\ t = 3.0 \text{ s}, & Q = 0 \text{ VAr} \rightarrow 300 \text{ VAr} \\ t = 4.0 \text{ s}, & Q = 300 \text{ VAr} \rightarrow 0 \text{ VAr} \end{cases}$$

Similarly, the input to the single-inverter state-space model is altered to mimic the simulation. By using the values of the equilibrium points in the simulation at $t = 0.99 \text{ s}$ accurate comparison can be achieved.

$$\begin{cases} u_1 = \Delta v_{b,d} = 120 \text{ V} \\ u_2 = \Delta v_{b,q} = 0 \text{ V} \\ u_3 = \Delta P^* = \begin{cases} 0 \text{ W}, & t < 1.0 \text{ s} \\ 300 \text{ W}, & 1.0 \text{ s} \leq t < 2.0 \text{ s} \\ 0 \text{ W}, & t \geq 2.0 \text{ s} \end{cases} \\ u_4 = \Delta Q^* = \begin{cases} 0 \text{ W}, & t < 3.0 \text{ s} \\ 300 \text{ W}, & 3.0 \text{ s} \leq t < 4.0 \text{ s} \\ 0 \text{ W}, & t \geq 4.0 \text{ s} \end{cases} \end{cases}$$

Notice, that the bus voltage, or in this case grid voltage, has been set as an input. This is equivalent to keeping the input as 0 and adding the state variables' equilibrium points afterwards, due to the linear nature of the model.

To evaluate the dynamic accuracy of the state-space model, the non-integrator states are compared to that of the simulation, including the $\Delta\omega$ output of the PLL but disregarding the delayed voltage reference. The 9 states and the 1 output can be seen compared to the simulation results in Figure 4.10. On the left side is the full step, whereas on the right side is a zoomed in version to better see the dynamics. Only the active power step up is shown in Figure 4.10. The rest can be found in Section B.4.1.

Taking a look at the full step (left), the state-space model can be seen to accurately represent the dynamics at this time scale. Almost no noticeable deviation can be observed. However, when

looking at the smaller time scale on the right, the dynamics show some slight deviation, though compared to the step size is very small. Noticeably, there is an ≈ 3333 Hz oscillation happening at the capacitor voltage, and consequently also on $\Delta\omega$ and the currents. This indicates a poorly damped mode in the system. The oscillation in the state-space model matches well with the simulation. The error in dynamics observed on the zoomed-in plots is strongly influenced by the solver settings used in the simulation. See Section B.4.1 for more thorough information. Therefore, it is likely that all residual error can be attributed to solver-related issues and non-linearities, and not any modelling error.

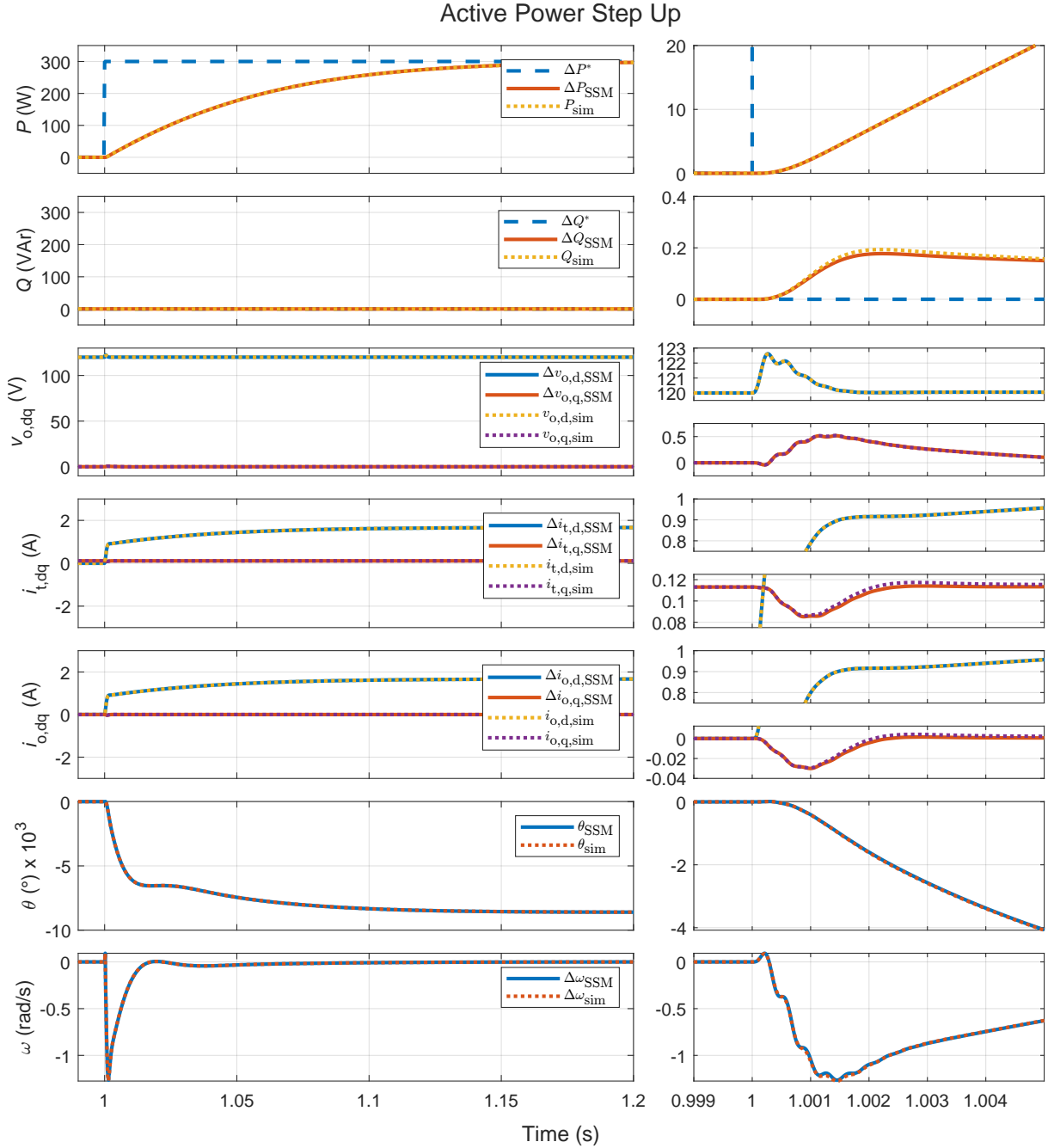


Figure 4.10 Comparison of non-integrator state variables to simulation results

Taking a closer look at the error between the state-space model and simulation, it can generally be seen to be low. In Figure 4.11 the maximum error and *root mean square error* (RMSE) are

plotted on the left, whereas the normalised maximum error and *normalised root mean square error* (NRMSE) are plotted on the right. These help describe the error between the state-space model and simulation.

The maximum error, likely found during transients, show the maximum deviation in absolute units. For example, the power seems to deviate the most with a little more than 0.04 W/VAr in deviation. Most other values are way below this and show no major differences for the maximum error.

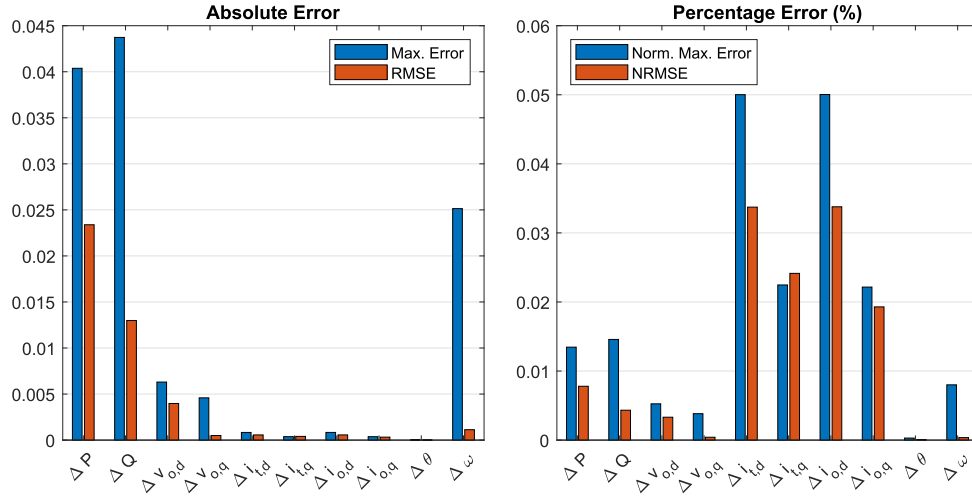


Figure 4.11 Bar chart of absolute errors and percentage errors for an active power step up.

Looking at the RMSE, it can be seen that this error, which takes into account the full step, shows minimal deviation and mostly agree with the maximum error. By normalising the maximum error and RMSE, a better picture can be given of the significance of the error. The maximum error and RMSE are normalised with factors based on the step size and voltage, i.e. $P_{\text{norm}} = 300 \text{ W}$, $V_{\text{norm}} = 120 \text{ V}$, the current is computed from the dq power calculation, $I_{\text{norm}} = \frac{P_{\text{norm}}}{3/2 \cdot V_{\text{norm}}} = 1.667 \text{ A}$, the angle is divided by 2π and the angular frequency is divided by $2\pi 50$.

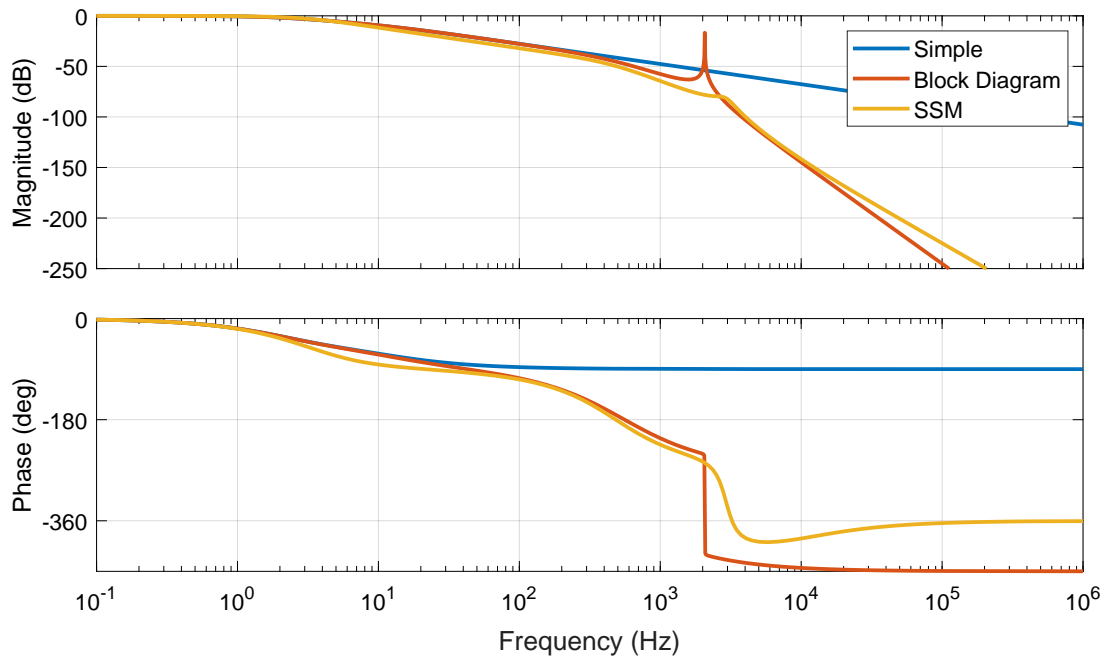
The normalised errors are generally low and show percentage errors way below 5 %, as has been used to validate state-space models in [1]. In fact, the percentage error shows a maximum of around 0.05 %, which is a factor 100 from the validation requirement. In the normalised errors there is a clear trend that the currents, $\Delta i_{t,dq}$ and $\Delta i_{o,dq}$, have the largest deviation from the simulation, as was also observed in Figure 4.10. This likely indicates non-linear effects due to the PLL aligning the dq frame or issues related to the solver settings in Simulink. The bar charts of the errors for the other steps can be found in Section B.4.1. The data used in Figure 4.11 can be seen in Table 4.2 with a precision of 6 decimals.

Table 4.2 Overview of state-space model errors compared to simulation with bold font highlighting the larger deviations.

State Variable	Max. Abs. Error	Norm. Max. Abs. Error (%)	RMSE	NRMSE (%)
ΔP	0.040375	0.013459	0.023384	0.007795
ΔQ	0.043729	0.014576	0.012984	0.004328
$\Delta v_{o,d}$	0.006303	0.005252	0.003976	0.003314
$\Delta v_{o,q}$	0.004589	0.003824	0.000497	0.000414
$\Delta i_{t,d}$	0.000834	0.050015	0.000562	0.033734
$\Delta i_{t,q}$	0.000374	0.022463	0.000402	0.024140
$\Delta i_{o,d}$	0.000834	0.050033	0.000563	0.033781
$\Delta i_{o,q}$	0.000369	0.022156	0.000321	0.019289
$\Delta \theta$	0.000018	0.000294	0.000003	0.000055
$\Delta \omega$	0.025138	0.008002	0.001129	0.000360

4.5.2 Comparison of Single-Inverter Closed-Loop Transfer Functions

The dynamics of the single-inverter state-space model has now been validated. Therefore, it is appropriate to compare the derived power plant transfer function from Section 3.2.2 to the resulting closed-loop transfer function of the state-space model. The result of this comparison can be seen in Figure 4.12. The closed-loop bode plot comparison includes the simple plant transfer function, the detailed plant transfer function, derived using block diagram reduction, and the state-space model transfer function. The simple transfer function is a second-order transfer function, the block diagram transfer function is a seven-order transfer function and the state-space model is a 16-order transfer function.

**Figure 4.12** Bode plot comparison of closed-loop transfer functions.

As can be seen, the block diagram transfer function has an attenuation similar to the state-space model, especially at lower frequencies. At higher frequencies, the attenuation deviates more. Additionally, the block diagram transfer function shows much poorer damping of the

resonance peak than is the actual case. The simple transfer function shows similar attenuation at lower frequencies but deviates heavily beyond that.

Furthermore, the phase of the simple transfer function matches decently at lower frequencies but stop declining at 30 Hz, i.e. the cut-off frequency. The block diagram transfer function matches the phase of the state-space model well, especially at lower frequencies and up until the resonance frequency. The block diagram transfer function underestimates the damping of the resonance peak, which is clearly visible on the phase. However, for controller tuning purposes, the block diagram reduced transfer function is adequate and shows the important phase decline from 30 Hz to the resonance peak, which affect the phase margin of the open-loop system.

4.5.3 Comparison of Single-Inverter Stability

One advantage to making state-space models, is the ability to investigate the eigenvalue trajectories of the A -matrix during a parameter sweep. Depending on the accuracy of the state-space model, the trajectories can tell the tendency of changing a parameter and when that parameter makes the system unstable.

Often times for grid-connected inverters, the grid conditions change. This can be the voltage, the frequency and the strength of the grid or impedance. For this evaluation, the grid inductance has been chosen as the parameter for the sweep. In the simulation, and previously shown state-space model, the grid impedance was 0.17 mH, which is quite small. However, due to the second inductance of the LCL filter, the combined impedance, or coupling impedance, was $L_c = L_f + L_g$. Thus, the impedance between the grid voltage source and the filter capacitor was 1.97 mH. By using the ratings of Section 3.1, the SCR can be found to be 38.76, which is a very strong grid. Typically, grid-following inverters face issues with stability below an SCR of 3, which is considered a weak grid [25]. As discussed in Section 2.2, these are also the cases when power oscillation can become an issue for IBRs, especially at high active power output. Therefore, a eigenvalue parameter sweep is conducted on L_g . This is done at three active power levels: 300 W, 600 W and 900 W. At 900 W the corresponding d component of the output current is 5 A, which is the current limit of the inverters.

In Figure 4.13, the eigenvalues are plotted for each value of L_c . On the left, all the eigenvalues can be seen. In the middle and on the right, zoom-ins have been made to better see the behaviour of the eigenvalues close to the *right half-plane* (RHP). The starting point is marked with a green star, while the ending point is marked with a blue circle. The coupling inductance is varied from 110 mH to 150 mH. This corresponds to a change in SCR of 0.694 to 0.509 with an active power output of 300 W, which is quite low for grid-following inverters. The inverter system becomes unstable at a coupling inductance of 140.5 mH, which corresponds to a SCR of 0.544. However, this is also at relatively low power output.

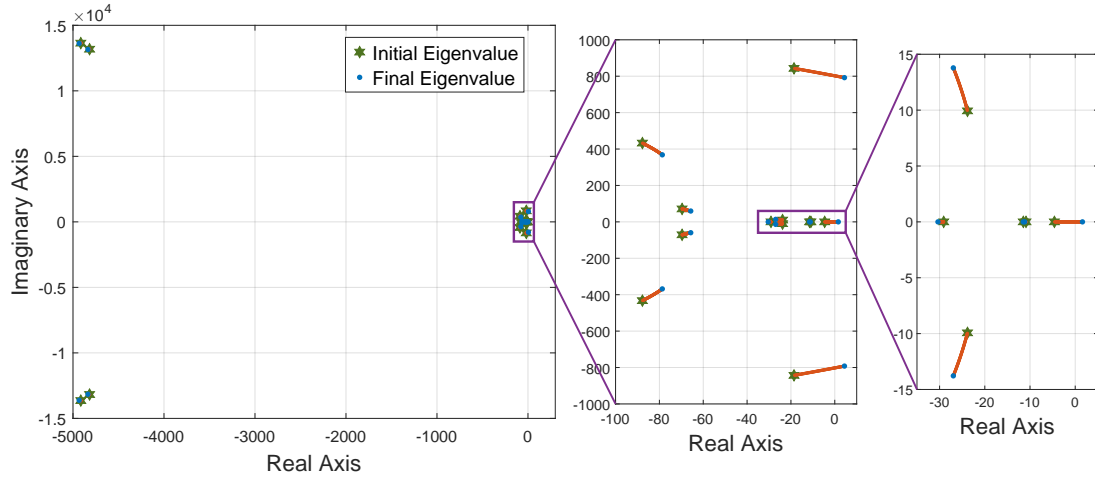


Figure 4.13 Eigenvalue plot at $P = 300$ W for L_g varying from $= 0.11$ H to 0.15 H, becoming unstable at 0.1405 H as the real part crosses zero.

Noticeably, the state-space model stability boundary is very sensitive to how close the starting point is to the unstable point. For these investigations, the equilibrium conditions were calculated close to the unstable point.

For the case of 600 W output power, the result can be seen in Figure 4.14. Here the coupling inductance is varied from 55 mH to 70 mH, which is a steep decrease compared with at 300 W. It corresponds to a SCR of 1.39 to 1.09 . The system becomes unstable at a coupling inductance of 65.46 mH, which corresponds to a SCR of 1.17 .

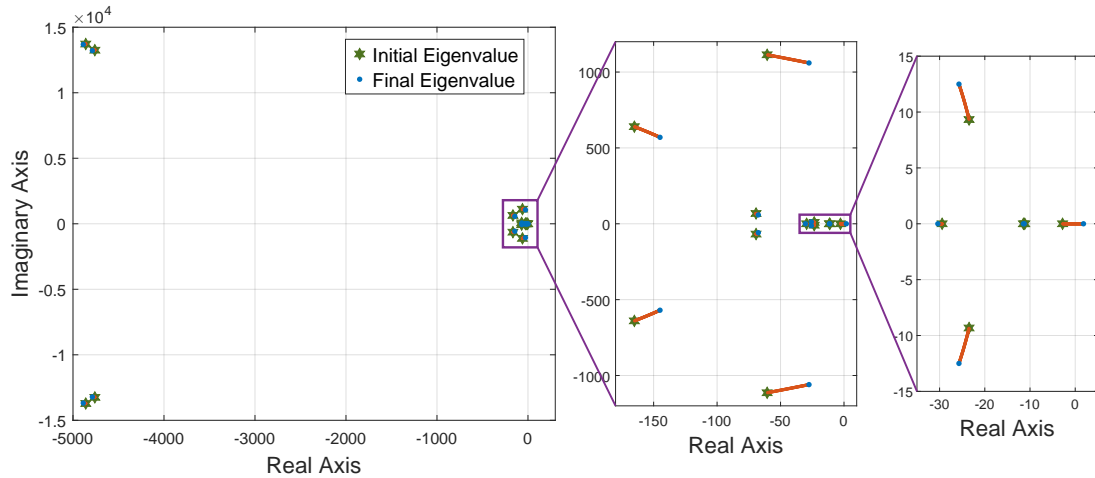


Figure 4.14 Eigenvalue plot at $P = 600$ W for L_g varying from $= 0.055$ H to 0.07 H, becoming unstable at 0.06546 H as the real part crosses zero.

Similarly, the eigenvalues can be investigate at 900 W, as seen in Figure 4.15. In this case, the coupling inductance is varied from 35 mH to 50 mH, which corresponds to a SCR of 2.18 to 1.53 . The inverter system became unstable at a coupling inductance of 48.83 mH, corresponding to a SCR of 1.56 . Taking this as 1 p.u. active power, similar results were achieved in [25].

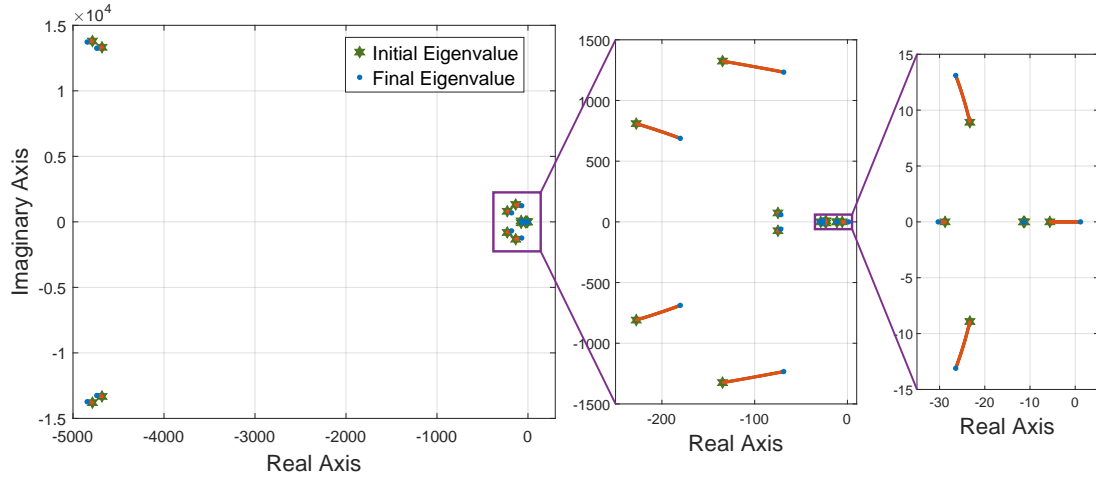


Figure 4.15 Eigenvalue plot at $P = 900$ W for L_g varying from $= 0.035$ H to 0.05 H, becoming unstable at 0.04883 H as the real part crosses zero.

For all the eigenvalue plots, similar trajectories can be observed. In all the cases the same eigenvalue crossed into the RHP. By investigating the participation factor of the eigenvalues at the crossing to instability, the reason for the instability can be found. This can be seen in Figure 4.16. The left y-axis shows each state variable, the x-axis shows each eigenvector and the colourbar on the right shows the participation factor.

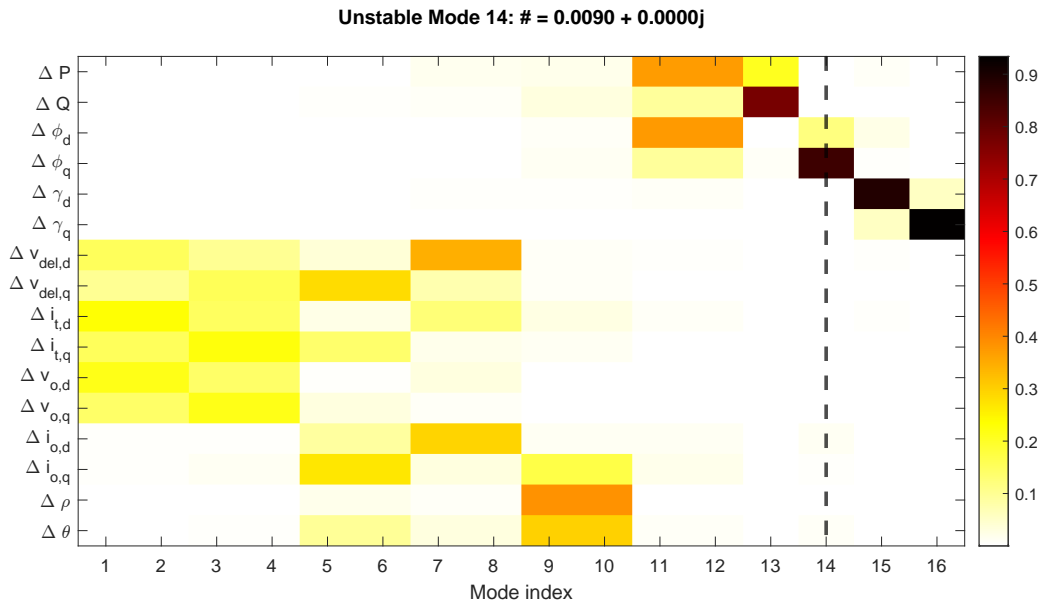


Figure 4.16 Heat map of participation factors of each state variable for each eigenvector with the inverter operating at an active power of 900 W.

As can be seen, the unstable mode is eigenvector 14, marked by the dashed line, which the integrator of the reactive power controller has a large participation in. The other noticeable participation is from the integrator of the active power controller. In other words, the power controller is becoming unstable at this increased coupling inductance. This could be due to the significant resonance peak and phase behaviour of the transfer function of the power controller, discussed in Sections 3.2.2 and 4.5.2. The participation factors at the other power levels can be found in Section B.4.3, though they show similar results.

As discussed previously, the eigenvalue-based stability analysis is highly sensitive to the equilibrium point around which the state-space model is linearized. Figure 4.17 illustrates how the predicted point of instability evolves with increasing active power.

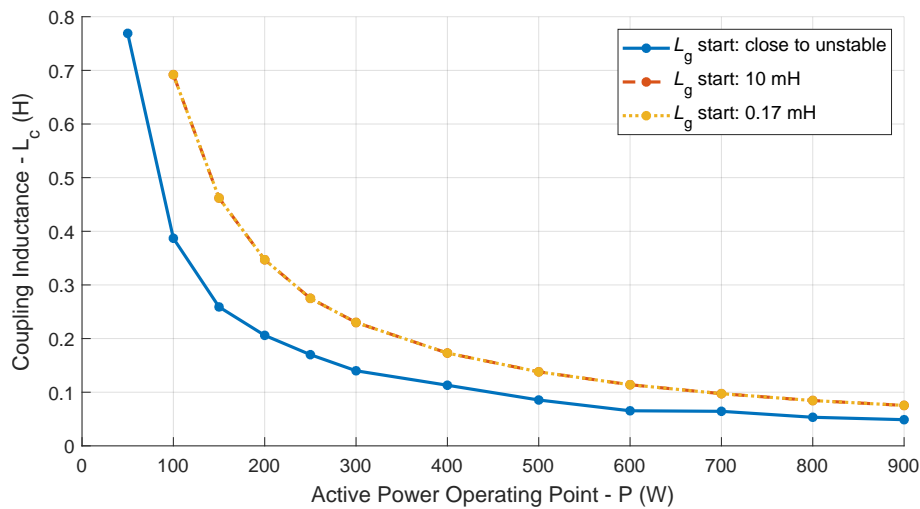


Figure 4.17 Diagram of instability trend with a varying L_g and active power.

Three curves are presented: the blue curve represents the most accurate estimate of the stability boundary, obtained by initiating the parameter sweep from values of grid inductance close to the boundary. In contrast, the orange and yellow curves correspond to sweeps starting at $L_g = 10$ mH and $L_g = 0.17$ mH, respectively. Despite the substantial difference in starting values, the resulting stability boundaries for the orange and yellow curves are nearly identical, indicating that the state-space model is more linear far from the critical point and does not significantly affect the identified instability threshold in this case.

However, both the orange and yellow curves slightly overestimate the stability boundary compared with blue one. When the parameter sweep begins closer to the actual transition point, as in the blue curve, the system is found to lose stability at a lower value of L_g . This discrepancy is likely due to non-linear effects becoming more pronounced near the boundary, where the accuracy of the linearised model deteriorates. Additionally, numerical sensitivity increases in this region, meaning small differences in the equilibrium point can lead to significant shifts in the system's eigenvalues.

Since the result is highly sensitive to the specified equilibrium point, the starting inductance is varied incrementally, digit by digit within the numerical limits of the solver, in order to examine how the stability boundary converges with respect to the initial inductance used for both the equilibrium point calculation and the subsequent parameter sweep. This is illustrated in Figure 4.18 for an active power of 900 W.

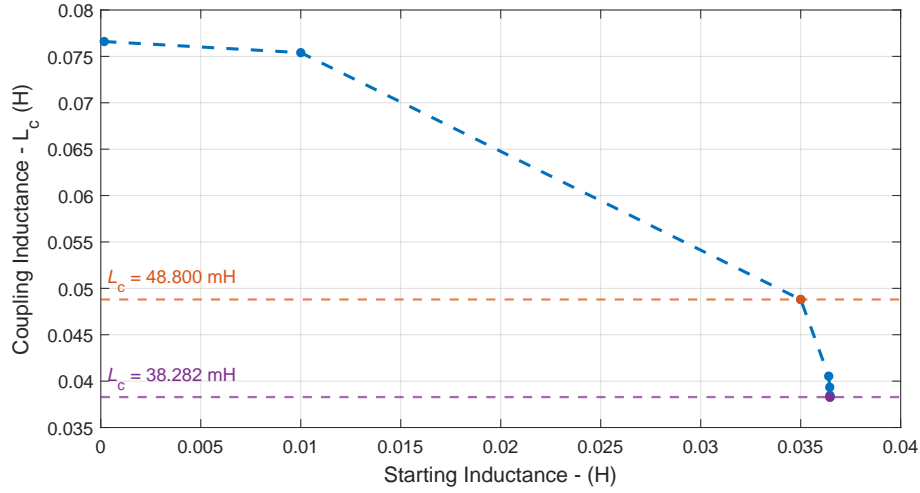


Figure 4.18 Convergence of instability against starting inductance for active power of 900 W.

The orange line and dot are identical to the value found in Figure 4.15, which compared to the new purple line and dot is significantly larger. The value at which the purple line and dot indicate that the system becomes unstable converges on $L_g = 38.282$ mH, which is a reduction of 21.6 % compared with the orange. Similar was done for 600 W and 300 W and the convergence figures can be found in Section B.4.3. The value at which the system becomes unstable converges on $L_g = 57.4001$ mH and $L_g = 114.658$ mH for 600 W and 300 W, respectively. These correspond to a reduction of 13.9 % and 18.6 %, respectively. A table summarising the steps for the convergence at each power level can be seen in Table 4.3.

Table 4.3 Summary of values used for convergence plots, where $L_{g,s}$ is the starting inductance and $L_{g,u}$ is the value at which the system is unstable.

Active Power	300 W		600 W		900 W	
Step	$L_{g,s}$ (mH)	$L_{g,u}$ (mH)	$L_{g,s}$ (mH)	$L_{g,u}$ (mH)	$L_{g,s}$ (mH)	$L_{g,u}$ (mH)
1	0.1700	115.000	0.17000	115.000	0.170000	76.600
2	10.0000	230.000	10.00000	114.000	10.000000	75.400
3	110.0000	140.500	55.00000	65.400	35.000000	48.800
4	112.0000	128.000	55.50000	60.080	36.400000	40.535
5	112.8000	117.230	55.56000	57.940	36.450000	39.345
6	112.8500	115.030	55.56200	57.650	36.463500	38.466
7	112.8580	114.660	55.56250	57.508	36.463970	38.284
8	112.8583	114.658*	55.56257	57.419	36.463973	38.282*
9	--	--	55.562579	57.4017	--	--
10	--	--	55.5625799	57.4001*	--	--

* Convergence at a relative error less than $1.0e-5$

To validate the eigenvalue-based stability analysis, a simulation will be performed where the inductance is increased in steps, to see when the system becomes unstable. The steps are made by having inductors connected in parallel with breakers. Initially, 6 inductors will be in parallel and every 0.5 s a breaker will be opened, as done in [25]. However, the transient dynamics of switching the breaker is not included in the eigenvalue-based stability analysis. Thus, discrepancies are expected. Nonetheless, the simulation was done as seen in Figure 4.19.

The figure shows the active- and reactive power, dq voltages, dq currents and frequency. Marked above the dashed line is the value of inductance that is being switched to.

As can be seen, the transient at the switching instance is increasing in magnitude and length as the inductance increases. This is especially noticeable when looking at the frequency. The voltage d component can be seen to decrease with every step in inductance, representing the increased voltage drop across the coupling inductance. This causes the current d component to increase to meet the active power reference, which can also be seen by the active power deviation from the reference of 900 W.

When the inductance is switched from 35.559 mH to 38.282 mH, the system becomes unstable, and all values can be seen to continuously increase, i.e., the system is undamped. A zoom-in of the phase voltages and currents can be seen in Figure 4.20. This indicates that the eigenvalue analysis can approximately predict when the system becomes unstable. However, the exact point of instability may lie between 35.559 mH and 38.282 mH. Since the simulation includes non-linearities, it is more accurate near the stability boundary. Nevertheless, solver-related issues have previously been observed, and as discussed, the transient introduced by the inductor switching can also move the system into an unstable region. Thus, discrepancies can be attributed to these factors. Nonetheless, the eigenvalue-based stability analysis has demonstrated a reasonable ability to predict the stability boundary, which, for all practical purposes, should not be approached and will be difficult to recreate in reality. This validates the derived state-space model for stability analysis. Together with the dynamic validation in Section 4.5.1, the state-space model can be considered fully validated and reliable for predicting trends in system stability.

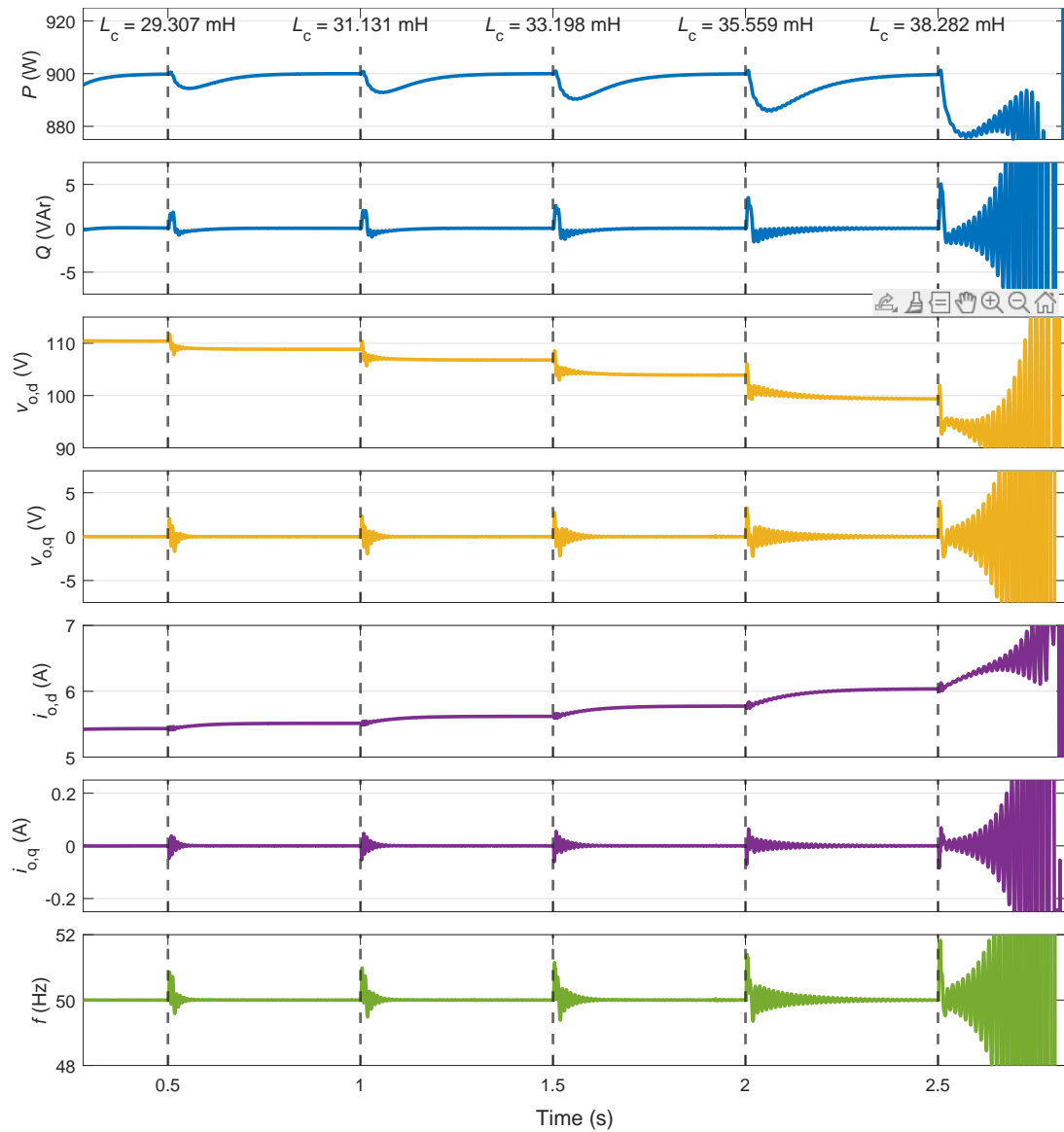


Figure 4.19 Varying the coupling inductance until the system is unstable.

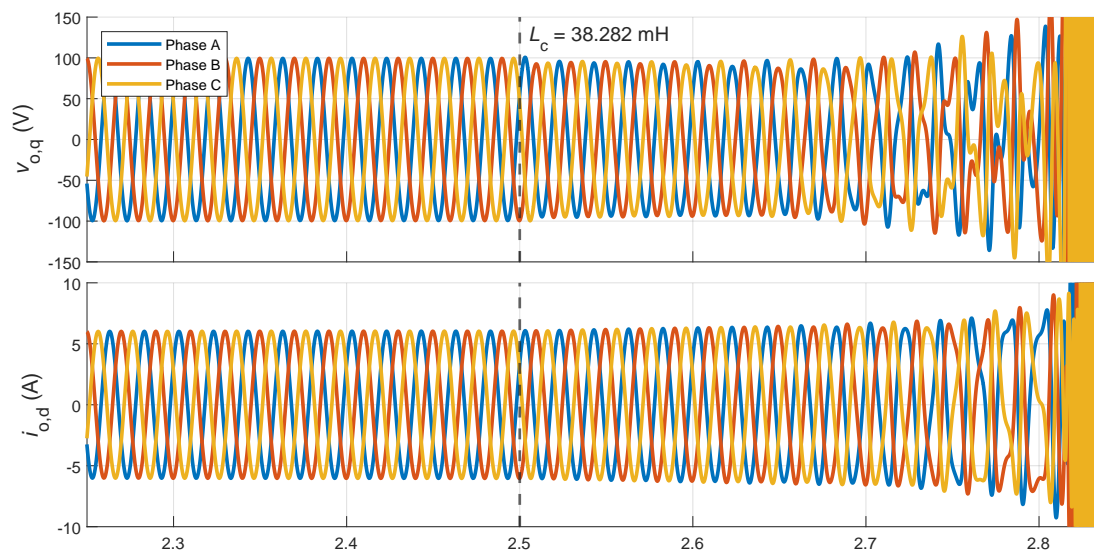


Figure 4.20 Zoom-in of voltages and current when instability occurs.

4.5.4 Comparison of Multi-Inverter Dynamics

To validate the multi-inverter state-space model, the results of active power steps will be compared with the results of the simulation. The inverters will be stepped as follows:

$$\left\{ \begin{array}{l} t = 1.0 \text{ s}, \quad P_1 = 0 \text{ W} \rightarrow 200 \text{ W} \\ t = 2.0 \text{ s}, \quad P_2 = 0 \text{ W} \rightarrow 200 \text{ W} \\ t = 3.0 \text{ s}, \quad P_3 = 0 \text{ W} \rightarrow 200 \text{ W} \\ t = 4.0 \text{ s}, \quad P_1 = 200 \text{ W} \rightarrow 0 \text{ W} \\ t = 5.0 \text{ s}, \quad P_2 = 200 \text{ W} \rightarrow 0 \text{ W} \\ t = 6.0 \text{ s}, \quad P_3 = 200 \text{ W} \rightarrow 0 \text{ W} \end{array} \right.$$

The result of the simulation and the state-space model can be seen in Figure 4.21. The columns represent each inverter and the rows indicate the variable of interest. In the figure, the active- and reactive power, voltage and current are shown with a broad time frame.

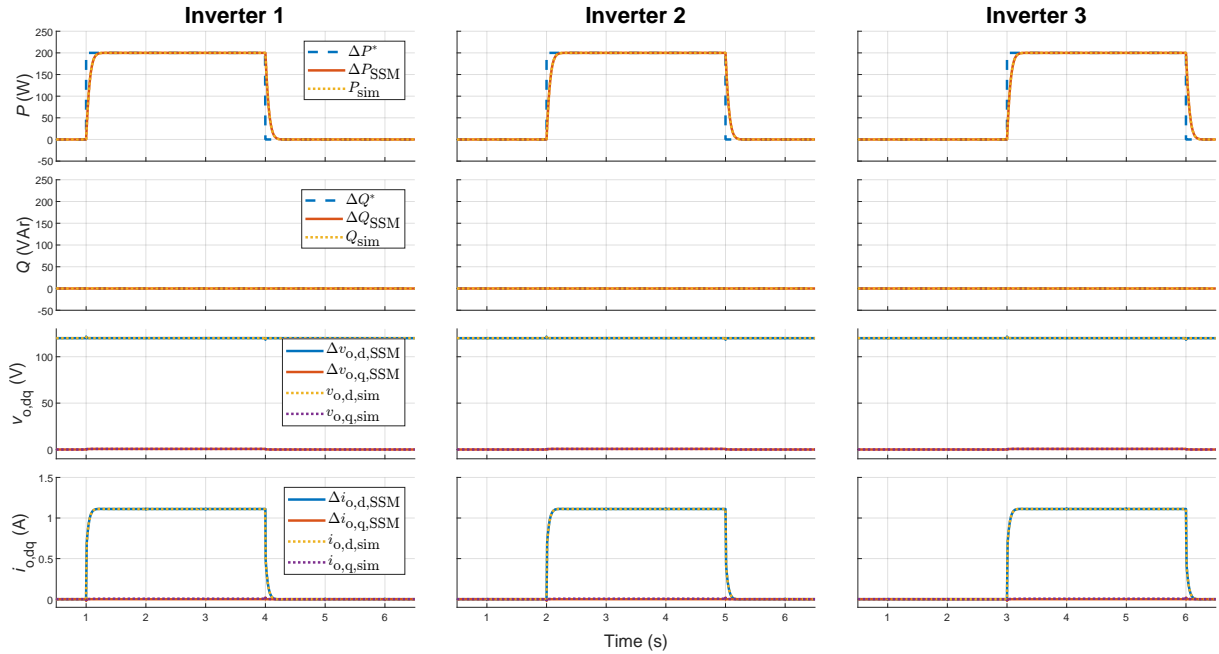


Figure 4.21 Active- and reactive power, voltage and current comparison during active power steps for the multi inverter models.

As can be seen, the state-space model and the simulation match well at this zoom scale, and the overall dynamics are captured well. No significant effect of one inverter on another can be seen. When zooming in on each step, for each inverter and variable, some impact and proof of connection can be seen, as shown in Figure 4.22. The figure shows the active- and reactive power of each inverter, zoomed in on each step. The x-axis covers just over 0.3s, so this is still a zoomed-out look on the dynamics. The figure shows that the active power dynamics are captured well throughout all inverters.

Conversely, some deviation is observed when looking at the reactive power, where the two results clearly deviate from each other. However, the y-axis for the reactive power is zoomed in on a lot compared with the active power. Additionally, this deviation is relatively small compared with the size of the step.

Furthermore, issues with the solver and getting correct results have been observed in Simulink. Therefore, it could be argued that the error could be due to the increased complexity of the model, when the solver settings are kept the same. Though, without having a proper reference to determine what is correct, it is hard to tell which of the results, or both, are wrong.

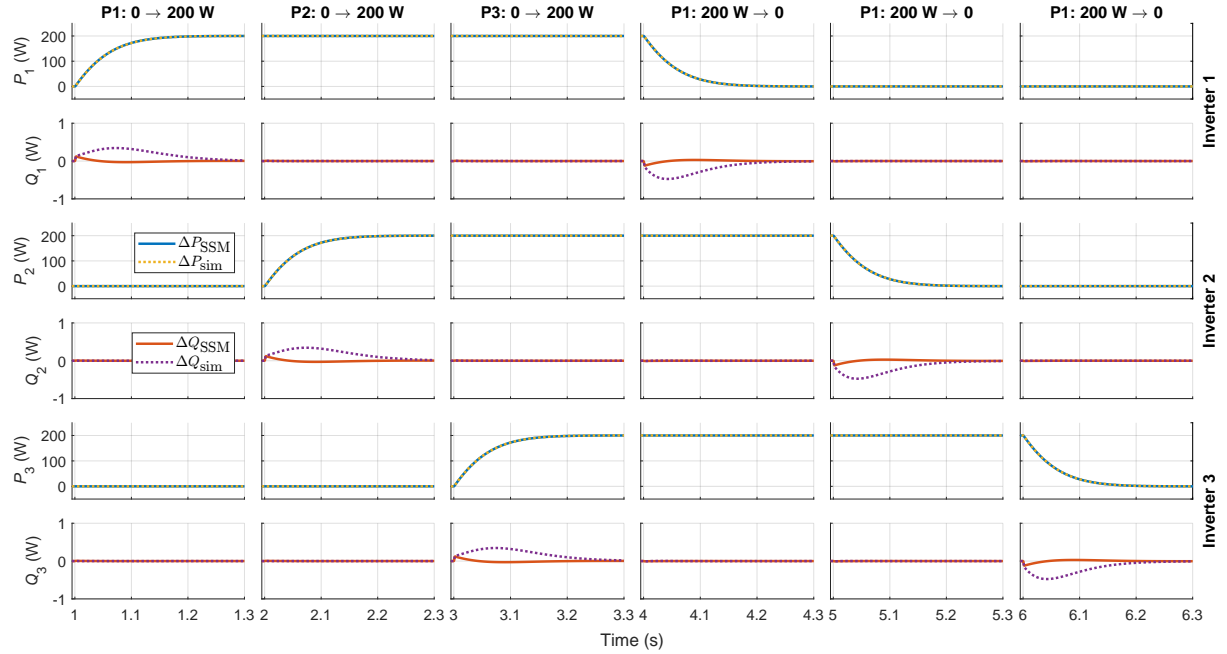


Figure 4.22 Active- and reactive power zoom-in comparison during active power steps for the multi-inverter models.

Comparing the reactive power during an active power step up to the results for the single-inverter case in Figure 4.10, the reactive power from the multi-inverter state-space model appears to match the single-inverter results more closely. This could indicate that the multi-inverter state-space model is the more accurate one, though without knowing the impact of multiple inverters in parallel and without a reference for comparison, it is difficult to draw a definitive conclusion.

To further investigate the relation between the inverters, and the accuracy of the state-space model, the voltage at a close zoom is investigated, as seen in Figure 4.23. Similarly to the power, the voltage d- and q-components are shown for each step and inverter. When investigating the voltage at this zoom, a clear interaction between inverters is seen every time a step is performed. Additionally, the dynamics of the voltage are matched very well for both the d- and q-component. This also indicates that the PLL model rotates the dq frame correctly for the capacitor voltages. Overall, the voltage dynamics are very well presented in the state-space model.

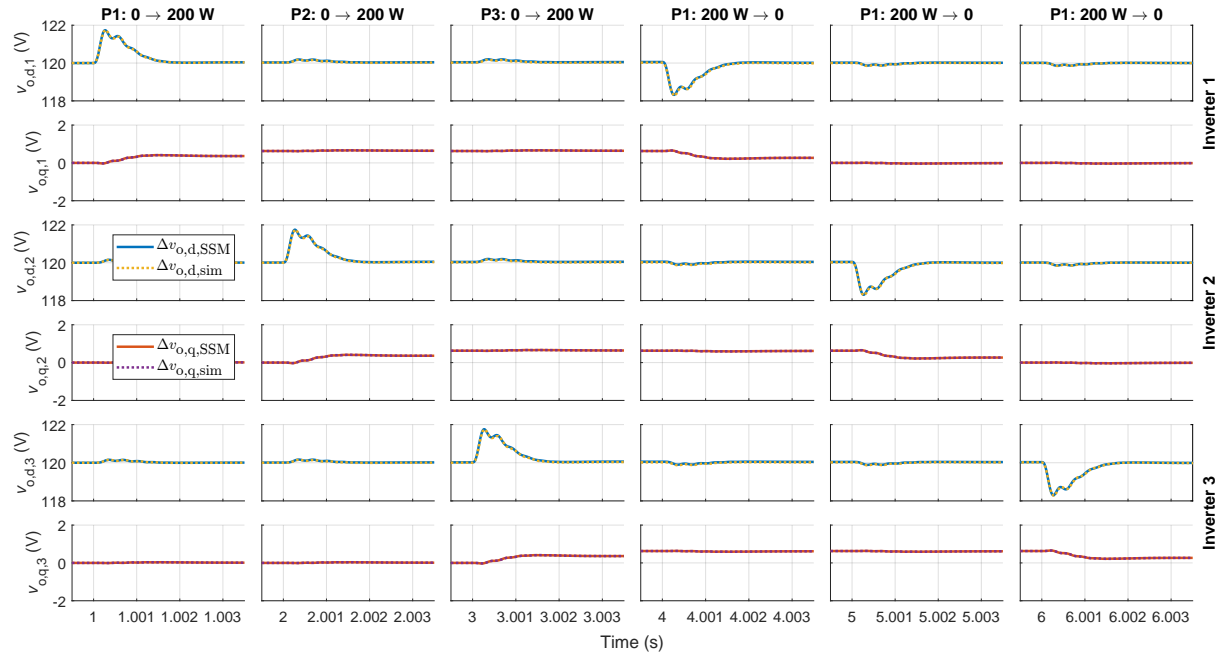


Figure 4.23 Voltage zoom-in comparison during active power steps for the multi-inverter models.

The zoom-ins of the output current of each inverter can be seen in Figure 4.24. Common for all the inverters, the current, both the d- and q-components, seem to match well before and during the steps. However, especially the q-component of the current settles at a lower value than the Simulink model does, indicating some steady-state error compared with the simulation. Note that, the y-axis for the current q-component is quite small and the deviations here are mainly visible due to this zoom. The reason for this discrepancy could be due to the way the bus voltage is modelled. For the bus voltage to not be stiff, the model requires some current to pass through the virtual resistor. This inherently will generate some steady-state error.

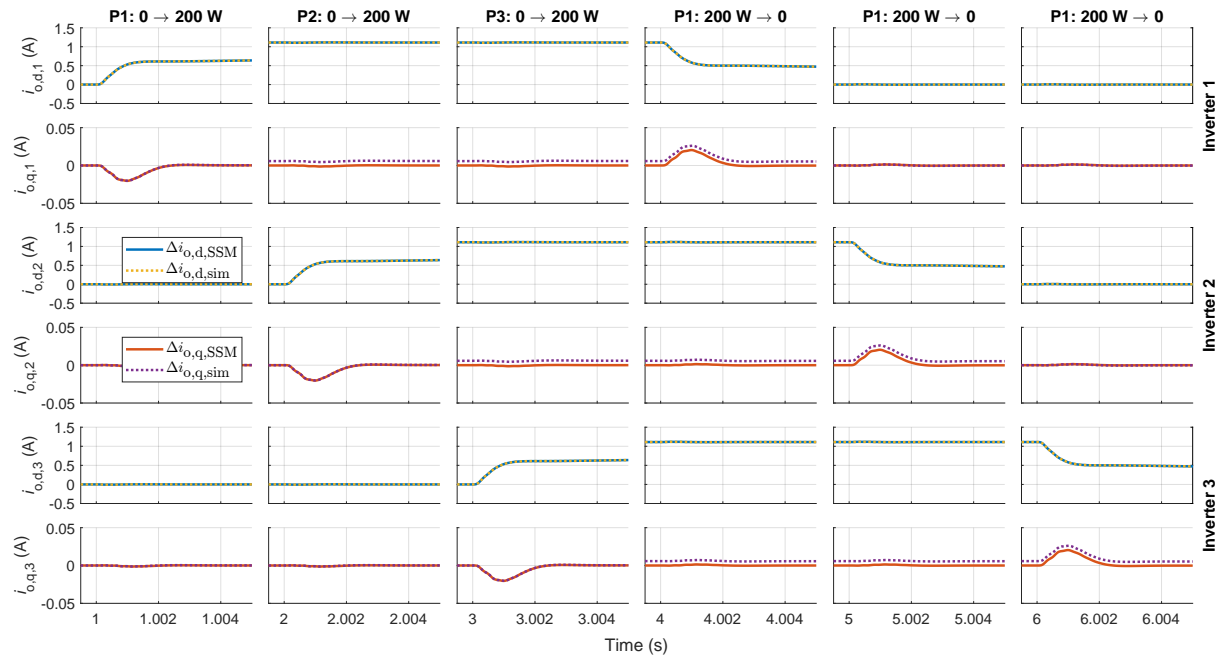


Figure 4.24 Current zoom-in comparison during active power steps for the multi-inverter models.

The bus voltage and grid current can be seen in Figure 4.25. Looking at the bus voltage, it can

be seen that the state-space model match well with the dynamics of the Simulink model. This is similar to the capacitor voltages for each inverter, where the d- and q-component aligned well with the Simulink model.

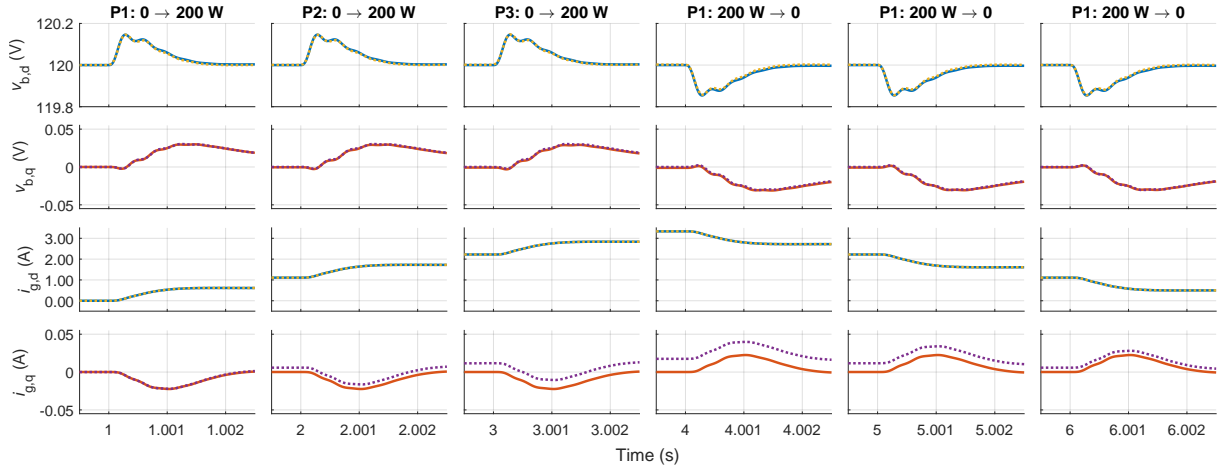


Figure 4.25 Zoom-in of bus voltage and grid current during active power steps.

Looking at the grid current, it can be seen to, in general, match well with the dynamics of the Simulink model. However, some steady-state error can be observed, though the y-axis scale is very small. This is similar to the output current of each inverter and could be due to method of implementing a virtual resistance. Nonetheless, the dynamics are well modelled by the state-space model.

To quantify the errors seen, bar charts are made of the maximum absolute error, the RMSE, the normalised maximum error and the NRMSE. This is done for each of the active power steps, and focuses on the variables related to the inverter that is doing the active power step. In Figure 4.26, the errors can be seen for inverter 1.

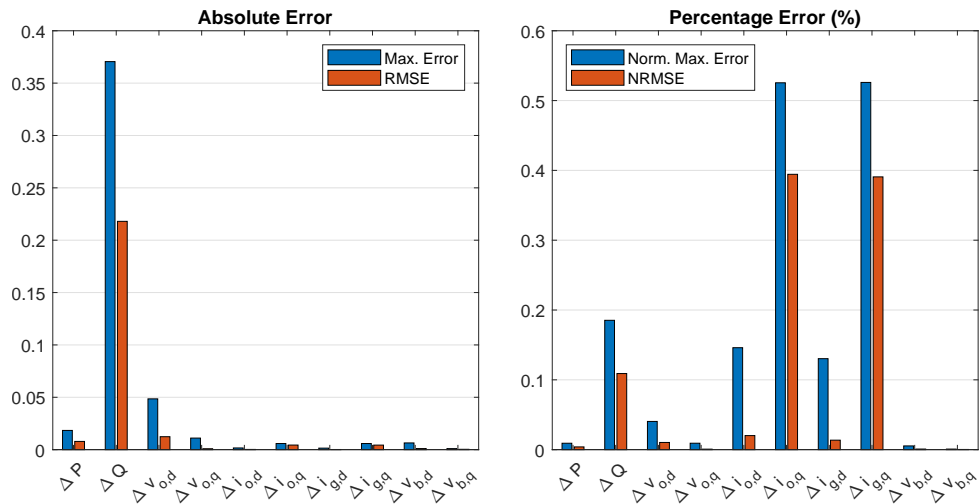


Figure 4.26 Bar chart of absolute errors and percentage errors for inverter 1 for the active power step up of inverter 1.

The absolute error shows that only the reactive power has a significant deviation in absolute terms. This was also seen on the result. However, when normalising, the reactive power is not the most significant deviation. The q-component of the output and grid current are seen to

deviate the most with just under an NRMSE of 0.4. This is well below the limit of 5% described in [1]. The errors during the other steps and for the other inverters can be found in Section B.4.2. In summary, the multi-inverter state-space model matches well with the simulation. Thus, the dynamics of the state-space model can be said to be validated.

4.5.5 Comparison of Multi-Inverter Eigenvalues

To evaluate the stability of the multi-inverter state-space model, the eigenvalues can be compared to those of the single-inverter state-space model. This can be seen in Figure 4.27, where the blue circles mark the single-inverter eigenvalues and the orange plusses mark the multi-inverter eigenvalues. The left plot shows all the eigenvalues, where the large real part of a complex conjugate pair zooms out the plot. These are eigenvalues related to the small grid impedance, $L_g = 0.17 \text{ mH}$ and $R_g = 0.001 \Omega$.

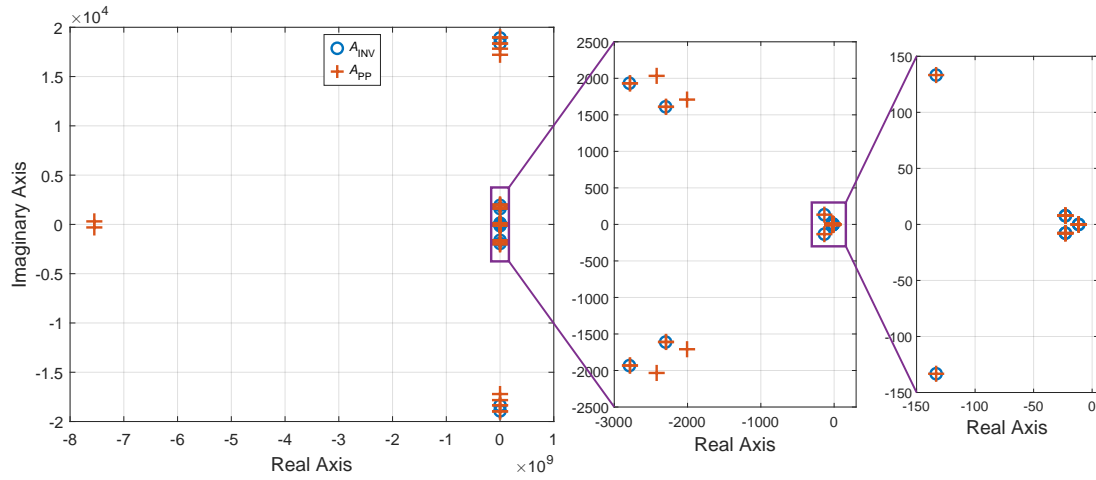


Figure 4.27 Comparison of multi-inverter eigenvalues with those of the single inverter.

In the middle plot, many of the eigenvalues are located in the same spot but some of them are new. The new eigenvalues are the result of the parallel connected LCL filters to the same bus. On the right plot, the eigenvalues mainly associated with the controllers can be seen to be in almost the exact same spot. Note that, there are multiple identical eigenvalues, due to the same control parameters, located in the same spot.

This result indicates, that besides the different system with more LCL filters connected, no significant change happens to the common eigenvalues. However, the sensitivity of the eigenvalues can have changed. To investigate this, a parameter sweep of the grid inductance, L_g , is conducted, as seen in Figure 4.28.

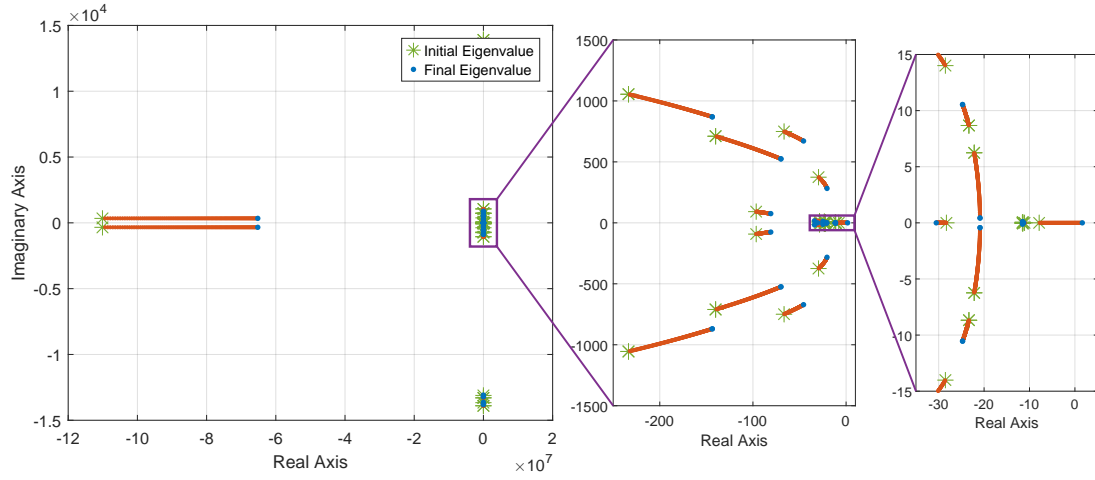


Figure 4.28 Eigenvalue plot at $P = 900$ W (300 W for each inverter) for L_g varying from $= 0.035$ H to 0.06 H, becoming unstable at 0.05545 H as the real part crosses zero.

The grid inductance varies from 0.035 H to 0.06 H, similar to what was done for the single-inverter case. The operating point is computed with 300 W from each inverter, i.e. a total of approximately 900 W. The eigenvalues move in a similar way as for the single inverter, except new eigenvalues are present. The system becomes unstable at a grid inductance of 55.45 mH, which is similar to the 48.83 mH that was seen for the single-inverter.

Figures 4.27 and 4.28, together with the dynamic comparison in Section 4.5.4, indicate that the presence of multiple paralleled inverters does not significantly affect the system dynamics, stability trends, or stability limits. In addition, the single-inverter state-space model is considerably less complex and more tractable for analysis. Consequently, it is used in the subsequent investigation of the impact of implementing POD on system stability.

4.6 POD Control Stability Analysis

This section will analyse the impact on stability of implementing POD control in the inverter control scheme. To assess the impact of the POD controller on the inverter dynamics, the eigenvalues of the system matrix without POD, A_{INV} , and with POD included, $A_{INV+POD}$, will be compared. First for POD-P then for POD-Q using the tuned values presented in Section 3.3.1.

4.6.1 POD-P Stability Analysis

The POD-P controller implementation can be validated by injecting a sinusoidal perturbation on the single-inverter bus voltage input. In other words, for the case of a 2 Hz oscillation, $\Delta v_{b,d} = 12 \sin(2\pi \cdot 2 \cdot t)$. In the developed state-space model it is not possible to do perturbation on the frequency, which is why the voltage magnitude is chosen instead. The result of the state-space simulation with and without POD-P can be seen in Figure 4.29.

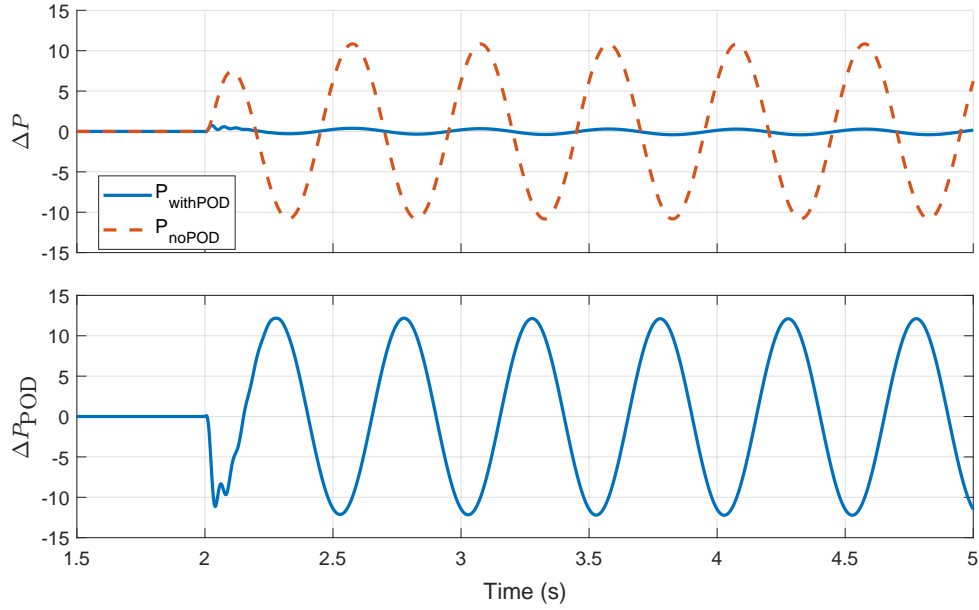


Figure 4.29 State-space simulation with and without POD-P.

At the top, the measured power with and without POD-P can be seen, whereas the bottom shows the POD-P output. As can be seen, the POD-P controller almost entirely and instantly reduce the forced oscillation. A noticeable transient at the start can be seen, which is of a higher frequency than the oscillation, but disappears within 250 ms. This is due to power controller and POD-P controller interactions. Noticeably, there is no double frequency oscillation present, as was seen in Section 3.3.3. This is because the small-signal state-space model is a linearised model and the non-linear effects have been neglected.

To evaluate the impact on small-signal stability of the POD-P controller, the eigenvalues of the single-inverter state-space model with and without POD control are plotted in Figure 4.30. As can be seen, all of the high-frequency eigenvalues are visibly unaffected by the implementation of the POD control. Similar can be seen for the medium-frequency eigenvalues, except the creation of new eigenvalues. For the low-frequency eigenvalues, some are not affected and some have changed a lot.

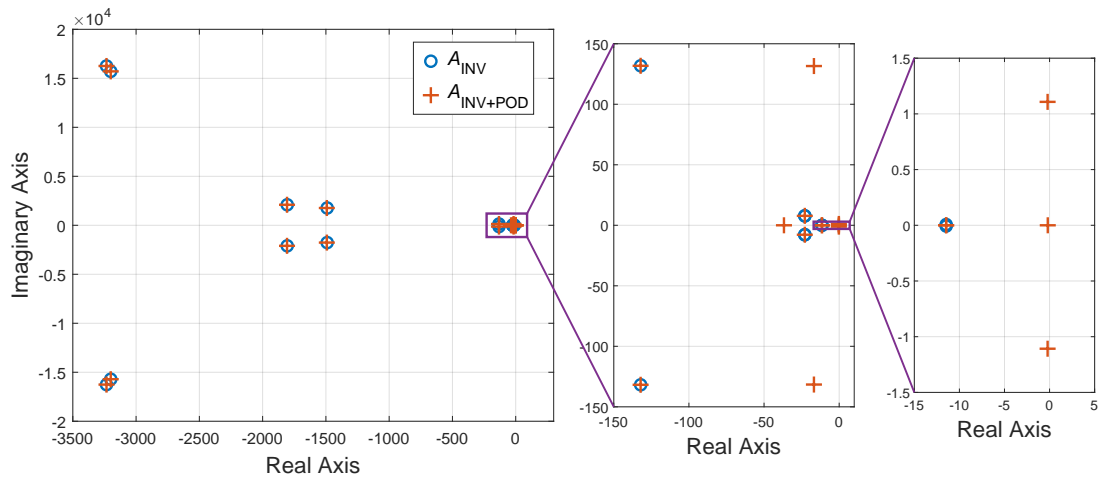


Figure 4.30 Eigenvalues of single-inverter A -matrix with and without POD-P control.

An overview of the eigenvalue and their change can be found in Table 4.4. The table shows that all the values have some numerical change, but for most of them, the change is minimal. Noticeably, the eigenvalues 11-12 appear to have reduced damping and increased frequency, whereas 13-14 remains largely unchanged. Additionally, the complex or oscillatory part of eigenvalues 15-16 have been removed entirely.

Table 4.4 Comparison of eigenvalues for with and without POD-P control.

Mode Index*	Eigenvalue		Comment
	$\lambda : A_{INV}$	$\lambda : A_{INV+POD}$	
1-2	$-3233.8 \pm j16259$	$-3233.8 \pm j16259$	Non-visible change
3-4	$-3200.3 \pm j15709$	$-3200.3 \pm j15709$	Non-visible change
5-6	$-1805.6 \pm j2095.3$	$-1807.2 \pm j2095.0$	Minimal change
7-8	$-1490.0 \pm j1765.2$	$-1492.7 \pm j1764.5$	Minimal change
9-10	$-132.12 \pm j131.80$	$-132.14 \pm j131.79$	Minimal change
11-12	$-22.931 \pm j7.8952$	$-16.802 \pm j131.58$	Reduced real part, increased frequency
13-14	$-22.833 \pm j7.6973$	$-22.880 \pm j7.8026$	Slight variation
15-16	$-11.468 \pm j0.0068$	$-11.470 \pm j0$	Oscillatory part removed
—	—	-36.749	New real mode
—	—	$-0.2166 \pm j1.1079$	New conjugate poles
—	—	-0.1989	Very slow real pole

* Indexed according to eigenvalues of A_{INV}

To investigate how these changes relate physically to the system, the participation factors of both matrices are plotted, as seen in Figure 4.31. The left plot shows the participation factors of the inverter matrix without POD control and the right plot shows with POD control. Starting on the left plot, the participation factors are very regionalised: eigenvalues 1-8 are most related to the electrical circuit, eigenvalues 9-10 are most related to the PLL, eigenvalues 11-14 are related to the power controller and eigenvalues 15-16 are related to the current controller.

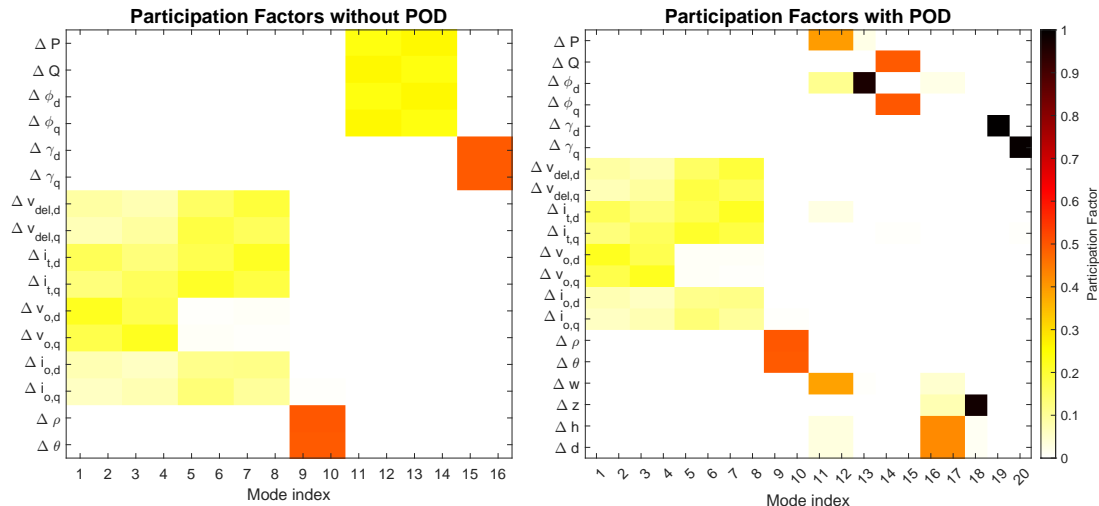


Figure 4.31 Participation factors of the matrices with and without POD-P control.

Similarly, for the right plot, the participation factors are generally regionalised: eigenvalues 1-8 are most related to the electrical circuit, eigenvalues 9-10 are most related to the PLL, eigenvalues 11-13 are most related to the active power controller and LPF input to the POD

control, eigenvalues 14-15 are most related to the reactive power controller, eigenvalues 16-17 are most related to the lead-lag filters, eigenvalue 18 is almost entirely related to the washout filter and eigenvalues 19-20 are most related to the current controller. Note that, the POD controller has shifted the current controller eigenvalues to the end and the eigenvalues related to the POD controller is placed by the active power controller, before the reactive power controller. Therefore, the mode index will not be a 1-to-1 comparison with that of without POD control.

Most interesting, is that the d- and q-component of the power and current controller have split up, not being as dependant any more. This results in the low-frequency mode of the current controller being removed entirely. Similar has happened for the power controller, except the active power controller now has reduced real part and increased imaginary part. This causes the power controller to have a poorly damped mode when the POD control is on. This appears to be the only stability concern when investigating the eigenvalues of the single-inverter state-space model with POD control.

However, this was done for a specific gain. It could be that a lower gain offers adequate damping of power oscillation without compromising the inverter stability as much. To investigate this, a parameter sweep of the POD-P gain, k , is performed for the single-inverter state-space model with POD-P control. This can be seen in Figure 4.32.

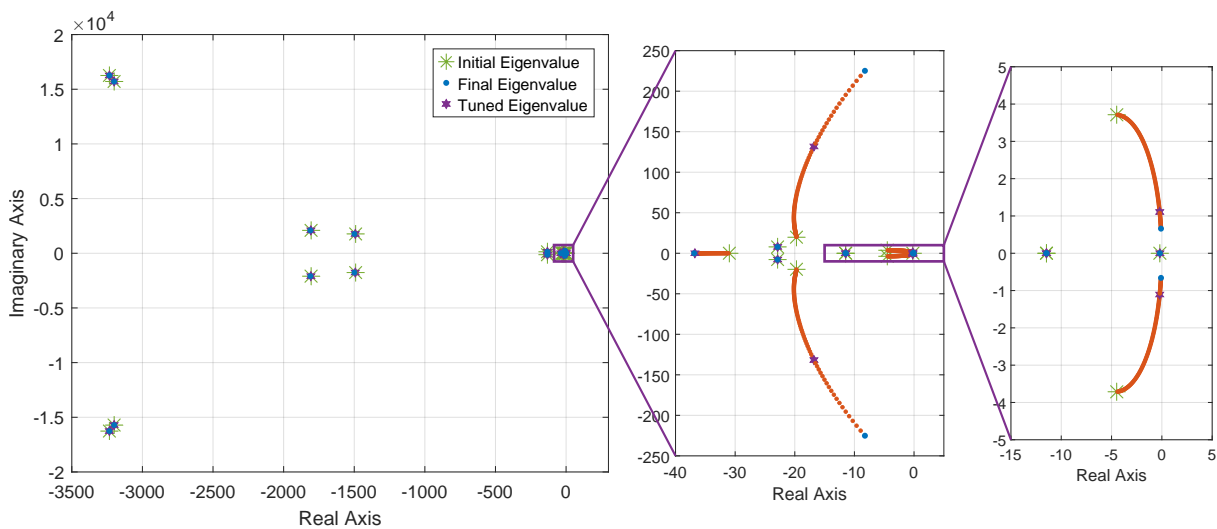


Figure 4.32 Eigenvalue parameter sweep of POD-P gain, where $k = -0.0001 \dots - 0.03$.

As can be seen, the parameter sweep has practically no effect on the high-frequency eigenvalues. In the middle plot, some eigenvalues can be seen move to the left, some not move at all, but mostly move to the right. Additionally, the active power control eigenvalues can be seen to increase its frequency and after a while, start reducing its real part. This indicates, that if only a little disturbance is desired on the active power controller, the gain should be kept small, though the power oscillation damping capability will have to be taken into consideration to make this choice, though currently, only little change in the system can make it unstable.

4.6.2 POD-Q Stability Analysis

The POD-Q controller implementation can be validated by injecting a sinusoidal perturbation on the single-inverter bus voltage input, like what was done for POD-P. The result of the state-space simulation with and without POD-Q can be seen in Figure 4.29.

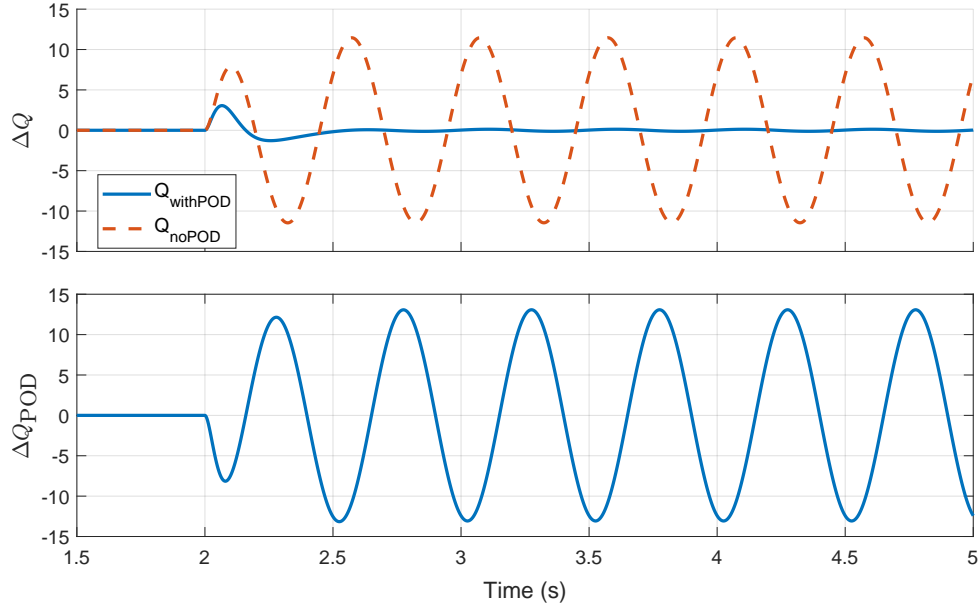


Figure 4.33 State-space simulation with and without POD-Q.

To evaluate the impact of POD-Q control on the stability of the inverter system, the eigenvalues of the single-inverter state-space model with and without POD-Q control can be seen in Figure 4.34. No significant shifts in eigenvalues are observed for the high-frequency eigenvalues. On the medium-frequency and low-frequency eigenvalues, no observable changes can be noticed, except the eigenvalues related to the reactive power controller, located at $-24.6265 \pm j7.1894$, and the new eigenvalues by the POD-Q control.

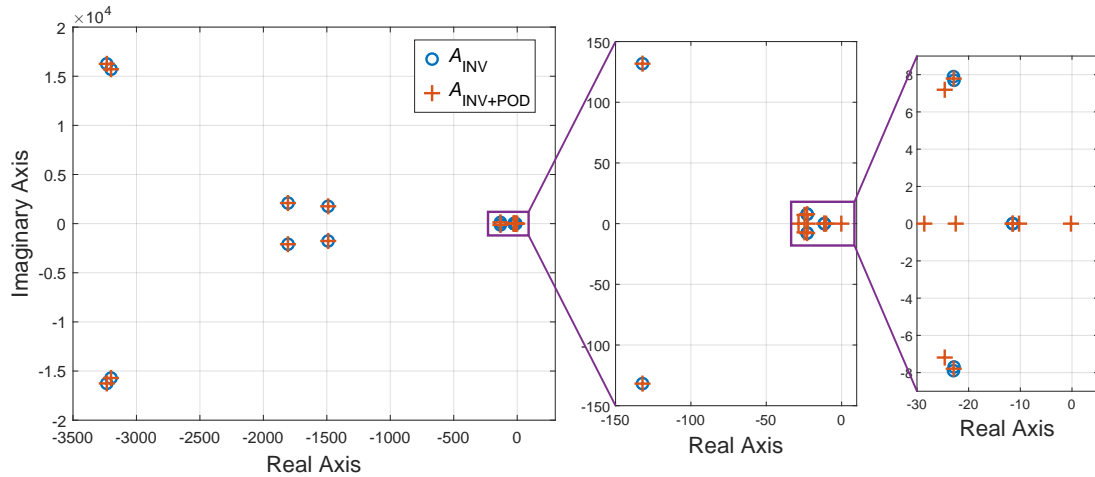


Figure 4.34 Eigenvalues of single-inverter A -matrix with and without POD-Q control.

An overview of the eigenvalues and their change can be seen in Table 4.5. Compared with the case for POD-P, much less change is observed. The high-frequency eigenvalues are affected slightly more but this change is negligible. Noticeably, the power controller eigenvalues are

affected much less. The eigenvalues related to the reactive power control, eigenvalues 13-14, are only slightly changed. This indicates, that POD-Q can achieve adequate damping without changing the system eigenvalues significantly and is thus more stable.

Table 4.5 Comparison of eigenvalues for with and without POD-Q control.

Mode Index*	Eigenvalue		Comment
	$\lambda : A_{INV}$	$\lambda : A_{INV+POD}$	
1-2	$-3233.8 \pm j16259$	$-3233.6 \pm j16259$	Minimal change
3-4	$-3200.3 \pm j15709$	$-3200.4 \pm j15709$	Minimal change
5-6	$-1805.6 \pm j2095.3$	$-1806.4 \pm j2095.3$	Minimal change
7-8	$-1490.0 \pm j1765.2$	$-1490.0 \pm j1765.2$	Minimal change
9-10	$-132.12 \pm j131.80$	$-132.12 \pm j131.80$	Minimal change
11-12	$-22.931 \pm j7.8952$	$-22.891 \pm j7.7900$	Minimal change
13-14	$-22.833 \pm j7.6973$	$-24.6265 \pm j7.1894$	Slight variation
15-16	$-11.468 \pm j0.0068$	$-11.467 \pm j0.0079$	Slight variation
—	—	-28.584	New real pole
—	—	-22.505	New real pole
—	—	-10.248	New real pole
—	—	-0.2000	New real pole

* Indexed according to eigenvalues of A_{INV}

To better understand the physical meaning of the change, the participation factors for the single-inverter state-space model with and without POD-Q control can be seen in Figure 4.35. The participations factors for without POD-Q control are the same as for the POD-P analysis. Similar to what was seen for the POD-P control, the current controller eigenvalues have shifted to index 19 and 20. Eigenvalue 11 is most related to the washout filter, eigenvalues 12-13 relate mostly to the active power control, eigenvalues 14-17 relate mostly to the reactive power control and lead-lag filters and eigenvalue 18 is mostly related to the LPF. Note that, the power controller has split participation factors for active- and reactive power control, whereas the current controller d- and q-component are still together, unlike for POD-P.

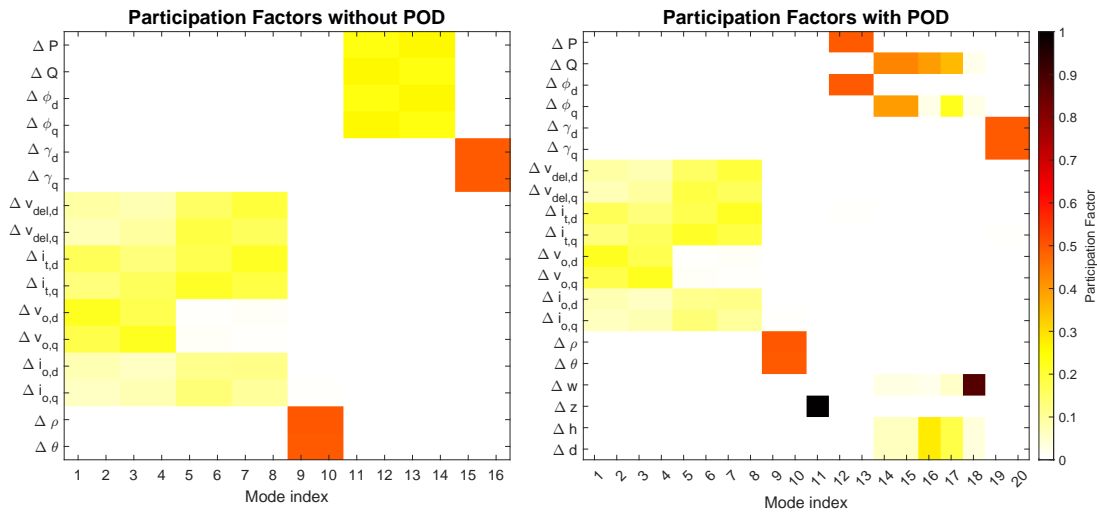


Figure 4.35 Participation factors of the matrices with and without POD-Q control.

To further investigate the effect on stability of the POD-Q control, a parameter sweep of the

POD-Q gain, k , is performed. The result of this can be seen in Figure 4.36. Looking at the left plot, no significant shift in eigenvalues can be observed. In the middle plot, which is quite zoomed in, only a slight shift in eigenvalues can be seen. Noticeably, the eigenvalues related to reactive power initially decrease in frequency and later increase again. They also increase their real part. Furthermore, the eigenvalues that are real poles shift both right and left, though none of them move considerably towards the RHP.

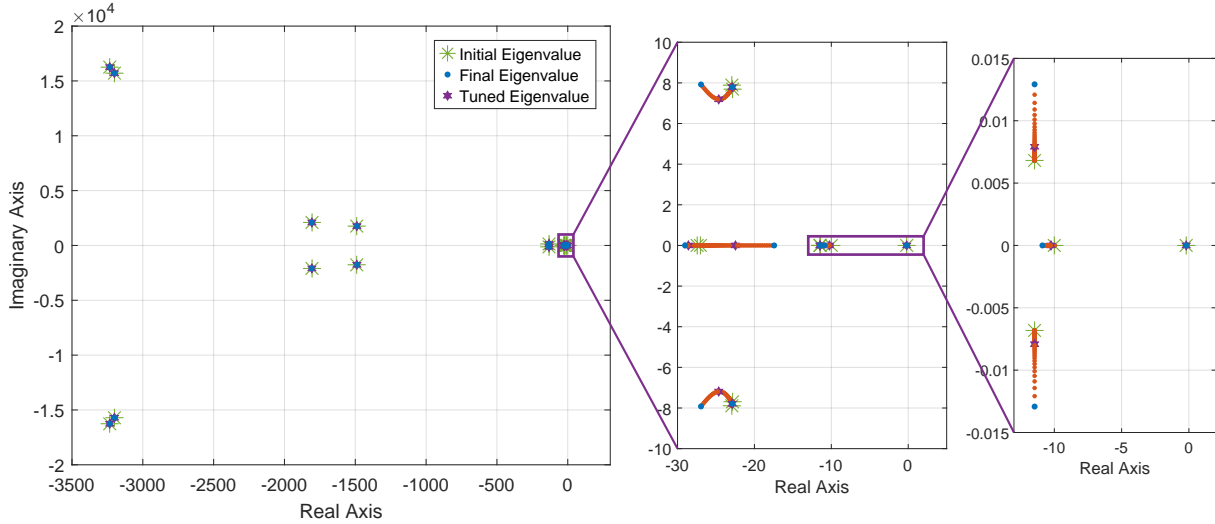


Figure 4.36 Eigenvalue parameter sweep of POD-Q gain, where $k = -0.0001 \dots - 0.03$.

Compared with the results for POD-P, the POD-Q parameter sweep shows less impact on the stability of the eigenvalues. Mostly, the eigenvalues related to the POD filters shift, which do not change considerably with changes in the system. Therefore, the POD-Q implementation has minimal impact on system stability. This could be due to the voltage being used as input, instead of the controlled power. This might indicate, that if substantial damping and limited impact on system stability are desired, then the input parameter should be a non-controlled parameter.

4.7 Summary

In this chapter, the concept of small-signal state-space modelling has been described and applied to a single- and multi-inverter model configuration. Additionally, the POD control scheme has been modified for implementation in the single-inverter state-space model. The states-space models showed almost identical dynamics and stability trends when validated against time-domain simulations. A small-signal stability analysis determined that POD-P with active power deviation as input impacted the power plant stability the most, whereas POD-Q with voltage magnitude deviation as input had almost no adverse effect on the power plant small-signal stability.

5 Experimental Validation

This chapter will present the experimental work performed to validate the simulation results. First, the experimental setup will be explained along with any relevant data. Then, the initial grid synchronisation will be presented. Afterward, the results for the single inverter active- and reactive power steps will be presented to ensure that the dynamics of the developed control are similar. Then, similar will be done for the multi inverter system with the same purpose. Finally, the experimental results of the POD will be presented and explained.

5.1 Experimental Setup

This section will present the experimental setup and the specific parameters used. The experimental setup is located in the AAU Energy, *Center for Research on Microgrids* (CROM), and is called the *Microgrid Research Laboratory* (MGLab). It consists of multiple setups which are configurable to AC and DC microgrids. One of these are used for the experimental validation of the developed control schemes. The setup consists of a DC source, 4 Danfoss inverters, 4 LCL filters, LEM measuring boards, a dSPACE platform and a dSPACE interface board. Additionally, several relays are there to adjust connection configuration with inverters, load and/or grid. The dSPACE platform allows for real-time simulation and hardware-in-the-loop testing. The control schemes developed in MATLAB Simulink will be compiled to a .sdf file and uploaded to the dSPACE platform. By connection between the dSPACE and a computer, real-time data capture and control references and logic can be altered from the setup computer. The different components of the setup can be seen in Figures 5.2 and 5.1.



Figure 5.1 Front of lab setup.

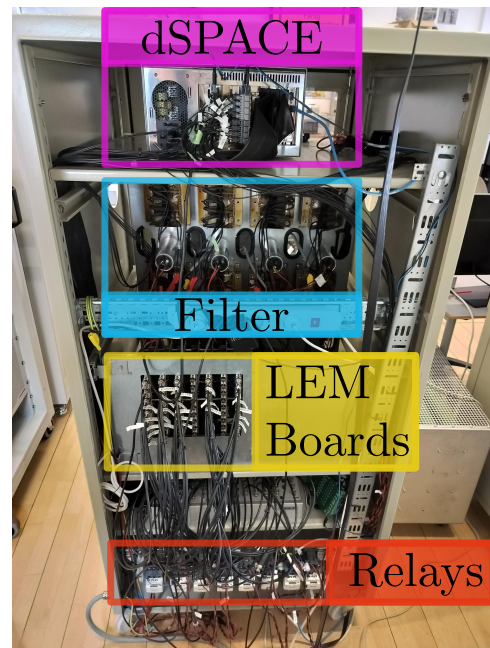


Figure 5.2 Back of lab setup.

Initially, the intention was to use the grid emulator present at the MGLab. However, it was not functional. Therefore, a dual-loop control scheme was implemented on one of the inverters, specifically Inverter 2. This way, a voltage across its capacitor could be defined and controlled, which the other inverters can synchronise to. The configuration used for all the experimental work can be seen in Figure 5.3. As can be seen, $v_{o,2}$ will be the POC and the PLL will use this voltage to synchronise all the inverters. Notice, that all the filters have the same parameters and therefore same values. Depending on the experiment, the relays will be opened or closed.

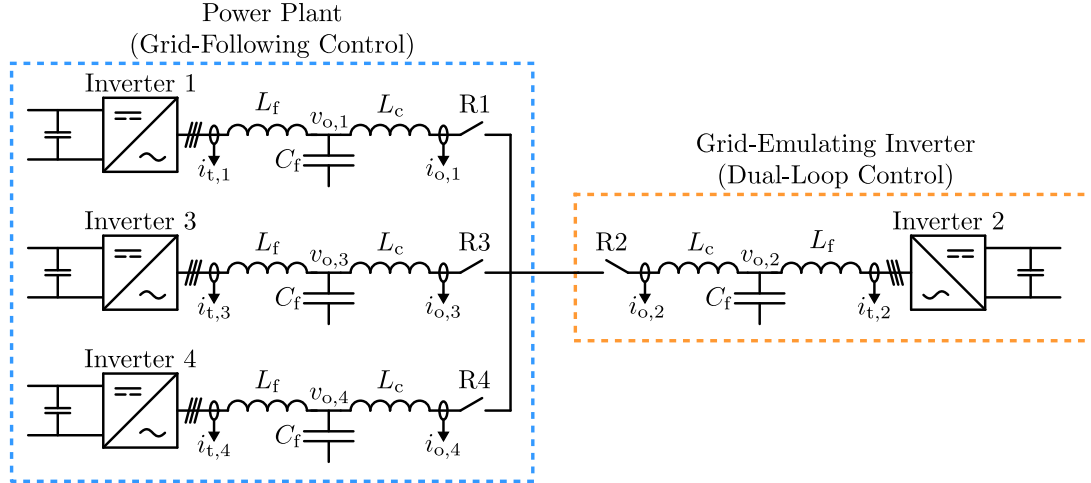


Figure 5.3 Illustration of the configuration of the inverters in the experimental setup.

The parameters for the filter can be found in Table 5.1. Additionally, the Danfoss inverter ratings, sampling and switching can be found in the table. At the bottom of the table, some limits have been implemented for the limits since the voltage has been reduced from nominal. The power limit comes from the dq power calculation $P = \frac{3}{2} V_d I_d$, which for $V_d = 120$ V and $I_d = 5$ A yields $P = 900$ W. The operating voltage was selected through practical testing of the laboratory setup, with consideration given to signal quality and overall system behaviour. Although the hardware supports up to 350 V, a lower voltage was ultimately chosen. At higher voltages, the resulting currents were smaller in magnitude, which made them appear more susceptible to measurement noise and reduced the effective signal-to-noise ratio. Lowering the voltage increased the current levels, improving the clarity of the measured signals and the reliability of the control response. The chosen voltage level therefore represents a compromise that ensures stable operation while maintaining adequate measurement quality.

Lab Parameters	Values
V_{DC}	650 V
$V_{nom,peak}$	325 V
f_{sw}	10 kHz
T_s	0.0001 s
S_{rated}	2.2 kVA
$I_{t,rated}$	5.5 A
L_f	1.8 mH
R_f	0.02 Ω
C_f	3 μ F
L_c	1.8 mH
R_c	0.02 Ω
Chosen Parameters	Values
$V_{op,peak}$	120 V
S_{max}	900 VA
$I_{t,max}$	5 A

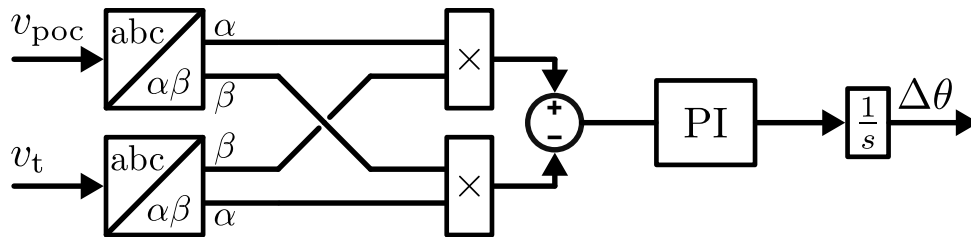
Table 5.1 Data for experimental setup.

5.2 Initial Grid Synchronisation

When the inverter is connected to the grid it will follow the voltage set by the grid and therefore only the phase angle is needed for keeping synchronisation. However, initially when the inverter is turned on, a voltage will have to be established on the inverter end before connecting it to the grid in order to avoid overcurrents.

Before the inverter is connected to the grid, it uses a modulation signal with the nominal frequency and designated voltage instead of the power and current controllers. To synchronise it to the grid voltage, the phase angle difference and voltage magnitude difference are estimated and used to change the modulation signal until these differences become zero, or close to.

For the phase angle, a PI controller is implemented to minimise the cross product of the Clarke transformation of the capacitor and grid voltage. If the cross product of the two voltage vectors in the α - β plane is zero, it indicates that the two vectors are parallel (or anti-parallel). In terms of the phase angles of these voltages, this would mean that their phase angles are aligned. The cross product can therefore be used as the error signal in a PI control loop whose output is a small change in phase angle. Assuming balanced voltages on both sides of the breaker, the phase synchronisation can be reduced to the block diagram seen in Figure 5.4.

**Figure 5.4** Block diagram of Phase Synchronization

To ensure the voltage magnitudes are similar before closing the breaker, a PI controller is

implemented. It is using the difference in v_d of the two three-phase voltages as the error signal and the output is used to modify the voltage magnitude of the inverter.

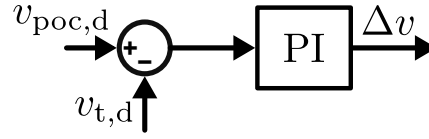


Figure 5.5 Block diagram of voltage magnitude synchronisation.

Figure 5.5 shows the block diagram of the voltage magnitude synchronisation. Notice that the direct-axis voltage for both the inverter and grid side is calculated by two separate PLLs.

5.3 Single Inverter

This section will present the experimental results of the single inverter system, as well as the comparison to the state-space model. The state-space model has been chosen for comparison due to ease of use and since the dynamics were validated against the Simulink simulation in Chapter 4.

In Figure 5.6, an active power step can be seen, where the active power, reactive power, capacitor voltage and output current can be seen. The voltage and current are in the dq reference frame.

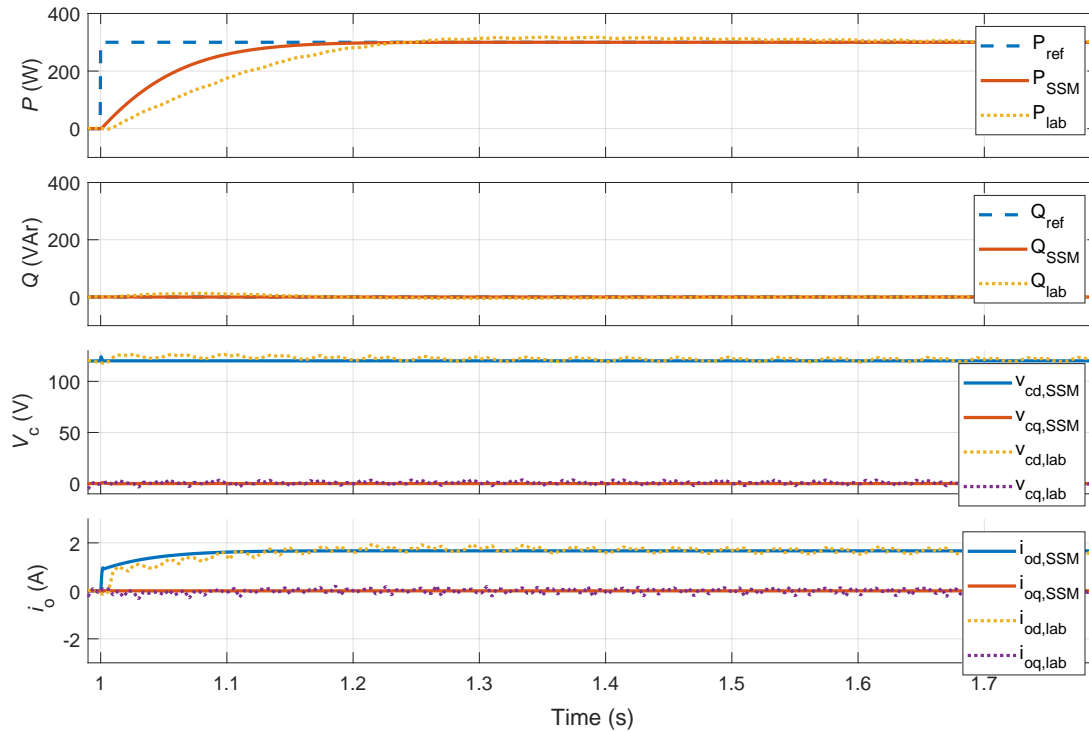


Figure 5.6 Comparison of experimental results to SSM for a 300W active power step up.

The active power steps at $t = 1$ s and the state-space model settles after 226 ms, whereas the experimental results show a settling time of approximately 602 ms. This is significant difference. Additionally, the experimental active power shows some overshoot of 5.67 %, compared with the target of 0%. Three primary factors may contribute to this behaviour: deviations in filter/impedance parameters, the presence of additional delays in the experimental

setup and the influence of noise in the measured signals. Delays associated with signal measurement, computation, and data transmission can induce overshoot by effectively degrading the responsiveness of the control system. In addition, inspection of the dq-domain voltages and currents, as seen in Figure 5.7, reveals some signal noise. This can impair the controllers' ability to operate accurately, thereby cause dynamic deviations such as overshoot.

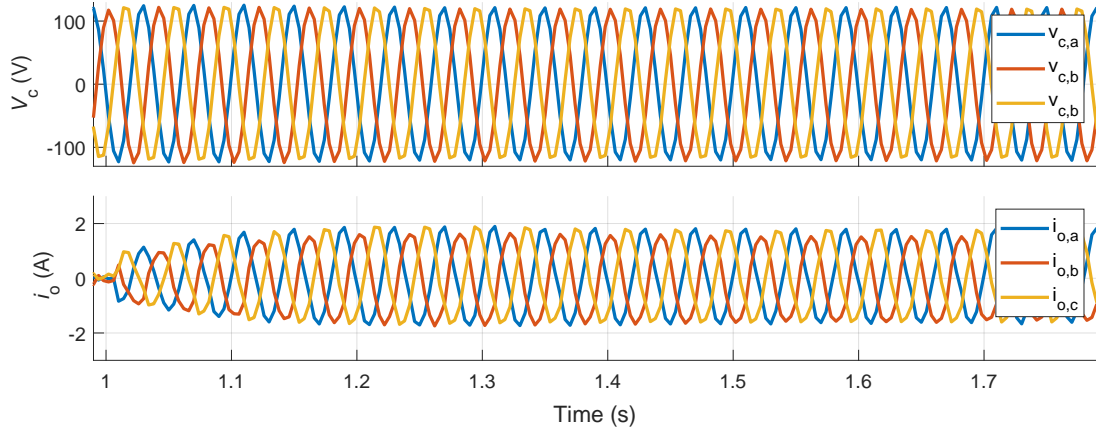


Figure 5.7 Experimental results during a 300W active power step up.

Additionally, the measured voltages and, in particular, the currents exhibit signs of imbalance. Both magnitude discrepancies and DC offsets are observed across the three phases. These issues were thoroughly investigated during the experimental testing. Adjustments to offset and magnitude were attempted based on oscilloscope measurements obtained using a current probe. However, the offset and magnitude varied between phases and changed with different power levels, complicating the implementation of a single consistent correction. Moreover, these values appeared to fluctuate over time, with noticeable deviations occurring throughout the week. Ultimately, no correction was applied to the measured signals, as it was determined that such adjustments were not essential for fulfilling the scope of the project.

The experimental setup was also evaluated under an active power step down, a reactive power step up, and a reactive power step down. These tests exhibited dynamics and deviations similar to those observed during the active power step-up, as documented in Section C.1. In summary, while the experimental setup demonstrates dynamic behaviour that differs from the expected results, it successfully tracks reference signals, maintains synchronization with the grid, and performs appropriate regulation of terminal voltage and current. Despite the observed deviations, the experimental setup is considered sufficient for validating the POD control functionality.

5.4 Multi Inverter

This section will present the results of the multi-inverter system to validate the proper functioning of the control scheme when applied in parallel configuration. For the tests, each inverter will be stepped up, to reach a total active power of 600 W and a total reactive power of 600 VAR. The reason for the reduced power compared with the 300 W and 300 VAR used for the single inverter test, are that the inverters share the same DC source. This causes circulating currents between the inverters, especially considering the delta connection of the filter capacitor.

Therefore, the terminal current has been found to be much higher than expected, even at 0 output current. This inherently limits the power the multi-inverter system can take, due to reaching the 5 A max of the inverter protection earlier. The voltage level could be increased to lower the magnitude of the current but as discussed in Section 5.1, this will affect the signal-to-noise ratio, which is not desired.

The inverters are stepped one at a time, so that the total active/reactive power reaches 600 W/600 VAR. Then the inverter that first stepped up, will step back down to 0, and so on. This procedure, for active power, can be seen in Figure 5.8, where the active- and reactive power are shown.

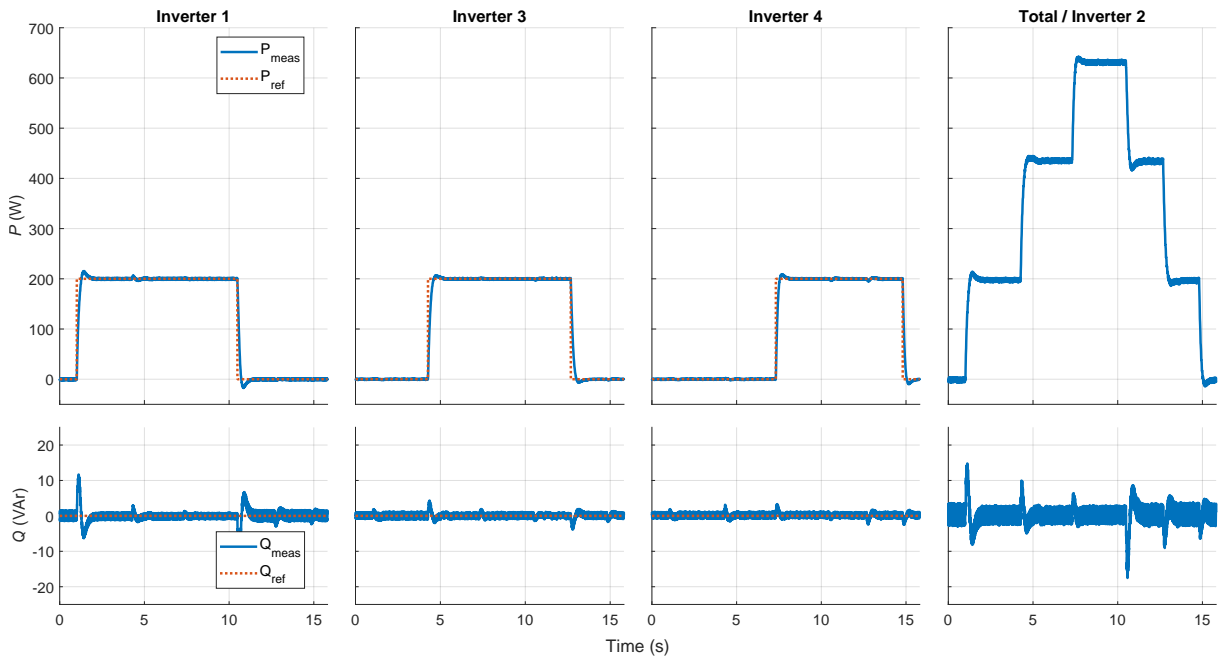


Figure 5.8 Multi inverter active power steps.

The active- and reactive power show some noise, similar to what was observed during the single inverter experiments. The distortion does not seem to increase on any single inverter, except inverter 2 that also handles more current. When investigating the active power, inverter 1 can be seen to have the largest overshoot and undershoot of 7.8 % and 8.8 %. Inverter 3 and 4 seem to have similar responses with overshoot and undershoot of 4.6 % and 5.0 %, respectively. Additionally, each inverter shows some deviation from their setpoint when the other inverters are stepped but quickly track the reference again. A noticeable interaction occurs around 4s, when inverter 1 is visibly affected by a step in inverter 3. Conversely, inverters 3 and 4 exhibit a response when inverters 1 and 3 are stepped down at around 11s and 13s, respectively. A similar pattern is observed in the reactive power behaviour, with inverter 1 again exhibiting the largest deviation.

Most significantly, the active power of inverter 2 deviates from the active power delivered by the other 3 inverters. The inverter 2 active power should be below 400 W and 600 W, but settles above this. The deviation is due to improper scaling and offset of the measured currents, as was discussed in Section 5.3. Thus, if the measured power on inverter 2's side does not match the

combined power of the other inverters, it indicates a measurement inconsistency. This could be due to either an overestimation in the current measured by inverter 2, or an underestimation in the current measured by one or more of the other inverters, causing them to track incorrect power references. Of course, this could also be caused by measurement error on the voltage. However, only few inconsistencies were observed during experiments, making the current measurement the likely cause. In this case, the difference between 0 W and after the inverter 1 has stepped is 198 W, the difference between 198 W and after inverter 3 has stepped is 237 W, and the difference between this power and after inverter 4 has stepped is 195 W. This indicates that inverters 1 and 4 have adequate scaling of the powers, whereas inverter 3 underestimates the current with around 20 %.

The current can be further investigated by zooming in on each step in active power. This can be seen in Figure 5.9, where the columns have the same time axis and the rows represent each inverter measurement.

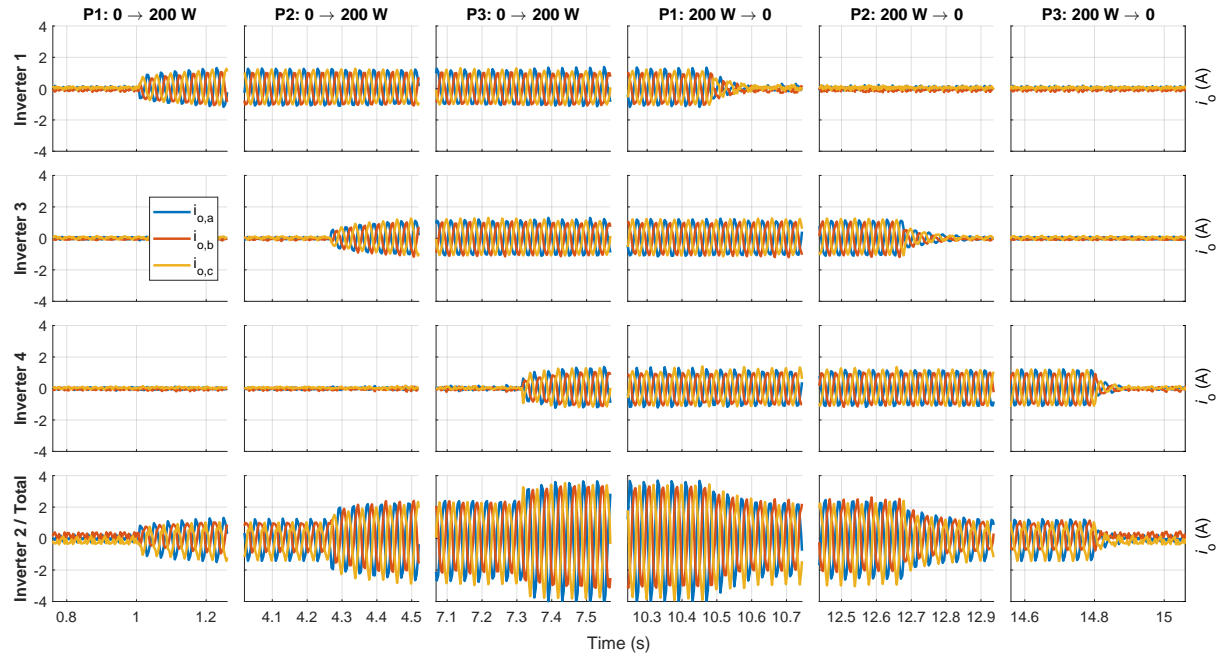


Figure 5.9 Output current of each inverter for each active power step.

Generally, the inverters show a slight unbalance, with inverter 2 also showing some DC offset in current, clearly visible at 0 current. The unbalance and offset issue becomes very clear at higher magnitudes of current on inverter 2. The currents show no clearly visible disturbance when the other inverters are stepped and the currents behave as expected, similar to what was seen in Section 5.3 for the single inverter experiment.

Overall, the multi inverter setup performs well, with some measurement errors and possible unbalance. For the purpose of this project, the multi-inverter setup serves the purpose of testing the POD control in a power plant like setting.

5.5 POD Control

This section will present the implementation and results of the POD control in experimental setup. First, the implementation of the oscillations are described and a few modifications to the control structure are presented. Next, the method used to select the time constants for the lead-lag compensators is described. Finally, the results obtained using POD-P and POD-Q for damping the oscillations are presented.

5.5.1 Implementation

Only two of the four inverters are utilised for POD tests. Inverter 1 in grid-following mode and Inverter 2 setting the voltage. Inverter 2 sets the voltage and Inverter 1 synchronises to this using the PLL. The power oscillation are then generated by varying the reference voltage of Inverter 2. This is done to mimic oscillations between a power plant and the grid by changing the voltage at POC, the point between the two inverters. The power will then oscillate between them.

The active power oscillations are created by varying the frequency of the grid voltage. The output voltage of Inverter 2 are generated by keeping constant reference V_d and V_q while varying the frequency used for the angle generation to the dq-abc transformation. The oscillating frequency results in measurable oscillation in the active power, which in turn can be used as the input for the POD-P.

When a frequency oscillation is introduced on the voltage, two strong oscillations are present in the active power. One at the forced oscillation frequency and one at twice the forced oscillation frequency. A visualisation of this can be seen in the simulation example in Figure 5.10, where a 2 Hz oscillation is added to the grid frequency. The measured power in Figure 5.10 consists of two oscillations. The first at 2 Hz and a second at 4 Hz. The oscillations in the frequency used in the example is relatively high in order to better show the presence of the two frequency components.

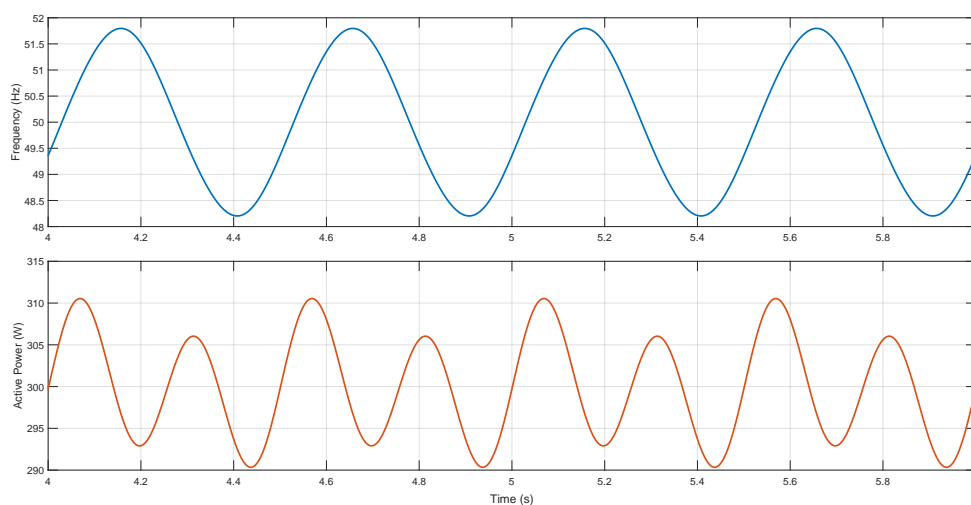


Figure 5.10 Power measurement response to a force frequency oscillation

POD-P only modulate the phase and magnitude of the input signal and will there for only

dampen frequencies present in the input. Therefore, if frequency measurements were to be used as the input signal for the POD-P in the example shown in Figure 5.10, then a 4 Hz signal would still be present in the power measurement, even with perfect alignment of the output. Instead the measured power can be used as input to the POD-P and thereby achieving an output signal which includes both oscillations. A similar effect will be happening for the reactive power and POD-Q if the voltage is used as the input.

Through the experimental tests the dual frequency effect were more prevalent in the active power than the reactive power. The active power measurement were therefore chosen as the input for the POD-P instead of the frequency while the voltage magnitude is used as the input for POD-Q.

Furthermore, it was observed that the measured power had unwanted high-frequency oscillations which caused problems for POD when the power were used as input. A second-order filter were therefore included on POD-P input signal in order to attenuate the oscillations.

Oscillations were also observed on frequency which oscillated roughly between 50.25 Hz and 49.75 Hz which was deemed inadequate. The bandwidth of the PLL for the POD was therefore lowered to 3Hz instead of 30Hz. This reduced the frequency oscillation to be between 50.004 Hz and 49.996 Hz

The values used for POD-P and POD-Q filter during the experiments can be seen in Table 5.2 below.

Table 5.2 POD parameters used for experimental results

Parameter	POD-P	POD-Q
Time constant LPF	0.1	0.1
Time constant wo	5	5
Time constant lead 1	0.74585	0.98504
Time constant lag 2	0.20704	0.019668
Time constant lead 1	0.74585	0.98504
Time constant lag 2	0.20704	0.019668
Gain	-0.4	-0.02

5.5.2 POD-P Results

In the experimental setup continuous forced oscillations is generated through an inverter with dual-loop control, which enforces the frequency rigidly and thereby obscuring the impact of the POD-P on the frequency. It would, however, still be possible to verify the functionality of the POD-P by comparing the frequency oscillation with the power output. But the effects would not results in a decrease in frequency oscillations. In contrast, the transferred power can be modified so the net transfer due to the forced oscillations is reduced.

The power input is calculated using the inverter output current, measured after the LCL filter, and the voltage across the filter capacitor. Due to imbalances in the signal, particularly in the current, the resulting power measurement contained high-frequency ripple components. To

mitigate these unwanted oscillations, an additional low-pass filter was included in the POD-P path. A second order Bessel filter was selected, which has the advantage of having a flat group delay, while still attenuating high-frequency noise. The flat group delay of Bessel filter is the reason for choosing this type, as it will preserve the signal waveform shape which is crucial for effective damping. Spectral analysis of the power measurement revealed that the main power oscillations due to the measurement imbalances was around 37 Hz. A cut-off frequency of 12 Hz was therefore chosen. This ensures that the frequency range of interest (0.1 Hz to 2.5 Hz) lies well within the filter's passband, while the 37 Hz ripple is effectively attenuated.

Figure 5.11 shows the response of the POD-P compensator under forced oscillations at four different frequencies. In each case, the injection magnitude was set to 0.2 Hz.

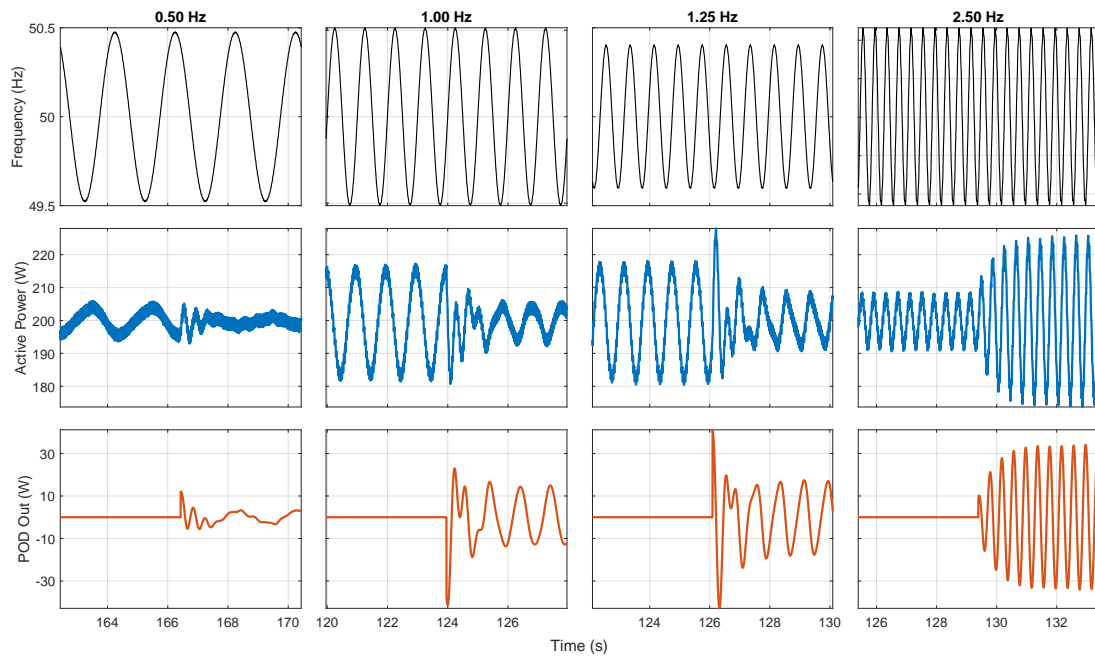


Figure 5.11 Active Power oscillation damping at different frequencies

The signals displayed in the first row of Figure 5.11 are the oscillation frequencies as measured by the PLL. Note that, despite identical input magnitudes, the PLL's measured oscillation amplitudes vary with frequency. The second and third row are measured output power of the inverter and the reference adjustment from POD-P, respectively. For the first three cases the power oscillation amplitudes decrease as the POD-P is activated, with varying effectiveness. However, for the fourth case at a 2.5 Hz oscillation, the POD-P has adverse effect on the power oscillations. The POD-P at 2.5 Hz adds to a positive feedback loop due to miss alignment of the reference output compared with the power oscillation, which increases the power oscillation instead of decreasing it. The situation is only stable due to a saturation block limiting the POD-P output. This saturation block is set to allow at maximum reference change of up to 100 W in either direction.

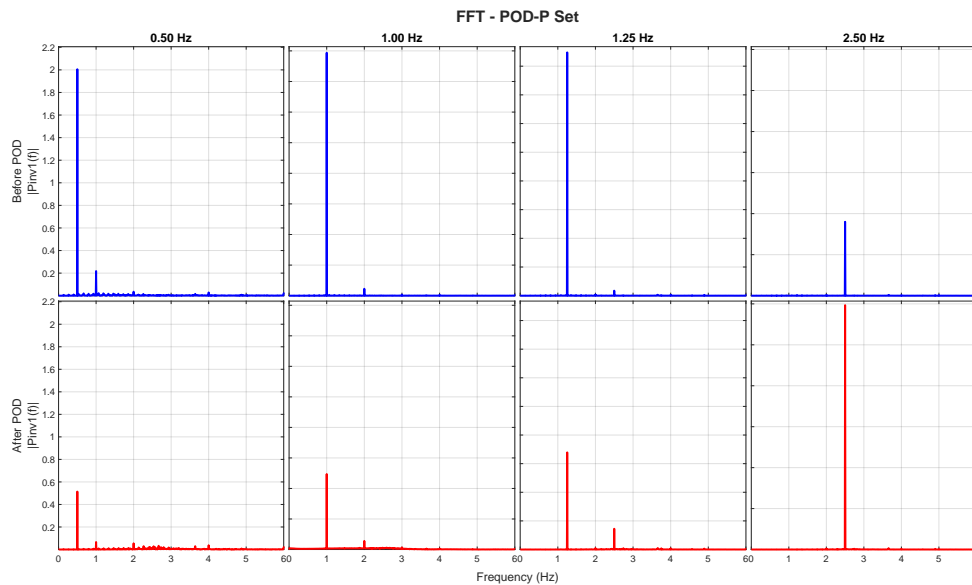
The reduction of the amplitude of the active power oscillations at the different frequencies is summarised in Table 5.3.

Table 5.3 Amplitude reduction at various oscillation frequencies for POD-P.

Frequency (Hz)	Amp. Pre	Amp. Post	Reduction (%)
0.5	12.301	6.4459	47.599
1	35.718	13.537	62.100
1.25	37.685	18.689	50.408
2.5	17.844	52.156	-192.3

The adverse effect observed at the 2.5 Hz oscillation could likely be mitigated by characterising the experimental setup's true frequency response and retuning the POD-P filter accordingly. In practice, however, the physical hardware may introduce dynamics such as delays, component tolerances and measurement noise, that cause the real system to deviate from the idealised mathematical model. As a result, a set of filter coefficients or compensator gains that work perfectly in simulation will not yield identical performance in a hardware setup, and must therefore be retuned experimentally to account for these non-idealities.

Figure 5.12 show the frequency components of measured active power before and after the activation of the POD. The signals are dominated by two frequencies, the first being at the oscillation input frequency and the second twice the oscillation frequency.

**Figure 5.12** FFT analysis of measured active power before and after POD-P.

From the spectral analysis it is evident that the POD damping are different for each frequency and that it is more effective for the lower frequencies and becomes less effective as the frequency of the oscillation increases.

5.5.3 POD-Q Results

The reactive power oscillation are generated by introducing oscillations on the reference voltage of Inverter 2's V_d component. This causes both the active and reactive power to oscillate. To increase the reactive power oscillations, the reactive power reference of Inverters 1 is set to 200 VAR. Unlike the active power when the oscillation on the frequency is introduced, the

reactive power oscillation does not have a significant second order harmonic and it was therefore not found necessary to change the input signal to be the measured reactive power. Instead the voltage magnitude was used as the input signal. The voltage magnitude oscillations are found by equation (5.1)

$$V_{\text{osc}} = \sqrt{V_d^2 + V_q^2} - V_{\text{mag,avg}} \quad (5.1)$$

Where V_d and V_q is the direct- and quadrature component of the capacitor voltage of Inverter 1 and $V_{\text{mag,avg}}$ is the average voltage magnitude which is found feeding the first term of (5.1) to a strong low-pass filter in order to extract its DC-component.

Figure 5.13 shows the results of the oscillation damping using POD-Q. The first row shows the V_d of Inverters 2's capacitor voltage. The second row is the measured reactive power between the two inverters and the third row is the reactive power reference adjustment from the POD-Q.

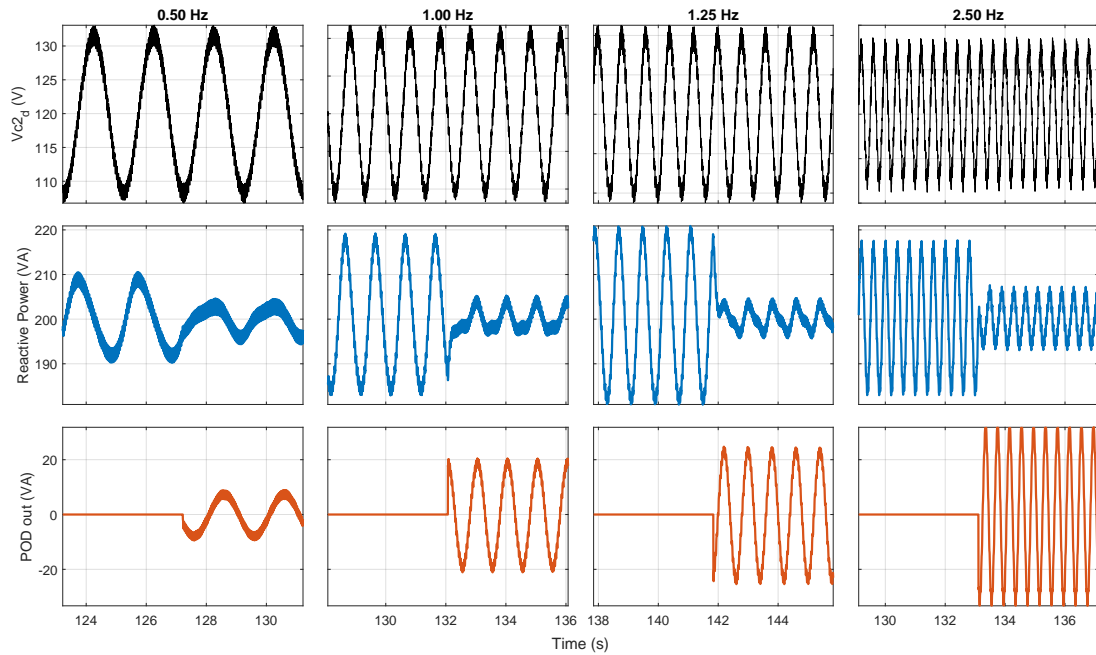


Figure 5.13 Reactive Power oscillation damping at different frequencies.

In all four cases activation POD-Q results in significant reduction in the power oscillations. With greatest reduction being 77.328 % for the 1.25 Hz case and the case with least reduction being the 0.5 Hz case, where the reduction was only 52.241 %. A summary of all four cases can be seen in Table 5.4.

Table 5.4 Amplitude reduction at various oscillation frequencies for POD-Q.

Frequency (Hz)	Amp. Pre	Amp. Post	Reduction (%)
0.5	20.294	9.6923	52.241
1	36.124	8.9704	75.168
1.25	40.000	9.0686	77.328
2.5	34.739	14.221	59.064

The reactive power's frequency composition can be seen in Figure 5.14. Here it can be seen that the POD-Q is most effective at damping the frequencies oscillation around 1.25 Hz this

in contrast to the POD-P which had a clear trend of a decrease in damping with increased frequencies.

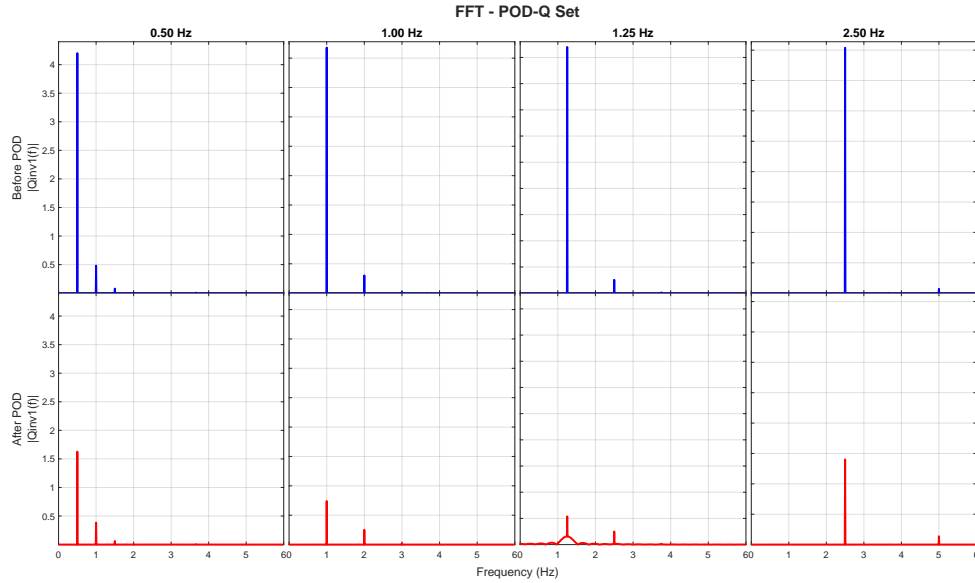


Figure 5.14 FFT analysis of the measured reactive power before and after activation of POD-Q.

All four POD-Q cases show a greater reduction in power oscillations compared to their POD-P counterparts. Part of this difference may be attributed to better alignment between the direction of power reference modulation and the dominant mode of oscillation, which could potentially be improved in the POD-P cases by adjusting the lead-lag controller time constants. Additionally, the initial power oscillation magnitudes in the POD-P cases were roughly half of those in the POD-Q cases. As a result, the signal-to-noise ratio was lower for POD-P, limiting the compensator's ability to target the oscillatory component. Since the POD are designed to suppress low-frequency oscillations and do not actively respond to high-frequency noise (which is filtered out), the effective compensable portion of the power signal was greater in the POD-Q cases. This led to more significant reductions in oscillation magnitudes.

The experimental validation of the POD-P and POD-Q controllers confirms that both control strategies are effective in attenuating power oscillations in a practical inverter-based setup. The measured data shows a noticeable reduction in oscillation amplitude upon activation of the controllers, particularly within the targeted frequency band of 0.2–1.0 Hz. However, at higher frequencies the damping were less pronounced and for 5 Hz case in POD-P the oscillation increased in magnitude.

The level of damping achieved in the experiments was also less pronounced compared to both the time-domain simulations conducted in Simulink and the state-space model results. This discrepancy is likely due to differences between the modelled system and the physical implementation. Potential contributing factors include unmodelled communication delays and deviations in the closed-loop dynamics of the inverter. Further investigation into these aspects—such as quantifying control latencies and validating the actual inverter response could help improve the experimental results.

Furthermore, it is evident from the experimental results that neither the POD-P nor the POD-Q controllers were able to completely eliminate active or reactive power oscillations. This limitation highlights a key drawback of the implemented controller architecture: both PODs are implemented as passive lead-lag compensators with fixed parameters. While this design provides simplicity and ease of implementation, it inherently lacks adaptability to varying grid conditions.

In practical grid-connected applications the grid impedance, strength, and general system dynamic behavior can vary over time. Since the effectiveness of a lead-lag compensator is highly dependent on the system's operating point and the frequency characteristics of the oscillations, a fixed-parameter filter is unlikely to provide optimal performance across all scenarios. As a result, compensators tuned for one set of conditions may offer suboptimal damping, or even contribute to instability, under others conditions.

Moreover, power oscillation damping requirements typically cover a range of frequencies rather than a single narrow band. A passive compensator, by design, has limited bandwidth and must be carefully tuned to target a specific frequency, which complicates implementation when the oscillation modes are uncertain or variable. This further reinforces the need for more advanced, adaptive control strategies that can identify the dominant oscillation modes in real time and adjust the damping response accordingly.

To address these limitations, future research should explore alternative control approaches such as adaptive parameter POD schemes. This may offer greater robustness and flexibility, enabling reliable damping across a broader set of grid conditions and system configurations.

5.6 Summary

In this chapter, the feasibility and performance of the developed grid-following control and POD schemes were validated in an experimental environment. The single-inverter experiments were compared with simulation and state-space model predictions. Some discrepancies were observed, for instance, the experimental settling time and overshoot differed from simulation results. These differences were attributed to practical issues such as measurement noise, communication delays, and component imbalances.

The multi-inverter test extended the validation to a parallel inverter configuration. While the inverters largely tracked the desired references, measurement inconsistencies and current imbalances were noted, particularly affecting one inverter's power measurement.

Finally, experiments on POD control were conducted using both POD-P and POD-Q. The POD-P controller initially faced challenges due to noise in the power measurements, which was mitigated by adding a second-order low-pass filter. However, the POD-P still had adverse effects on the 2.5 Hz oscillation. POD-Q performed more robustly in damping oscillations across the whole frequency range. Overall, while both damping schemes reduced oscillation amplitudes as intended, their effectiveness was limited by the fixed, passive nature of the compensators and the practical challenges of the experimental environment.

Collectively, the experimental studies confirm the basic functionality of the grid-following control and POD schemes, while also highlighting areas, such as measurement noise, tuning discrepancies, and inverter interactions, that need further improvement for practical, real-world application.

6 Discussion

In this report, grid-following control was designed for both single- and multi-inverter configurations with the aim of implementing a POD control scheme. The primary objective was to investigate the implementation of POD in power plants, validate its functionality, and evaluate its impact on system stability. To achieve this, the electrical system was modelled, and control strategies were developed accordingly. Furthermore, to assess small-signal stability, state-space models representing both single- and multi-inverter configurations with POD control were formulated and validated against time-domain simulations. In addition, the performance of the grid-following control and the POD functionality was validated experimentally using a hardware setup comprising of inverters, LCL filters, and a dSPACE. This discussion will first delve into the results from the stability analysis. Afterwards, the experimental results and observations will be discussed. Finally, a combined discussion will be made on the POD control scheme, its limitations, and aspects of the practical implementation.

To evaluate the impact of implementing the POD control scheme in power plants, a small-signal state-space model of a single-inverter configuration with POD was formulated. This configuration was chosen for its simplicity and its eigenvalue behaviour, which resembled that of the multi-inverter system. Although some deviations between the single- and multi-inverter configurations were observed, the eigenvalue trends were sufficiently similar. Therefore, the single-inverter model was considered adequate for assessing the impact of the POD control scheme. The investigation into the stability consequence of adding POD was split into two parts, namely POD-P and POD-Q. The active power damping control scheme, POD-P, was implemented using the active power deviation as input, whereas the POD-Q control scheme was implemented with the voltage magnitude deviation as input. The POD-P and POD-Q control schemes were tuned to achieve similar damping of power oscillations.

Using the tuned parameters for the POD-P control scheme, the eigenvalues without POD-P could be compared to the eigenvalues with POD-P. The comparison showed that no major shift occurred on the high- and medium-frequency eigenvalues. However, the low-frequency eigenvalues, mainly related to controller eigenvalues, showed more deviation. Specifically for the eigenvalues related to the power controller, the real part had reduced by half and the imaginary part had increased with more than a factor of 10. This is a drastic shift in eigenvalues, which moves the power controller closer to instability. Notably, for all eigenvalue-based stability analyses done in this project, the power controller was the first to become unstable. Thus, such a shift in power controller eigenvalues, severely affects the stability margin of the system. However, during a parameter sweep of the POD-P gain, it was seen that a lower gain yielded a lesser shift in eigenvalues, though this will be at the consequence of poorer power oscillation damping. This indicates that for POD-P with the active power deviation as input, less damping can be achieved when aiming for limited impact on the stability of the power plant.

Similarly, using the tuned parameters for the POD-Q control scheme, the eigenvalues with

and without the POD-Q control scheme could be compared. The comparison showed that the eigenvalues shift for the high- and medium-frequency eigenvalues are minimal, and that only slight deviations in the low-frequency eigenvalues occurred. Similar to POD-P, the reactive power control eigenvalues shifted the most. However, for POD-Q the eigenvalues moved only slightly, the real part increased and the imaginary part decreased. The parameter sweep of the POD-Q gain showed, that much less change happened with the eigenvalues than what was seen of POD-P and most eigenvalues became more stable. This indicates that for POD-Q with the voltage magnitude deviation as input to the POD control scheme, good damping can be achieved without compromising the small-signal stability of the power plant.

This poses the question as to why the POD-Q does not have the same stability consequences as was seen for POD-P. It could be related to the selected input parameter to the POD control schemes. The POD-P uses the active power deviation as input, which is also a parameter dominantly controlled by the inverter active power controller, whereas the voltage magnitude deviation used for POD-Q is less dependant on the reactive power controller. In addition, the power controller was tuned based on general performance considerations, and due to the resonance peak introduced by the filter capacitor and grid inductance, resulted in a closed-loop bandwidth of approximately 2.91 Hz. This bandwidth coincides with the frequency range of the POD regulation and may therefore contribute to the observed reduction in stability for POD-P when using the active power deviation as input.

To validate the control design and evaluate the functionality of the POD control schemes, the developed control was implemented in an experimental setup. The setup configuration was identical to the configuration used for control design and state-space model formulation. However, when validating the grid-following control design, deviations were observed. There were significant delay in the experimental setup, and imbalances, noise and parameter uncertainty affected the control performance. The settling time of the power controller deviated with a factor of around 3 and overshoot was observed. Furthermore, the delay was clearly evident in the current regulation, although its overall shape aligned well with expectations. Similar was seen for the case of the three-inverter configuration. Ultimately, the experimental setup functioned well and was deemed adequate for testing the implementation and functionality of POD control schemes.

When implementing the POD control schemes in the experimental setup, some of the observed deviations played a role. The disturbance in the voltage and current measurements resulted in a power oscillation-to-noise ratio that was too low for the POD-P control scheme to provide adequate damping in its current form. Therefore, a second-order low-pass filter was included to reduce some of the higher frequency disturbances. This cleared up the measured active power oscillation, and allowed for the intended use of the POD-P control scheme. This was not the case for POD-Q, as the voltage magnitude deviation was used instead. Thus, for POD control schemes with power deviations as input, the control schemes commonly presented in literature, as described in Section 2.2, is not adequate for experimental implementation.

Nonetheless, both the POD-P and POD-Q control schemes were successfully implemented in the experimental setup. As the experimental setup deviated substantially from the design basis,

the POD parameters had to be retuned to function properly. The POD with the retuned parameters showed substantial damping of forced power oscillations for most cases. The POD-P control scheme showed a reduction in active power oscillation of 47.6 %, 62.1 % and 50.4 % for power oscillations of 0.5 Hz, 1 Hz and 1.25 Hz, respectively. However, for a power oscillation of 2.5 Hz, the POD-P control scheme had adverse effect on the oscillation and increased until the saturation limit was reached. Since the power controller showed no signs of instability, this indicates that the reason for the adverse effect was due to miss-alignment issues. Therefore, it is likely that a different tuning could yield similar damping for oscillations of 2.5 Hz as well. Although significant damping was achieved, it was not on the same scale as was shown in the simulations. This is likely also due to imperfect tuning of the POD-P parameters. Predicting the exact delay and phase shifts in the experimental setup is difficult, and was not made any easier by the noise and disturbance on the signals, which is why better performance of the POD-P control scheme was not achieved.

In comparison, the implementation of the POD-Q control scheme did not require any changes to the control scheme, and only the tuning of the parameters was changed. The POD-Q control functioned well and showed adequate damping between around 50 % and 80 % for all oscillation frequencies. Though, as high sensitivity to the gain and filter parameters has been observed, the improved damping could be coincidental rather than a generic result. Similar to POD-P, better performance of the POD-Q control scheme was not achieved due to the same reasons.

7 Conclusion

This report explored the design, implementation, and validation of POD control schemes in grid-following inverter-based power plants. POD control schemes were developed for active power, POD-P, and reactive power, POD-Q. The POD control schemes were developed and evaluated through modelling, small-signal stability analysis, and experimental testing, with the aim of assessing its functionality and impact on system stability. The models were validated against time-domain simulations and used to analyse the stability implications of introducing POD control.

The results demonstrated that the developed POD-P and POD-Q control schemes exhibit significantly different effects on system stability. While POD-P provided effective damping in simulation, it also introduced a considerable shift in the power controller eigenvalues, reducing the overall stability margin. In contrast, POD-Q exhibited minimal adverse impact on the system's eigenvalue trajectories, suggesting that it can offer effective damping without compromising small-signal stability. These differences were attributed to the interaction between the POD input signals and the underlying power control loops.

The experimental validation confirmed the functionality of both POD schemes. However, it also highlighted challenges in practical implementation. The POD-P control scheme required the introduction of additional filtering to mitigate noise in the power measurements, and retuning was necessary to achieve effective damping. The performance of POD-P was highly sensitive to tuning and delay effects in the setup, which limited its effectiveness at higher oscillation frequencies. POD-Q, on the other hand, could be implemented without modifications to the control structure and showed more robust performance across a range of frequencies, though it exhibited sensitivity to parameter tuning too.

Overall, the study concludes that POD control schemes can enhance power oscillation damping in grid-following hybrid power plants, but their design must account for stability trade-offs, practical implementation effects, and interactions related to input signals. Among the two control schemes, POD-Q based on voltage magnitude deviation demonstrated greater stability and robustness.

8 Future Work

Although the present study has successfully developed and validated both POD-P and POD-Q control schemes for grid-following inverter-based systems, several aspects remain to be explored further in order to improve practical performance and enhance overall system robustness.

One area that could be improved is the tuning of the POD controllers for the experimental setup. In the experiments, the power step response of the power controller exhibited clear deviations from the time-domain simulation results. Since the tuning of both the POD-P and POD-Q controllers depend critically on the closed-loop phase response of the power controller, it is necessary to retune these controllers based on measured loop characteristics. Future work should involve extensive experimental testing to characterise the closed-loop behaviour of the experimental setup under varying operational conditions. This information could be used to adjust the controller parameters over the full range of oscillation frequencies, rather than relying on tuning for a single frequency.

Moreover, the current study has mainly focused on a single inverter model with POD control. Further investigation is required to assess the performance of POD schemes in a multi-inverter environment. It is important to explore both the behaviour of POD control on an individual inverter level and the possibility of implementing a coordinated or shared POD strategy among inverters. In this framework, integrating the hybrid power plant controller with POD control strategies could offer improved performance over a broader range of operating conditions, ensuring that the individual contributions of the various inverter subsystems are properly coordinated.

Additionally, the results indicate that the selection of the input parameter for the POD controllers has a significant impact on both damping performance and small-signal stability. In the present work, the POD-P controller utilised active power deviation as its input while the POD-Q used the voltage magnitude deviation. Future efforts should explore alternative choices of inputs, such as using frequency deviation for POD-P and reactive power for POD-Q to investigate whether these alterations can improve damping or reduce adverse stability impacts. The observed differences in small-signal stability between POD-P and POD-Q may be linked to their respective input signals and tuning strategies, which could be investigated further.

Finally, further refinement of the state-space models would enable a more comprehensive evaluation of damping effects versus stability consequences. For example, it would be beneficial to include frequency perturbations as part of the grid input, and to extend the POD framework to the multi-inverter state-space model. A grid-scaled model in which the grid exhibits naturally poorly damped eigenmodes could be developed. This could provide insights into how much damping the POD controllers add to the power system compared to the adverse effects on the power plant stability.

Collectively, these areas of future work offer a promising pathway toward enhanced control of inverter-based power plants. With better model accuracy and more flexible control strategies, it should be possible to achieve effective power oscillation damping while maintaining good system stability across various grid conditions.

Bibliography

- [1] Lennart Petersen. Proof-of-concept on next generation hybrid power plant control, 2020.
- [2] L. Petersen, P. H. Nielsen, G. C. Tarnowski, and T. Lund. Addressing power oscillations damping requirements for wind power plants. In *20th International Workshop on Large-Scale Integration of Wind Power into Power Systems as well as on Transmission Networks for Offshore Wind Power Plants (WIW 2021)*, volume 2021, pages 403–413, 2021.
- [3] Prabha Kundur. *Power System Stability and Control*. The EPRI Power System Engineering Series. McGraw-Hill, 1994.
- [4] Zimran Rafique, Haris M. Khalid, S.M. Muyeen, and Innocent Kamwa. Bibliographic review on power system oscillations damping: An era of conventional grids and renewable energy integration. *International Journal of Electrical Power & Energy Systems*, 136:107556, 2022.
- [5] GreenPowerMonitor. Enhancing grid stability: Power oscillation damping controls. 2025. Accessed: 2025-02-07.
- [6] Nikolay Nikolaev, Kiril Dimitrov, and Yulian Rangelov. A comprehensive review of small-signal stability and power oscillation damping through photovoltaic inverters. *Energies*, 14(21), 2021.
- [7] Energinet. Anmeldelse af Ændring af rfg-krav (anmeldelsesudgave december 2022), 2022. Regulation submitted for approval by the Danish Utilities Authority.
- [8] Arwindra Rizqiawan, Pradita Hadi, and Goro Fujita. Development of grid-connected inverter experiment modules for microgrid learning. *Energies*, 12:476, 02 2019.
- [9] Bikash Pal and Balarko Chaudhuri. *Robust Control in Power Systems*. Power Electronics and Power Systems. Springer, 2005.
- [10] Ping Jiang, Shuang Feng, and Xi Wu. Robust design method for power oscillation damping controller of statcom based on residue and tls-esprit. *International Transactions on Electrical Energy Systems*, 24, 10 2014.
- [11] José Luis Domínguez-García, Oriol Gomis-Bellmunt, Fernando D. Bianchi, and Andreas Sumper. Power oscillation damping supported by wind power: A review. *Renewable and Sustainable Energy Reviews*, 16(7), 2012.
- [12] D. P. S. Gupta and I. Sen. Low frequency oscillations in power systems: A physical account and adaptive stabilizers. *Sadhana*, 18:843–868, 1993.
- [13] Gopal R. Gajjar and Shreevardhan A. Soman. Power system oscillation modes identifications: Guidelines for applying tls-esprit method. *International Journal of Emerging Electric Power Systems*, 14(1):57–66, 2013.

- [14] European Commission. Commission Regulation (EU) 2016/631 of 14 April 2016 establishing a network code on requirements for grid connection of generators, 2016. Official Journal of the European Union, L 112, 27 April 2016, pp. 1–68.
- [15] The European Union Agency for the Cooperation of Energy Regulators. Recommendation no 03/2023 of the european union agency for the cooperation of energy regulators, 2023. ACER recommendations to Requirement for Generators 2.0.
- [16] Svenska kraftnät. Svenska kraftnät’s draft update of eifs 2018:2, 2024. Draft for update to the Swedish technical regulation.
- [17] Fingrid. Grid code specifications for power generating facilities vjv2018, 2018.
- [18] Red Eléctrica de España. *Guide for the Implementation of Power Oscillation Damping Controllers*, September 2024.
- [19] Xian Gao, Dao Zhou, Amjad Anvari-Moghaddam, and Frede Blaabjerg. Impact of digital control delay on stability of grid-following converters. In *2022 IEEE 13th International Symposium on Power Electronics for Distributed Generation Systems (PEDG)*, 2022.
- [20] Jinwei He, Yun Wei Li, and Frede Blaabjerg. A general design method of lcl filter for three-phase grid-connected inverter in distributed power generation systems. *IEEE Transactions on Industrial Electronics*, 60(10):4248–4257, 2013.
- [21] Liang Huang, Chao Wu, Dao Zhou, and Frede Blaabjerg. Mixed grid-forming and grid-following inverters with secondary control providing fast voltage and frequency support. In *2023 25th European Conference on Power Electronics and Applications (EPE’23 ECCE Europe)*, pages 1–10. IEEE, 2023.
- [22] Saeed Golestan and Josep M. Guerrero. Conventional synchronous reference frame phase-locked loop is an adaptive complex filter. *IEEE Transactions on Industrial Electronics*, 62(3):1679–1682, 2015.
- [23] Charles L. Phillips and John M. Parr. *Feedback Control Systems*. Pearson Prentice Hall, Upper Saddle River, NJ, 5 edition, 2006.
- [24] Nagaraju Pogaku, Milan Prodanovic, and Timothy C. Green. Modeling, analysis and testing of autonomous operation of an inverter-based microgrid. *IEEE Transactions on Power Electronics*, 22(2):613–625, 2007.
- [25] Xian Gao, Dao Zhou, Amjad Anvari-Moghaddam, and Frede Blaabjerg. Stability analysis of grid-following and grid-forming converters based on state-space modelling. *IEEE Transactions on Industry Applications*, 60(3):4910–4920, 2024.
- [26] Liang Huang, Chao Wu, Dao Zhou, and Frede Blaabjerg. Comparison of three small-signal stability analysis methods for grid-following inverter. In *2021 International Aegean Conference on Electrical Machines and Power Electronics (ACEMP) & 2021 International Conference on Optimization of Electrical and Electronic Equipment (OPTIM)*, pages 34–41, 2021.

A Modelling

A.1 Control

A.1.1 Current Control

Beginning with the KVL equation:

$$\begin{bmatrix} v_{t,a} \\ v_{t,b} \\ v_{t,c} \end{bmatrix} = R_f \begin{bmatrix} i_{t,a} \\ i_{t,b} \\ i_{t,c} \end{bmatrix} + L_f \frac{d}{dt} \begin{bmatrix} i_{t,a} \\ i_{t,b} \\ i_{t,c} \end{bmatrix} + \begin{bmatrix} v_{o,a} \\ v_{o,b} \\ v_{o,c} \end{bmatrix} \quad (\text{A.1})$$

By designating T as the abc-to-dq0 transformation matrix and T^{-1} as the dq0-to-abc transformation matrix, a new equation can be made:

$$T^{-1} \begin{bmatrix} v_{t,d} \\ v_{t,q} \\ v_{t,0} \end{bmatrix} = R_f T^{-1} \begin{bmatrix} i_{t,d} \\ i_{t,q} \\ i_{t,0} \end{bmatrix} + L_f \frac{d}{dt} \left(T^{-1} \begin{bmatrix} i_{t,d} \\ i_{t,q} \\ i_{t,0} \end{bmatrix} \right) + T^{-1} \begin{bmatrix} v_{o,d} \\ v_{o,q} \\ v_{o,0} \end{bmatrix} \quad (\text{A.2})$$

The d/dt term can be expanded:

$$T^{-1} \begin{bmatrix} v_{t,d} \\ v_{t,q} \\ v_{t,0} \end{bmatrix} = R_f T^{-1} \begin{bmatrix} i_{t,d} \\ i_{t,q} \\ i_{t,0} \end{bmatrix} + \left(L_f \left(\frac{d}{dt} T^{-1} \right) \begin{bmatrix} i_{t,d} \\ i_{t,q} \\ i_{t,0} \end{bmatrix} + L_f T^{-1} \left(\frac{d}{dt} \begin{bmatrix} i_{t,d} \\ i_{t,q} \\ i_{t,0} \end{bmatrix} \right) \right) + T^{-1} \begin{bmatrix} v_{o,d} \\ v_{o,q} \\ v_{o,0} \end{bmatrix} \quad (\text{A.3})$$

The first derivative term can be simplified by:

$$L_f \frac{d}{dt} T^{-1} = \begin{bmatrix} 0 & -\omega L_f & 0 \\ \omega L_f & 0 & 0 \\ 0 & 0 & 0 \end{bmatrix} \quad (\text{A.4})$$

Thus, by using the above term and the relationship $T \cdot T^{-1} = 1$ the equation becomes:

$$\begin{bmatrix} v_{t,d} \\ v_{t,q} \\ v_{t,0} \end{bmatrix} = R_f \begin{bmatrix} i_{t,d} \\ i_{t,q} \\ i_{t,0} \end{bmatrix} + \begin{bmatrix} 0 & -\omega L_f & 0 \\ \omega L_f & 0 & 0 \\ 0 & 0 & 0 \end{bmatrix} \begin{bmatrix} i_{t,d} \\ i_{t,q} \\ i_{t,0} \end{bmatrix} + L_f \left(\frac{d}{dt} \begin{bmatrix} i_{t,d} \\ i_{t,q} \\ i_{t,0} \end{bmatrix} \right) + \begin{bmatrix} v_{o,d} \\ v_{o,q} \\ v_{o,0} \end{bmatrix} \quad (\text{A.5})$$

By gathering the R_f and L_f terms the following equation can be found:

$$\begin{bmatrix} v_{t,d} \\ v_{t,q} \\ v_{t,0} \end{bmatrix} = (L_f \frac{d}{dt} + R_f) \begin{bmatrix} i_{t,d} \\ i_{t,q} \\ i_{t,0} \end{bmatrix} + \begin{bmatrix} 0 & -\omega L_f & 0 \\ \omega L_f & 0 & 0 \\ 0 & 0 & 0 \end{bmatrix} \begin{bmatrix} i_{t,d} \\ i_{t,q} \\ i_{t,0} \end{bmatrix} + \begin{bmatrix} v_{o,d} \\ v_{o,q} \\ v_{o,0} \end{bmatrix} \quad (\text{A.6})$$

By transforming to Laplace the following is found:

$$\begin{bmatrix} v_{t,d} \\ v_{t,q} \\ v_{t,0} \end{bmatrix} = (sL_f + R_f) \begin{bmatrix} i_{t,d} \\ i_{t,q} \\ i_{t,0} \end{bmatrix} + \begin{bmatrix} 0 & -\omega L_f & 0 \\ \omega L_f & 0 & 0 \\ 0 & 0 & 0 \end{bmatrix} \begin{bmatrix} i_{t,d} \\ i_{t,q} \\ i_{t,0} \end{bmatrix} + \begin{bmatrix} v_{o,d} \\ v_{o,q} \\ v_{o,0} \end{bmatrix} \quad (\text{A.7})$$

By isolating for the left $i_{t,dq0}$ term, the final equation can be found:

$$\begin{bmatrix} i_{t,d} \\ i_{t,q} \\ i_{t,0} \end{bmatrix} = \frac{1}{sL_f + R_f} \left(\begin{bmatrix} v_{t,d} \\ v_{t,q} \\ v_{t,0} \end{bmatrix} - \begin{bmatrix} v_{o,d} \\ v_{o,q} \\ v_{o,0} \end{bmatrix} + \begin{bmatrix} 0 & -\omega L_f & 0 \\ \omega L_f & 0 & 0 \\ 0 & 0 & 0 \end{bmatrix} \begin{bmatrix} i_{t,d} \\ i_{t,q} \\ i_{t,0} \end{bmatrix} \right) \quad (\text{A.8})$$

A.1.2 SRF-PLL Transfer Function Derivation

$$V_q(s) = K_d(\theta_{\text{in}}(s) - \theta_{\text{est}}(s)) \quad (\text{A.9})$$

In case of a normalised input K_d can be assumed zero.

$$\omega_{\text{est}} = K_{p,\text{pll}}V_q + \frac{K_{i,\text{pll}}V_q}{s} \quad (\text{A.10})$$

$$\theta_{\text{est}} = \frac{\omega_{\text{est}}}{s} \quad (\text{A.11})$$

$$\theta_{\text{est}} = \frac{\left(K_{p,\text{pll}} + \frac{K_{i,\text{pll}}}{s}\right)}{s} K_d(\theta_{\text{in}}(s) - \theta_{\text{est}}(s)) \quad (\text{A.12})$$

$$\frac{\theta_{\text{est}}}{\theta_{\text{in}}} = \frac{K_d K_{p,\text{pll}} s + K_d K_{i,\text{pll}}}{s^2 + K_d K_{p,\text{pll}} s + K_d K_{i,\text{pll}}} \quad (\text{A.13})$$

$$H(s) = \frac{K_d K_{p,\text{pll}} s + K_d K_{i,\text{pll}}}{s^2 + K_d K_{p,\text{pll}} s + K_d K_{i,\text{pll}}} \quad (\text{A.14})$$

$$\text{Characteristic equation: } s^2 + K_d K_{p,\text{pll}} s + K_d K_{i,\text{pll}} = 0 \quad (\text{A.15})$$

$$\text{Comparing with standard form: } s^2 + 2\zeta\omega_n s + \omega_n^2 = 0 \quad (\text{A.16})$$

$$K_{p,\text{pll}} = \frac{2\zeta\omega_n}{K_d} K_{i,\text{pll}} = \frac{\omega_n^2}{K_d} \quad (\text{A.17})$$

B Stability

B.1 Single Inverter State-Space Model

B.1.1 Power Controller

The power calculation in the dq0 reference frame can be written as seen in Equation (??).

$$P = \frac{\omega_{\text{LPF}}}{\omega_{\text{LPF}} + s} \frac{3}{2} (v_{o,d} i_{o,d} + v_{o,q} i_{o,q}) \quad Q = \frac{\omega_{\text{LPF}}}{\omega_{\text{LPF}} + s} \frac{3}{2} (v_{o,q} i_{o,d} - v_{o,d} i_{o,q}) \quad (\text{B.1})$$

Moving around and adding doing small-signal linearisation.

$$P(\omega_{\text{LPF}} + s) = \omega_{\text{LPF}} \frac{3}{2} (v_{o,d} i_{o,d} + v_{o,q} i_{o,q}) \quad (\text{B.2})$$

$$(P + \Delta P)(\omega_{\text{LPF}} + s) = \omega_{\text{LPF}} \frac{3}{2} ((V_{o,d} + \Delta v_{o,d})(I_{o,d} + \Delta i_{o,d}) + (V_{o,q} + \Delta v_{o,q})(I_{o,q} + \Delta i_{o,q})) \quad (\text{B.3})$$

Multiplying terms together. Ignoring terms with perturbation multiplied by perturbation and removing the steady-state part.

$$\Delta P(\omega_{\text{LPF}} + s) = \omega_{\text{LPF}} \frac{3}{2} (V_{o,d} \Delta i_{o,d} + I_{o,d} \Delta v_{o,d} + V_{o,q} \Delta i_{o,q} + I_{o,q} \Delta v_{o,q}) \Rightarrow \quad (\text{B.4})$$

$$\Delta \dot{P} = -\omega_{\text{LPF}} \Delta P + \omega_{\text{LPF}} \frac{3}{2} (V_{o,d} \Delta i_{o,d} + I_{o,d} \Delta v_{o,d} + V_{o,q} \Delta i_{o,q} + I_{o,q} \Delta v_{o,q}) \quad (\text{B.5})$$

Doing the same for reactive power. Moving around and doing small-signal linearisation.

$$Q(\omega_{\text{LPF}} + s) = \omega_{\text{LPF}} \frac{3}{2} (v_{o,q} i_{o,d} - v_{o,d} i_{o,q}) \quad (\text{B.6})$$

$$(Q + \Delta Q)(\omega_{\text{LPF}} + s) = \omega_{\text{LPF}} \frac{3}{2} ((V_{o,q} + \Delta v_{o,q})(I_{o,d} + \Delta i_{o,d}) - (V_{o,d} + \Delta v_{o,d})(I_{o,q} + \Delta i_{o,q})) \quad (\text{B.7})$$

Letting steady-state terms cancel out and ignoring perturbation with perturbation multiplication.

$$\Delta Q(\omega_{\text{LPF}} + s) = \omega_{\text{LPF}} \frac{3}{2} (V_{o,q} \Delta i_{o,d} + I_{o,d} \Delta v_{o,q} - V_{o,d} \Delta i_{o,q} - I_{o,q} \Delta v_{o,d}) \quad (\text{B.8})$$

$$\Delta \dot{Q} = -\omega_{\text{LPF}} \Delta Q + \omega_{\text{LPF}} \frac{3}{2} (V_{o,q} \Delta i_{o,d} + I_{o,d} \Delta v_{o,q} - V_{o,d} \Delta i_{o,q} - I_{o,q} \Delta v_{o,d}) \quad (\text{B.9})$$

The control equations for the power controller can be seen:

$$i_{o,d}^* = k_{p,p} (P^* - P) + k_{i,p} (P^* - P) \quad i_{o,q}^* = k_{p,p} (Q^* - Q) + k_{i,p} (Q^* - Q) \quad (\text{B.10})$$

The integral action of the PI controller creates the state equations.

$$\phi_d = \int (P^* - P) dt \Rightarrow \frac{d\phi_d}{dt} = P^* - P \quad \phi_q = \int (Q^* - Q) dt \Rightarrow \frac{d\phi_q}{dt} = Q^* - Q \quad (\text{B.11})$$

Doing small-signal linearisation on Equation (??), Equation (??) can be derived.

$$\Delta \dot{\phi}_d = \Delta P^* - \Delta P \quad \Delta \dot{\phi}_q = \Delta Q^* - \Delta Q \quad (\text{B.12})$$

Similarly, by doing small-signal linearisation can be derived.

$$(I_{o,d}^* + \Delta i_{o,d}^*) = k_{p,p} ((P^* + \Delta P^*) - (P + \Delta P)) + k_{i,p} (\Phi_d + \Delta \phi_d) \quad (\text{B.13})$$

$$(I_{o,q}^* + \Delta i_{o,q}^*) = k_{p,p} ((Q^* + \Delta Q^*) - (Q + \Delta Q)) + k_{i,p} (\Phi_q + \Delta \phi_q) \quad (\text{B.14})$$

Steady-state terms cancels out.

$$\Delta i_{o,d}^* = k_{p,p} (\Delta P^* - \Delta P) + k_{i,p} \Delta \phi_d \quad \Delta i_{o,q}^* = k_{p,p} (\Delta Q^* - \Delta Q) + k_{i,p} \Delta \phi_q \quad (\text{B.15})$$

B.1.2 Current Controller

The integral part of the current PI controller can be written as:

$$\gamma_d = \int (i_{t,d}^* - i_{t,d}) dt \Rightarrow \frac{d\gamma_d}{dt} = i_{t,d}^* - i_{t,d} \quad \gamma_q = \int (i_{t,q}^* - i_{t,q}) dt \Rightarrow \frac{d\gamma_q}{dt} = i_{t,q}^* - i_{t,q} \quad (\text{B.16})$$

The two equations can be small-signal linearised as follows.

$$\frac{d}{dt} (\Gamma_d + \Delta \gamma_d) = (I_{t,d}^* + \Delta i_{t,d}^*) - (I_{t,d} + \Delta i_{t,d}) \quad (\text{B.17})$$

$$\frac{d}{dt} (\Gamma_q + \Delta \gamma_q) = (I_{t,q}^* + \Delta i_{t,q}^*) - (I_{t,q} + \Delta i_{t,q}) \quad (\text{B.18})$$

The steady-state terms cancel out.

$$\frac{d\Delta \gamma_d}{dt} = \Delta i_{t,d}^* - \Delta i_{t,d} \quad \frac{d\Delta \gamma_q}{dt} = \Delta i_{t,q}^* - \Delta i_{t,q} \quad (\text{B.19})$$

The algebraic equation of the control equation is then:

$$v_{t,d}^* = -\omega_n L_f i_{t,q} + v_{o,d} + k_{p,c} (i_{t,d}^* - i_{t,d}) + k_{i,c} \gamma_d \quad (\text{B.20})$$

$$v_{t,q}^* = \omega_n L_f i_{t,d} + v_{o,q} + k_{p,c} (i_{t,q}^* - i_{t,q}) + k_{i,c} \gamma_q \quad (\text{B.21})$$

By doing small-signal linearisation, the following equation can be reached.

$$\begin{aligned} (V_{t,d}^* + \Delta v_{t,d}^*) = & -\omega_n L_f (I_{t,q} + \Delta i_{t,q}) + (V_{o,d} + \Delta v_{o,d}) \\ & + k_{p,c} \left((I_{t,d}^* + \Delta i_{t,d}^*) - (I_{t,d} + \Delta i_{t,d}) \right) + k_{i,c} (\Gamma_d + \Delta \gamma_d) \end{aligned} \quad (\text{B.22})$$

$$\begin{aligned} (V_{t,q}^* + \Delta v_{t,q}^*) = & \omega_n L_f (I_{t,d} + \Delta i_{t,d}) + (V_{o,q} + \Delta v_{o,q}) \\ & + k_{p,c} \left((I_{t,q}^* + \Delta i_{t,q}^*) - (I_{t,q} + \Delta i_{t,q}) \right) + k_{i,c} (\Gamma_q + \Delta \gamma_q) \end{aligned} \quad (\text{B.23})$$

The steady-state terms cancel out, leaving the following:

$$\Delta v_{t,d}^* = -\omega_n L_f \Delta i_{t,q} + \Delta v_{o,d} + k_{p,c} (\Delta i_{t,d}^* - \Delta i_{t,d}) + k_{i,c} \Delta \gamma_d \quad (\text{B.24})$$

$$\Delta v_{t,q}^* = \omega_n L_f \Delta i_{t,d} + \Delta v_{o,q} + k_{p,c} (\Delta i_{t,q}^* - \Delta i_{t,q}) + k_{i,c} \Delta \gamma_q \quad (\text{B.25})$$

B.1.3 Delay

For the controller tuning, the delay was implemented as a transfer function approximation. Using this transfer function and input-output relations, the equation can be written in the correct form.

$$\begin{aligned}
G_d(s) &= \frac{Y(s)}{U(s)} = \frac{1}{1.5T_s s + 1} \Rightarrow \\
(1.5T_s s + 1)Y(s) &= U(s) \Rightarrow \\
1.5T_s \dot{y}(t) + y(t) &= u(t) \Rightarrow \\
\dot{y}(t) &= -\frac{1}{1.5T_s}y(t) + \frac{1}{1.5T_s}u(t)
\end{aligned} \tag{B.26}$$

Now that the delay equation is written in a form similar to the state-space representation, the inputs and outputs can be replaced with the correct parameters.

$$\dot{v}_{\text{del,d}} = -\frac{1}{1.5T_s}v_{\text{del,d}} + \frac{1}{1.5T_s}v_{\text{t,d}}^* \quad \dot{v}_{\text{del,q}} = -\frac{1}{1.5T_s}v_{\text{del,q}} + \frac{1}{1.5T_s}v_{\text{t,d}}^* \tag{B.27}$$

The equations can be small-signal linearised.

$$(\dot{V}_{\text{del,d}} + \Delta \dot{v}_{\text{del,d}}) = -\frac{1}{1.5T_s}(V_{\text{del,d}} + \Delta v_{\text{del,d}}) + \frac{1}{1.5T_s}(V_{\text{t,d}}^* + \Delta v_{\text{t,d}}^*) \tag{B.28}$$

$$(\dot{V}_{\text{del,q}} + \Delta \dot{v}_{\text{del,q}}) = -\frac{1}{1.5T_s}(V_{\text{del,q}} + \Delta v_{\text{del,q}}) + \frac{1}{1.5T_s}(V_{\text{t,d}}^* + \Delta v_{\text{t,d}}^*) \tag{B.29}$$

And as the steady-state terms cancel out, they can be written as follows.

$$\Delta \dot{v}_{\text{del,d}} = -\frac{1}{1.5T_s}\Delta v_{\text{del,d}} + \frac{1}{1.5T_s}\Delta v_{\text{t,d}}^* \tag{B.30}$$

$$\Delta \dot{v}_{\text{del,q}} = -\frac{1}{1.5T_s}\Delta v_{\text{del,q}} + \frac{1}{1.5T_s}\Delta v_{\text{t,d}}^* \tag{B.31}$$

B.1.4 LCL Filter

The equations for the LCL filter can be defined as was done in Chapter 3 for the transfer function derivation.

$$\begin{cases}
\frac{di_{\text{t,d}}}{dt} = \frac{-R_f}{L_f}i_{\text{t,d}} + \omega i_{\text{t,q}} + \frac{1}{L_f}v_{\text{t,d}} - \frac{1}{L_f}v_{\text{o,d}} \\
\frac{di_{\text{t,q}}}{dt} = \frac{-R_f}{L_f}i_{\text{t,q}} - \omega i_{\text{t,d}} + \frac{1}{L_f}v_{\text{t,d}} - \frac{1}{L_f}v_{\text{o,q}} \\
\frac{dv_{\text{o,d}}}{dt} = \omega v_{\text{o,q}} + \frac{1}{C_f}i_{\text{t,d}} - \frac{1}{C_f}i_{\text{o,d}} \\
\frac{dv_{\text{o,q}}}{dt} = -\omega v_{\text{o,d}} + \frac{1}{C_f}i_{\text{t,q}} - \frac{1}{C_f}i_{\text{o,q}} \\
\frac{di_{\text{o,d}}}{dt} = \frac{-R_c}{L_c}i_{\text{o,d}} + \omega i_{\text{o,q}} + \frac{1}{L_c}v_{\text{o,d}} - \frac{1}{L_c}v_{\text{b,d}} \\
\frac{di_{\text{o,q}}}{dt} = \frac{-R_c}{L_c}i_{\text{o,q}} - \omega i_{\text{o,d}} + \frac{1}{L_c}v_{\text{o,q}} - \frac{1}{L_c}v_{\text{b,q}}
\end{cases} \tag{B.32}$$

Doing small-signal linearisation, the following can be achieved.

$$\left\{ \begin{array}{l} \frac{d}{dt} (I_{t,d} + \Delta i_{t,d}) = \frac{-R_f}{L_f} (I_{t,d} + \Delta i_{t,d}) + (\omega_n + \Delta\omega) (I_{t,q} + \Delta i_{t,q}) \\ \quad + \frac{1}{L_f} (V_{t,d} + \Delta v_{t,d}) - \frac{1}{L_f} (V_{o,d} + \Delta v_{o,d}) \\ \frac{d}{dt} (I_{t,q} + \Delta i_{t,q}) = \frac{-R_f}{L_f} (I_{t,q} + \Delta i_{t,q}) - (\omega_n + \Delta\omega) (I_{t,d} + \Delta i_{t,d}) \\ \quad + \frac{1}{L_f} (V_{t,d} + \Delta v_{t,d}) - \frac{1}{L_f} (V_{o,q} + \Delta v_{o,q}) \\ \frac{d}{dt} (V_{o,d} + \Delta v_{o,d}) = (\omega_n + \Delta\omega) (V_{o,q} + \Delta v_{o,q}) + \frac{1}{C_f} (I_{t,d} + \Delta i_{t,d}) \\ \quad - \frac{1}{C_f} (I_{o,d} + \Delta i_{o,d}) \\ \frac{d}{dt} (V_{o,q} + \Delta v_{o,q}) = -(\omega_n + \Delta\omega) (V_{o,d} + \Delta v_{o,d}) + \frac{1}{C_f} (I_{t,q} + \Delta i_{t,q}) \\ \quad - \frac{1}{C_f} (I_{o,q} + \Delta i_{o,q}) \\ \frac{d}{dt} (I_{o,d} + \Delta i_{o,d}) = \frac{-R_c}{L_c} (I_{o,d} + \Delta i_{o,d}) + (\omega_n + \Delta\omega) (I_{o,q} + \Delta i_{o,q}) \\ \quad + \frac{1}{L_c} (V_{o,d} + \Delta v_{o,d}) - \frac{1}{L_c} (V_{b,d} + \Delta v_{b,d}) \\ \frac{d}{dt} (I_{o,q} + \Delta i_{o,q}) = \frac{-R_c}{L_c} (I_{o,q} + \Delta i_{o,q}) - (\omega_n + \Delta\omega) (I_{o,d} + \Delta i_{o,d}) \\ \quad + \frac{1}{L_c} (V_{o,q} + \Delta v_{o,q}) - \frac{1}{L_c} (V_{b,q} + \Delta v_{b,q}) \end{array} \right. \quad (B.33)$$

Letting the steady-state terms cancel out, the final equations can be reached.

$$\left\{ \begin{array}{l} \frac{d\Delta i_{t,d}}{dt} = \frac{-R_f}{L_f} \Delta i_{t,d} + \omega_n \Delta i_{t,q} + \Delta\omega I_{t,q} + \frac{1}{L_f} \Delta v_{t,d} - \frac{1}{L_f} \Delta v_{o,d} \\ \frac{d\Delta i_{t,q}}{dt} = \frac{-R_f}{L_f} \Delta i_{t,q} - \omega_n \Delta i_{t,d} - \Delta\omega I_{t,d} + \frac{1}{L_f} \Delta v_{t,d} - \frac{1}{L_f} \Delta v_{o,q} \\ \frac{d\Delta v_{o,d}}{dt} = \omega_n \Delta v_{o,q} + \Delta\omega V_{o,q} + \frac{1}{C_f} \Delta i_{t,d} - \frac{1}{C_f} \Delta i_{o,d} \\ \frac{d\Delta v_{o,q}}{dt} = -\omega_n \Delta v_{o,d} - \Delta\omega V_{o,d} + \frac{1}{C_f} \Delta i_{t,q} - \frac{1}{C_f} \Delta i_{o,q} \\ \frac{d\Delta i_{o,d}}{dt} = \frac{-R_c}{L_c} \Delta i_{o,d} + \omega_n \Delta i_{o,q} + \Delta\omega I_{o,q} + \frac{1}{L_c} \Delta v_{o,d} - \frac{1}{L_c} \Delta v_{b,d} \\ \frac{d\Delta i_{o,q}}{dt} = \frac{-R_c}{L_c} \Delta i_{o,q} - \omega_n \Delta i_{o,d} - \Delta\omega I_{o,d} + \frac{1}{L_c} \Delta v_{o,q} - \frac{1}{L_c} \Delta v_{b,q} \end{array} \right. \quad (B.34)$$

B.1.5 PLL

The PLL is identical to what was presented in Chapter 3. The control equation can be written as follows.

$$\omega = \dot{\theta} = k_{p,PLL} v_{o,q} + k_{i,PLL} \int v_{o,q} dt + \omega_n \quad (B.35)$$

With the integral part of the PI controller being taken as an intermediate equation.

$$\rho = \int v_{o,q} dt \Rightarrow \frac{d\rho}{dt} = v_{o,q} \quad (B.36)$$

By applying small-signal linearisation, the following can be reached.

$$\dot{\Theta} + \Delta\dot{\theta} = k_{p,PLL} (V_{o,q} + \Delta v_{o,q}) + k_{i,PLL} (P + \Delta\rho) + \omega_n \quad (B.37)$$

This reduces to the following.

$$\Delta\dot{\theta} = k_{p,PLL} \Delta v_{o,q} + k_{i,PLL} \Delta\rho \quad (B.38)$$

$$\Delta\dot{\rho} = \Delta v_{o,q} \quad (B.39)$$

For the PLL rotation dynamics, the rotation can be expressed by the following equation.

$$T = \begin{bmatrix} \cos(\theta_{\text{PLL}} - \theta_0) & \sin(\theta_{\text{PLL}} - \theta_0) \\ -\sin(\theta_{\text{PLL}} - \theta_0) & \cos(\theta_{\text{PLL}} - \theta_0) \end{bmatrix} \approx \begin{bmatrix} 1 & \theta_{\text{PLL}} - \theta_0 \\ -(\theta_{\text{PLL}} - \theta_0) & 1 \end{bmatrix} \quad (\text{B.40})$$

Thus, a rotation can be applied to any variables in a dq frame, as seen in the following equation.

$$\begin{bmatrix} x_{\text{d}}^{\text{PLL}} \\ x_{\text{q}}^{\text{PLL}} \end{bmatrix} = \begin{bmatrix} 1 & \theta_{\text{PLL}} - \theta_0 \\ -(\theta_{\text{PLL}} - \theta_0) & 1 \end{bmatrix} \begin{bmatrix} x_{\text{d}}^0 \\ x_{\text{q}}^0 \end{bmatrix} \quad (\text{B.41})$$

By doing small-signal linearisation, the following equation can be achieved.

$$\begin{bmatrix} X_{\text{d}}^{\text{PLL}} + \Delta x_{\text{d}}^{\text{PLL}} \\ X_{\text{q}}^{\text{PLL}} + \Delta x_{\text{q}}^{\text{PLL}} \end{bmatrix} = \begin{bmatrix} 1 & \Delta\theta \\ -\Delta\theta & 1 \end{bmatrix} \begin{bmatrix} X_{\text{d}}^0 + \Delta x_{\text{d}}^0 \\ X_{\text{q}}^0 + \Delta x_{\text{q}}^0 \end{bmatrix} \quad (\text{B.42})$$

This can be reduced to the following equations by cancelling out the steady-state term.

$$\begin{bmatrix} X_{\text{d}}^{\text{PLL}} + \Delta x_{\text{d}}^{\text{PLL}} \\ X_{\text{q}}^{\text{PLL}} + \Delta x_{\text{q}}^{\text{PLL}} \end{bmatrix} = \begin{bmatrix} X_{\text{d}}^0 + \Delta x_{\text{d}}^0 + \Delta\theta(X_{\text{q}}^0 + \Delta x_{\text{q}}^0) \\ -\Delta\theta(X_{\text{d}}^0 + \Delta x_{\text{d}}^0) + X_{\text{q}}^0 + \Delta x_{\text{q}}^0 \end{bmatrix} \quad (\text{B.43})$$

$$\begin{bmatrix} \Delta x_{\text{d}}^{\text{PLL}} \\ \Delta x_{\text{q}}^{\text{PLL}} \end{bmatrix} = \begin{bmatrix} \Delta x_{\text{d}}^0 + \Delta\theta X_{\text{q}}^0 \\ -\Delta\theta X_{\text{d}}^0 + \Delta x_{\text{q}}^0 \end{bmatrix} = \begin{bmatrix} \Delta x_{\text{d}}^0 \\ \Delta x_{\text{q}}^0 \end{bmatrix} + \begin{bmatrix} X_{\text{q}}^0 \\ -X_{\text{d}}^0 \end{bmatrix} [\Delta\theta] \quad (\text{B.44})$$

B.1.6 Single Inverter

To begin with, insert power controller output, y_1 , into current controller.

$$\begin{aligned} \dot{x}_2 &= B_{\text{C1}} \left(C_{\text{P}} \begin{bmatrix} \Delta P \\ \Delta Q \\ \Delta\phi_{\text{d}} \\ \Delta\phi_{\text{q}} \end{bmatrix} + D_{\text{P}} \begin{bmatrix} \Delta P^* \\ \Delta Q^* \end{bmatrix} \right) + B_{\text{C2}} \begin{bmatrix} \Delta i_{\text{t,dq}} \\ \Delta v_{\text{o,dq}} \\ \Delta i_{\text{o,dq}} \end{bmatrix} + B_{\text{C2}} B_{\text{E}} \begin{bmatrix} \Delta\rho \\ \Delta\theta \end{bmatrix} \\ &= B_{\text{C1}} C_{\text{P}} \begin{bmatrix} \Delta P \\ \Delta Q \\ \Delta\phi_{\text{d}} \\ \Delta\phi_{\text{q}} \end{bmatrix} + B_{\text{C1}} D_{\text{P}} \begin{bmatrix} \Delta P^* \\ \Delta Q^* \end{bmatrix} + B_{\text{C2}} \begin{bmatrix} \Delta i_{\text{t,dq}} \\ \Delta v_{\text{o,dq}} \\ \Delta i_{\text{o,dq}} \end{bmatrix} + B_{\text{C2}} B_{\text{E}} \begin{bmatrix} \Delta\rho \\ \Delta\theta \end{bmatrix} \end{aligned} \quad (\text{B.45})$$

And insert it into the output.

$$\begin{aligned} y_2 &= C_{\text{C}} \Delta\gamma_{\text{dq}} + D_{\text{C1}} \left(C_{\text{P}} \begin{bmatrix} \Delta P \\ \Delta Q \\ \Delta\phi_{\text{d}} \\ \Delta\phi_{\text{q}} \end{bmatrix} + D_{\text{P}} \begin{bmatrix} \Delta P^* \\ \Delta Q^* \end{bmatrix} \right) + D_{\text{C2}} \begin{bmatrix} \Delta i_{\text{t,dq}} \\ \Delta v_{\text{o,dq}} \\ \Delta i_{\text{o,dq}} \end{bmatrix} + D_{\text{C2}} B_{\text{E}} \begin{bmatrix} \Delta\rho \\ \Delta\theta \end{bmatrix} \\ &= C_{\text{C}} \Delta\gamma_{\text{dq}} + D_{\text{C1}} C_{\text{P}} \begin{bmatrix} \Delta P \\ \Delta Q \\ \Delta\phi_{\text{d}} \\ \Delta\phi_{\text{q}} \end{bmatrix} + D_{\text{C1}} D_{\text{P}} \begin{bmatrix} \Delta P^* \\ \Delta Q^* \end{bmatrix} + D_{\text{C2}} \begin{bmatrix} \Delta i_{\text{t,dq}} \\ \Delta v_{\text{o,dq}} \\ \Delta i_{\text{o,dq}} \end{bmatrix} + D_{\text{C2}} B_{\text{E}} \begin{bmatrix} \Delta\rho \\ \Delta\theta \end{bmatrix} \end{aligned} \quad (\text{B.46})$$

Now, insert current controller output, y_2 , into delay model.

$$\begin{aligned}
\dot{x}_3 &= \begin{bmatrix} \Delta v_{\text{del,d}} \\ \Delta v_{\text{del,q}} \end{bmatrix} = A_{\text{del}} \begin{bmatrix} \Delta v_{\text{del,d}} \\ \Delta v_{\text{del,q}} \end{bmatrix} + B_{\text{del}} \\
&\quad \left(C_C \begin{bmatrix} \Delta \gamma_{\text{dq}} \end{bmatrix} + D_{C1} C_P \begin{bmatrix} \Delta P \\ \Delta Q \\ \Delta \phi_d \\ \Delta \phi_q \end{bmatrix} + D_{C1} D_P \begin{bmatrix} \Delta P^* \\ \Delta Q^* \end{bmatrix} + D_{C2} \begin{bmatrix} \Delta i_{\text{t,dq}} \\ \Delta v_{\text{o,dq}} \\ \Delta i_{\text{o,dq}} \end{bmatrix} + D_{C2} B_E \begin{bmatrix} \Delta \rho \\ \Delta \theta \end{bmatrix} \right) \\
&= A_{\text{del}} \begin{bmatrix} \Delta v_{\text{del,d}} \\ \Delta v_{\text{del,q}} \end{bmatrix} + B_{\text{del}} C_C \begin{bmatrix} \Delta \gamma_{\text{dq}} \end{bmatrix} + B_{\text{del}} D_{C1} C_P \begin{bmatrix} \Delta P \\ \Delta Q \\ \Delta \phi_d \\ \Delta \phi_q \end{bmatrix} \\
&\quad + B_{\text{del}} D_{C1} D_P \begin{bmatrix} \Delta P^* \\ \Delta Q^* \end{bmatrix} + B_{\text{del}} D_{C2} \begin{bmatrix} \Delta i_{\text{ldq}} \\ \Delta v_{\text{odq}} \\ \Delta i_{\text{odq}} \end{bmatrix} + B_{\text{del}} D_{C2} B_E \begin{bmatrix} \Delta \rho \\ \Delta \theta \end{bmatrix}
\end{aligned} \tag{B.47}$$

Now, insert PLL output, y_5 , into LCL filter.

$$\begin{aligned}
\dot{x}_4 &= A_{\text{LCL}} \begin{bmatrix} \Delta i_{\text{ldq}} \\ \Delta v_{\text{odq}} \\ \Delta i_{\text{odq}} \end{bmatrix} + A_{\text{LCL}} B_E \begin{bmatrix} \Delta \rho \\ \Delta \theta \end{bmatrix} + B_{\text{LCL1}} \begin{bmatrix} \Delta v_{\text{del,dq}}^* \end{bmatrix} + B_{\text{LCL2}} \begin{bmatrix} \Delta v_{\text{bdq}} \end{bmatrix} \\
&\quad + B_{\text{LCL3}} \left(C_{\text{PLL}} \begin{bmatrix} \Delta \rho \\ \Delta \theta \end{bmatrix} + D_{\text{PLL}} \begin{bmatrix} \Delta i_{\text{ldq}} \\ \Delta v_{\text{odq}} \\ \Delta i_{\text{odq}} \end{bmatrix} \right) \\
&= A_{\text{LCL}} \begin{bmatrix} \Delta i_{\text{ldq}} \\ \Delta v_{\text{odq}} \\ \Delta i_{\text{odq}} \end{bmatrix} + A_{\text{LCL}} B_E \begin{bmatrix} \Delta \rho \\ \Delta \theta \end{bmatrix} + B_{\text{LCL1}} \begin{bmatrix} \Delta v_{\text{del,dq}}^* \end{bmatrix} + B_{\text{LCL2}} \begin{bmatrix} \Delta v_{\text{bdq}} \end{bmatrix} \\
&\quad + B_{\text{LCL3}} C_{\text{PLL}} \begin{bmatrix} \Delta \rho \\ \Delta \theta \end{bmatrix} + B_{\text{LCL3}} D_{\text{PLL}} \begin{bmatrix} \Delta i_{\text{ldq}} \\ \Delta v_{\text{odq}} \\ \Delta i_{\text{odq}} \end{bmatrix}
\end{aligned} \tag{B.48}$$

Now writing each state-space model in order.

$$\dot{x}_1 = A_P \begin{bmatrix} \Delta P \\ \Delta Q \\ \Delta \phi_d \\ \Delta \phi_q \end{bmatrix} + B_{P1} \begin{bmatrix} \Delta i_{\text{ldq}} \\ \Delta v_{\text{odq}} \\ \Delta i_{\text{odq}} \end{bmatrix} + B_{P1} B_E \begin{bmatrix} \Delta \rho \\ \Delta \theta \end{bmatrix} + B_{P2} \begin{bmatrix} \Delta P^* \\ \Delta Q^* \end{bmatrix} \tag{B.49}$$

$$\dot{x}_2 = B_{C1} C_P \begin{bmatrix} \Delta P \\ \Delta Q \\ \Delta \phi_d \\ \Delta \phi_q \end{bmatrix} + B_{C2} \begin{bmatrix} \Delta i_{\text{ldq}} \\ \Delta v_{\text{odq}} \\ \Delta i_{\text{odq}} \end{bmatrix} + B_{C2} B_E \begin{bmatrix} \Delta \rho \\ \Delta \theta \end{bmatrix} + B_{C1} D_P \begin{bmatrix} \Delta P^* \\ \Delta Q^* \end{bmatrix} \tag{B.50}$$

$$\begin{aligned} \dot{x}_3 = & B_{\text{del}} D_{C1} C_P \begin{bmatrix} \Delta P \\ \Delta Q \\ \Delta \phi_d \\ \Delta \phi_q \end{bmatrix} + B_{\text{del}} C_C \begin{bmatrix} \Delta \gamma_{\text{dq}} \end{bmatrix} + A_{\text{del}} \begin{bmatrix} \Delta v_{\text{del},d} \\ \Delta v_{\text{del},q} \end{bmatrix} + B_{\text{del}} D_{C2} \begin{bmatrix} \Delta i_{\text{ldq}} \\ \Delta v_{\text{odq}} \\ \Delta i_{\text{odq}} \end{bmatrix} \\ & + B_{\text{del}} D_{C2} B_E \begin{bmatrix} \Delta \rho \\ \Delta \theta \end{bmatrix} + B_{\text{del}} D_{C1} D_P \begin{bmatrix} \Delta P^* \\ \Delta Q^* \end{bmatrix} \end{aligned} \quad (\text{B.51})$$

$$\begin{aligned} \dot{x}_4 = & B_{\text{LCL1}} \begin{bmatrix} \Delta v_{\text{del,dq}}^* \end{bmatrix} + (A_{\text{LCL}} + B_{\text{LCL3}} D_{\text{PLL}}) \begin{bmatrix} \Delta i_{\text{ldq}} \\ \Delta v_{\text{odq}} \\ \Delta i_{\text{odq}} \end{bmatrix} \\ & + (A_{\text{LCL}} B_E + B_{\text{LCL3}} C_{\text{PLL}}) \begin{bmatrix} \Delta \rho \\ \Delta \theta \end{bmatrix} + B_{\text{LCL2}} \begin{bmatrix} \Delta v_{\text{bdq}} \end{bmatrix} \end{aligned} \quad (\text{B.52})$$

$$\dot{x}_5 = B_{\text{PLL}} \begin{bmatrix} \Delta i_{\text{ldq}} \\ \Delta v_{\text{odq}} \\ \Delta i_{\text{odq}} \end{bmatrix} + A_{\text{PLL}} \begin{bmatrix} \Delta \rho \\ \Delta \theta \end{bmatrix} \quad (\text{B.53})$$

B.2 Multi Inverter State-Space Model

B.2.1 Modified Single Inverter

The PLL output and bus voltage can be inserted into the modified single inverter model, as seen in Equation (B.54).

$$\begin{aligned} \Delta \dot{x}_{\text{INV}i} = & A_{\text{INV}i} [\Delta x_{\text{INV}i}] + B_{\text{CORR}i} [\Delta x_{\text{PLL}}] + B_{\text{Xi}} C_{\text{PLL}} [\Delta x_{\text{PLL}}] + B_{\text{Xi}} D_{\text{PLL}} H [\Delta x_{\text{grid}}] \\ & + B_{\text{Xi}} D_{\text{PLL}} M C_{\text{INV}1} [\Delta x_{\text{INV}1}] + B_{\text{Xi}} D_{\text{PLL}} M C_{\text{INV}2} [\Delta x_{\text{INV}2}] \\ & + B_{\text{Xi}} D_{\text{PLL}} M C_{\text{INV}3} [\Delta x_{\text{INV}3}] + B_{\text{INV}i} H [\Delta x_{\text{grid}}] + B_{\text{INV}i} M C_{\text{INV}1} [\Delta x_{\text{INV}1}] \\ & + B_{\text{INV}i} M C_{\text{INV}2} [\Delta x_{\text{INV}2}] + B_{\text{INV}i} M C_{\text{INV}3} [\Delta x_{\text{INV}3}] \\ & + B_{\text{CTRL}i} \begin{bmatrix} \Delta P_i^* \\ \Delta Q_i^* \end{bmatrix} \end{aligned} \quad (\text{B.54})$$

By gathering by common inputs, the equation can be reduced, as seen in Equation (B.55).

$$\begin{aligned} \Delta \dot{x}_{\text{INV}i} = & A_{\text{INV}i} [\Delta x_{\text{INV}i}] + (B_{\text{Xi}} D_{\text{PLL}} + B_{\text{INV}i}) M C_{\text{INV}1} [\Delta x_{\text{INV}1}] \\ & + (B_{\text{Xi}} D_{\text{PLL}} + B_{\text{INV}i}) M C_{\text{INV}2} [\Delta x_{\text{INV}2}] + (B_{\text{Xi}} D_{\text{PLL}} + B_{\text{INV}i}) M C_{\text{INV}3} [\Delta x_{\text{INV}3}] \\ & + (B_{\text{CORR}i} + B_{\text{Xi}} C_{\text{PLL}}) [\Delta x_{\text{PLL}}] + (B_{\text{Xi}} D_{\text{PLL}} + B_{\text{INV}i}) H [\Delta x_{\text{grid}}] + B_{\text{CTRL}i} \begin{bmatrix} \Delta P_i^* \\ \Delta Q_i^* \end{bmatrix} \end{aligned} \quad (\text{B.55})$$

This then represents the state-space model of the i^{th} inverter. Notice the i in the equations, which denotes which matrices are specific to the inverter number.

Similar can be done for the grid state-space model, as seen in Equation (B.56).

$$\begin{aligned}\dot{\Delta x}_{\text{grid}} = & (A_G + B_{G1}H)[\Delta x_{\text{grid}}] + B_{G1}MC_{\text{INV1}}[\Delta x_{\text{INV1}}] + B_{G1}MC_{\text{INV2}}[\Delta x_{\text{INV2}}] \\ & + B_{G1}MC_{\text{INV3}}[\Delta x_{\text{INV3}}] + B_{G2}[\Delta v_{\text{g,dq}}] + B_{\text{EQ}}C_{\text{PLL}}[\Delta x_{\text{PLL}}] + B_{\text{EQ}}D_{\text{PLL}}H[\Delta x_{\text{grid}}] \\ & + B_{\text{EQ}}D_{\text{PLL}}MC_{\text{INV1}}[\Delta x_{\text{INV1}}] + B_{\text{EQ}}D_{\text{PLL}}MC_{\text{INV2}}[\Delta x_{\text{INV2}}] \\ & + B_{\text{EQ}}D_{\text{PLL}}MC_{\text{INV3}}[\Delta x_{\text{INV3}}]\end{aligned}\tag{B.56}$$

Which reduces to Equation (B.57).

$$\begin{aligned}\dot{\Delta x}_{\text{grid}} = & (A_G + B_{G1}H + B_{\text{EQ}}D_{\text{PLL}}H)[\Delta x_{\text{grid}}] + (B_{G1}MC_{\text{INV1}} + B_{\text{EQ}}D_{\text{PLL}}MC_{\text{INV1}})[\Delta x_{\text{INV1}}] \\ & + (B_{G1}MC_{\text{INV2}} + B_{\text{EQ}}D_{\text{PLL}}MC_{\text{INV2}})[\Delta x_{\text{INV2}}] \\ & + (B_{G1}MC_{\text{INV3}} + B_{\text{EQ}}D_{\text{PLL}}MC_{\text{INV3}})[\Delta x_{\text{INV3}}] + B_{\text{EQ}}C_{\text{PLL}}[\Delta x_{\text{PLL}}] + B_{G2}[\Delta v_{\text{g,dq}}]\end{aligned}\tag{B.57}$$

B.3 POD State-Space Model

When deriving the state-space model for the washout filter, the use of the intermediate state, Z' , has to be used. The washout filter is split into two equations as follows.

$$\frac{Z(s)}{W(s)} = \frac{T_W s}{T_W s + 1} \Rightarrow \frac{Z'(s)}{W(s)} = \frac{1}{T_W s + 1} \quad \frac{Z(s)}{Z'(s)} = T_W s\tag{B.58}$$

Starting with the first, which is equivalent to a washout filter, the transfer function can be made into the following equation.

$$\frac{Z'(s)}{W(s)} = \frac{1}{T_W s + 1} \Rightarrow Z'(s)(T_W s + 1) = W(s)\tag{B.59}$$

By doing small-signal linearisation, the state-space model can be made for this part of the filter, as seen in the following equation.

$$\dot{\Delta z}'T_W + \Delta z' = \Delta w \Rightarrow \dot{\Delta z}' = -\frac{1}{T_W}\Delta z' + \frac{1}{T_W}\Delta w\tag{B.60}$$

However, the last part of the filter should be included. The following equations shows the isolation of the output of the washout filter, namely Z .

$$\frac{Z(s)}{Z'(s)} = T_W s \Rightarrow Z(s) = Z'(s)T_W s\tag{B.61}$$

By doing small-signal linearisation, the algebraic equation can be made, and by inserting for the derivative term of the intermediate state, $\dot{\Delta z}'$, the following equation can be reached.

$$\Delta z = -\dot{\Delta z}'T_W \Rightarrow \Delta z = -\Delta z' + \Delta w\tag{B.62}$$

This functions as the output of the state-space model of the washout filter.

A similar approach can be taken for the lead-lag filters, except that the numerator differs. The transfer functions can be split into two parts, as seen in the following equation.

$$\frac{H(s)}{Z(s)} = \frac{T_1 s + 1}{T_2 s + 1} \Rightarrow \frac{H'(s)}{Z(s)} = \frac{1}{T_2 s + 1} \quad \frac{H(s)}{H'(s)} = T_1 s + 1\tag{B.63}$$

The first part can be put on the correct form, as seen in the following equation.

$$\frac{H'(s)}{Z(s)} = \frac{1}{T_2 s + 1} \Rightarrow H'(s)(T_2 s + 1) = Z(s) \quad (\text{B.64})$$

By doing small-signal linearisation and isolating for the derivative term, the state-space model can be made.

$$\Delta \dot{h}' T_2 + \Delta h' = \Delta z \Rightarrow \Delta \dot{h}' = -\frac{1}{T_2} \Delta h' + \frac{1}{T_2} \Delta z \quad (\text{B.65})$$

Similar, the last part of the transfer function can be put on the correct form, as seen in the following equation.

$$\frac{H(s)}{H'(s)} = T_1 s + 1 \Rightarrow H(s) = H'(s)(T_1 s + 1) \quad (\text{B.66})$$

By doing small signal linearisation and moving around, the output equation can be made, as seen in the following equation.

$$\Delta h = \Delta \dot{h}' T_1 + \Delta h' = \left(1 - \frac{T_1}{T_2}\right) \Delta h' + \frac{T_1}{T_2} \Delta z \quad (\text{B.67})$$

Nothing needs to be inserted into state-space models of the low-pass filter and washout filter. However, the output of the washout filter needs to be inserted into the state-space model of the first lead-lag state-space model. The output can be seen inserted into the state-space model in Equation (B.68).

$$\Delta \dot{h}' = -\frac{1}{T_2} \Delta h' + \frac{1}{T_2} (-\Delta z' + \Delta w) = -\frac{1}{T_2} \Delta h' - \frac{1}{T_2} \Delta z' + \frac{1}{T_2} \Delta w \quad (\text{B.68})$$

Similar can be done for the output equation, as seen in Equation (B.69).

$$\Delta h = \left(1 - \frac{T_1}{T_2}\right) \Delta h' + \frac{T_1}{T_2} (-\Delta z' + \Delta w) = \left(1 - \frac{T_1}{T_2}\right) \Delta h' - \frac{T_1}{T_2} \Delta z' + \frac{T_1}{T_2} \Delta w \quad (\text{B.69})$$

The same approach is taken for the second lead lag filter, except it will be Equation (B.69) that will be inserted. This can be seen in Equation (B.70).

$$\begin{aligned} \Delta \dot{d}' &= -\frac{1}{T_4} \Delta d' + \frac{1}{T_4} \left(\left(1 - \frac{T_1}{T_2}\right) \Delta h' - \frac{T_1}{T_2} \Delta z' + \frac{T_1}{T_2} \Delta w \right) \\ &= -\frac{1}{T_4} \Delta d' + \left(\frac{1}{T_4} - \frac{T_1}{T_2 T_4} \right) \Delta h' - \frac{T_1}{T_2 T_4} \Delta z' + \frac{T_1}{T_2 T_4} \Delta w \end{aligned} \quad (\text{B.70})$$

Similar can be done for the output equation, as seen in Equation (B.71).

$$\begin{aligned} \Delta d &= \left(1 - \frac{T_3}{T_4}\right) \Delta d' + \frac{T_3}{T_4} \left(\left(1 - \frac{T_1}{T_2}\right) \Delta h' - \frac{T_1}{T_2} \Delta z' + \frac{T_1}{T_2} \Delta w \right) \\ &= \left(1 - \frac{T_3}{T_4}\right) \Delta d' + \left(\frac{T_3}{T_4} - \frac{T_1 T_3}{T_2 T_4} \right) \Delta h' - \frac{T_1 T_3}{T_2 T_4} \Delta z' + \frac{T_1 T_3}{T_2 T_4} \Delta w \end{aligned} \quad (\text{B.71})$$

B.4 Comparison of SSM to Simulation

B.4.1 Single Inverter Comparison

Active Power Step Down

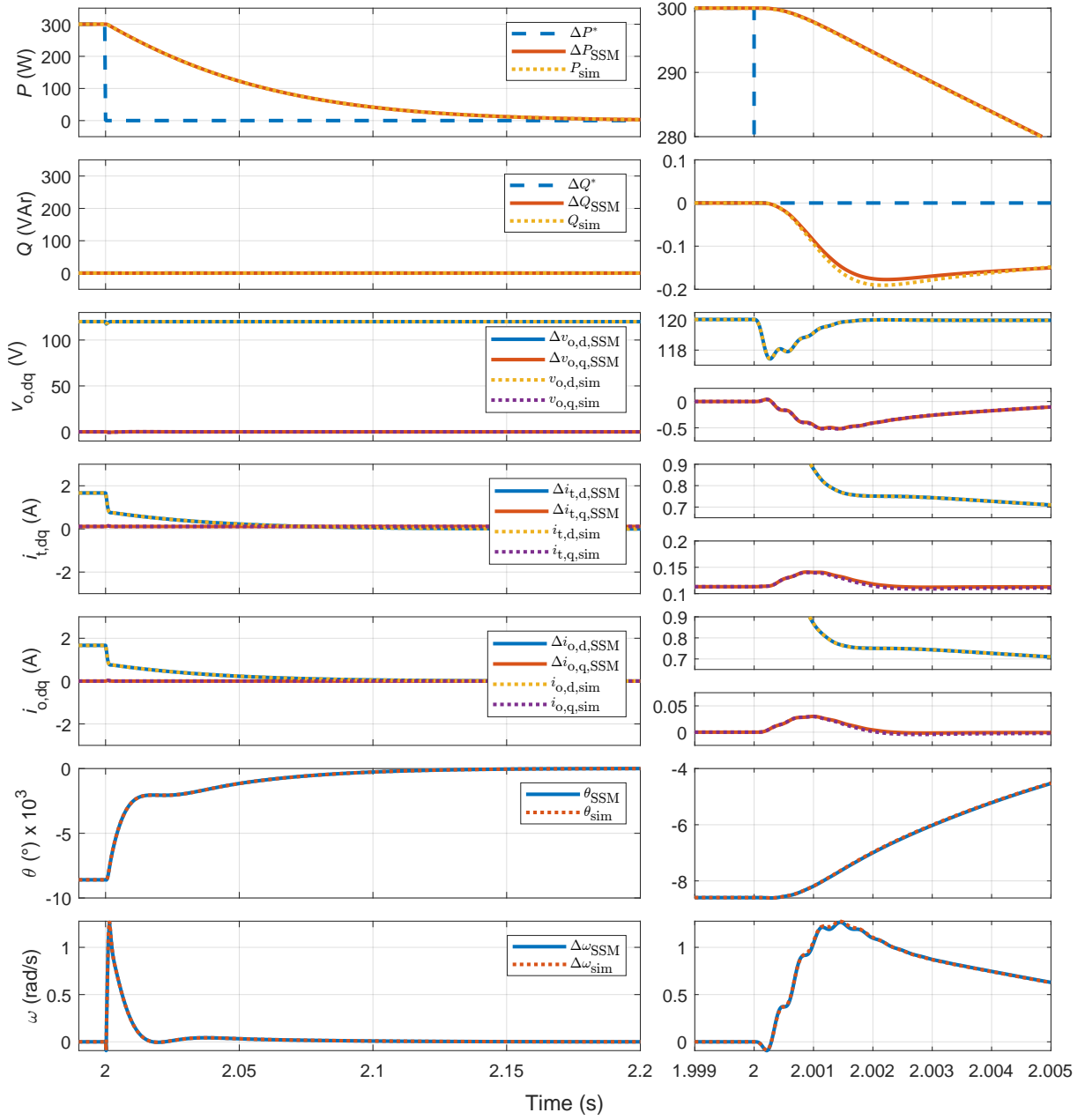


Figure B.4.1 Comparison of non-integrator state variables to simulation results

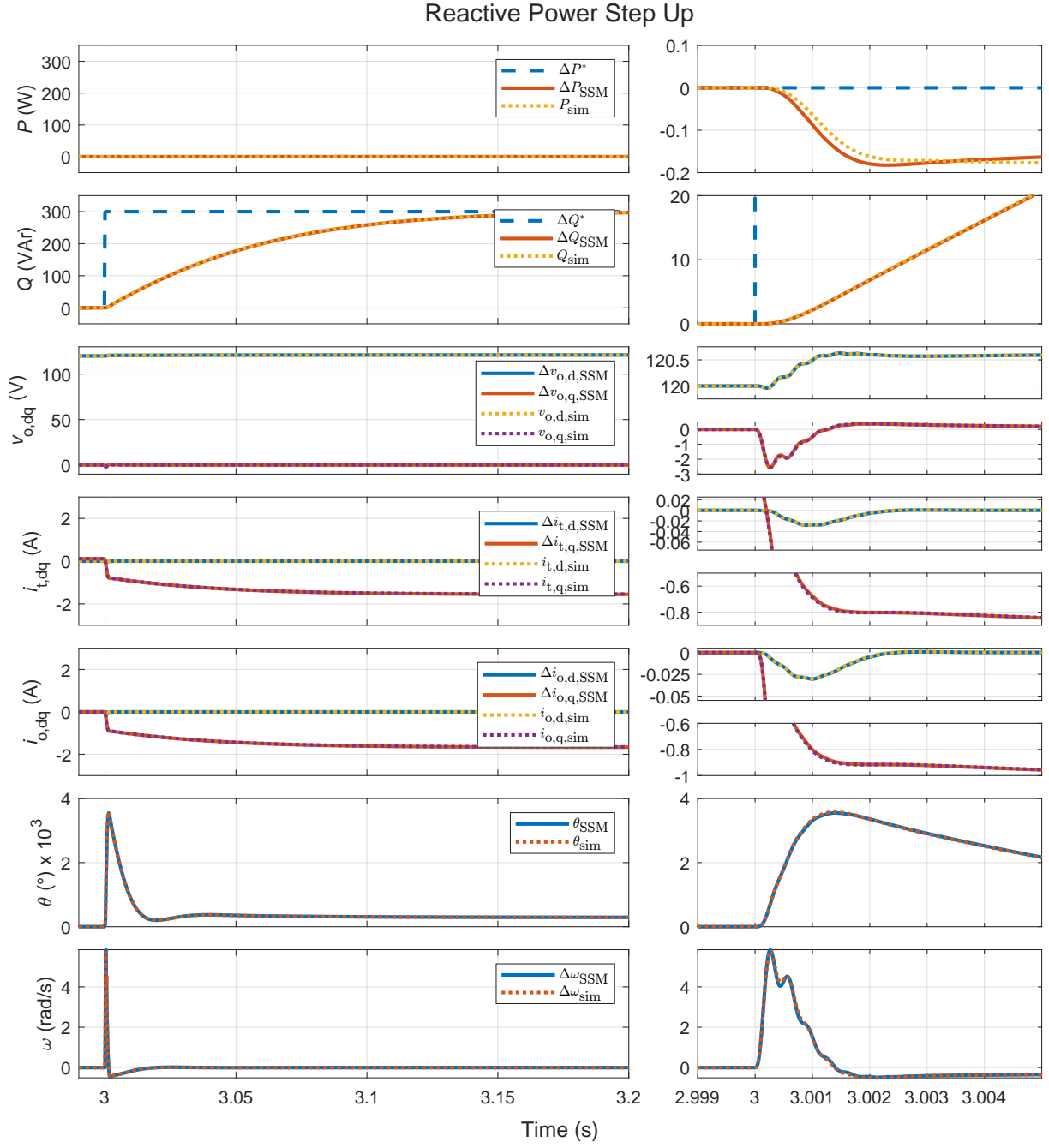


Figure B.4.2 Comparison of non-integrator state variables to simulation results

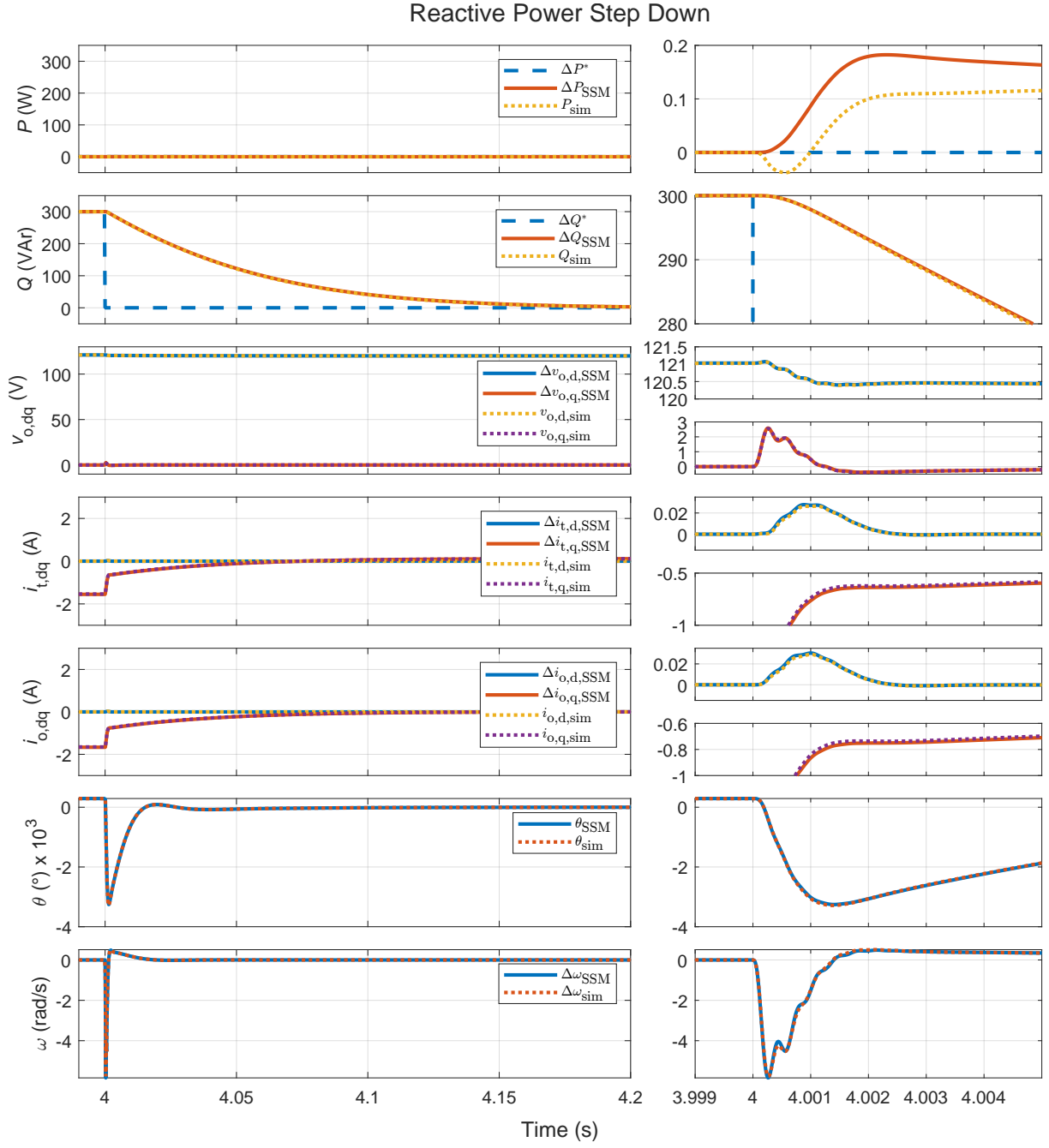


Figure B.4.3 Comparison of non-integrator state variables to simulation results

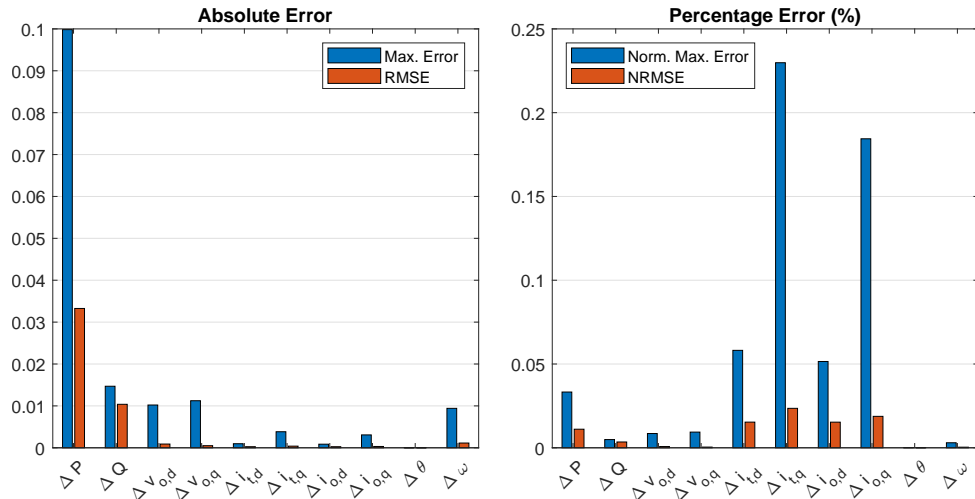


Figure B.4.4 Bar chart of absolute errors and percentage errors for an active power step down.

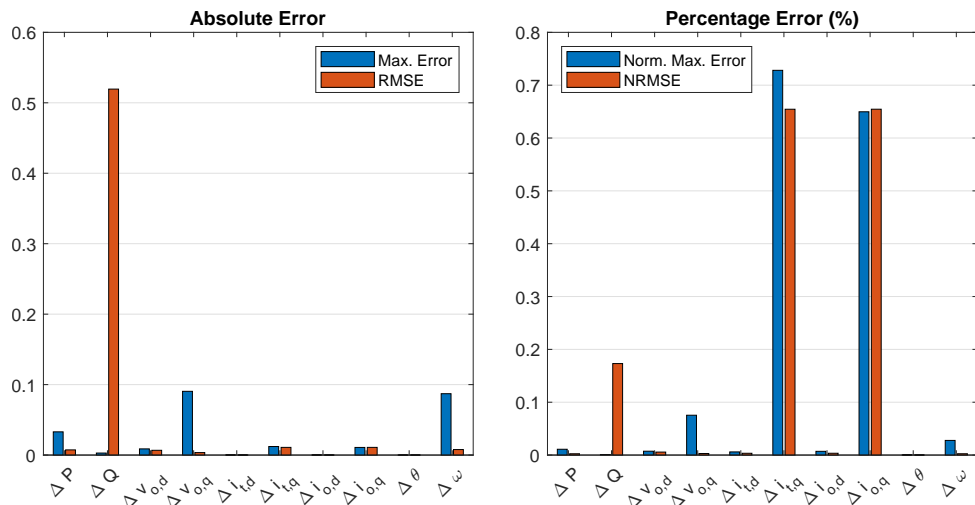


Figure B.4.5 Bar chart of absolute errors and percentage errors for an reactive power step up.

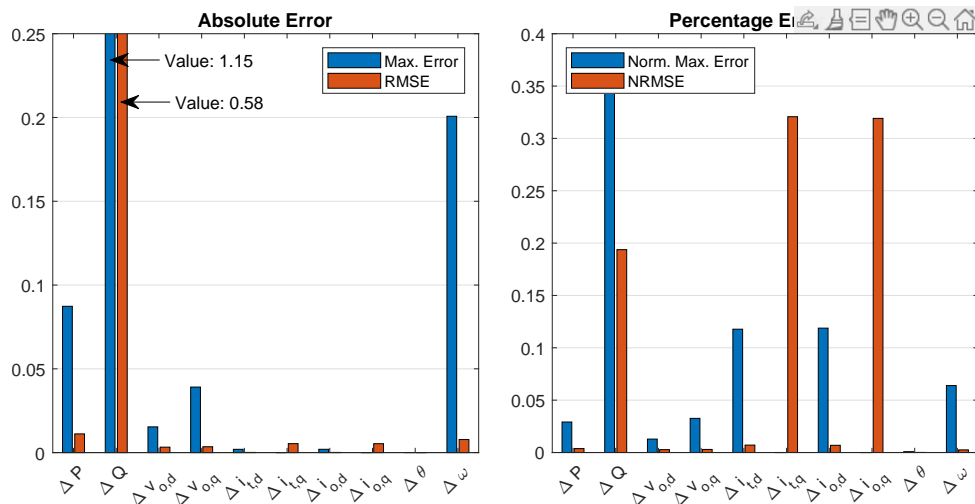


Figure B.4.6 Bar chart of absolute errors and percentage errors for an reactive power step down.

Comparing Results with Different Solver Settings

Throughout many iterations of simulations it was discovered that there was a noticeable difference in results depending on solver settings. Of course, when using a discrete solver compared to continuous solver had significant impact, due to inherent zero-order hold function, unit delay and more. However, when a continuous model was compared to the state-space model, some discrepancy was discovered. Though, similar the results differed in dynamics. This can be seen on the left column in Figure B.4.7.

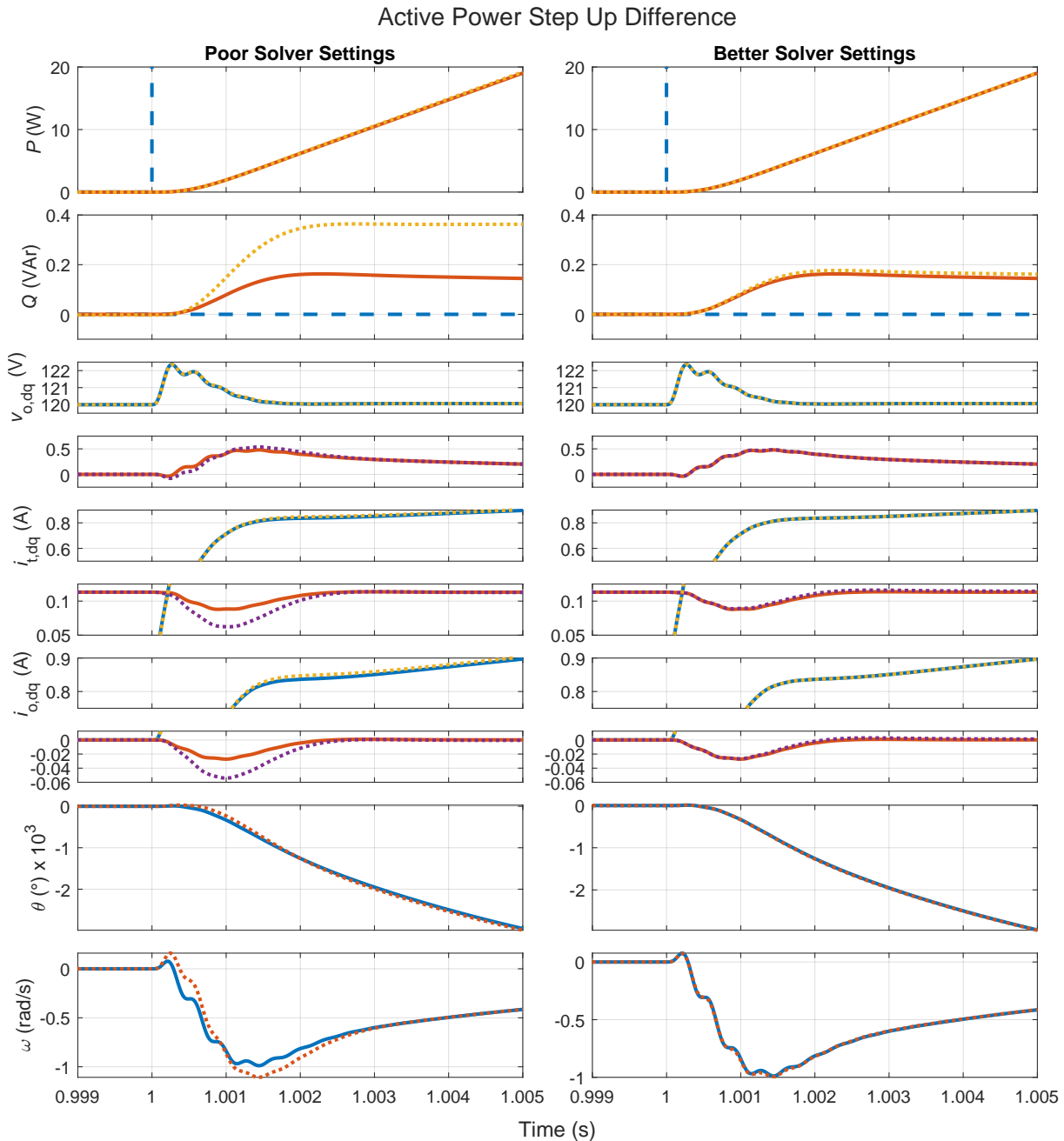


Figure B.4.7 Comparison of results for two different solver settings (solid: state-space model; dashed: simulation).

When the solver settings were iteratively changed and results examined, it was evident that it had an impact on the dynamics. When increasing the relative tolerance of the solver and

using MATLAB Simulink's algebraic loop solver instead of adding a small transport delay, e.g. $1 \cdot 10^{-6}$ s, the results became much more similar to the results of the state-space model. This can be seen on the right column in Figure B.4.7. Though the error on the left column is small, the dynamics were not matched. On the right column, the dynamics are almost exactly matched. With more time invested in the specifics of solver setting, the error can likely be reduced even further. However, the computational time also increased a lot with the better settings. Additionally, since the dynamics slightly differ, this can also have an effect on stability, especially near the stability boundary, where non-linear effects are more prevalent. This will likely also have an effect on the eigenvalue stability analysis.

In this case, several simulation settings were modified to improve the alignment between the Simulink model and the corresponding state-space model. Specifically, the relative tolerance was adjusted from $1 \cdot 10^{-3}$ to $1 \cdot 10^{-6}$, the solver was explicitly set to ode45 (Dormand-Prince), the "Enable minimal zero-crossing impact integration" option was activated, and the "Normalize using nominal values" setting was enabled. Furthermore, it was observed that even minor transport delays had a substantial impact on the simulation behaviour. It remains uncertain whether all of these adjustments are necessary to achieve accurate correspondence with the state-space model. However, due to time constraints, no further investigation into the issue was conducted.

B.4.2 Multi Inverter Comparison

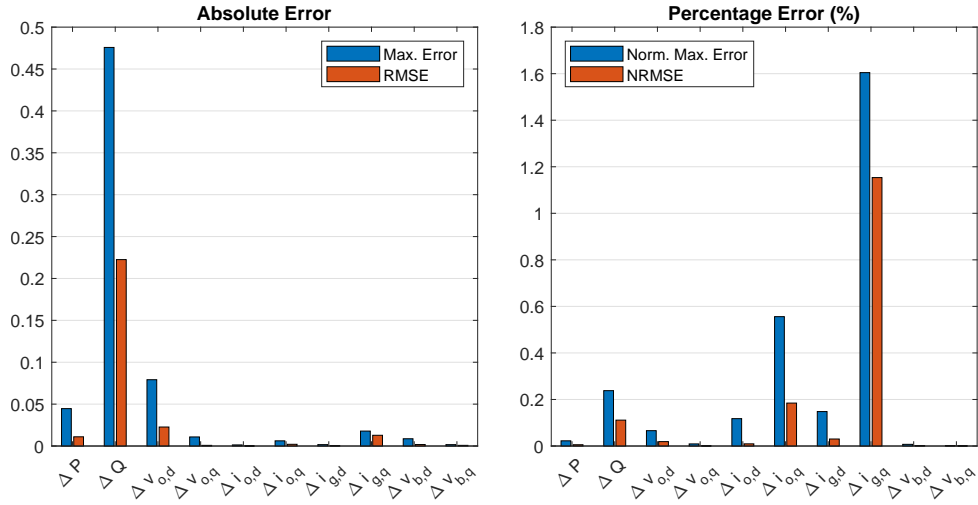


Figure B.4.8 Bar chart of absolute errors and percentage errors for inverter 1 for an active power step down.

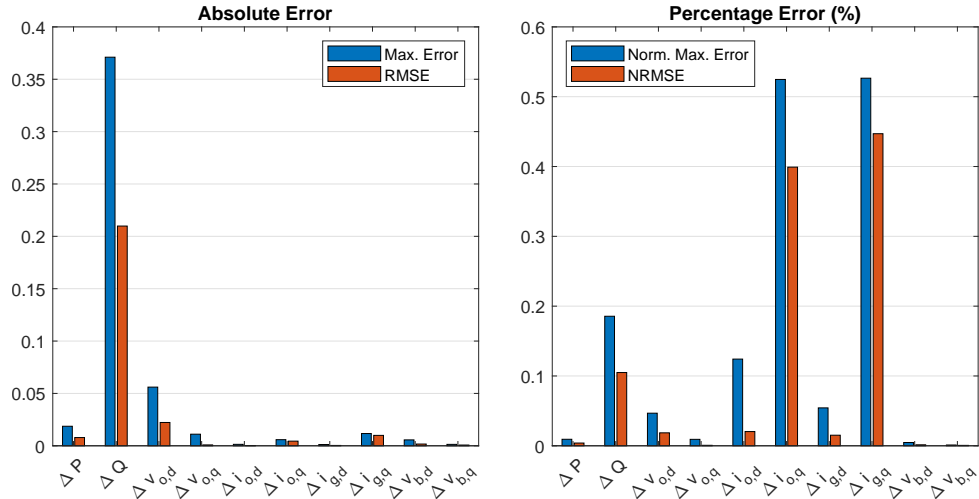


Figure B.4.9 Bar chart of absolute errors and percentage errors for inverter 2 for an active power step up.

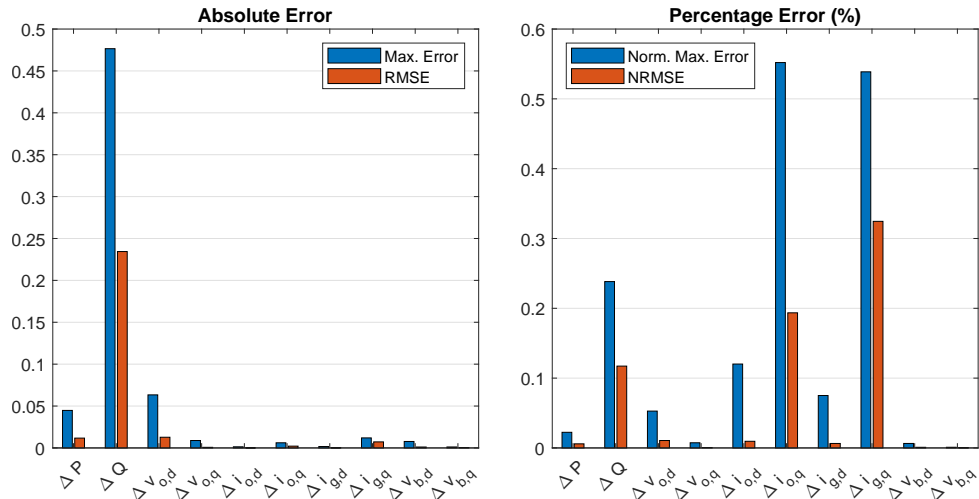


Figure B.4.10 Bar chart of absolute errors and percentage errors for inverter 2 for an active power step down.

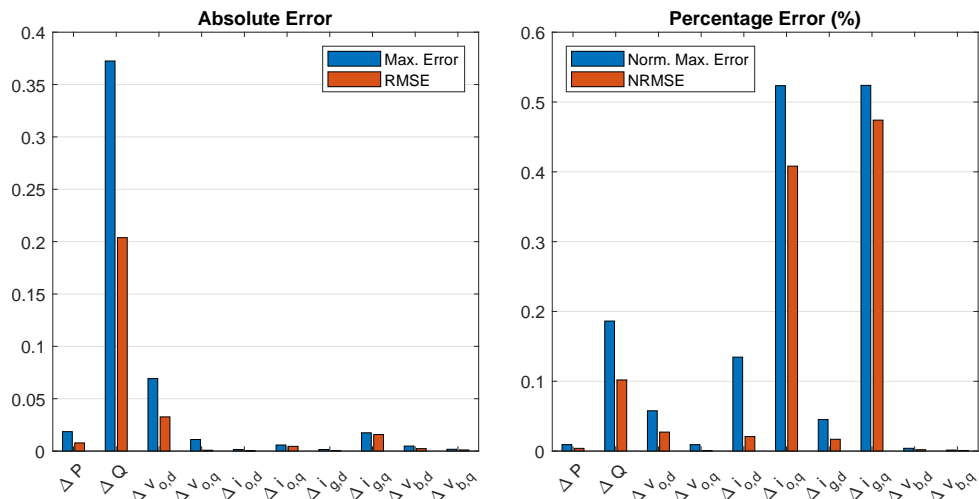


Figure B.4.11 Bar chart of absolute errors and percentage errors for inverter 3 for an active power step up.

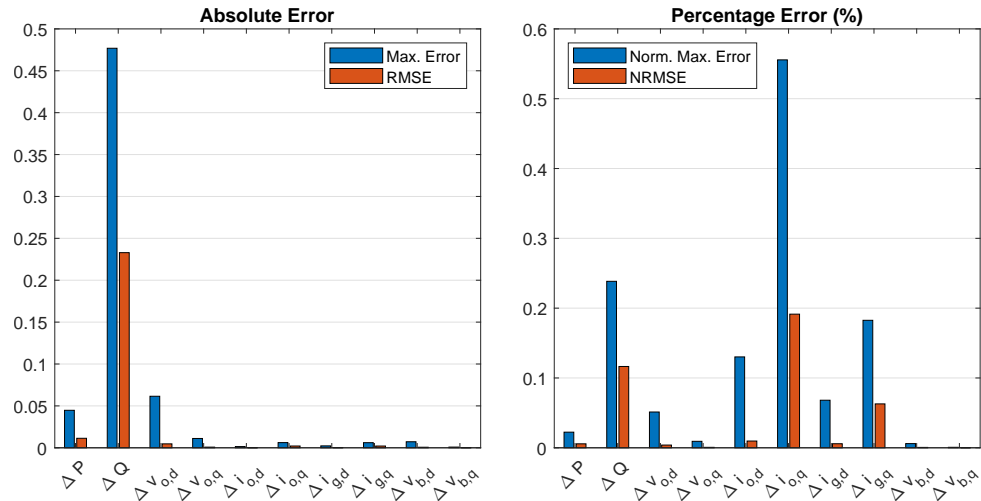


Figure B.4.12 Bar chart of absolute errors and percentage errors for inverter 3 for an active power step down.

B.4.3 Stability Analysis Comparison

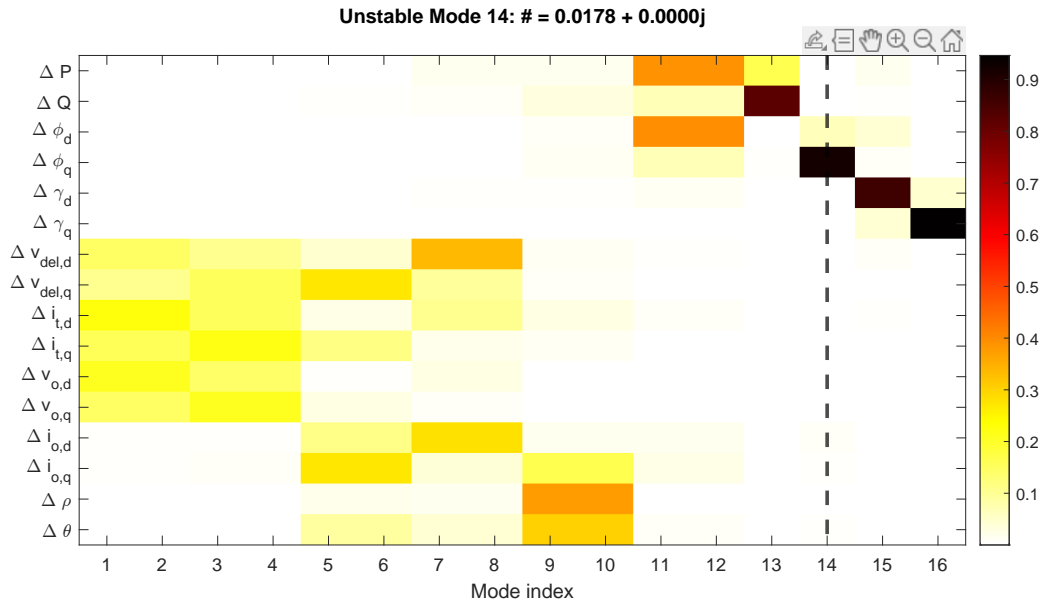


Figure B.4.13 Heat map of participation factor of each state variable belonging to each eigenvector at 600 W.

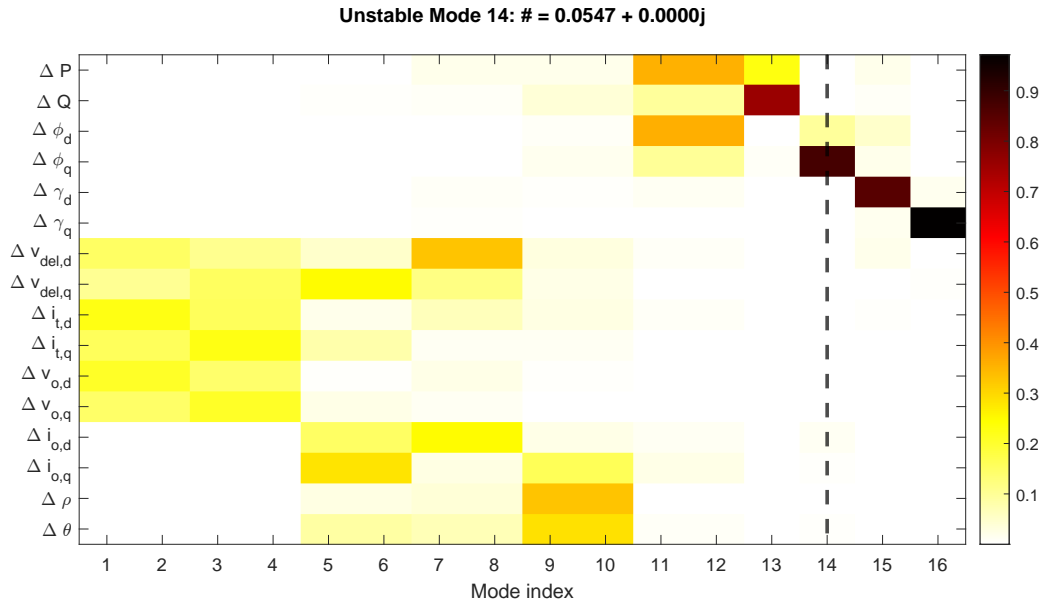


Figure B.4.14 Heat map of participation factor of each state variable belonging to each eigenvector at 300 W.

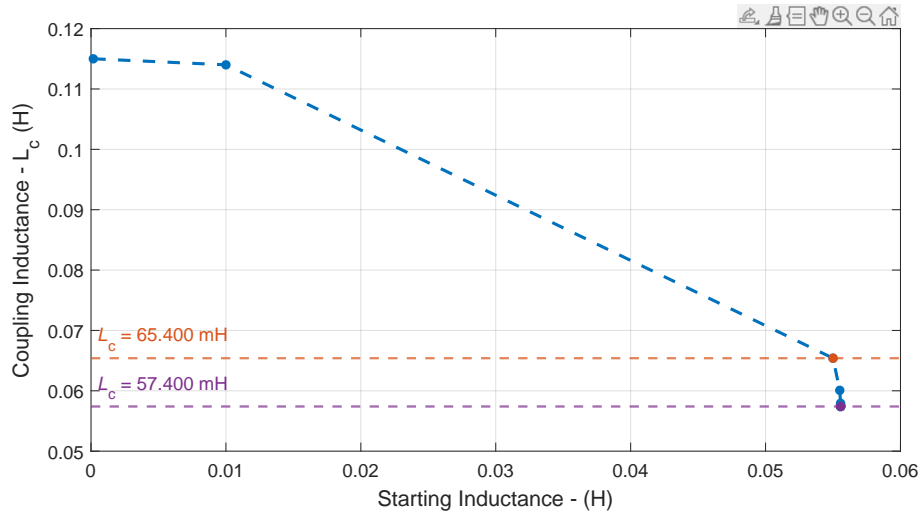


Figure B.4.15 Convergence of instability against starting inductance for active power of 600 W.

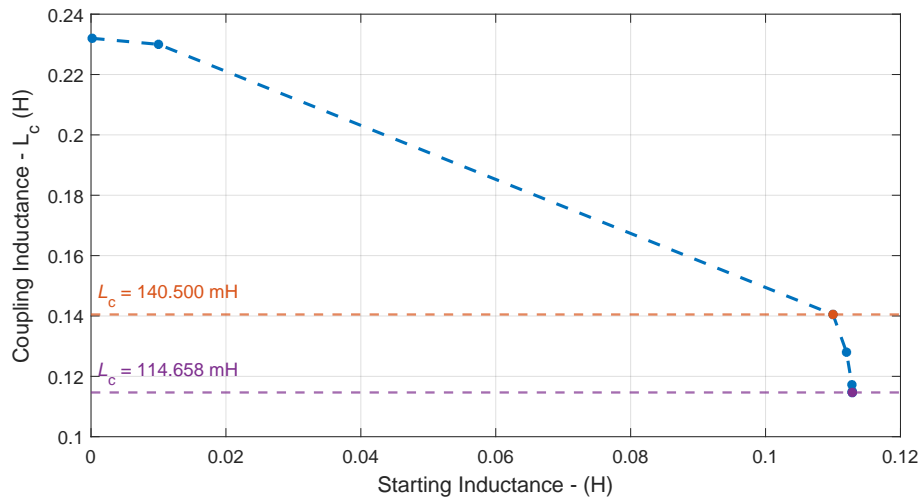


Figure B.4.16 Convergence of instability against starting inductance for active power of 300 W.

C Experimental Validation

C.1 Single Inverter

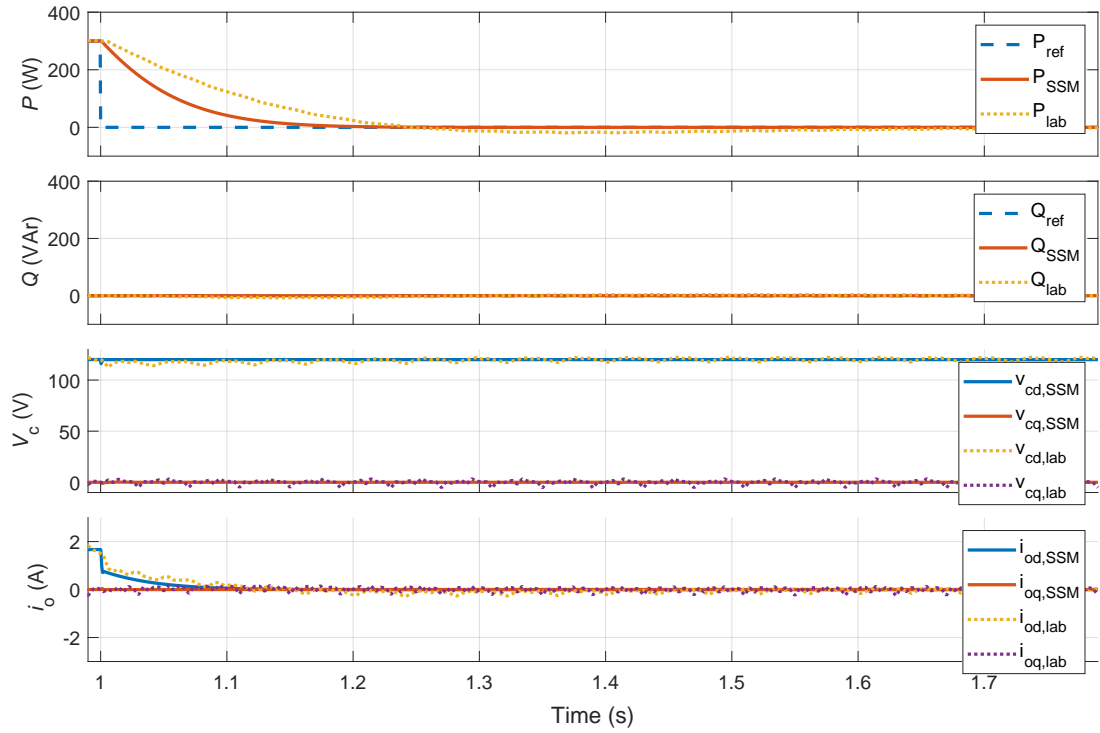


Figure C.1.1 Comparison of experimental results to SSM for a 300W active power step down.

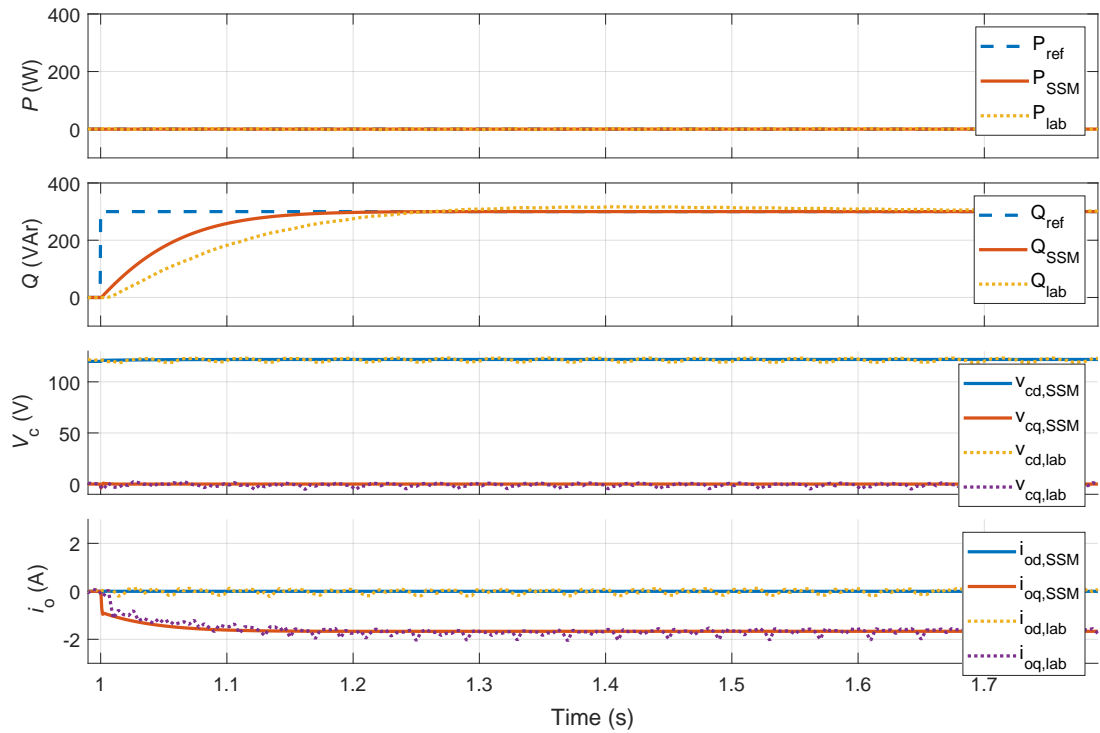


Figure C.1.2 Comparison of experimental results to SSM for a 300VAr reactive power step up.

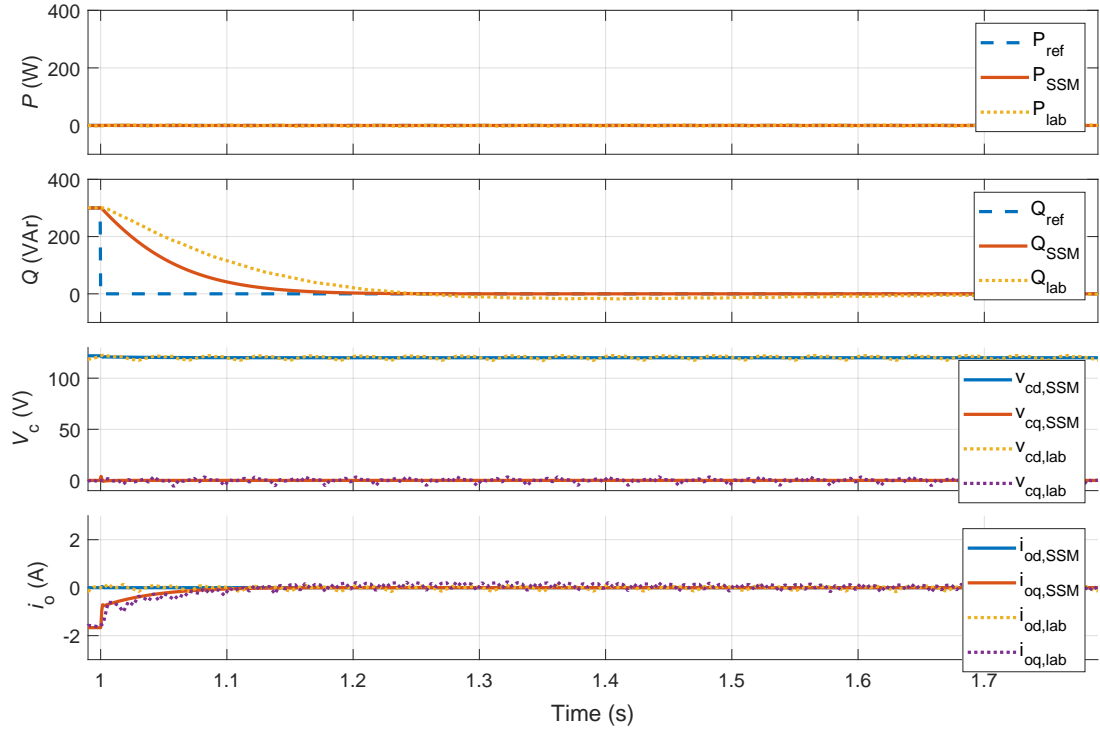


Figure C.1.3 Comparison of experimental results to SSM for a 300VAr reactive power step down.

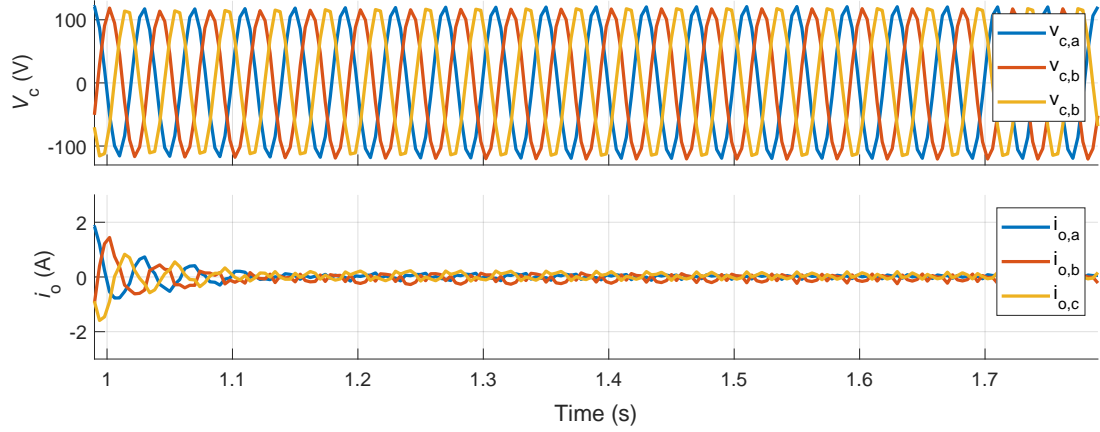


Figure C.1.4 Experimental results during a 300W active power step down.

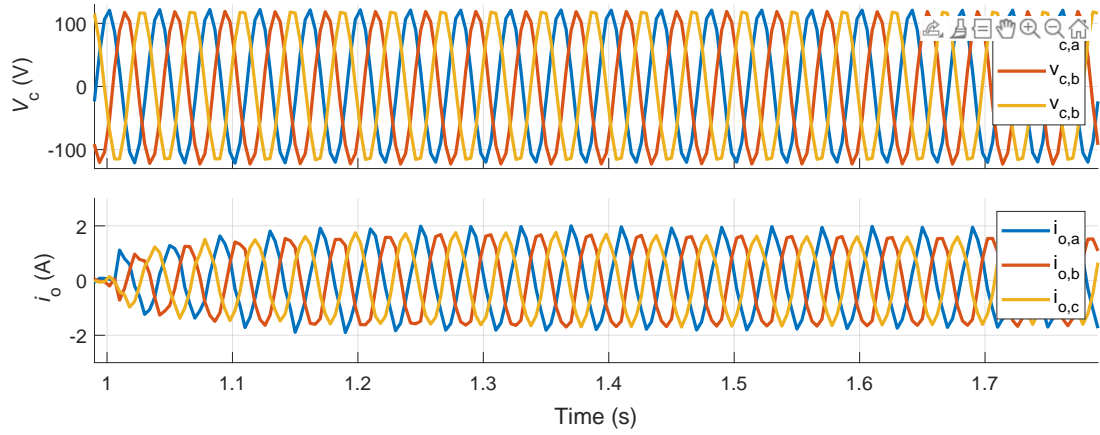


Figure C.1.5 Experimental results during a 300VAr reactive power step up.

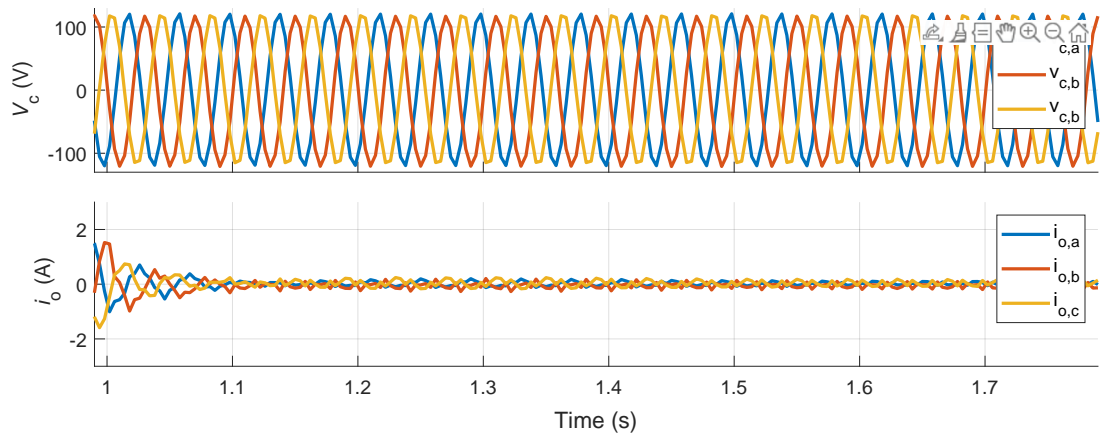


Figure C.1.6 Experimental results during a 300VAr reactive power step down.

C.2 Multi Inverter

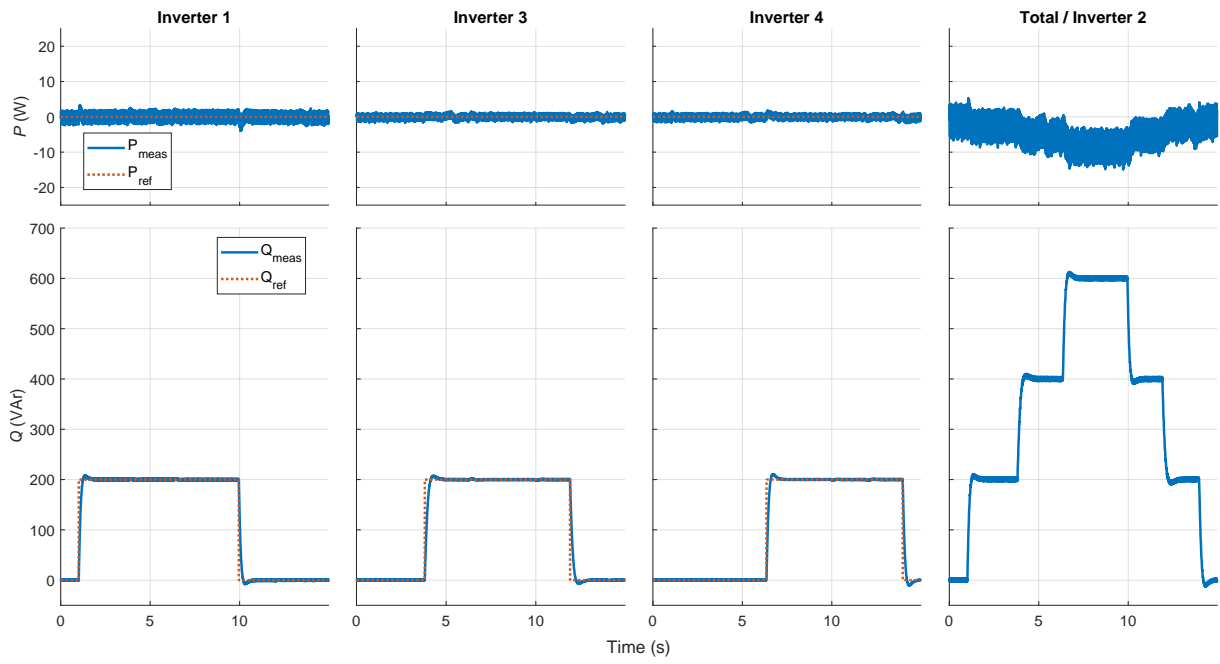


Figure C.2.1 Multi inverter reactive power steps.

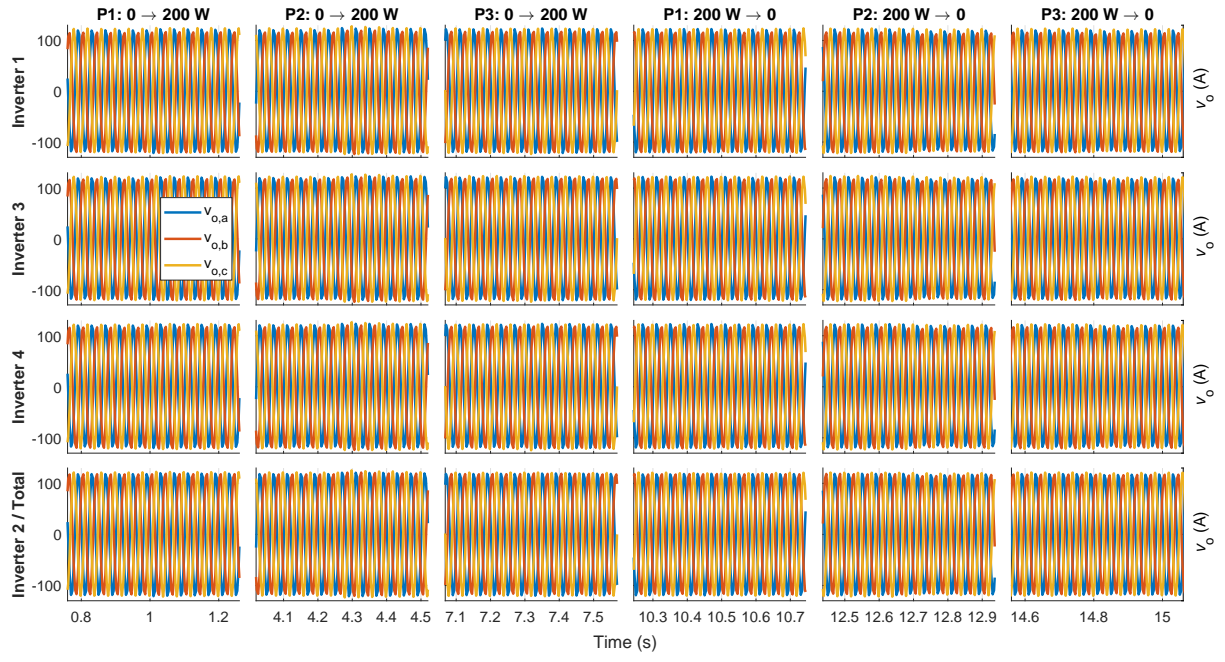


Figure C.2.2 Capacitor voltage of each inverter for each active power step.

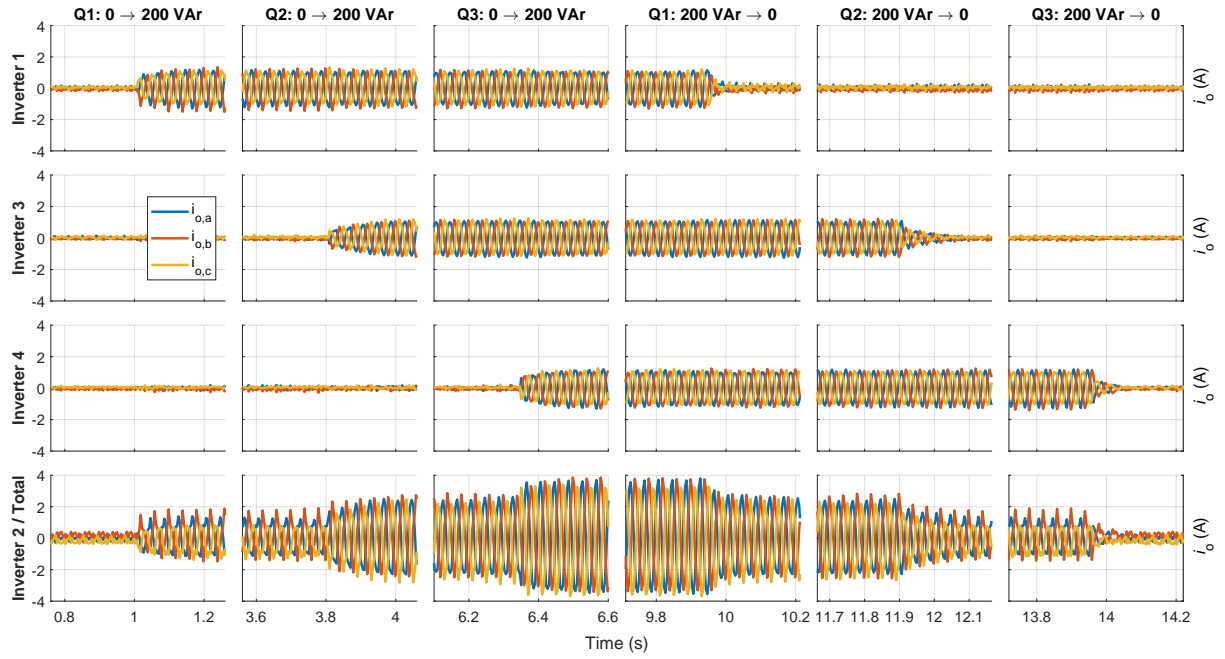


Figure C.2.3 Output current of each inverter for each reactive power step.

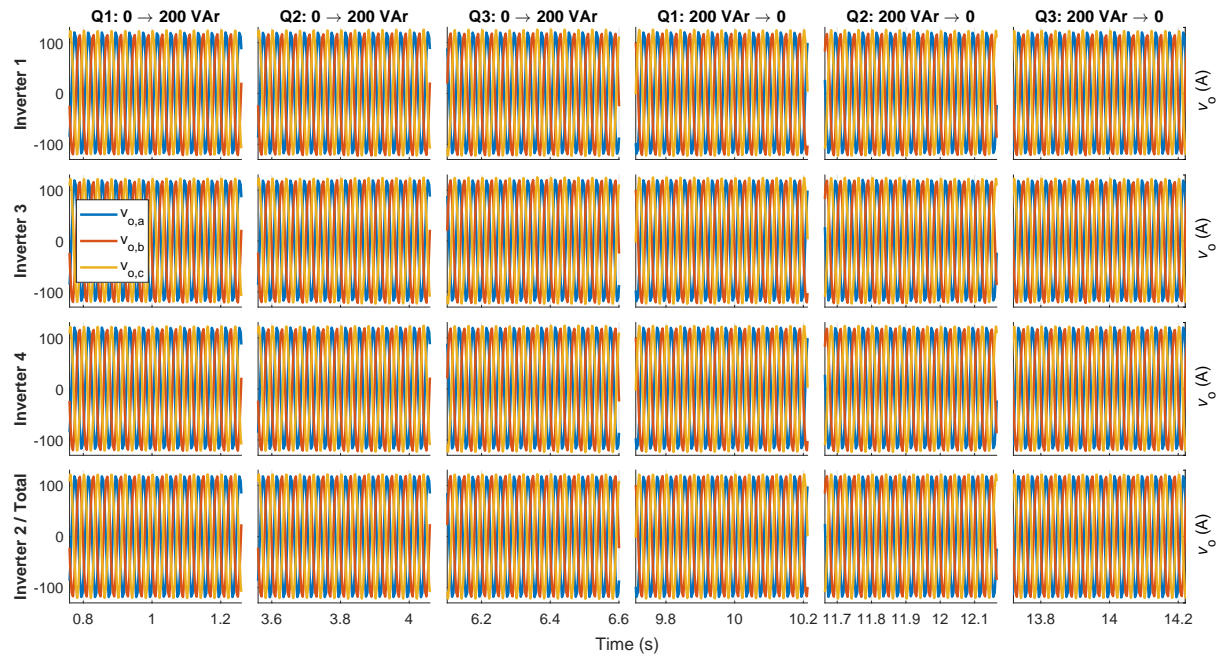


Figure C.2.4 Capacitor voltage of each inverter for each active power step.